REPUBLIQUE ALGERIENNE DEMOCRATIQUE ET POPULAIRE

Ministère de l'Enseignement Supérieur et de la Recherche Scientifique

Université du 20 Août 1955 Skikda

Faculté de Technologie

Département de Génie Mécanique

N° d'ordre : D012126003D

Thèse de doctorat

Présentée en vue de l'obtention du diplôme de

Docteur en Électromécanique (LMD)

Spécialité : Électromécanique

Par :

BELDJAATIT Chahinez

Contribution aux techniques de diagnostic et pronostic d'un système de conversion d'énergie de type éolienne

Soutenue le :14/01/2026

Devant le Jury composé par :

Nom et prénom	Grade	Qualité	Affiliation
KELLAIAIA Ridha	Professeur	Président	Université 20 août 1955-Skikda
SEBBAGH Toufik	MCA	Rapporteur	Université 20 août 1955-Skikda
KHERIEF Nacereddine Mohamed	Professeur	Examinateur	ENSET-Skikda
BOUSSAHA Elhadi	MCA	Examinateur	Université 20 août 1955-Skikda
MATTALLAH Sabrina	MCA	Examinateur	Université 20 août 1955-Skikda

Année universitaire : 2025/2026

PEOPLE'S DEMOCRATIC REPUBLIC OF ALGERIA

Ministry of Higher Education and Scientific Research

University of 20 August 1955 Skikda

Faculty of Technology

Mechanical Engineering Department

Ref: D012126003D

THESIS

Presented with a view to obtaining the diploma of

DOCTOR

Sector: Electromechanics

Speciality: Electromechanics

By:

BELDJAATIT Chahinez

Contribution to diagnosis and prognosis techniques for a wind-type energy conversion system

Defended on:14/01/2026

Before a jury composed of:

Name and Surname	Grade	Quality	Affiliation
KELLAIAIA Ridha	Professor	President	University of Skikda
SEBBAGH Toufik	MCA	Supervisor	University of Skikda
KHERIEF Nacereddine Mohamed	Professor	Examiner	ENSET-Skikda
BOUSSAHA Elhadi	MCA	Examiner	University of Skikda
MATTALLAH Sabrina	MCA	Examiner	University of Skikda

Academic year : 2025/2026


بسم الله الرحمن الرحيم

Dedication

To my beloved family,
whose unwavering love, patience, and encouragement have been my most meaningful source of strength.

I dedicate this work to my beloved parents, whose unconditional love, support, and sacrifices have been the foundation of my success. To my dear mother, whose endless care, encouragement, and strength have guided me through every step of this journey, and to my father, whose wisdom and quiet perseverance have inspired me to keep moving forward, I am deeply grateful for all you have done to help me reach this milestone.

To my sisters, ***Khawla****,* ***Wiam****, and* ***Loudjaine****, and my brothers,* ***Yasser*** *and* ***Amine****, for their support, humor, and motivation that helped me keep going.*

To my friends for their unwavering support, kindness, and encouragement during the most challenging moments.

Finally, to everyone who stood by me throughout this journey, your presence meant more than words can express.

Acknowledgments

First and foremost, I thank Allah for all the bounties and opportunities he has bestowed upon me throughout my life, especially for providing me with such a fantastic opportunity and the perseverance and enthusiasm required to complete my Ph.D. dissertation.

I extend my heartfelt appreciation to my esteemed thesis director, Dr. Toufik Sebbagh, Professor at the University of Skikda, for having trusted me and for guiding, encouraging, advising, and continually helping me throughout the realization of this thesis.

I would also like to express my gratitude to Dr. DJABALLAH Said and Dr. GUENTRI Hocine for their guidance, encouragement, and invaluable advice. Their professional guidance has been the cornerstone of this work, without which its successful completion would not have been possible.

I would like to express my sincere thanks to the doctoral training committee for their guidance and support throughout my PhD studies.

My deep gratitude also goes to the LGMM laboratory for providing a stimulating research environment and the necessary resources that greatly contributed to the successful completion of this work.

I would also like to thank the members of the jury for the honor of reviewing and evaluating this thesis: Professor at the University of Skikda, KELAIAIA Ridha, for agreeing to chair the jury. I would also like to thank Mr. KHERIEF Nacereddine Mohamed, Professor at ENSET-Skikda, Dr. BOUSSAHA Elhadi, and Dr. MATTALLAH Sabrina, for agreeing to serve as examiners on this jury.

Undoubtedly, my deepest gratitude goes to my family, whose unwavering love, kindness, and support have been instrumental in bringing me to this point. I am indebted to my father, Elhani, and my mother, Rebiha BILEK, for their continuous care, prayers, and encouragement throughout the years. My brothers and sisters have been a constant source of love and motivation, always cheering me on with their endless support.

Finally, I would like to thank everyone who supported and helped me to complete this work, especially my family and friends.

Beldjaatit Chahinez.

Abstract

The growing global shift toward renewable energy has significantly increased the deployment of wind turbine systems as a clean and sustainable power source. As these systems become larger and more technologically sophisticated, their operational complexity rises, particularly in offshore and remote installations, making them more susceptible to mechanical failures and performance degradation. Among the critical components, bearings and rotating parts are highly prone to wear and damage due to dynamic loads and harsh environmental conditions. Consequently, there is an urgent need for advanced and reliable condition monitoring and fault diagnosis strategies to ensure the continuous, safe, and cost-effective operation of wind turbines, reduce unplanned downtime, and extend the lifespan of equipment. This research proposes two complementary diagnostic frameworks designed to enhance the accuracy and robustness of fault detection in wind turbine systems, with a particular focus on bearing-related failures. The first method utilizes signal processing techniques by combining the Discrete Wavelet Transform (DWT) and the Fast Fourier Transform (FFT) to extract fault-sensitive features from vibration signals. This approach is applied to the benchmark Case Western Reserve University (CWRU) bearing dataset, which comprises four different bearing health conditions, allowing for the accurate identification of fault characteristics based on multiresolution energy analysis and frequency-domain patterns. The second suggested approach presents an innovative hybrid artificial intelligence framework (2DCNN-SC) that combines a deep learning model, specifically a two-dimensional Convolutional Neural Network (2D-CNN), with a stacking ensemble classifier comprising considerable base learners. This hybrid methodology is assessed using two datasets: the CWRU bearing fault dataset and the Aventa AV-7 wind turbine SCADA dataset, which has five categories of authentic operational failures. We evaluate the efficacy of the proposed method in terms of defect classification rate, specificity, and precision. The suggested system attains exceptional diagnostic performance, with classification accuracies of 99.6% on the CWRU dataset and 99.76% on the Aventa dataset. The results demonstrate the effectiveness of integrating deep feature extraction with ensemble learning for intelligent defect identification in real-world wind turbine settings.

Keywords : Wind turbine, Fault detection, Artificial intelligence, Diagnosis, Vibration analysis, Convolutional neural network.

Résumé

L'évolution mondiale croissante vers les énergies renouvelables a considérablement augmenté le déploiement des systèmes éoliens en tant que source d'énergie propre et durable. À mesure que ces systèmes deviennent plus grands et plus sophistiqués sur le plan technologique, leur complexité opérationnelle augmente, en particulier dans les installations offshores et éloignées, ce qui les rend plus sensibles aux défaillances mécaniques et à la dégradation des performances. Parmi les composants critiques, les roulements et les pièces rotatives sont très sensibles à l'usure et aux dommages dus aux charges dynamiques et aux conditions environnementales difficiles. Par conséquent, il existe un besoin urgent de stratégies avancées et fiables de surveillance de l'état et de diagnostic des défaillances pour assurer le fonctionnement continu, sûr et rentable des éoliennes, réduire les temps d'arrêt imprévus et prolonger la durée de vie de l'équipement. Cette recherche propose deux stratégies de diagnostic complémentaires conçus pour améliorer la précision et la robustesse de la détection des défaillances dans les systèmes d'éoliennes, en mettant l'accent sur les défaillances liées aux roulements. La première méthode utilise des techniques de traitement des signaux en combinant la transformée en ondelettes discrète (DWT) et la transformée de Fourier rapide (FFT) pour extraire des caractéristiques sensibles aux défauts à partir des signaux de vibration. Cette approche est appliquée à l'ensemble de données de référence des roulements de la Case Western Reserve Université (CWRU), qui comprend quatre états de santé différents des roulements, ce qui permet d'identifier avec précision les caractéristiques des défauts sur la base d'une analyse énergétique multirésolution et de modèles dans le domaine des fréquences. La deuxième approche proposée présente un modèle d'intelligence artificielle hybride innovant (2DCNN-SC) qui combine une méthode d'apprentissage profond, en particulier un réseau neuronal convolutionnel bidimensionnel (2D-CNN), avec un classificateur d'ensemble d'empilement comprenant des apprenants de base considérables. Cette méthodologie hybride est évaluée à l'aide de deux ensembles de données : l'ensemble de données sur les défauts de roulements de la CWRU et l'ensemble de données SCADA de l'éolienne Aventa AV-7, qui comporte cinq catégories de défaillances opérationnelles authentiques. Nous évaluons l'efficacité de la méthode proposée en termes de taux de classification des défauts, de spécificité et de précision. Le système proposé atteint des performances de diagnostic exceptionnelles, avec des précisions de classification de 99,6 % sur l'ensemble de données CWRU et de 99,76 % sur l'ensemble de données Aventa. Les résultats démontrent l'efficacité de l'intégration de l'extraction de caractéristiques profondes avec

l'apprentissage d'ensemble pour l'identification intelligente des défauts dans le monde réel des éoliennes.

Mots-clés : Turbine éolienne, Détection des défauts, Intelligence artificiel, Diagnostic, Analyse vibratoire, Réseau neuronal convolutionnel.

ملخص

أدى التحول العالمي المتزايد نحو الطاقة المتجددة إلى زيادة كبيرة في نشـــر أنظمة توربينات الرياح كمصـــدر طاقة نظيفة ومستدامة. وكلما أصبحت هذه الأنظمة أكبر حجماً وأكثر تطوراً من الناحية التكنولوجية، يزداد تعقيدها التشغيلي، خاصةً في المنشـــآت البحرية والنائية، مما يجعلها أكثر عرضـــة للأعطال الميكانيكية وتدهور الأداء. من بين المكونات المهمة، المحامل والأجزاء الدوارة معرضة بشكل كبير للتآكل والتلف بسبب الأحمال الديناميكية والظروف البيئية القاسية. وبالتالي، هناك حاجة ملحة إلى استراتيجيات متقدمة وموثوقة لمراقبة الحالة وتشخيص الأعطال لضمان التشغيل المستمر والآمن والفعال من حيث التكلفة لتوربينات الرياح، وتقليل وقت التوقف غير المخطط له، وإطالة عمر المعدات. يقترح هذا البحث إطارين تشخيصيين تكميليين مصممين لتعزيز دقة وقوة اكتشاف الأعطال في أنظمة توربينات الرياح، مع التركيز بشكل خاص على الأعطال المتعلقة بالمحمل. تستخدم الطريقة الأولى الإشارات من خلال الجمع بين التحويل الموجي المنفصل (DWT) والتحويل السريع للفوريه (FFT) لاستخراج السمات الحساسة للأعطال من إشارات الاهتزاز. يتم تطبيق هذا النهج على مجموعة بيانات محامل CWRU، والتي تضم أربعة ظروف صحية مختلفة للمحمل، مما يسمح بتحديد دقيق لخصـــائص العطل بناءً على تحليل الطاقة متعدد الدقة وأنماط المجال الترددي. تقدم المنهجية الثانية المقترحة إطار ذكاء اصطناعي هجين مبتكر (2DCNN-SC) يجمع بين نموذج التعلم العميق، وتحديداً الشبكة العصبية التلافيفية ثنائية الأبعاد (2D-CNN) مع مصـــنف تجميعي يضـــم العديد من المتعلمين الأســـاســـيين. يتم تقييم هذه المنهجية الهجينة باســـتخدام مجموعتي بيانات: مجموعة بيانات أعطال محامل CWRU ومجموعة بيانات Aventa AV-7 SCADA لتوربينات الرياح، والتي تحتوي على خمس فئات من الأعطال التشغيلية الأصلية. نقوم بتقييم فعالية الطريقة المقترحة من حيث معدل تصنيف العيوب والخصوصية والدقة. يحقق النظام المقترح أداءً تشخيصياً استثنائياً، حيث بلغت دقة التصنيف 99.6% على مجموعة بيانات CWRU و99.76% على مجموعة بيانات Aventa. تُظهر النتائج فعالية دمج الاستخراج العميق للميزات مع التعلم التجميعي للتعرف الذكي على العيوب في إعدادات توربينات الرياح في العالم الحقيقي.

الكلمـــــات المفتاحيـــــة: توربينـــات الريـــاح، الكشـــف عـــن الأعطـــال، الـــذكاء الاصـــطناعي، التشـــخيص، تحليل الاهتزازات، الشبكة العصبية التلافيفية.

Table of Contents

Liste of Figures

List of tables

Acronyms and Abbreviations

PHM	Prognostics and health management
CBM	Condition-Based Maintenance
RUL	remaining usable life
CM	Condition monitoring
STFT	Short-time Fourier transform
EMD	Empirical modal decomposition
VMD	Variational modal decomposition
ANNs	Artificial Neural Networks
SVMs	Support Vector Machines
DL	Deep learning
AEs	Auto Encoders
DBN	Deep Belief Networks
CNN	Convolutional Neural Network
CWRU	Case Western Reserve University
DWT	Discrete wavelet transform
FFT	Fast Fourier transform
XGBoost	Extreme gradient boosting
LightGBM	Light gradient boosting machine
SVC	Support Vector classifier
CWT	Continuous Wavelet Transform
SCADA	Supervisory control and data acquisition
CO_2	Carbon Dioxide
WECS	Wind energy conversion system
WT	Wind turbine
GW	Gigawatts
HAWTS	Horizontal axis wind turbines
VAWTS	Vertical axis wind turbines
KW	Kilowatt

MW	Megawatt
WGS	Wind generation system
PDM	Predictive maintenance
NDE	Non-destructive evaluation
AE	Acoustic emission
ASTM	American society for testing and materials
FO	Fiber optic
MEMS	Micro-Electro-Mechanical system
IRT	Infrared thermography
ISO	International organization for standardization
RMS	Root-mean-square
IOT	Internet of things
WECs	White etching cracks
TDA	Time domain analysis
WTG	Wind turbine gearbox
CF	Crest factor
FDA	Frequency domain analysis
FT	Fourier transform
HT	Hilbert transform
WVT	Wigner-Vill transform
HHT	Hilbert-Huang transform
LMD	Local mean decomposition
TFA	Time frequency analysis
MRA	Multiresolution analysis
EEMD	Ensemble Empirical mode decomposition
MEMD	Multivariate EMD
AI	Artificial intelligence
ML	Machine Learning
KNN	K-Nearest neighbor
DT	Decision tree

LR	Logistic regression
RNNs	Recurrent neural networks
DQNs	Deep Q networks
GANs	Generative adversarial networks
RBF	Radial basis function
t-SNE	t-Distributed Stochastic Neighbor Embedding
TSR	Tip speed ratio

General Introduction

As the global economy continues to expand rapidly, the issue of energy has become increasingly important, leading to a growing demand for green energy on the part of humanity [1]. All over the world, policies to combat climate change are enticing huge investments in the renewable energy sector. Wind power can be considered an inexhaustible renewable energy resource and the ultimate candidate for power generation due to its replicability, cleanliness, and reliability [2]. Although wind power is an environmentally friendly, fuel-free means of generating electricity, wind power systems will inevitably need to be operated and maintained. In current smart manufacturing systems, the gearbox plays an essential role as a vital component of rotating machinery. The health of the gearbox has a direct impact on the safety and reliability of the entire system. Wind turbines (WTs) consist mainly of multiple subsystems, with the gearbox playing a crucial role in transferring power from the rotor hub to the generator. Given the complex design of WTs and the harsh operating environment they face over long periods, including extreme temperatures, unstable loads, and manufacturing imperfections, many components are susceptible to unexpected failure [3].

Prognostics and Health Management (PHM) is a discipline centered on anomaly detection, defect diagnosis, and deterioration prognosis for machinery and equipment. The objectives of PHM encompass improving dependability, minimizing maintenance expenses, optimizing production availability, and preventing catastrophic breakdowns. An effective maintenance planning strategy is essential for minimizing unanticipated downtime. A Condition-Based Maintenance (CBM) technique involves planning maintenance according to the health status of machinery. Fault prognosis techniques can also be employed to estimate the remaining usable life (RUL) [4] prior to the occurrence of defects. These techniques assist operators in assessing maintenance urgency and preparing for coming tasks, thereby lowering maintenance expenses. Many conditions monitoring (CM) techniques have been proposed to diagnose wind turbine bearing to avoid catastrophic malfunctions, including vibration analysis, electrical signal examination, lubricant analysis, thermal imagery, and acoustic emission [5]. The most prevalent among them is the vibration-based method. The process of extracting defect information from acquired signals is one of the least essential phases. In recent years, the primary emphasis of signal feature extraction methods from the acquired vibration signals has been based on the time domain, frequency domain, and time-frequency analysis [6].

Intelligent fault diagnosis approaches based on data typically consist of two stages: feature extraction achieved through signal processing techniques and fault acknowledgment executed using classification algorithms. Feature extraction is crucial for diminishing input dimensionality and mitigating random noise by deriving significant health indicators based on time-frequency analysis. To determine the working condition of bearings, typical time-frequency signal processing methods encompass the short-time Fourier transform (STFT), empirical modal decomposition (EMD), wavelet transform, variational modal decomposition (VMD), and others. Conventional classification methods, including Artificial Neural Networks (ANNs), Support Vector Machines (SVMs), and ensemble techniques, are extensively utilized owing to their rapid implementation and effective classification performance. Nonetheless, constrained by their superficial designs, they struggle to learn effectively selective features from raw high-dimensional inputs[7].

In recent years, deep learning-based intelligent defect diagnosis methods have garnered heightened interest. Deep learning (DL) models involve the aggregation of numerous non-linear processing layers to create hierarchical architectures, facilitating the extraction of representations from raw or preprocessed data, including time series, spectrum, and time-frequency maps. Diverse deep network architectures and their modifications, including Auto Encoders (AEs), Deep Belief Networks (DBN)[8], and Convolutional Neural Networks (CNN)[9], have been utilized for addressing various diagnostic problems. Convolutional Neural Networks (CNNs) are extensively utilized among deep learning algorithms and have attained superior diagnostic performance for wind turbine faults due to their robust local feature extraction abilities and adaptable topologies[10].

Contribution

The general framework of this research work is to make the following main contributions:

- A signal-processing framework is proposed for vibration-based fault diagnosis, specifically applied to the Case Western Reserve University (CWRU) bearing dataset. The method employs discrete wavelet transform (DWT) to decompose the raw vibration signals into multiple frequency sub-bands, enabling effective time-frequency localization. Subsequently, energy analysis is performed on the decomposed signals to extract discriminative features, which are then analyzed using fast Fourier transform (FFT) to identify fault signatures. This approach enhances the capability to detect subtle fault patterns and improves diagnostic accuracy in rotating machinery applications.

- A novel diagnostic DL approach (2DCNN-SC) is proposed, combining the feature extraction capabilities of a Convolutional Neural Network (CNN) with the decision-level fusion strength of a stacking ensemble strategy built upon multiple base classifiers, using extreme gradient boosting (XGBoost), light gradient boosting machine (LightGBM), and a support vector classifier (SVC).

- The use of Continuous Wavelet Transform (CWT) is employed to convert the original vibration and operational signals into RGB image representations. This transformation enables a rich visualization of the time-frequency characteristics associated with different bearing health states and various wind turbine fault conditions. By capturing both temporal and spectral information, the CWT-based representation significantly enhances the ability to distinguish between normal operation, specific bearing faults, and multiple types of wind turbine anomalies with greater clarity and precision.

- The study assesses the feature extraction capabilities of CNN architectures across different batch sizes and conducts a sensitivity analysis on the kernel function types of the meta-classifier.

- The effectiveness of the proposed method is validated on two different datasets: the benchmark CWRU dataset for bearing fault diagnosis, and the real-world Aventa AV-7 wind turbine SCADA dataset for detecting various operational faults.

- This work establishes a comprehensive comparison to validate the performance of the proposed framework against various existing machine-learning models. The results confirm that the hybrid method consistently achieves superior diagnostic accuracy and robustness across both bearing faults and real-world wind turbine defects.

Thesis structure

The structure of this thesis is organized into four chapters, presented in detail below:

Chapter one introduces the fundamentals of wind energy and explains how wind turbines, particularly horizontal-axis types, operate. It outlines the main components and working principles of wind turbines and presents detailed mathematical models for each part of the aerodynamic system. These models, implemented in MATLAB/Simulink, help simulate turbine behavior under various conditions. The chapter also analyzes key performance parameters such as tip speed ratio, power coefficient, blade pitch angle, and mechanical power to identify optimal energy conversion conditions.

Chapter two presents an overview of wind turbine maintenance approaches, highlighting the shift toward Condition-Based Maintenance (CBM) for improved reliability and cost-effectiveness. It also addresses the common tribological failures in wind turbine bearings and details typical fault modes, emphasizing their significance in turbine performance and the need for effective diagnostic techniques.

Chapter three first reviews key signal processing methods for diagnosing wind turbine bearing faults, covering time-domain, frequency-domain, and time-frequency techniques, with a focus on their effectiveness in handling non-stationary signals. The second part presents a suggested vibration-based diagnostic framework using the CWRU-bearing dataset. It combines discrete wavelet transform (DWT) and fast Fourier transform (FFT) to extract features and detect faults, offering a solid baseline for future application to wind turbine systems.

Finally, Chapter 4 introduces a novel artificial intelligence-based technique for diagnosing wind turbine failures. It begins with a concise review of machine learning approaches, including both traditional and deep learning methods, emphasizing their application in condition monitoring using SCADA data. The chapter then presents a developed hybrid diagnostic framework that integrates a Convolutional Neural Network (CNN) with a stacking ensemble of diverse classifiers (XGBoost, LightGBM, and SVC) to enhance accuracy and robustness. This approach is evaluated using the CWRU bearing dataset and the Aventa wind turbine SCADA dataset, demonstrating high effectiveness in detecting both benchmark and real-world operational faults. The proposed model leverages the combined strengths of deep learning, boosting, and ensemble techniques, making it particularly robust under varying operating conditions.

The thesis ends with a general conclusion and offers recommendations for future research to encourage continued progress in the field of this study.

CHAPTER I

Modeling and Simulation of a Wind Turbine

I.1. Introduction

Wind power production is a well-established technology in the renewable energy generation sector, and it serves as the foundation for achieving worldwide energy transition and sustainable development. Wind turbines are the core of wind energy conversion. These turbines have undergone significant technical evolutions over the previous several decades. They work based on a basic concept: converting the wind's kinetic energy into mechanical energy, which is subsequently converted into electrical power. Optimizing the conversion process is vital to ensuring optimal outcomes from wind turbines, thereby improving the energy captured from each wind gust. Rapid and precise modeling of wind turbine services yields critical parameters for the secure management of functions, significantly enhancing the flexible supervision of power systems, increasing the capture rate of clean energy, and reducing their costs. Due to their size and complexity, wind turbines require computer modeling and simulation examination of load, design dynamics, and aerodynamic reliability across all operating conditions[11].

In this chapter, an extensive mathematical model for every component of the wind turbine's aerodynamic system is presented, making it easier to understand and simulate wind turbine operation using MATLAB/Simulink. The chapter also provides a detailed analysis of turbine behavior under different conditions based on key parameters such as power coefficient and its relationship to tip speed ratio and blade pitch angle, as well as mechanical power. This helps determine optimal operating conditions to maximize energy conversion performance.

I.2 Wind Energy

In recent decades, energy shortages and environmental contamination have become significant issues for human life and community growth. The primary factors that have influenced the adoption of renewable energy sources include the attribution of climate change to the carbon dioxide (CO2) emissions resulting from the combustion of fossil fuels. Given the necessity for clean electricity, there has been a rise in the investment in renewable energy resources, including hydrogen, biomass, hydro, wind, and solar[12]. Wind energy is recognized as one of the world's largest sources of sustainable energy, making it an essential tool in the reducing carbon emissions strategy. Numerous industries aim to establish multiple wind farms, thereby augmenting the production of sustainable electric energy. Concurrently, innumerable nations have implemented incentives and subsidies for these initiatives to adhere to the Kyoto Protocol and mitigate the release of CO2.

Wind energy is an indirect form of thermal energy emitted by the sun. It is the kinetic energy of air masses moving around the globe. The sun's beams are absorbed by the atmosphere, leading to temperature and pressure variations. Subsequently, the air masses accrue kinetic power and move, the source of the wind. Approximately 2% of the planet's solar energy is converted to wind energy. Wind power is generated by converting the moving energy of the wind into mechanical power. The wind energy sector has experienced substantial progress and is now firmly established as a resilient and flourishing worldwide industry. It has seen significant growth over the past five years, as illustrated by the new installation data for onshore and offshore wind capacity from Global Wind Energy Council (GWEC) in Figure 1. This report provides an overview of the annual new installations from 2019 to 2023 and underscores the accelerating impetus behind the worldwide development of wind energy. 2019 represented the start of a consistent rise in wind power installations, with onshore wind projects accounting for most of the new capacity. In 2020, the wind energy sector experienced substantial growth, with total installations increasing by approximately 57% compared to 2019. 117 gigawatts (GW) of total installations in 2023 represents a 50% year-over-year increase from 2022 [13]. The substantial increase in 2023 highlights the potential for continued growth and the importance of both onshore and offshore wind energy in the global transition to renewable energy sources.

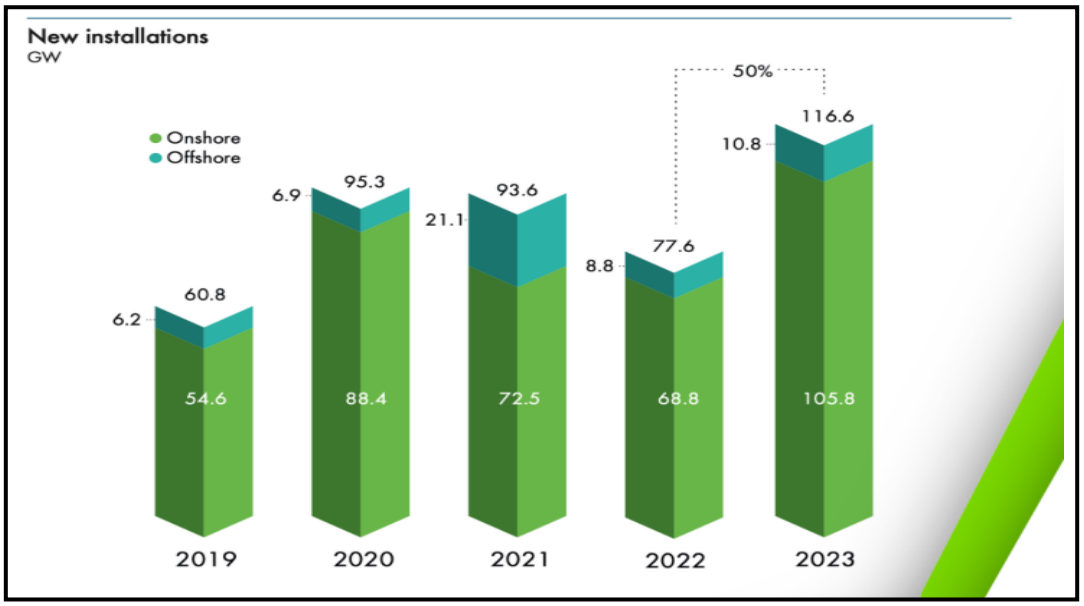

Figure I.1 The report of annual new wind energy installations (2019-2023) [13].

I.3 Overview on Wind Turbines

A wind energy conversion system (WECS) is implemented to obtain electrical power from wind in a regulated, dependable, and productive manner [14]. The overall structure of the conversion is depicted in Figure I.2. The WECS comprises three primary aspects:

- Aerodynamic part.
- Mechanical part.
- Electrical part.

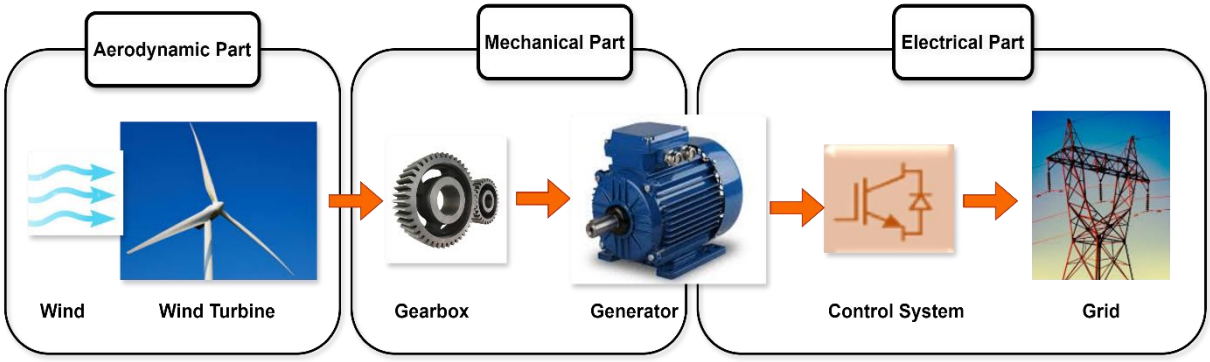

Figure I.2 Wind energy conversion system.

The latest advancements in wind generation systems (WGS) have resulted in cost reductions, making them highly competitive with traditional energy generation systems (such as oil and coal) [15]. Given the rapid growth of the sector, a great deal of attention has been paid to improving the profitability and efficiency of wind turbines, which are the significant elements of wind energy conversion systems. A wind turbine (WT) is a mechatronic device that converts the kinetic energy of an airflow into electric energy through a rotor. The blades of the rotor, which are in contact with the wind, generate aerodynamic forces that cause the electrical generator to rotate. The mechanical components mainly transform mechanical power and transmit it to the electrical elements of the system. The electrical aspect of WECS encompasses a generator and a controller system coupled with a utility grid. The mighty WECS exhibit low rotational speed and high torque at the turbine. On the other hand, the generator shaft is distinguished by its lower torque and high speed. A gearbox is incorporated to substantially decrease torque and increase speed, enabling the generator to produce electrical power [16].

I.3.1 Types of wind turbines

The wind turbines (WTs) are classified into various types based on diverse criteria. The most prevalent classification of WT depends on the orientation of the rotating axis. Regarding wind

turbine technology, there are two main groups: onshore (on land) wind turbines and offshore (in the sea) wind turbines. Based on the wind turbine's rotational speed, WECS are categorized into two types: variable speed and fixed speed [14].

I.3.1.1 Rotational Axis

From the standpoint of physical configuration, as shown in Figure I.3, there are two types of WTs: horizontal axis wind turbines (HAWTs) and vertical axis wind turbines (VAWTs)[17].

a) ***Horizontal Axis Wind Turbines:*** The generator and turbine shafts are positioned parallel to the ground. In HAWTs, the blades are oriented towards the windward direction. Horizontal-axis wind turbines are typically employed in producing large-scale wind power due to their durability and higher aerodynamic efficiency[18]. Three-bladed commercial turbines are specially equipped with the HAWT design.

b) ***Vertical Axis Wind Turbines:*** This turbine type comprises rotor blades linked to a vertical shaft to yield electrical energy. Minimizing unwanted mechanical complications is one critical reason for pursuing VAWT technology, which is intended to attain a higher level of durability for different applications[19]. This category of turbines is relatively less costly and more straightforward to install and maintain than other varieties.

Figure I.3 Wind turbine types.

I.3.1.2 Output Power

Wind turbines can also be divided into three groups based on their output-rated power, which are:

a) ***Law power WT:*** These turbine systems can produce a median maximum power of 30 kW.

b) ***Medium Power WT:*** Within this category are turbines that generate outputs between 30 and 300 kW.

c) ***High Power WT:*** These devices induce a substantial amount of electricity, more than 1 MW.

I.3.2 Wind Turbine Components

Comprehending the fundamental constituents of a wind turbine is vital for understanding the operation and impact of these systems on renewable energy generation. Each component plays a critical role in ensuring robust and effective electricity production. Turbines' functionality is contingent upon the blades, nacelle, and tower [20]. Figure I.4 displays the cross-section of a standard horizontal-axis wind turbine. The following is a summary of the principal elements of a wind turbine.

- **Rotor**: is the aerodynamic component of the apparatus, which encompasses the hub (where the blades are fastened), the nose cone, and the blades, is responsible for converting the wind stream's kinetic energy into torque. The rotor blades have to be engineered to optimize the amount of energy harnessed while simultaneously reducing friction and turbulence.

- **Nacelle**: is the central part of the turbine, where the essential mechanical and electrical components are housed, such as the gearbox and generator. The overall size of the nacelle can vary according to the type of wind turbine, but it often has a limited surface area for maintenance tasks [21].

- **Tower:** the tower rests on a solid concrete base, supporting both the blades and the nacelle from an elevated position where the wind speed is high and stable. It is designed to be strong enough to withstand not only aerodynamic and mechanical loads, but also its weight and other forces caused by fluid dynamics[20].

- **The Main Shaft:** also known as the low-speed shaft, it is an essential wind turbine element that transmits rotational energy from the rotor blades to the gearbox.

- **Gearbox**: the gearbox is positioned between the generator and the main shaft. It augments the spinning velocity of the turbine's rotor to move the generator at the necessary velocity. The gearbox generally comprises a series of bearings and gears that transfer energy from the rotating part to the generator.

- **Generator**: The generator is an electric machine that converts mechanical energy into electrical energy, which is then fed into the power grid for distribution and use.

- **Control systems**: The control systems of a wind turbine supervise and regulate its entire operation. These systems are usually located on the nacelle and comprise hardware and software components that optimize the machine's safe and efficient operation.

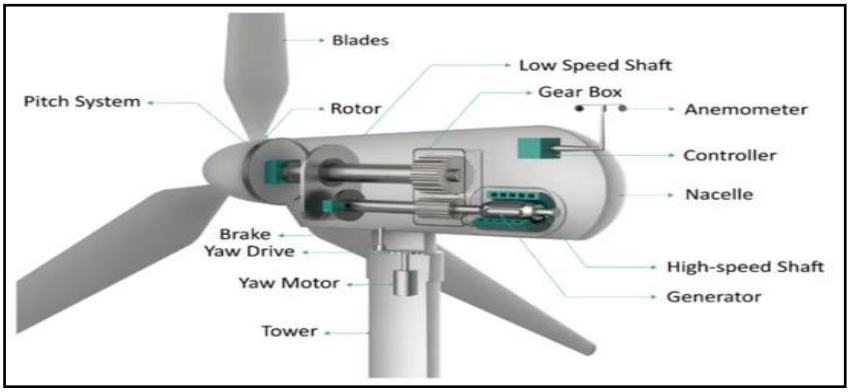

Figure I.4 Components of WT [22].

I.3.3 Wind Turbine Operating Regions

Given the uncertain nature of wind and the increasing prevalence of wind turbines in electricity utilities, which pose considerable problems in terms of the reliability and balance of these systems, obtaining as much wind power as possible is imperative. To assess the performance and efficiency of a wind turbine, it is essential to understand its power output under varying wind conditions. The wind turbine power curve provides a graphical representation of the nonlinear relationship between the output power of the turbine and wind speed, detailing how the turbine's electrical power output changes with different wind speeds[23]. Figure I.5 represents the wind turbine's power output as a function of wind speed. It is split into four distinct regions, each of which corresponds to different operating conditions of the wind turbine:

1. Below cut-in speed(v_{cut-in}): The wind speed is too low to generate any significant power. The turbine is not active, and the power output is zero. WT starts generating power at "cutting speed."

2. Between cut-in wind speed (v_{cut-in}) and rated wind speed (v_{rated}): Production capacity is rapidly growing. The wind turbine produces power at an increasing rate until it reaches its "rated speed."

3. Between rated wind speed (v_{rated}) and cut-off wind speed ($v_{cut-off}$): A wind turbine generates power at a stable rate, which is its maximum rated power until the cut-off speed is achieved.

4. Above the cut-off speed ($v_{cut-off}$): The wind speed is too high, and the turbines are turned off to prevent damage, so no power is produced in this zone.

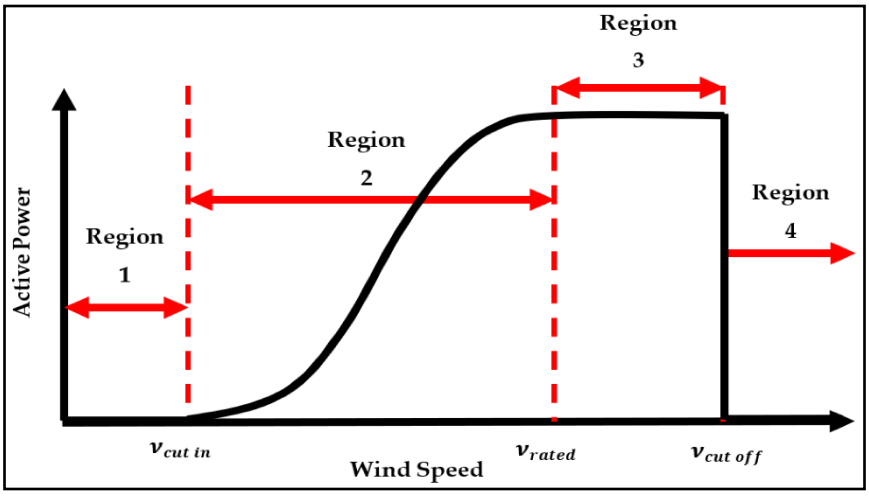

Figure I.5 The operating zones of WT [24].

I.4 Aerodynamics Aspects of Wind Turbine

The first theoretical approach, which relies on mass conservation and energy conservation in wind flow, determines the basic concepts governing the layout and functioning of wind turbines. The examination of wind turbine aerodynamic characteristics can be initiated without any particular turbine configuration by solely focusing on the manner of energy extraction. A simple model, generally known as the actuator disc model, in which the turbine is composed of a slender disk capable of rotating freely around its axis, results in a pressure discrepancy within the airflow stream tube [25]. This simple model, based on Betz's theory, can be used to determine the power generated by an optimized turbine rotor, the wind force exerted on the rotor, and the impact of rotor activity on the surrounding wind patterns.

I.4.1 Betz's Law or Axial Momentum Theory

The German physicist Albert Betz introduced Betz's law in 1919, which defines the upper limit of power that may be obtained from the wind, regardless of the specific design of a wind turbine operating in open airflow. Additionally, Betz's law estimates use energy balance concepts that apply to all wind turbines, HAWTs can reach performance levels of 40-45%, while VAWTs typically attain 20-30% performance levels[26]. The turbine, even in its idealized form, can only fully harness the energy from the fluid if the speed ratio between the outflow and inflow streams is precisely one-third (3:1), which is known as the Betz condition. It is necessary to emphasize that while the actuator disc theory is valuable for analyzing the overall effectiveness of turbines, it cannot be employed for the purpose of designing turbine blades to get a certain performance.

In the idealized model shown in Figure I.6, homogeneity is assumed throughout the entire area covered by the rotor, and the air velocity outside the rotor is considered to be in the same direction as the rotor axis. The wind speed moving the turbine rotor is denoted by v_2, where v_1 is the velocity at the front of the rotor and v_3 represents the velocity of the fluid downstream of the rotor. In the upstream location, the fluid movement reduces, and the steady pressure rises. In addition, the pressure reverts to the free stream value as it moves downstream, resulting in a continuous drop in fluid velocity until it reaches a final value $v_3 < v_2 < v_1$.

The speed exhibits a continuous variation, resulting in an augmentation of the cross-sectional area of the stream tube from the turbine's upstream A_1, to its downstream location A_3, and $A_1 < A_2 < A_3$, where A_2 is the area of the turbine rotor.

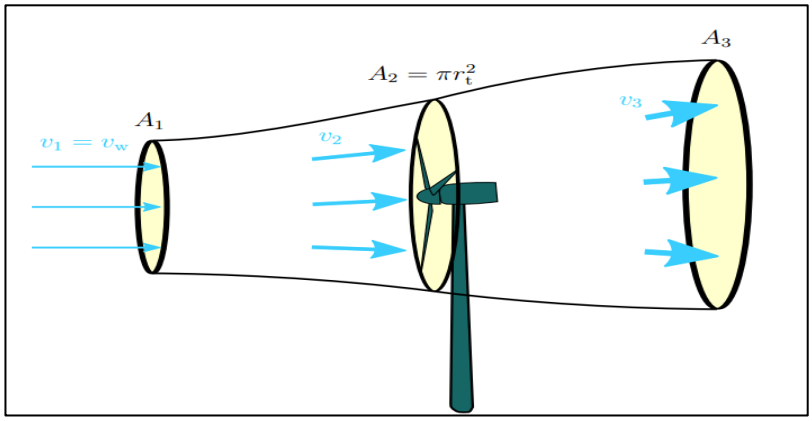

Figure I.6 An actuator disk model for wind turbines in Axial Momentum Theory [27].

By applying the principle of conservation of mass or the continuity equation, we can determine the mass flow rate as follows [28]:

$$\dot{m} = \rho A_1 v_1 = \rho A_2 v_2 = \rho A_3 v_3 \tag{I.1}$$

With ρ is the fluid density.

Based on the axial momentum theorem, the thrust on the disk will be equal and opposite to the difference in momentum flow between points 1 and 3.

$$T = \rho v_1 A_1 v_1 - \rho v_3 A_3 v_3 \ = \rho A_2 v_2 (v_1 - v_3) \tag{I.2}$$

The pressure drop along the rotor can also be used to describe the power produced by the fluid on the turbine rotor:

$$T = \rho A_2 v_2 (v_1 - v_3) = A_2 (p^+ - p^-) \quad \text{(I.3)}$$

Using the Bernoulli function on the two control volumes on both sides of the rotor disk, giving:

$$p^+ - p^- = \frac{1}{2}\rho(v_1^2 - v_3^2) \quad \text{(I.4)}$$

From equations (I.3) and (I.4) we have:

$$v_2(v_1 - v_3) = \frac{1}{2}(v_1 - v_3)(v_1 + v_3) \quad \text{(I.5)}$$

The final expression implies that:

$$v_2 = \frac{1}{2}(v_1 + v_3), \forall\ v_1 \neq v_3 \quad \text{(I.6)}$$

The fluid speed at the rotor plane can be considered as the mean of the upstream and downstream wind velocities. To further derive the equation, we will incorporate two dimensionless factors known as the axial induction coefficients, a and b, as proposed by Froude. These coefficients relate the velocities in different sections to the starting speed, then

$$v_2 = (1 - a)v_1 \quad \text{(I.7)}$$

$$v_3 = (1 - b)v_1 \quad \text{(I.8)}$$

Using equation (I.6), we can establish a relationship between the two parameters a and b:

$$(1 - a)v_1 = \frac{1}{2}[v_1 + (1 - b)v_1] \quad \text{(I.9)}$$

$$a = \frac{1}{2}b \quad \text{(I.10)}$$

From equation (I.6), the thrust can be expressed as:

$$T = \frac{1}{2}\rho A_2(v_1^2 - v_3^2) \quad \text{(I.11)}$$

The last result allows us to calculate the power P extracted by the turbine in terms of the thrust T and the velocity of the wind at the rotor disk v_2 as:

$$\text{P}= T.v_2 = \frac{1}{2}\rho A_2(v_1^2 - v_3^2)v_2 \quad \text{(I.12)}$$

The kinetic energy of a wind flow collected upstream at $v_2 = v_1$ and flowing over a cross-sectional area is:

$$P_t = \frac{1}{2}\rho A_2 v_1^3 \quad \text{(I.13)}$$

The power coefficient C_p can define as the ratio of the obtainable power P to the total kinetic power P_t:

$$C_p = \frac{P}{P_t} \tag{I.14}$$

The performance coefficient is feasible to represent as a function of the induction coefficient a. By replacing the equations for P obtained from equation (I.12) and for P_t obtained from equation (I.13), we get:

$$C_p = 4a(1-a)^2 \tag{I.15}$$

The optimal value of the performance coefficient C_p is as follows:

$$\boldsymbol{C_{p,max}} = \frac{16}{27} = 0.59259 = 59.26\ percent \tag{I.16}$$

Typically known as the Betz Limit or the Betz Criterion, this indicates that the maximum attainable wind power generated by an ideal wind turbine from the available kinetic energy of the wind is 59. 3 % [29].

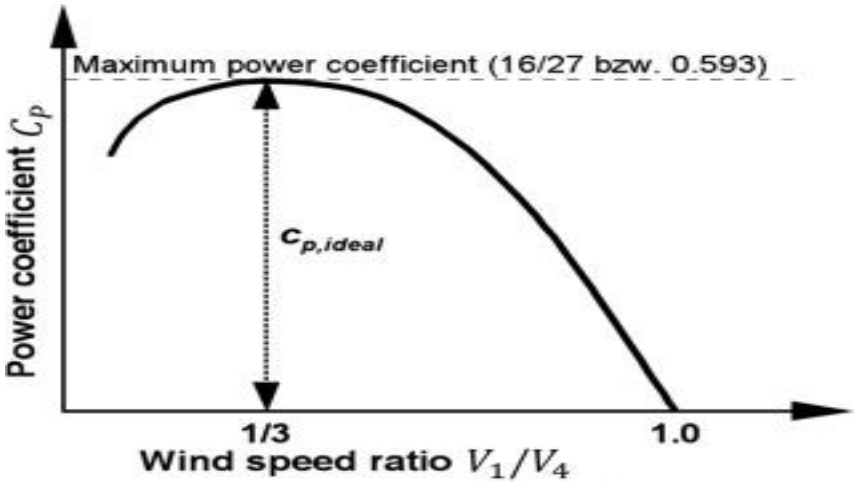

Figure I.7 The optimal power coefficient C_p [30]

I.5 Wind Turbine Modeling and Simulation

Diverse subsystems of the wind turbine model can be distinguished, such as the aerodynamic model, the mechanical model and drive train, the electromechanical model of the generator, control system model, and the model of the power converter [31]. The primary objective of this investigation was to conduct an aerodynamic simulation of a wind turbine under different conditions. The WT yields mechanical energy from the wind's kinetic energy, which is determined by its rotational velocity and mechanical torque. Nevertheless, the effectiveness of this energy conversion strategy is somewhat complex and is affected by several elements, such

as wind speed, blade angle, turbine design, and atmospheric conditions [32]. Power generation from wind turbines is contingent upon the interaction between the rotor and the available wind. According to Betz theory, the extractable mechanical power in the turbine is given by [29]:

$$P_{mech} = \frac{1}{2} C_p(\lambda, \beta) \rho A V_w^3 \tag{I.17}$$

$$A = \pi R^2 \tag{I.18}$$

Where ρ is the air density (1.225 kg/m3), Blade surface area (m2) is denoted by A, while rotor radius (m) is denoted as R, $C_p(\lambda, \beta)$ is the power coefficient of the WECS, and V_w is the wind speed (m/s).

I.5.1 Power coefficient (C_p) calculation

The strength of the wind influences the blades of a wind turbine, but not all of it can be harnessed. Establishing a suitable strategy for examining this phenomenon requires careful consideration of several factors. The power coefficient is one of the most essential elements of WECS, precisely defined as the proportion of the wind energy successfully captured by the turbine [33]. Moreover, the power coefficient is determined by both the blade pitch angle β and the tip speed ratio λ. In the literature, several equations have been developed to express C_p; the analytical expression employed to model this coefficient in this work is indicated by Equation (I.19) [34].

$$C_p = 0.5176\left(\frac{116}{\lambda_i} - 0.4\beta - 5\right)e^{\frac{-21}{\lambda_i}} + 0.0068\lambda \tag{I.19}$$

Where:

$$\frac{1}{\lambda_i} = \frac{1}{\lambda + 0.08\beta} - \frac{0.035}{\beta^3 + 1} \tag{I.20}$$

Here, the angle between the plane of rotation and the blade cross section chord is denoted by β.

The tip speed ratio or TSR is the quotient obtained by dividing the wind turbine's rotational speed by the wind speed. TSR is a critical factor used to evaluate the effectiveness and reliability of wind turbines. Generally, most contemporary wind turbines work at a TSR that falls from 5 to 8. Mathematically, the tip speed ratio can be expressed as:

$$\lambda = \frac{\Omega_t R}{V_w} \tag{I.21}$$

Where: Ω_t is the rotational angular velocity of a wind turbine (rad/s).

I.5.2 Aerodynamic torque calculation

To simulate the operational characteristics of wind turbines, the mechanical torque developed by the rotor blades is calculated practically from the mechanical power (P_{mech}) utilizing the rotational speed (Ω_t) of the wind turbine. The aerodynamic torque generated (in Nm) is computed as below:

$$T_{mech} = \frac{P_{mech}}{\Omega_t} \tag{I.22}$$

Formulas (I.23) and (I.24) provide an algebraic calculation of the multiplier for the mechanical component [35].

$$\Omega_{mec} = G\Omega_t \tag{I.23}$$

$$T_{mech} = GT_g \tag{I.24}$$

Where: Ω_{mec} denote the angular velocity of the generator in rad/s, and G be the gain of the speed multiplier.

$$J = \frac{J_{turbine}}{G^2} + J_g \tag{I.25}$$

The fundamental dynamic expression for estimating the evolution of mechanical speed from the total mechanical torque T_{mec} exerted on the rotor is given by [36]:

$$J\frac{d\Omega_{mec}}{dt} = T_{mec} \tag{I.26}$$

J: is the moment of inertia acting on the rotor of the generator.

The overall mechanical torque is contingent upon the gearbox torque (T_g), the viscous friction torque (T_{vis}), and the electromagnetic torque (T_{em}) produced by the generator.

$$T_{mec} = T_g - T_{em} - T_{vis} \tag{I.27}$$

The viscous friction torque is represented formally as:

$$T_{vis} = f.\Omega_{mec} \tag{I.28}$$

f: is the viscous friction coefficient.

I.5.3 Aerodynamic simulation block

The system investigated in this work consists of a wind turbine, illustrated in Figure I.7, with a rated power of 1.8 MW. This structure focuses on fundamental aspects of wind turbine design and operation, such as the effect of blade pitch and rotor speed and the use of gearbox to optimize generator efficiency. The assembly consists of blades with a radius of 23.2 meters, which drive a generator through a gain multiplier of 23.75. Additional characteristics are listed in Table I.1.

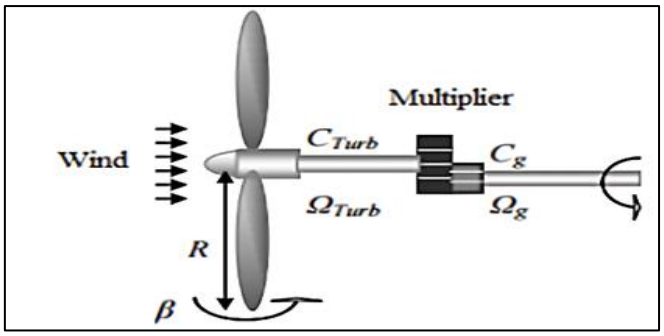

Figure I.8 Wind turbine model [37]

Table **I.1** displays the numerical values for several parameters of the wind turbine. These values provide the basic information required for precisely modeling the turbine's performance and simulated operational parts under various wind conditions.

Table I.1 Wind turbine model parameters [38]

Parameters	**Values**
Rotor diameter	D=23.2 m
Multiplier coefficient	G=23.75
Number of blades	3
Air density	P=1.22Kg/m^3
Moment inertia of the turbine	J_T =102.8 Kg.m^2
coefficient of viscous friction	f=0. 0024N.m.s^{-1}

In MATLAB/Simulink, the entire kinematic chain of the wind turbine is simulated, providing a detailed representation of its mechanical dynamics, as illustrated in Figure I.9. The model is rigorously evolved based on the basic equations and principles discussed earlier, ensuring that every aspect of wind turbine operation, such as torque generation, rotational speed, and power

conversion, is accurately represented. The subsystems of aerodynamics and power coefficient are shown in Figure I.10 and Figure I.11 respectively [39].

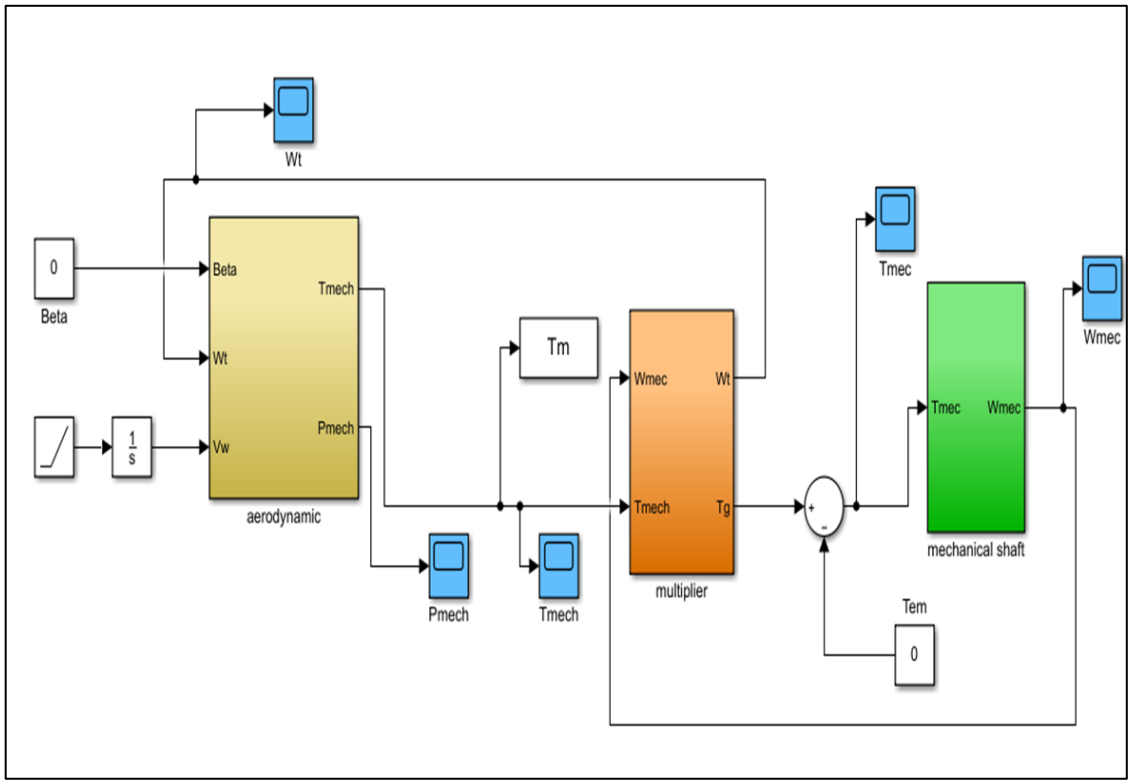

Figure I.9 Wind turbine simulation model.

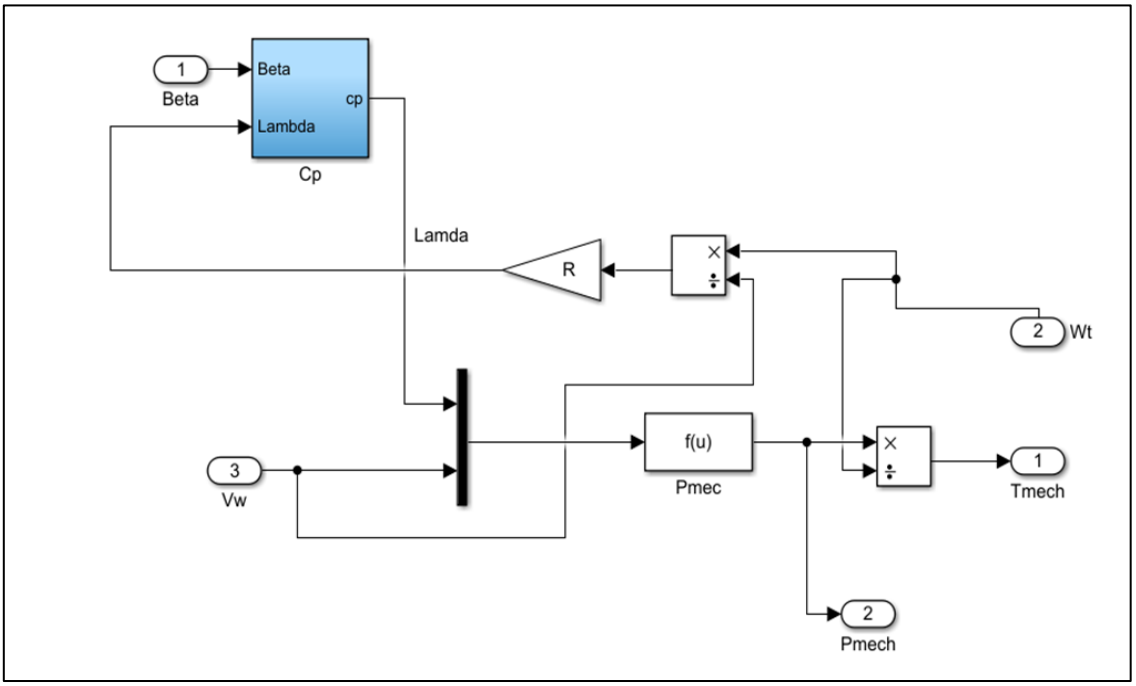

Figure I.10 Aerodynamics simulation model.

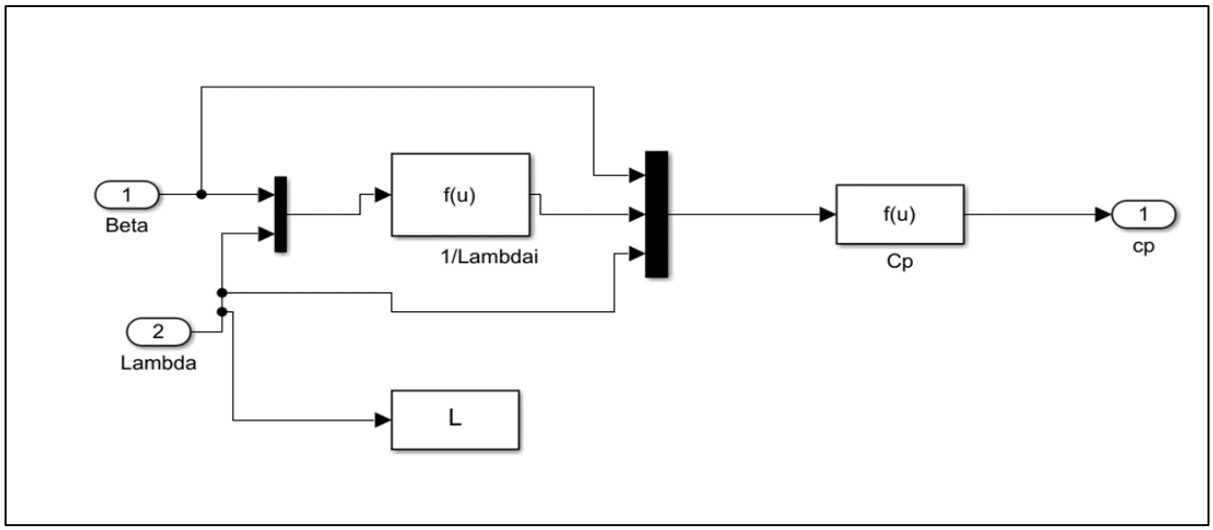

Figure I.11 Power coefficient simulation model.

I.6 Simulation Results and Discussion

The following part shows the aerodynamic model simulation results and offers an in-depth analysis of their consequences. Through meticulous study of these findings, our objective is to acquire an improved understanding of the operational and efficacy aspects of the wind turbine configuration under various conditions. This extensive investigation and discourse aim to offer a full knowledge of the aerodynamic sub-system and its simulated behavior in this work. This section typically presents key aerodynamic parameters, including power output, torque, performance coefficient, and blade loading, to demonstrate how the wind interacts with the turbine at different wind speeds.

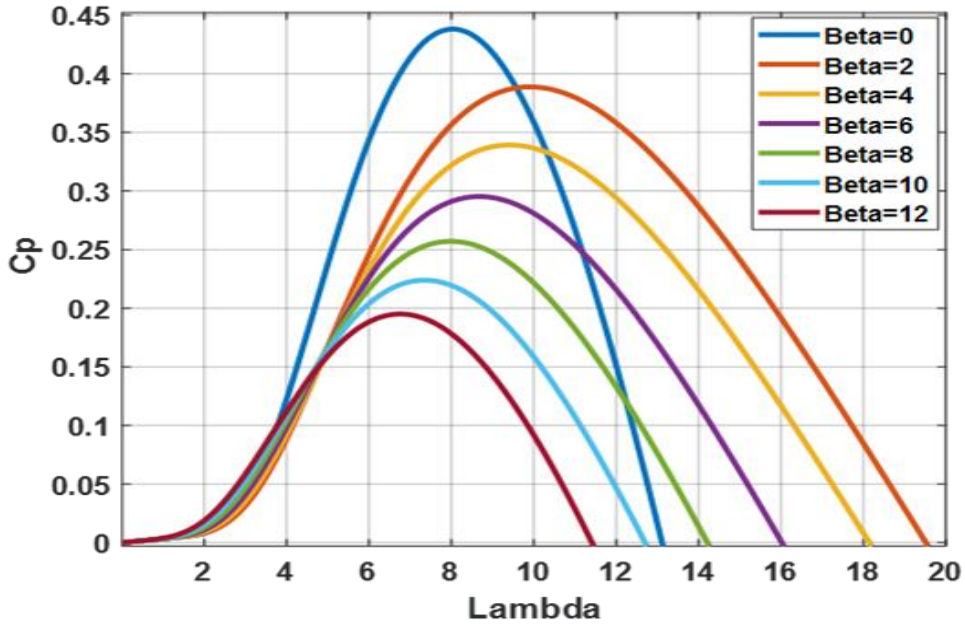

Figure I.12 Characteristics of C_p vs. Tip Speed Ratio (Lambda) for Various Blade Pitch Angles.

Figure I.12 illustrates the relationship between the power coefficient (C_p), a metric that reflects a wind turbine's efficacy, and the tip-speed ratio (Lambda) for a variety of blade pitch angles (Beta). The curves depict the aerodynamic performance characteristics of the turbine at different angles, and their patterns provide valuable information about the most favorable operating conditions and the effect of blade pitch adjustments. Analysis of this curve is crucial for optimizing the produced electrical power. The x-axis represents the tip-speed ratio (Lambda); it quantifies the rotational velocity of the turbine blades in terms of wind speed. Lambda numerical values range from 0 to 20. An increase in Lambda leads to an initial improvement in the turbine's power coefficient achievement for each blade pitch angle. The y-axis shows the power coefficient (C_p). The C_p usually reaches its highest point at an ideal tip-speed ratio and then decreases as the blades develop excessive rotational speed compared to the wind. Any of the coefficients does not exceed the Betz limit. Each curve corresponds to a distinct blade pitch angle (Beta), which varies between 0 and 12 degrees. When Beta = 0 (blue curve), the blades operate at their maximum aerodynamic capacity (flat angle), leading to the highest peak power coefficient of around 0.45, at a Lambda value of perhaps 8 (λ_{op}=8). As Beta increases, the peak efficiency (C_p) decreases, resulting in lower effectiveness. These findings indicate that higher blade pitch angles diminish the turbine's capacity to harness wind energy efficiently. However, it may be essential for particular operational situations, such as severe winds. The trade-off is necessary to maximize the productivity of wind turbine design and operation.

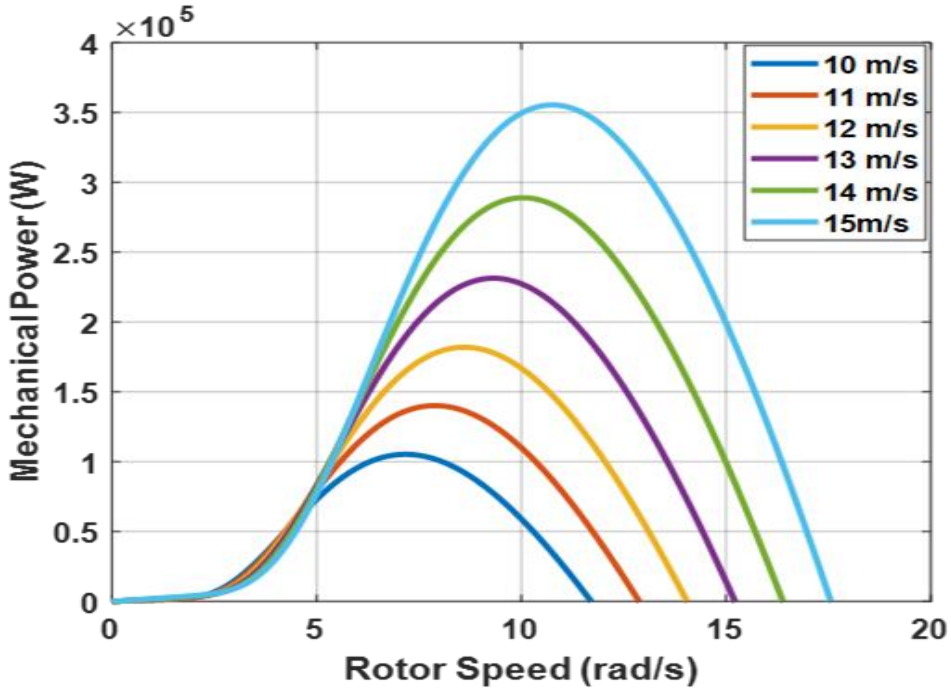

Figure I.13 Curves of mechanical power against rotor speed at various rotor speeds, while the pitch angle is set to zero.

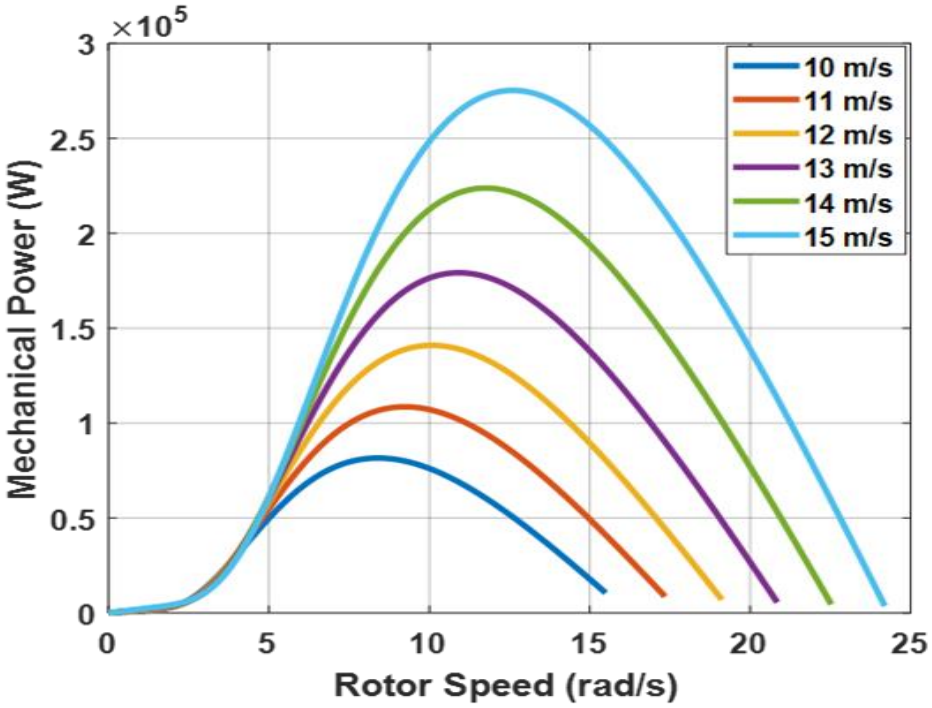

Figure I.14 Mechanical power curves versus rotor velocity at different wind speeds with a pitch angle of 4 degrees.

The graphs displaying the simulation results for mechanical power against rotor velocity at different wind speeds are presented in **Figure I.13** and **Figure I.14**, with blade pitch angles of 0 and 4 degrees, respectively. The power curve of a wind turbine is the most basic indicator of its success. The graph incorporates six curves, each according to a different wind speed: 10 m/s, 11 m/s, 12 m/s, 13 m/s, 14 m/s, and 15 m/s. Initially, the mechanical power rises with the rotor speed until it reaches an optimum value, following which it decreases as the rotor speed grows. As indicated by each curve, the utmost mechanical power is achieved for a specific wind speed at the optimum rotor speed. Working at this optimal velocity guarantees the maximum yield of energy from the wind. Once the rotor speeds above this ideal point, the mechanical power suffers from limitations in energy conversion. These findings show that performance drops dramatically when the rotor is operated at speeds much higher than the ideal speed. Proper operation of turbine control systems is crucial since exceeding the maximum rotor speed might result in diminished power generation and avoidable impact on the entire system. Moreover, the Coriolis forces [40] might contribute to the decrease in power. In the absence of equilibrium between frictional and pressure gradient forces, the Coriolis effect induces a shift in wind direction. The resulting imbalance induces a rotating effect on the flow of wind. Thus, the Coriolis force exerted on the imbalanced forces causes the wind's direction to vary with altitude.

The increasing wind speed is directly related to the growing development of the maximum mechanical power output. This effect is anticipated due to the direct proportionality between wind power and the cube of wind velocity. Consequently, even minor increments in wind speed can substantially augment electrical power. The optimum rotor rotation velocity rises linearly with the increase in wind speed. This implies that the rotor must rotate at higher wind speeds to sustain the greatest energy extraction.

According to the blade pitch angle, power output is greater at all wind speeds when the blade pitch angle is 0 degrees (Figure 1.13) than at 4 degrees (Figure I.14). These results demonstrate that an increased pitch angle decreases the total energy captured from the wind. By raising the blade pitch angle to 4 degrees, the aerodynamic efficiency of the turbine is diminished. This is expected because the angle of attack of the airflow on the blades is reduced as the pitch angle rises.

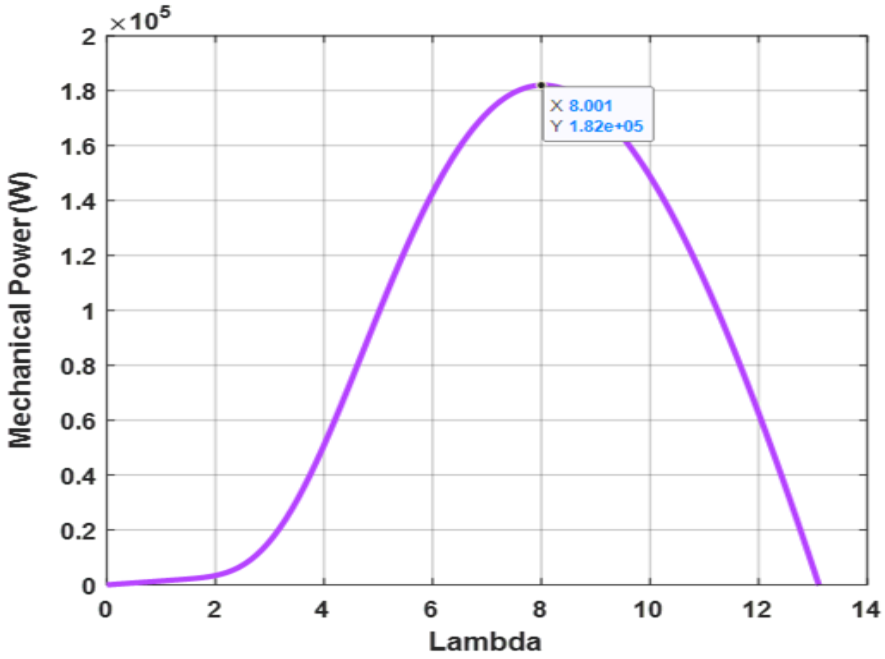

Figure I.15 Mechanical power vs. TSR.

Figure I.15 displays the results of simulation of mechanical power versus lambda (λ). The graph shows that the peak mechanical power is about 1.82×10^5 W when the tip speed ratio is 8. This value represents the ideal tip speed ratio at which wind turbines operate optimally to generate maximum power. Predictably, the power output reaches its highest point at the optimal TSR value and then decreases because of stalling. The figure underscores the need to maintain a suitable tip speed ratio to ensure excellent wind farm performance. Additionally, the simulation results emphasize the direct impact of wind speed and tip speed ratio on mechanical power while realizing the monitoring system's role in controlling operation beyond design limitations.

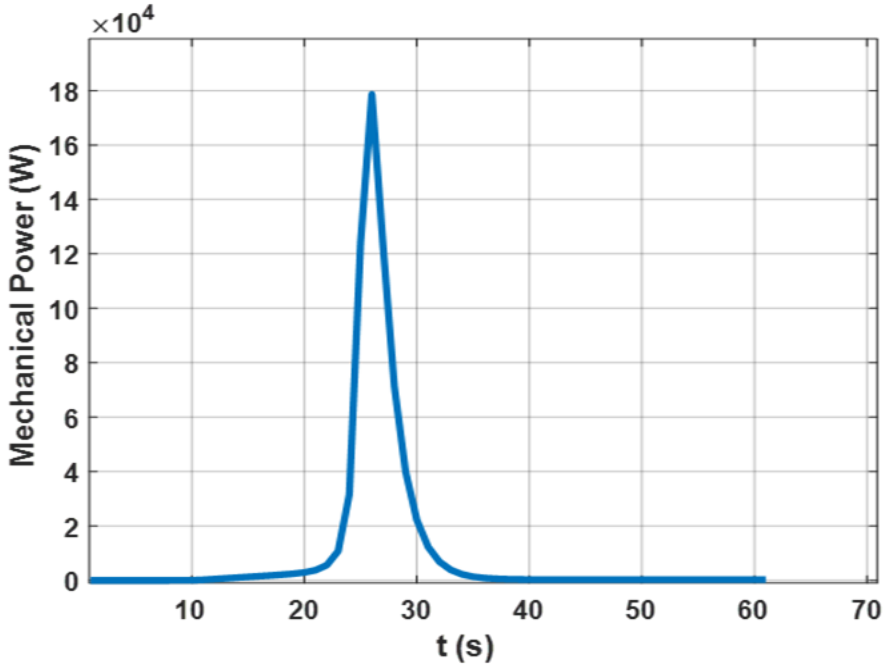

Figure I.16 Mechanical power (W) versus time (s).

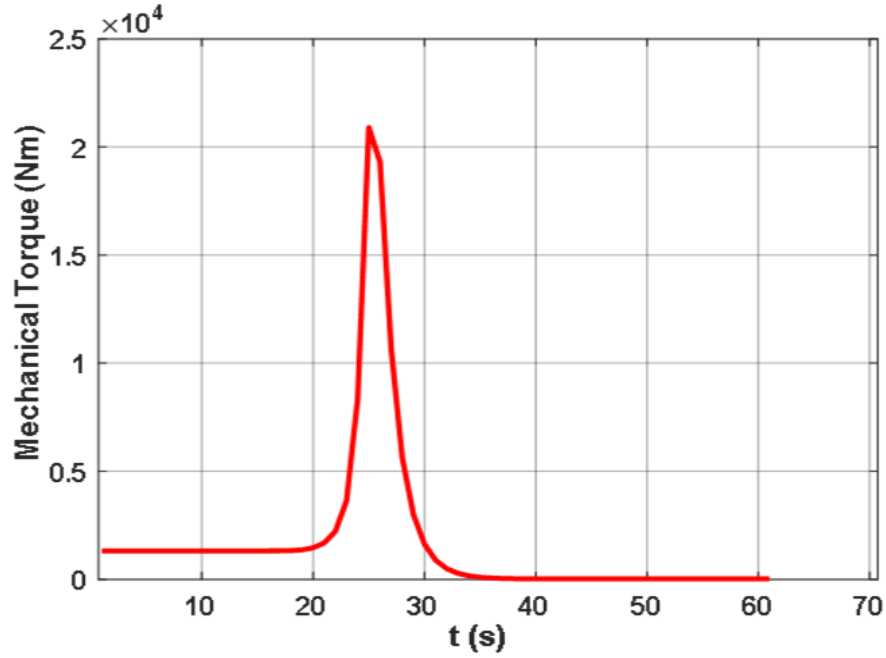

Figure I.17 Mechanical torque (Nm) versus time (s).

Figures I.16 and **I.17** exhibit time-dependent changes in the turbine's mechanical power and torque under fixed wind speed conditions, respectively. They exhibit a transitory behavior characterized by a sudden surge in power production followed by a quick decline over time.

For a constant wind speed (V_w= $12m/s$), at roughly t = 25 seconds, the curve displays a sharp increase in mechanical power, reaching its highest point at around 18×10^4 W. Once it reaches its peak, the power exponentially declines to almost zero, resulting in a spike-like pattern on the graph. Within the initial 20 seconds, the mechanical power and torque remain relatively low, almost negligible, suggesting that the system is either in a state of initial growth or experiencing dormancy. Within 20 to 30 seconds, mechanical power and torque rapidly and significantly increase, ultimately reaching its maximum point. This may be attributed to an abrupt occurrence or a modification in operational parameters, such as the initiation of a mechanism, the wind reaching a specific velocity limit, or some external influence. The mechanical energy drops significantly after the maximum point at about 25 seconds, reaching almost zero at the 40-second point within a short period. After a significant reduction, mechanical energy levels remain almost zero for the rest of the duration, indicating that the system has stopped producing mechanical energy and has returned to inactivity. These outcomes greatly enhance the understanding of wind turbine dynamics by offering practical insights and opening up prospects for further study of the intricate relationships between parameters and external factors.

I.7 Conclusion

Wind turbine theories have been thoroughly analyzed, leading to the modelling of the aerodynamic subsystem using mathematical simulation techniques to understand its operation comprehensively. The complex interaction of the aerodynamic system parts, including the rotor, gearbox, and generator, was investigated to comprehend their combined role in energy conversion. Developing and modelling a mathematical model utilizing MATLAB/Simulink acquired significant knowledge about the dynamics of wind turbines.

The simulations undertaken in this study demonstrated substantial correlations among the power coefficient, tip speed ratio, and blade pitch angle. Regulating the pitch angle is necessary for optimal energy generation at designated wind speeds, underscoring a vital factor for effective wind turbine deployments. The assessment of mechanical power and torque under different wind speeds yielded details about wind turbines' intricate behavior. Additionally, the power coefficient characteristics were found out for various blade pitch angle. In order to guarantee reliable optimal energy conversion, the simulation results are utilized as a basis for refining wind turbine performance under a variety of conditions.

CHAPTER II

Maintenance Strategies and The Analysis of Common Failure Modes in Wind Turbines

II.1 Introduction

The rapid expansion of wind energy as a renewable energy source has emphasized wind turbines' reliability and efficiency. Nonetheless, due to complicated operational and environmental conditions over long periods, the wind industry is encountering unexpected damages to the main parts of wind turbines, which directly impact maintenance, dependability, and operational expenses. The drivetrain, particularly the gearbox and its inside bearings, has the most significant maintenance costs and breakdown rates among the diverse elements. The health of bearings is essential for wind turbine operation, as many failure modes (including wear, white-etched cracks, corrosion, etc.) can cause catastrophic harm to turbine systems. Identifying the reasons of failures and formulating potential remedies is crucial to enhance the longevity of turbine parts and reduce maintenance expenses.

This chapter thoroughly examines maintenance techniques and investigates the many fault modes that may occur during operation. The prevalent tribological failures of wind turbine bearings are introduced, and the typical failure modes of these bearings are discussed in detail. These defects can each display unique vibration signatures and failure changes, essential for developing predictive maintenance procedures and early detection methods. The chapter also summarizes Condition-based maintenance techniques currently adopted in the machine industry, emphasizing the advantages of condition-monitoring strategies.

II.2 Maintenance Basics

II.2.1 Maintenance definition

Maintenance involves a combination of technical, administrative, and managerial tasks performed throughout an asset's lifecycle. These tasks aim to preserve or return the asset to a state where it can effectively perform its intended function while minimizing costs. A maintenance strategy is a structured approach to ensuring the proper functioning of equipment. It involves tasks like identifying, evaluating, and carrying out necessary repairs, replacements, and inspections. Implementing this strategy requires detailed operational plans that can be executed effectively [41]. Additionally, maintenance strategies must be regularly reassessed to adapt to evolving environmental conditions and business needs. Neglecting equipment during its initial phase of deterioration or opting for immediate replacement can result in increased

expenses. Optimal maintenance strategies can only be developed through on-site maintenance, which allows for assessing the degradation conditions of all equipment [42]. Numerous studies consider maintenance as a means to reduce the extent of equipment degradation.

Maintenance is categorized into four key concepts:

- ***Maintenance***: Involves continuous monitoring and preventive actions to ensure assets remain in optimal working condition.
- ***Reconditioning***: This process focuses on addressing and rectifying issues after failures, restoring equipment to its proper functioning state.
- ***Condition***: Specifies the necessary skills and targets for maintenance activities.
- ***Cost optimization***: Guides all procedures to achieve maximum economic efficiency.

II.2.2 Types of maintenance

Maintenance planning focuses on determining the most effective strategies for each machine or element in the plant, taking into account equipment availability requirements and the overall maintenance budget. Each part must be analyzed based on its failure rate, cost, and the potential impact of its failure on the entire system to determine the most effective solution. A well-thought-out maintenance program needs to customize different strategies for various equipment. Some will directly affect the company's daily operations, while others will address important safety concerns and require extensive maintenance [43]. Therefore, maintenance strategies serve as the approach for translating enterprise goals into actionable maintenance objectives. The right maintenance strategy for a particular asset or system relies on many important considerations, such as the equipment's importance, working environment, financial constraints, and available resources. A literature review reveals that maintenance strategies can categorized into Reactive (after failure) and Proactive (before failure) approaches as demonstrated in Figure II.1. Reactive strategies transpire after a failure, encompassing corrective maintenance that may be either immediate or scheduled. Proactive techniques, including preventive (scheduled periodically), condition-based, predictive, and prescriptive maintenance, seek to prevent failures before they occur.

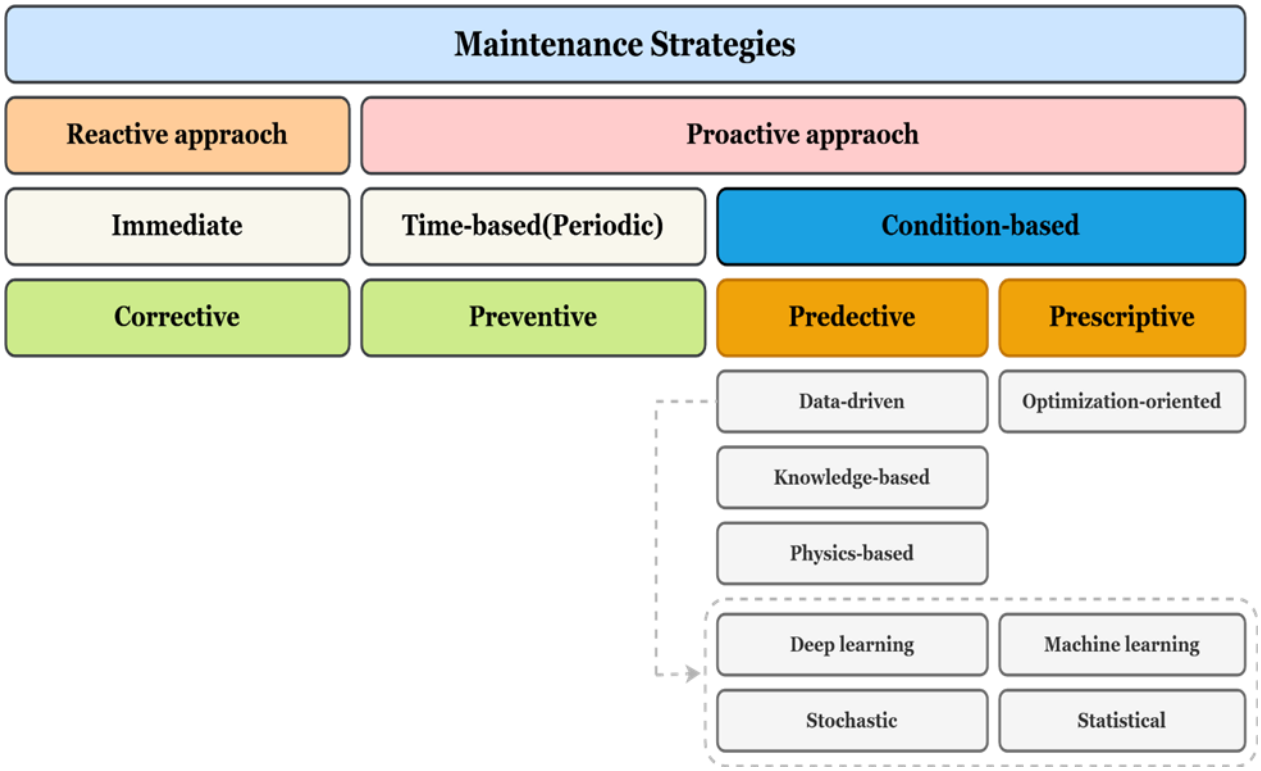

Figure II.1 Classification of maintenance strategies [Adapted from [44]].

II.2.2.1 Corrective maintenance

The term "corrective maintenance" describes the procedures used to restore equipment to working order after a malfunction. It is the most intuitive yet very expensive strategy, as it is implemented in response to failures and all the repercussions caused by the incident. Corrective maintenance involves identifying issues, inspecting, and replacing machine components following a stoppage or failure. This technique is ideal for non-critical systems where maintenance can occur swiftly and inexpensively, and failures do not result in serious consequences[45]. There are two basic categories of remedial maintenance: planned maintenance and unplanned maintenance, which involves unscheduled repairs and fixes as needed [46].

II.2.2.2 Preventive maintenance

The drawbacks of remedial action are addressed by preventive maintenance. Preventive maintenance focuses on component dependability, performed before a failure emerges. Preventive maintenance refers to a series of actions and processes carried out by the maintenance team to ensure machines and equipment remain in optimal working order. Its goal is to prevent unexpected failures or breakdowns by identifying and addressing potential issues

before they lead to operational disruptions [46]. This maintenance approach is described as scheduled, planned, or periodic maintenance. A robust preventative maintenance program is the key to efficient maintenance. Preventive maintenance can be divided into two distinct methodologies: predictive maintenance and periodic maintenance.

II.2.2.3 Condition-based maintenance (CBM)

CBM is a variant of preventive maintenance and is often categorized as a maintenance plan. Owing to the expanding technological capabilities for monitoring, storing, and analyzing situations, condition-based maintenance (CBM) solutions are becoming increasingly prevalent. Condition-based maintenance (CBM) is a procedure that monitors the health status of machine parts over time to identify and avert potential problems [47]. A CBM system seeks physical evidence that an issue has occurred or is imminent, utilizing real-time equipment data such as acoustic emission, vibration, temperature, lubricating oil, etc., obtained through condition monitoring to make maintenance decisions. Therefore, the significance of CBM relies on the accuracy of the monitoring process[48]. The initial difficulty is to ascertain the precise timing for maintenance and find the optimal operation plan. CBM is applied in numerous fields, including vibration modeling, sensor performance, signal processing, noise control, thermodynamic performance monitoring, lubricating oil analysis, and corrosion surveillance [49]. Choosing a suitable CBM and its optimization methods is consistently tricky and largely contingent upon the system. This maintenance setup significantly decreases machine breakdown costs, avoids disruptions to regular functions, lowers unscheduled downtime from defects, and improves machinery performance.

II.2.2.4 Predictive maintenance (PdM)

Predictive maintenance is a condition-based preventive maintenance strategy. It entails using advanced tools, including condition monitoring, evaluation of performance metrics and data analysis to mitigate possible defects and mechanical equipment degradation [50]. Predictive maintenance serves as a complement to both corrective and preventive maintenance strategies. It is possible to classify predictive maintenance work into regular surveillance. PdM is most effective when executed in real-time and can be conducted either online or offline. Some of today's most intelligent and helpful maintenance technologies, such as condition monitoring programs, originate from predictive repair methodologies. The primary objective is to forecast the occurrence of a fault and then identify the optimal timing for maintenance operation. The

applications of Industry 4.0, mainly the increasing volumes of heterogeneous data produced during the production process, have expedited the adoption of digitalized maintenance activities in production facilities [51].

Prognostic and health management (PHM) processes are the main actors in the industry 4.0 revolution. These systems seek to address challenges in efficient detection and provide an intelligent maintenance strategy via real-time monitoring and data analysis. Prognostic and health management includes CBM and PdM, as shown in Figure II.2. Diagnostics is the process of identifying components through the use of sensors. On the other hand, prognostics involves examining the device's operation and predicting the time of its downtime [52]. In contrast to CBM, PdM leads to decreased maintenance expenses [53]. According to [54], Predictive maintenance is an essential part of the more significant idea of condition-based maintenance (CBM), which has emerged from gradually incorporating new resources, including skills, technologies, techniques, and strategies, to enhance the maintenance function. Further, [55]classified PdM methods into three distinct categories: (a) data-driven, (b) knowledge-based, and (c) physics-based (Figure II.1). Data-driven relies on data analysis and machine learning technologies without comprehending the system's physical behaviors, where data is gathered from the components to predict failures. Knowledge-based PdM methods are models that enhance the maintenance process by relying on human knowledge, facts, concepts, or historical defect information. Physics-based (or model-based) processes emphasize methodologies established on mathematical models of system behaviors derived from physical rules, indicating a decline in system performance [56].

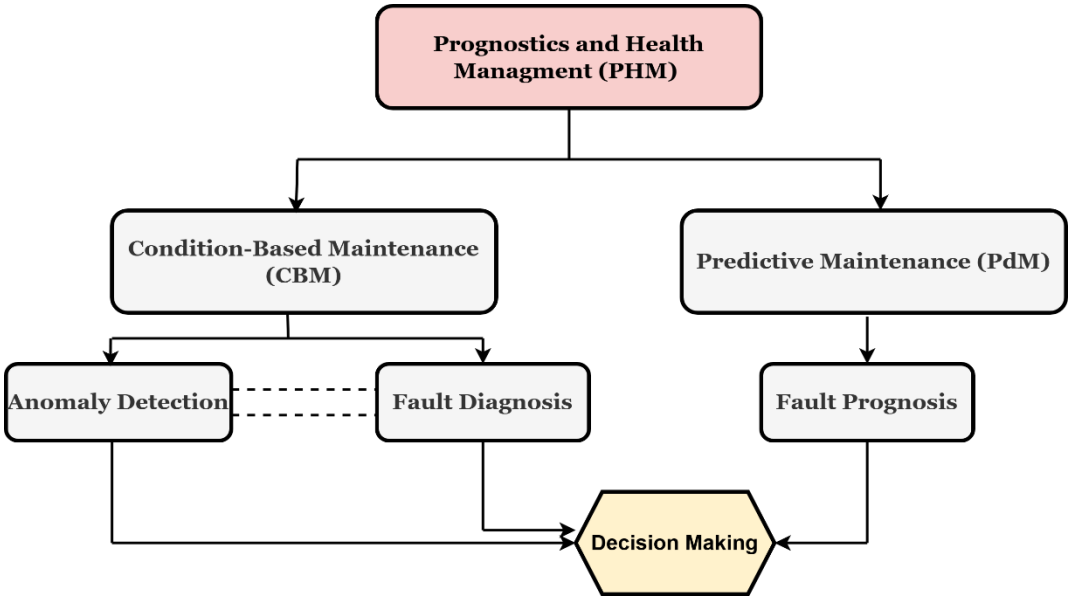

Figure II.2 Prognostics and health management process classification [47].

II.2.3 Condition-based maintenance techniques

The implementation of CBM often necessitates the selection of monitored components, the identification of monitoring methodologies, the installation of requisite technological tools, and the establishment of suitable data processing processes [57]. The viability of deploying CBMs must be assessed from organizational, financial, and technical viewpoints. As displayed in Figure II.3, the CBM process can be delineated through a series of basic stages. In general, a typical CBM system comprises three key phases: (1) data acquisition, (2) data processing, and (3) maintenance decision-making [58]. Data acquisition pertains to the systematic collection and storage of valuable information through various sensors, including electrical, electronic, mechanical, and electro-mechanical, which pertaining to factors that can indicate the deterioration process of the components under observation. The collected data are subsequently processed to assess the condition of the system being examined. Once the data has been processed, it is inputted into designated algorithms, generally configured for identification, diagnosis, and/or forecast. Diagnostics and prognostics are two critical components of a condition-based maintenance strategy.

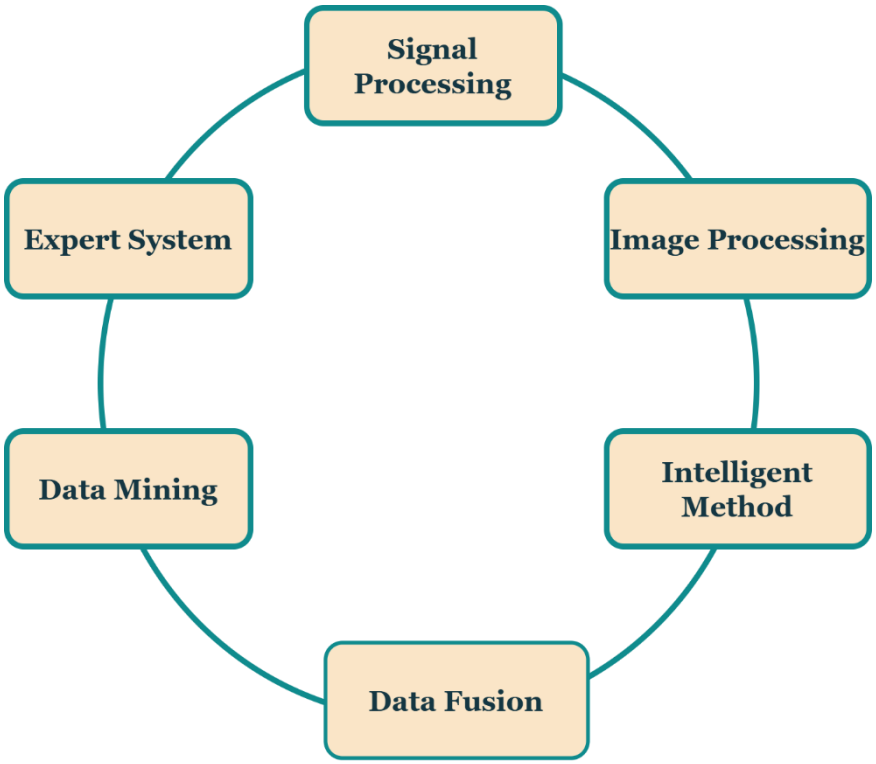

Figure II.3 The procedure of CBM[59].

The condition monitoring (CM) procedure is the essence of CBM, which involves continuously surveilling signals through specific detectors or suitable measurements to recognize a substantial change that signifies an emerging fault. The CM system can be conducted in two manners: online and offline. Online processing occurs during the apparatus's operational state, whereas offline processing is undertaken when the device is not operating [60]. As a result of the advent of Industry 4.0 in recent years, condition monitoring technologies of rotating machines have transformed from visual inspections and manual dataset analysis to the generation of real-time big data on diverse diagnostic parameters. These are based on techniques including Acoustic emissions, temperature, vibration analysis, currents, velocity, pressure, oil conditions, strain measurement, rotor-to-stator contact, and thermography by high-frequency sensors. [55]. Among these tools we list:

II.2.3.1 Vibration analysis

In the modern industry, vibration analysis is the most frequently efficient tool employed in condition-monitoring techniques for rotating machinery (e.g., bearings and gearboxes) during starts, shutdowns, and routine operations. Vibration measurements are generally conducted online, offering real-time diagnostic insights into the equipment's present state[61]. Every

apparatus possesses a standard level of vibration. Nevertheless, the device's vibration intensity sometimes escalates or becomes severe. The machine's vibration signatures can alert the operator to prompt repair or facilitate critical decision-making before significant issues or unplanned downtime occur [62]. Excessive vibration may be caused by various causes, such as misalignment, imbalance, eccentricity, deteriorated gears or bearings, cracked, or looseness. The issue's strength is indicated by the magnitude of the vibration signature, while the source of the fault can be determined by the frequency. Vibration signals can be obtained with vibration sensors affixed to each device bearing, such as accelerometers, velocity sensors, and displacement sensors, where accelerometers are the most dominant type. An accelerometer comprises a mass and numerous piezoelectric-crystal components and is distinguished by its extensive frequency range [63].

II.2.3.2 Lubricant monitoring

In recent years, lubricant Monitoring or oil analysis is used as an early detection system for machines and a tool for identifying and predicting failures within Condition Based Maintenance (CBM). The leading roles of lubricants encompass minimizing wear and friction, safeguarding against corrosion and rust, cleansing the system, and eliminating impurities from the oiled system. Lubricating grease and oil are commonly referred to as "lubricant" [64], which is produced by combining one or more basic oils with additives. A lubricating oil analysis system evaluates the condition of the oils, focusing on modifications or degradation that affect the lubricating properties and determining whether the oil is suited for other uses. Additionally, maintenance decision-making is facilitated by this knowledge, which is employed to mitigate any system faults [65]. For offline sensors that detect lubricating oil properties, a tangible sample of the oil must be extracted from the Lubrication System and then examined in a laboratory setting, separate from the working device. In contrast, online sensors mounted on the apparatus monitor the amount of the lubricating fluid in situ as it flows from the perpetually distributed lubricant through work [64]. Online oil analysis is increasingly gaining significance due to various existing experiments.

II.2.3.3 Acoustic emission analysis

The acoustic emission (AE) strategy is a highly sensitive method for detecting minor fractures in the upper-frequency band, making it an accurate tool for monitoring machinery conditions and defect diagnosis. AE is a well-established non-destructive evaluation (NDE) technique initially studied in the 1950s that detects ephemeral stress waves in components

[66]. According to the American Society for Testing and Materials (ASTM), Acoustic Emission (AE) is a phenomenon characterized by the swift release of localized source energy within a material, resulting in the generation of transient elastic waves, typically occurring within a frequency range of 10 kHz to 1000 kHz. AE is distinguished by its capacity to frequently monitor an entire structure without requiring it to be taken out of service, which could significantly reduce expenses more than other NDE methods, such as ultrasonic[67]. The acoustic sensor detects AE signals, which can be categorized as continuous signals and transient signals. The quality attributes of different AE sensors can indicate their measuring efficacy and are chosen according to the relevant detection frequencies. Nowadays, the primary types of AE sensors are piezoelectric, fiber optic (FO), and micro-electro-mechanical system (MEMS) sensors[66].

II.2.3.4 Infrared thermography

Infrared thermography (IRT) has been regarded as one of the most famous CM approaches that is non-invasive and non-contact in nature and has multiple applications, such as assessing plastic deformation, civil engineering, and Examining fatigue fractures[68]. The International Organization for Standardization (ISO) describes IRT as a discipline that collects and analyses thermal distribution data from contactless infrared imagining instruments[69]. It is predicated on infrared radiation, a type of electromagnetic energy characterized by longer wavelengths than visual light. Infrared radiation is emitted by any object at a temperature above absolute zero (-273.15 C°). The intensity and spectral content of radiation generated by a body are intrinsically connected to its surface properties[70]. The minimal hardware required is one of the most essential benefits of IRT in CM. The apparatus consists of a thermal camera, a tripod, and video output devices that display the infrared thermal images collected, called a thermogram.

II.3 Vibration Analysis Fundamentals

II.3.1 Definition

According to ISO 2041, vibration is the fluctuation of the intensity of an amount indicative of the movement or position of a mechanical system over time relative to a reference position caused by a force. The reference system typically consists of directions that relate to a mean or equilibrium location. Displacement can often be represented by either a rotation vector, a

translation vector, or a combination of both. Vibrational signals can be categorized into several types, including "random" and "periodic" where "random" refers to signals that cannot be accurately predicted. Periodic signals are analytically describable and repeatable. Vibration analysis include mathematical modeling, the creation of governing formulas, and the assessment of vibration signals[71]. The intensity of the vibrations differs amongst machines and depends on the loading conditions. Moreover, each mechanical defect produces a distinct vibration waveform based on the device's structure and working conditions[72]. The many elements of a machine oscillate at distinct frequencies and amplitudes, indicating that the vibration is primarily defined by its frequency, amplitude, and nature.

II.3.2 Measurable factors of vibration

Understanding the concepts and applications of different quantifiable factors is essential to analyze vibration modes accurately. In vibration amplitude graphs, fundamental components such as peak-to-peak, root-mean-square (RMS), and peak value can describe a function (Figure II.4). The three principal vibration parameters are as follows.

- ***Frequency***: Vibration frequency is a quantitative measurement that indicates the speed at which an object performs a complete cycle of oscillatory movement in one second, expressed in hertz (Hz). The frequency can be represented by cycles per minute (CPM) or revolutions per minute (RPM), where CPM equals RPM and Hz is equal to CPM/60 or a multiple of turning speed (TS). Frequency $\boldsymbol{f}$ is expressed as a function of period $\boldsymbol{T}$ by the following relationship: $f = 1 / T$
- ***Amplitude***: The amplitude denotes the maximum distance from the reference location, signifying the extent of the oscillation in terms of displacement, velocity, or acceleration. Amplitude measurements in vibration monitoring are commonly classified into three categories: broadband, narrowband, and component [72].
  - Displacement: Considering the direction, it is defined as the removal between an object's initial and ultimate positions. It is typically articulated in terms of peak-to-peak or peak.
  - Velocity: Measurement of the displacement of an object relative to a given time. Velocity is generally utilized for motion within the frequency range of 10 Hz to 1000 Hz. It can be expressed in units such as meters per second (m/s) and in terms of or peak or RMS.

- Acceleration: is the rate at which an object's velocity changes over time. Its standard unit is meters per second squared (m/s²). Vibration frequencies above 1000 Hz should always be expressed as acceleration.

- ***Phase***: quantifies the temporal disparity between two events happening at identical frequencies. Providing that the machinery structure is well comprehended, comparative phase readings can identify specific issues in equipment development.

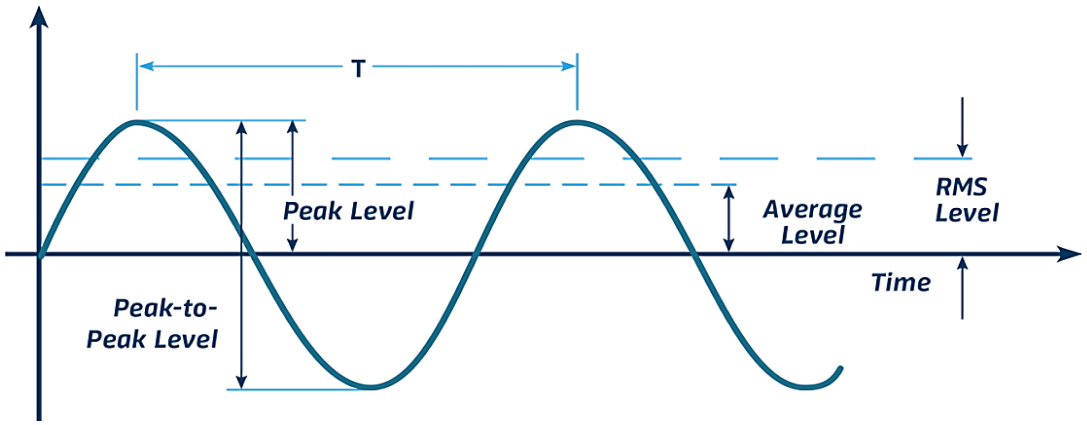

Figure II.4 Periodic vibration signal.

II.3.3 Vibration profile

There are two types of movement: harmonic movement and non-harmonic movement. For every entire cycle, harmonic vibrations are repeated. Conversely, non-harmonic movements result from the accumulation of moves from various causes with varying rates. A vibration characterized by a displacement that is a harmonic function of time is known as a simple harmonic vibration, the most fundamental form.

A sinusoidal waveform can be mathematically represented as:

- Displacement: $X(t) = A \sin(\omega t)$ (II.1)

Where A is the maximum amplitude, ω is the angular frequency ($\omega = 2\pi f$), and t is time.

The velocity and acceleration of this oscillatory displacement wave are theoretically linked through an interaction of frequency, amplitude, and time.

- Velocity: $V(t) = \mathrm{A}\omega \cos(\omega t) = A\omega \sin(\omega t + \frac{\pi}{2})$ (II.2)
- Acceleration: $a(t) = -A\omega^2 \sin(\omega t) = A\omega^2 \sin(\omega t + \pi)$ (II.3)

Every vibration can be represented as a sequence of sine functions, with the cyclic frequencies (ω_1, ω_2) designated as the harmonics of the fundamental frequency ω. A_1, A_2, etc. represent the amplitudes of the distinct vibrations, while Φ_1, Φ_2, etc. denote their respective phase angles. The formula is referred to as a Fourier series [72].

$$f(t) = A_0 + A_1 \sin(\omega t + \Phi_1) + A_2 \sin(2\omega t + \Phi_2) + A_3 \sin(3\omega t + \Phi_3) + \ldots\ldots \quad \text{(II.4)}$$

A vibration waveform can be depicted in both the frequency and time domains, as shown in Figure II.5. The time domain profile illustrates the relationship between amplitude and time. In contrast, a frequency domain profile (or spectrum) is produced by converting a time-domain signal using the Fast Fourier Transform (FFT) technique and displays amplitude against frequency. FFT allows for the representation of vibration signals as discrete frequency peaks.

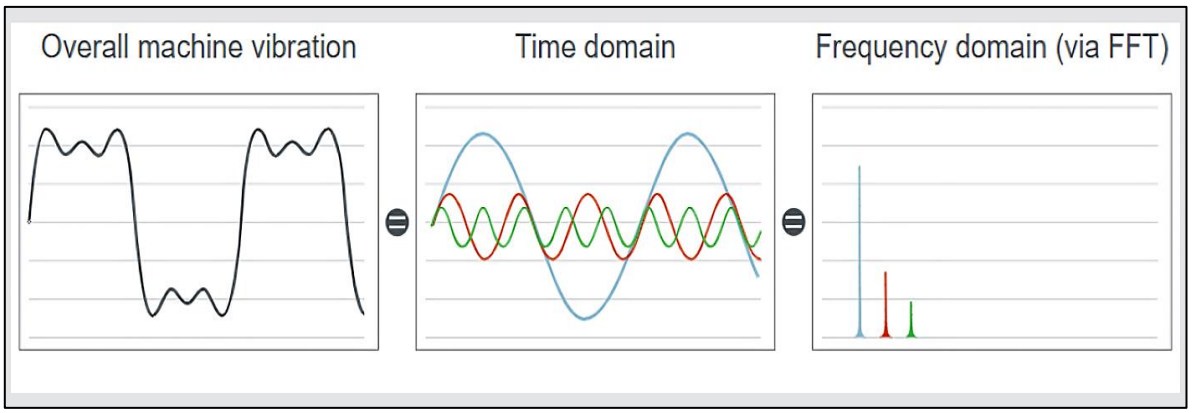

Figure II.5 An example of an oscillation signal in the time and frequency domain.

II.3.4 Vibration measurement

A vibratory analyzer is a device employed to assess the vibration data generated by machines, which comprises a sensor, amplifier, filter, and A/D converter (analogue to digital converter) [73]. In order to improve the signal-to-noise ratio and resolution, the output of the vibration sensor is passed through an amplifier. The enhanced signal then goes through a filter to prevent aliasing during the digitization process. In the A/D converter, the signal is converted to digital form and transmitted through the processing device. At this step, it can be represented as a time waveform or processed more deeply to obtain a frequency spectrum. There are two types of vibration analyzers: conventional and computer-based. A conventional vibration analyzer is a self-contained tool designed to handle vibration. This equipment is intricate and costly, and vibration specialists typically employ it. A computer-based vibration analyzer is an innovative

equipment that enables the simulated processing of vibration data using special software and a private computer.

II.3.4.1 Sensor

Vibration can be quantified using a transducer or a portable vibration analyzer. A transducer or sensor is an instrument that transforms variations in mechanical quantities into alterations in additional physical quantities, typically generating an electrical signal[74]. Commonly, three types of transducers are employed to measure vibrations: displacement sensor, velocity pickup, and accelerometers. Each transducer has its benefits and drawbacks, contingent upon the application. The frequency range, design, sensitivity, and operating limits are the primary factors determining the type of sensor used. A portable vibration analyzer is an equipment that can mathematically transform electrical signals into acceleration per unit of time, save and display data, and activate alerts when planned. Furthermore, selecting and adequately implementing a sensor mounting mechanism is crucial for effective vibration data acquisition. Vibration sensors are often affixed continuously at designated locations throughout the rotating machinery for online status monitoring. The four primary mounting techniques are stud-mounted, adhesive-mounted, magnet-mounted, and non-mounted[73]. The following subsections outline the key attributes of these three sensor kinds.

1. **Displacement sensor**: These transducers, called eddy current sensors (Figure II.6), employ capacitive, visual, or ultrasonic concepts to quantify the shaft's vibrational displacement. They are appropriate for monitoring vibration frequencies below 10 Hz, although they can also measure vibrations up to 300 Hz. The displacement unit might be in meters, centimeters, or millimeters. Displacement sensors are categorized into different types, with some operating based on induced currents and others based on variable resistance. Eddy-type proximity collection system components include a sensor and a signal adapter, giving us an excellent frequency response. Displacement probes can detect issues related to unbalance and misalignment. In comparison to other sensors, this type of sensor is distinguished by its exceptional thermal stability and its ability to perform low-frequency measurements [75]. On the other hand, the disadvantages are that these transducers are influenced by electrical and mechanical reading inaccuracies and minor fissures in the shaft can lead the transducer to perceive them as elevated vibrational activity. They need to be permanently installed, which is constantly expensive, and in some cases, impossible.

Figure II.6 Eddy current sensor

2. **Velocity Transducer:** The velocity sensors are electromechanical transducers that immediately measure the vibration's velocity. It is capable of functioning independently of any additional equipment and operates on the principle of electromagnetic induction [76]. Figure II.7 illustrates the schematic of the velocity sensor, which comprises a coil of delicate wire upheld by pliable springs, and a permanent magnet, securely affixed to the transducer's casing, generates a robust magnetic field surrounding the coil. As the material on which the sensor is affixed vibrates, the motion of a coil within a magnetic field induces a voltage across the coil's terminal wires. By transferring energy from the magnetic field of the magnet to the wire coil, this voltage is generated proportional to the velocity of the vibration. The sensitivity of the speed remains constant within a defined frequency interval, typically from 10 Hz to 1000 Hz. Velocity transducers are generally less expensive than other sensors, and their effortless installation makes them an advantageous choice for monitoring the vibration of rotational machines.

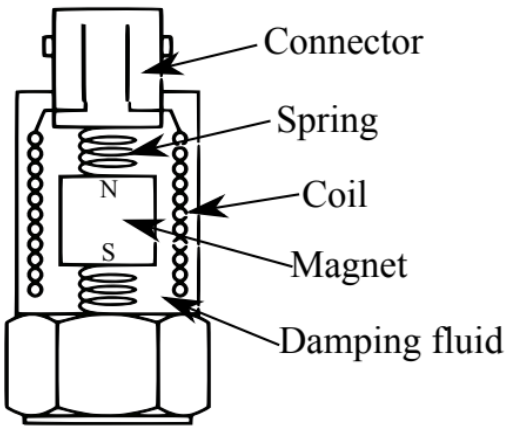

Figure II.7 Schematic of velocity sensor [77].

3. **Accelerometers:** An accelerometer is an electromechanical sensor utilized to quantify acceleration of an element and is the most prevalent transducer utilized in rotating machinery tasks owing to its dependability, straightforwardness, and durability. The operational principle is that when the piezoelectric substance in the accelerometer experiences a force, it generates a charge proportional to the force exerted. The force exerted on an object is equivalent to its mass multiplied by its acceleration (F = ma), which underpins the functionality of accelerometers [78]. Accelerometers operate based on the principle of inertia, and the force is directly related to the acceleration; therefore, any modification to this measure will result in an alteration in the charge generated, which is subsequently reinforced. These sensors can be uniaxial, sensing acceleration along a single axis, or triaxial, capable of identifying motions in three directions. In comparison to the uniaxial accelerometer, the triaxial accelerometer possesses greater storage space but is significantly more costly [73]. An accelerometer can be categorized into piezoelectric and micro-electromechanical system (MEMS) types. Piezoelectric accelerometers take advantage of the piezoelectric effect, which yields an electrical signal in particular materials when subjected to vibration. The amount of the electrical charge is directly correlated to the incident acceleration. There are numerous benefits to using a piezoelectric accelerometer, including its superior sensitivity, weightless design, improved dynamic range, and frequency, and it was specifically designed to assess vibrations in small constructions. Nonetheless, it is susceptible to external environmental intervention [62]. Figure II.8 (a) illustrates a depiction of the piezoelectric device and its various parts. MEMS accelerometers are the result of rapid advances in semiconductor micro-manufacturing techniques that have facilitated the advancement of instruments consisting of mechanical elements with sizes as small as a few micrometers[79]. It is possible to implement MEMS accelerometers using piezoresistive or capacitive concepts. A MEMS accelerometer typically contains a moving test mass with plates supported by a mechanical suspension structure attached to the frame [80]. Figure II.8 (b) shows these components. Since the transducer is stationary, the capacitance is uniform on all sides of the proof mass. While the equipment is subjected to acceleration, the mass flows in the contrary direction, resulting in disparate capacitances established between the fingers and the immobile layout on either side. As a result, the acceleration is quantified by observing variations in the disparity capacitance. Due to their simplicity in incorporating into Internet of Things (IoT) networks, MEMS accelerometers have been applied and verified for vibration

quantification in a diverse array of apparatus. Recent MEMS accelerometers deliver high-quality data at frequencies reaching many tens of kHz. Moreover, MEMS acceleration sensors provide the straightforward capture of analog or digital information. This represents the primary advantage over conventional accelerometers, which, while more accurate and dependable, necessitate wired connections for data transmission and demand a more sophisticated signal processing circuit[81].

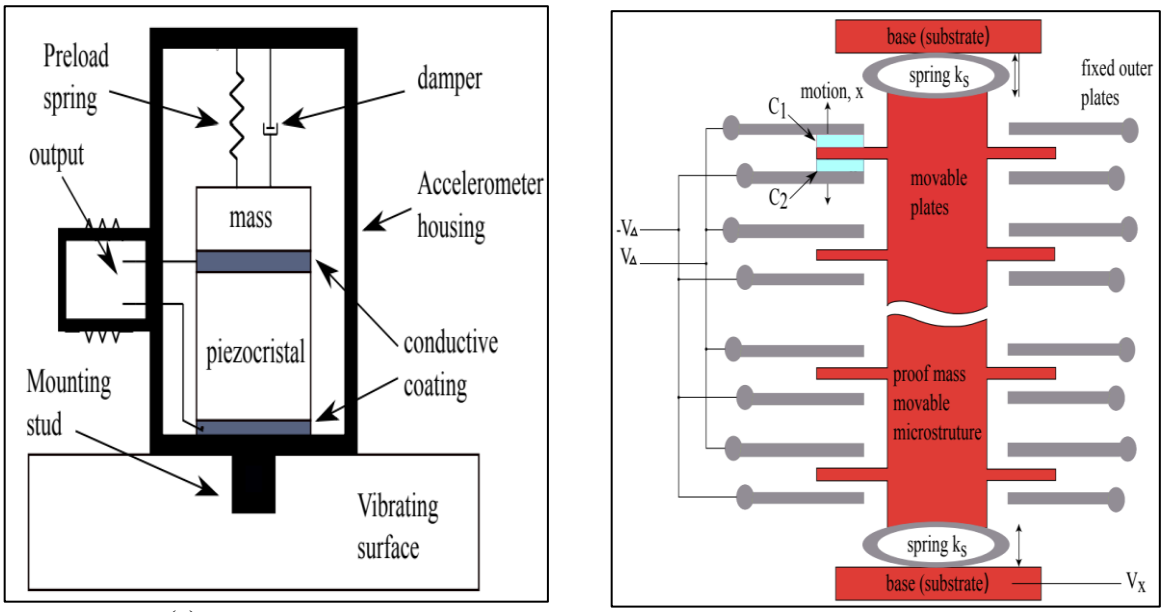

(a)
(b)

Figure II.8 Diagram of (a): Piezoelectric accelerometer, and (b): MEMS accelerometer [77].

II.4 Analysis of Common Failure Modes in Wind Turbines

With the ongoing advancement of the industrial sector, wind power stations were typically constructed offshore or in isolated highland regions, functioning in complex conditions to fulfill the demands for wind energy production[82]. One of the most critical components of a wind farm is wind turbines, which are intricate equipment composed of various technologies that operate under demanding climatic and operational conditions incorporating unexpected loads resulting from gusty winds, humidity, dust accumulation, corrosion, fatigue, wear, a broad spectrum of temperatures, and air pressures[83], this makes blades and towers particularly vulnerable to tribal influences. These delicate mechanical structures and severe conditions can lead to an increase in element faults and malfunctions in machines. Nevertheless, new issues emerged, and difficulties developed as the quantity of industrial wind turbine installations

escalated. Inevitable failures arise from damage to the wind turbine and surpassing the design fatigue threshold. In contrast, others stem from novel failure types resulting from material degradation, manufacturing flaws, and alterations in rotor size specifications, which cause a substantial rise in operational and maintenance expenses[84]. According to the wind turbine system, specific parts are more vital than others, so it is imperative to determine components with the maximum failure rate and downtime and categorize failure modes according to defect features.

Figure II.9 illustrates the percentage of each part relative to the overall failures in offshore wind turbines and the percentage of each part contributing to the downtime resulting from these defects. Recent research indicates that the generator and gearbox contribute the most to downtime in a wind turbine system, with the highest percentage at 33%, followed by blades at 22% and drivetrains at 11% downtime as shown in Figure II.9 (b) [85]. Blade, generator, and gearbox system failures are among the most prevalent forms of wind turbine breakdowns. The following is a summary of the frequent faults properties and their reasons.

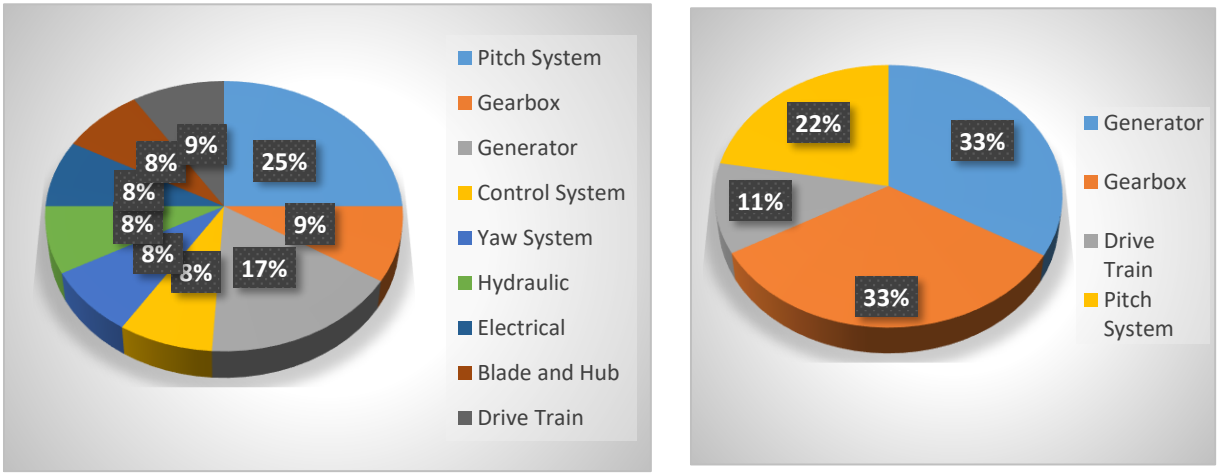

(a) (b)

Figure II.9 Failure and downtime rates of WT elements(Adapted from [85]): a) amount of overall failures for each element, (b): amount of overall downtime for each element .

II.4.1 Blade Faults

During WT operation, the blades are exposed to wind loads and are responsible for utilizing the wind's mechanical energy. Wind turbine blades consistently operate under extreme climate conditions, including air salinity, heavy rain, snow, and severe storms, etc. Such varying conditions may cause various blade damage events, and the extent of fault propagation is

contingent upon the blade profile. Another category of defects is the imperceptible ones resulting from process issues in the technology created by human fabrication. As the wind turbine is installed and operated, these hidden faults are subjected to repetitive extreme stresses and harsh external environments. The gradual development of unseen weaknesses may result in damage. The intricate composition and design of the blade material may result in each sort of damage arising from various reasons[86]. The cost of producing wind turbine blades accounts for approximately 15% to 20% of the turbine's total price[87]. The typical damage types and leading damage causes are analyzed below.

II.4.1.1 Damage caused by lightning

The prevalence of wind energy installations in rural and hilly areas, extended operational periods, and increased accumulation of contaminants on blade surfaces have resulted in a heightened susceptibility of wind energy facilities to lightning attacks[88]. Breakdown resulting from lightning hits on a blade is prevalent at the lightning catcher and many other sections of the blade. Lightning strikes can result in structural damage and a reduction in the strength of blade substances. Figure II.10 illustrates a blade destroyed by a bolt of lightning. When lightning hits the blade, the massive energy unleashed by the lightning causes a rapid rise in the temperature of the water-saturated fabric within the blade's structure. Subsequently, the decomposed gas extends at high temperatures, increasing pressure and leading to damage[89]. The electrical components of the turbine, such as the generator and control systems, can also be damaged by lightning. The level of harm inflicted by lightning on blades is largely contingent upon their material composition. Research indicates that the blades of wind turbines are exceedingly susceptible to lightning strikes due to the utilization of carbon fiber-reinforced polymer (CFRP)[90]. Delamination was the most frequent form of lightning damage, accounting for 72.4% of the overall blade degradation, followed by debonding of the shells (24.7%). In 1.4% of the cases examined, detachment occurred in both the shell and the tip[91].

Figure II.10 Wind turbine blade damaged by lightning.

II.4.1.2 Damage due to fatigue

Fatigue refers to a material's incapacity to consistently endure cyclically applied loads that are acceptable when used singularly or for a limited number of repetitions. Within their operational duration, Wind turbine blades withstand cyclic dynamic loads caused by wind gusts, turbulence, and rotational forces, contributing to the fatigue of the overall blade structure. Fatigue losses generally initiate as minor fractures or flaws and progressively develop under cyclic loading. These cracks have the potential to expand and ultimately result in dangerous blade failure if they are not promptly identified and fixed. The main factors influencing the likelihood and severity of fatigue loads, as well as fatigue failure in wind turbines, are environmental conditions and the topography of the installation site[91]. In addition, moisture can be a vital environmental factor leading to fatigue damage, mainly affecting wind turbine blades. The joint between the blade and the hub is the most fatigued component of a wind turbine blade, as it is responsible for transmitting and accumulating all mechanical loads passed to the blade at this point.

II.4.1.3 Damage caused by icing

During the winter season, wind turbine blades are incredibly exposed to icing in frigid climates. The buildup of ice on wind turbine blades is a significant problem. Due to the specific aerodynamic nature of wind turbine blades, any small amount of ice may alter blade shape, consequently raising friction and generating turbulence [90]. This malfunction can cause excessive stress on the blades and the whole turbine configuration. The aerodynamic efficiency of the blades is subsequently compromised, hence affecting the production of electricity. The mass of each blade is imbalanced due to icing, which results in random vibration. Blades

become worn and fail when this irregular vibration surpasses a specific limit. Nevertheless, the turbine should be halted if the load-bearing capacity limitation is exceeded or the structural integrity of the turbine is at risk due to an important ice-throwing hazard or for any other reason. The turbine's functional limit will differ in different scenarios and is dictated by its structural constraints regarding climate factors and adjacent safety regulations. Implementing de-icing systems or other methods, such as heating components or specialized coatings, is essential to eliminate ice accumulation and reduce the subsequent damage. Figure II.11 displays an example of ice accumulation on a wind turbine blade.

Figure II.11 Ice buildup on wind turbine blades[90].

II.4.2 Generator failures

The generator is a wind turbine's primary element, positioned behind the gearbox and propelled by a high-velocity shaft. Numerous generator types exist, with the double-fed asynchronous generator being the most prevalent. The electric generator contains the mechanical and electrical components necessary to transform the incoming rotational power into electricity[92]. The wind turbine generators represent a subsystem with a significant failure rate. Typical failure modes include air gap eccentricity, stator, rotor, and generator bearing failures[93]. Figure II.12 shows the common faults affecting wind turbine generators. Bearing failures are the most prevalent issue, representing 40% of all faults. The rotor failure is closely followed at 38%. Stator and other failures account for 10% and 12% of the faults, respectively. Some of the major electrical failures of these machines are: eccentricity of the stator, eccentricity of the rotor, broken rotor bars, rotor’s winding circuits, and looseness. The results of those faults may also be regarded as potential problems, including increased torque pulsation, reduced average torque, elevated losses, diminished performance, and overheating of the windings[94]. The shorted winding coil is one of the most significant electrical defects that impact these devices,

as it decreases the engine's synchronous reactance[95]. It is classified as critical, necessitating quick remedial action upon identification.

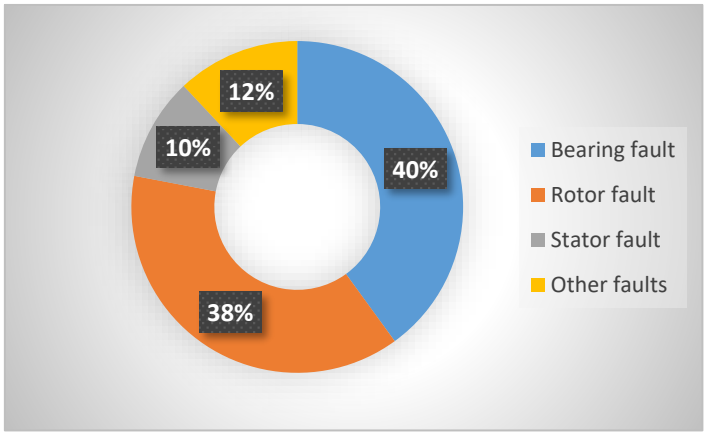

Figure II.12 Frequent failures of wind turbine generator(Adapted from [93]).

II.4.2.1 Stator failure

The four primary categories of stator winding issues are phase-to-phase short circuits, inter-turn short circuits, single-phase grounding, and three-phase grounding. Insulation damage, grounding, and high temperature of stator windings are the main symptoms of generator stator failures. The main reasons for insulation loss are wear, pollutants, fractures, and corrosion. On the other hand, short circuits between mechanical local laminations and mounting processes are the primary reason for winding failure [83]. In addition, stator winding damage results from the deterioration of dielectric elements caused by numerous influences during operations. If a stator turn-to-turn short-circuit problem happens, as shown in Figure II.13, and the apparatus is not promptly turned off for examination and maintenance, it may result in a phase-to-phase short circuit or a ground short circuit drawback. Winding issues are challenging to identify by online monitoring, although it is feasible to detect frequency elements indicative of shorted turns in the stator winding[96].

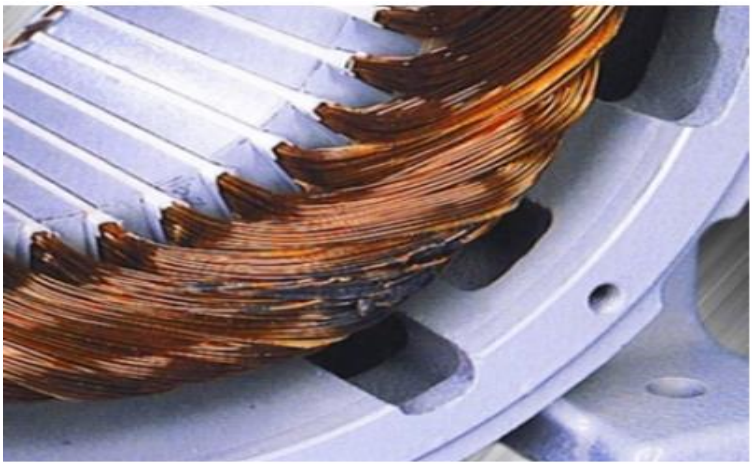

Figure II.13 Turn-to-turn short circuit fault.

II.4.2.2 Rotor Failure

Generator rotor malfunctions primarily consist of rotor winding defects and rotor body defects. Rotor body faults can be categorized into the following types: rotor eccentricity, broken rotor bar fault, and broken end-rings fault. These failures are accountable for generating additional problems that lead to significant malfunctions, such as winding and excitation imbalances or inter-turn short circuits. Rotor eccentricity occurs when a non-symmetrical air gap is created between the stator and the rotor due to the latter being displaced from its central position within the stator axis. Nevertheless, prompt detection is crucial, as serious consequences may occur in the engine's windings, stator core, and rotor cage if the stator contacts the rotor or vice versa[97], as shown in Figure II.14 . Broken rotor bars typically occur due to improper rotor geometry structure during function or recurrent heating and mechanical strains, which are common in regularly started machines. Insulation degradation is the primary cause of rotor winding failure, which is accomplished through grounding and inter-turn short circuits[93]. The rotor winding defect primarily consists of three aspects: one or two zones of the winding connecting the ground, inter-turn short circuits inside the winding, and a decreased or complete loss of rotor excitation current. Of these, the inter-turn short circuit of rotor winding is frequently observed in rotor winding failures and is one of the primary symptoms of rotor winding electrical defects.

Figure II.14 Rotor-stator contact resulting from an eccentricity defect[93]

Mechanical defects usually involve the destruction or loss of some mechanical system component, rendering it unable to perform its intended functions or even losing all of its functions. Damaged structure primarily characterizes all mechanical failures in the WT generator system, including the malfunction of the rotor body and its supporting structure and the malfunction of the generator base frame and its connected areas. Rotor shaft misalignment is another frequent issue, resulting in mechanical stresses and wear on components. The predominant mechanical problems in a wind turbine electrical generator encompass bearing failures, which are attributable to inadequate lubrication, contamination, or high load and result in heightened vibrations and overheating. A generator bearing establishes a connection between the stator and the rotor. Friction will happen when the bearing differs from the central axis of the generator stator. If the bearing is severely worn due to long-term functioning or an imbalance during setup, it will produce an exciting force during operation and cause anomalous friction.

II.4.3 Gearbox failure

The power transmission theory of the WT indicates that the blade velocity does not correspond to the generator's maximum speed. Consequently, wind energy transmission to the generator is employed to attain the requisite input velocity. Wind turbines with a constant-speed generator may attain higher aerodynamic efficiency by discreetly varying the rotational speed through a gearbox. The predominant wind turbine gearboxes usually consist of one or two planetary gear stages and one or two parallel stages[98]. The IEC 61400-4 standard identifies the most frequently used wind turbine gearbox layouts. Figure II.15 (a–d) represents the various categories of planetary gearbox technologies: helical gears, power split drive train, variable ratio gearbox, and hybrid transmission strategies[99]. A standard wind turbine gearbox

comprises an intermediate shaft, input shaft, low-speed shaft, planetary gear, and high-speed shaft. Figure 5 illustrates the wind turbine gearbox's structure[100]. Figure II.16 illustrates the wind turbine gearbox's structure.

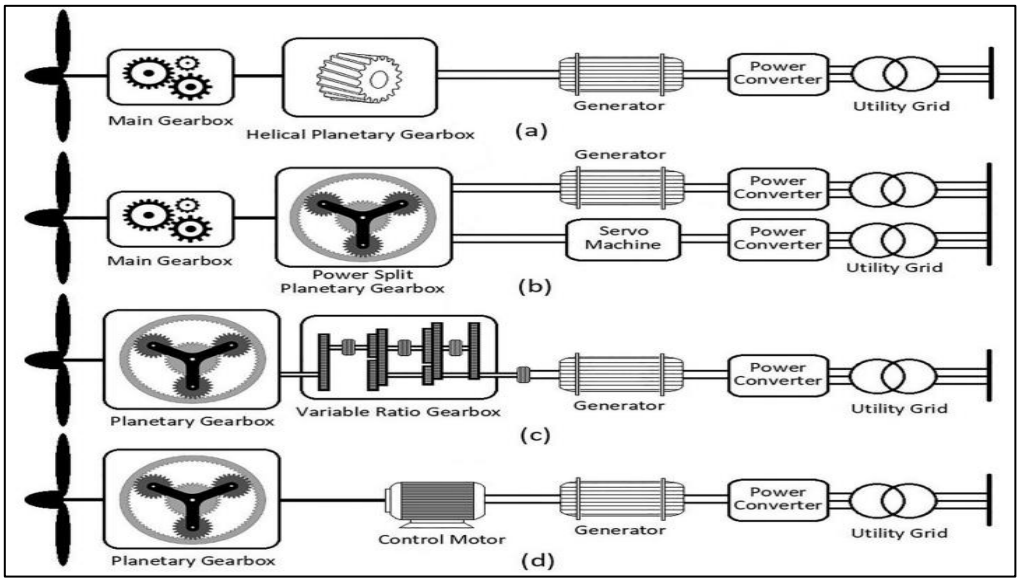

Figure II.15 Types and graphical representation of a planetary gearbox[99]: (a) Helical Gears (b) Power Split Drive Train (c) Variable ratio gearbox and (d) Hybrid transmission

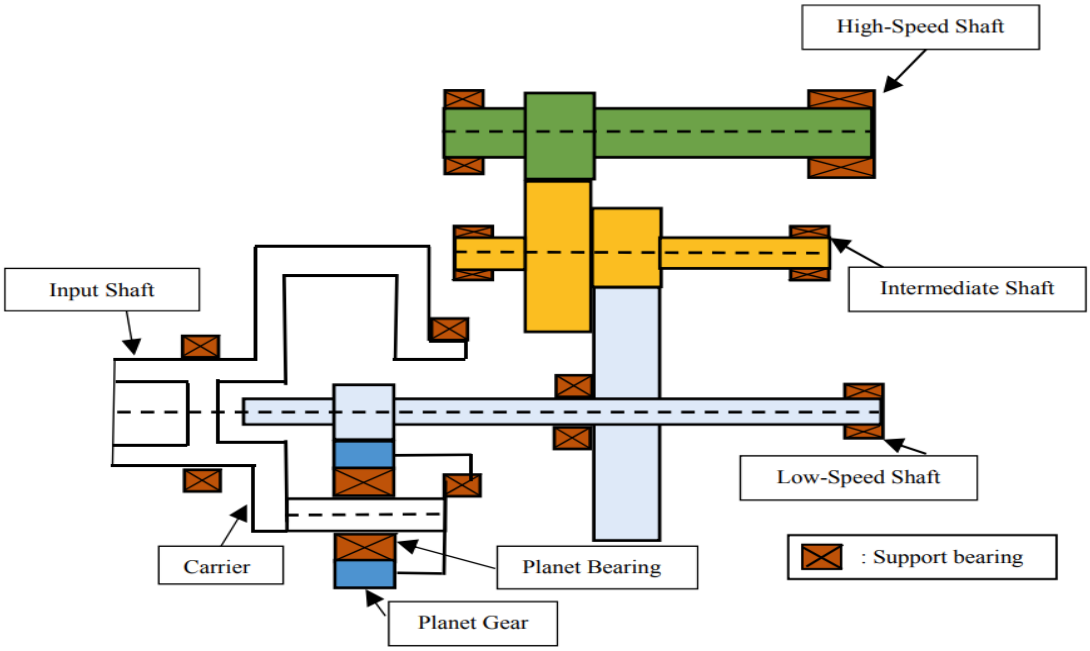

Figure II.16 Gearbox construction[100]

In recent decades, wind turbines' efficacy has improved as manufacturing technology has progressed; however, gearbox issues persist. Gearbox malfunction typically leads to the most prolonged downtime and the most significant financial loss compared to the damages related to

other wind turbine failures[101]. Wind turbine gearboxes are subject to extremely difficult operating conditions due to various factors, including environmental changes, humidity, temperature variations, stresses from high wind speed and force, and foreign bodies producing mechanical failure and corrosion events[102]. They are subjected to extreme weather conditions in the offshore environment, with wind velocities exceeding 25 m/s. This results in catastrophic incidents, including grid damages, wind gusts, and emergency pauses. Additionally, the offshore environment is damp and salty; thus, the wind turbine gearbox must be substantial in size. Gearboxes may experience failure through several types of damage that might impact their functionality. Massive elements of the gearbox may induce misalignment of gear mesh and bearings[100]. The most prevalent gearbox problems observed in industrial wind turbines include bearing and gear tooth deterioration, elevated oil temperature, and fractured shafts[103]. Bearing failures are the leading cause of numerous of these breakdowns, primarily due to micro pitting, scuffing, and cracking in the white etching area. Common kinds of gear tooth wear and damage include abrasive wear, bending fatigue, fretting corrosion, severe adhesion (scuffing), plastic deformation, tooth shear, contact fatigue, and misalignment diminished productivity[102].

Bearings are tribological elements designed to minimize friction between interacting surfaces while facilitating relative motion. Bearings are considered one of the most essential and susceptible elements of the drive-train, and the durability and efficacy of WT systems are significantly influenced by their precision, performance, and usefulness[104]. Therefore, it is the primary element of importance for condition monitoring. Generally, large-scale bearings are utilized in diverse mechanical WT systems, which can be organized into two classes: adjustment system bearings and transmission system bearings[105]. For the adjustment system bearings such as the yaw system and blade, it is necessary to employ slewing bearings. The transmission system bearings, comprising main bearings, gearbox bearings, and generator bearings, usually employ roller bearings designed to accommodate severe radial stresses. Moreover, owing to the variations in wind turbine dimensions and bearing configurations, each bearing type may exhibit several failure modes attributable to its design mechanisms and operational conditions[106]. The actual lifetime of the bearing is significantly reduced compared to its expected duration due to various to internal and external factors during operation. Figure II.17 displays that bearings contribute 84% of the defect rate of wind turbine powertrain parts, with the high-speed shaft bearing alone responsible for 30% of this rate. It is acknowledged that

merely 10% of bearings operate effectively throughout their lifecycle, whereas 90% of bearing failures are attributed to inadequate lubrication (30%), improper installation (40%), and manufacture faults (20%)[107]. Rolling bearings encompass several varieties, although their fundamental structures remain consistent. A rolling bearing generally comprises four components: the inner race, the outer race, the rolling elements (balls), and the cage, as illustrated in Figure II.18. The majority of bearing failures are associated with mechanical damages, which are of four types: inner ring failure, outer ring failure, rolling element failure, and cage failure.

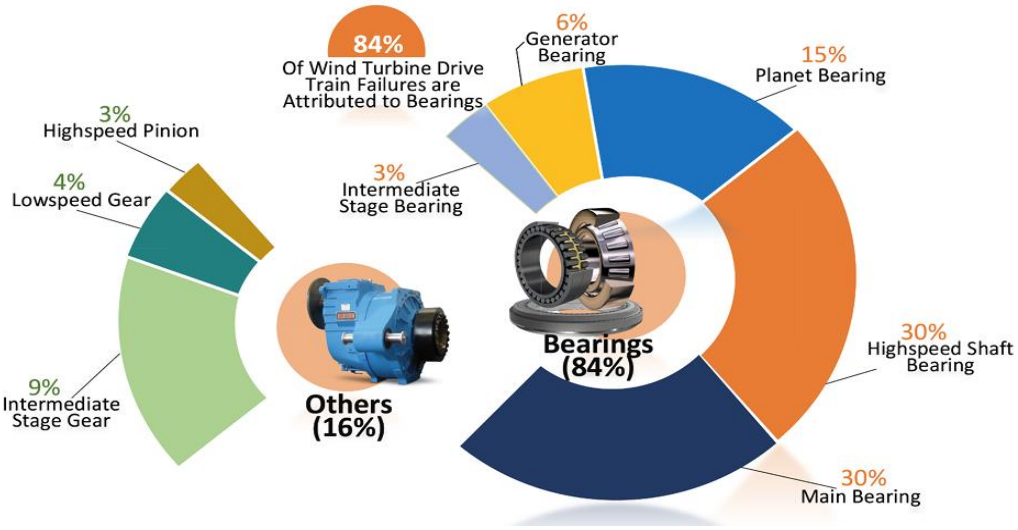

Figure II.17 Faults Percentage distribution of bearings in wind turbine power train systems[108].

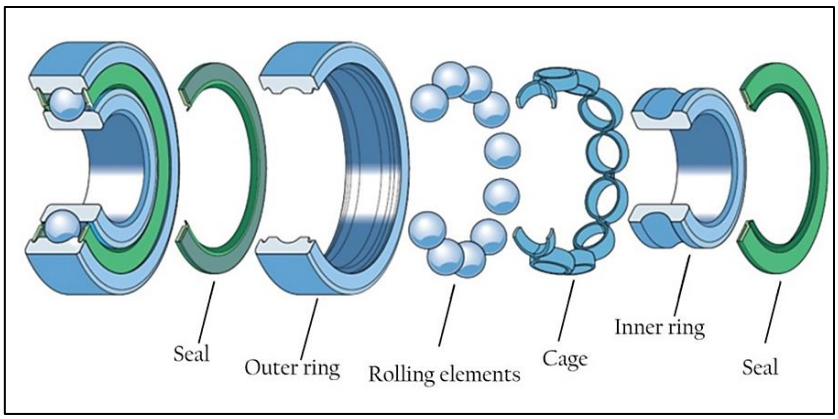

Figure II.18 Parts of a standard rolling bearing[108].

Approximately two-thirds of wind turbine gearboxes malfunction as an effect of bearing failure. Bearings in wind turbine gearboxes predominantly fail in three places: high-speed shaft bearings (which support lesser loads), planet bearings (which support larger loads), and

intermediate shaft bearings. High-speed shaft bearings exhibit a higher fault rate compared to others because of the elevated ratio of axial to radial load and a reduced contact angle, as shown in Figure II.17. Identifying the reason for any breakdown would enhance the dependability and effectiveness of the key wind turbine service for end customers[109]. Fatigue, wear, defects, cracks, and corrosion failures are among wind turbines' most prevalent bearing issues. The following are the characteristics and reasons for common failure modes.

a) Plastic deformation

Plastic deformation is highly complex, and its progression is irreversible [110]. When the wind turbine gearbox bearing is exposed to a long-term high load effect or an overheated environment, certain bearing components, including rolling elements, will deform. Failure occurs when permanent plastic deformation arises and the load surpasses the static load limit, specifically under substantial static or shock loads. There are two distinct forms of plastic deformations in bearings. The first is at the macro-level, where the deformation of large regions, such as heterogeneous craters on the surface of material interfaces, results from misalignment or high loading[111]. In addition, an improper oil lubrication parameter increases the severity of plastic deformation on the surface. Overall surface plastic deformation results from direct contact between two ragged surfaces without creating a lubricating coating. Consequently, it occurs when the oil film lubrication parameter falls below a specific threshold. The second type is on the micro-level, where plastic deformation occurs on a small area of contact, potentially leading to distortion, such as indentations[112]. Excessive load, misalignment, and improper installation can result in frequent indentations, bumping injuries, bruising, and scratches on the bearing surface[113], as shown in Figure II.19.

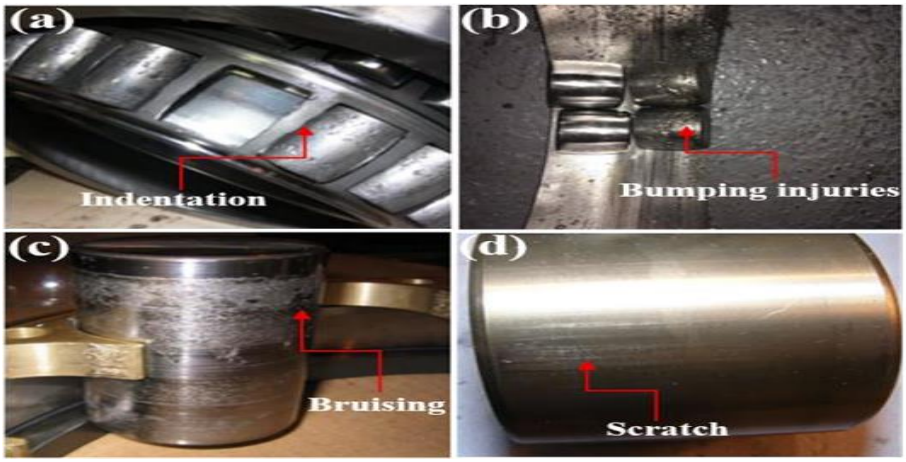

Figure II.19 Bearing plastic deformation failures, (a) Bearing rolling parts' indentation, (b) Bearing inner race bump injury, (c) Bearing rolling body bruises, (d) Bearing rolling body scratches[111].

b) Wear

Wear is the consequence of friction between materials in connection with poor lubricant, leading to metallic exhaustion or residual distortions that modify the bearing's friction characteristics. The building of an oil film on the raceway area is impeded by grime, dust, or flaking iron chips in the lubricant, exacerbating the wear progression. The bearing's inability to function correctly due to continuous abrasion is known as wear failure[114]. Moreover, the removal and combustion of material from the contact areas due to mechanical motions is called wear. Two types of material wear exist: adhesive wear and abrasive wear. Adhesive wear is a lubricant-induced degradation that ensues between two contacting surfaces in relative motion. This subsequently results in a modification of the shape of the contact areas[115], as illustrated in Figure II.20 (a). It is defined by frictional heat and material transfer between surfaces, resulting in a weld-like effect and an elevation in the bearing's total temperature[116]. Frictional heat generates localized stress concentrations, potentially causing breaking or spalling in the contact regions. Abrasive wear refers to the loss of substance from a softer surface caused by contact with a harder surface or particle during sliding. This is shown in Figure II.20 (b). It predominantly arises from insufficient lubrication or the intrusion of solid impurities. Dull surfaces typically characterize abrasive wear.

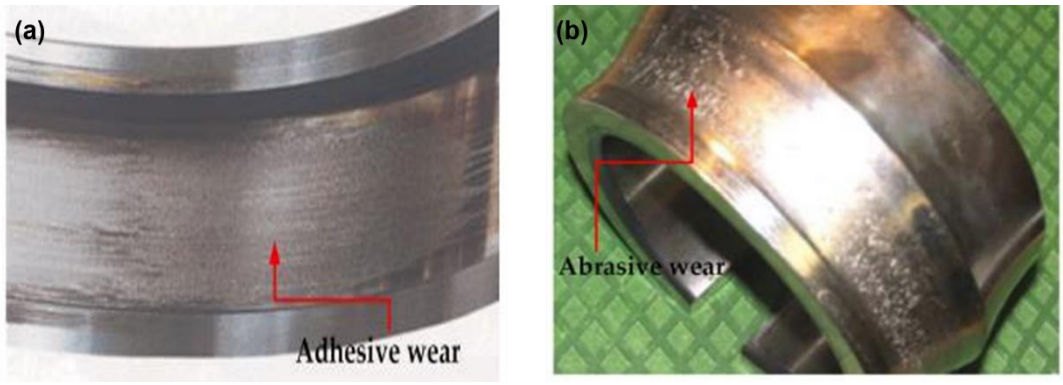

Figure II.20 Wind turbine bearing wear types (Adapted from [111]), (a) adhesive wear failure; (b) abrasive wear failure.

c) Fractures and cracks

Cracks result from micro-fracture occurring within or on the surface of a bearing when the stress, temperature, thermal shock, and force to which the bearing is subjected surpass the substance's fracture boundary. Fracture is the term used to describe the phenomenon in which the bearing portion of the material is entirely removed from the bearing structure due to the cracks expanding to a certain level[117]. Cracks and fractures are the most common failure forms for large-scale wind turbine bearings. The types of fractures in the gearbox bearing are forced fracture, fatigue fracture, and thermal cracks. A high-stress concentration relative to the material's tensile strength may result in a forced bearing fracture. White etching cracks (WECs) are a type of forced fracture that can be generated by excessive tensile strains[118]. In this instance, white etching fractures manifest on the bearing, eventually causing structural spalling that may lead to severe noise and vibration during operation, as illustrated in Figure II.21 (a). Fatigue fracture primarily refers to the impact of cyclic alternating stress on a bearing structure, which leads to alterations and faults within the interior substance. Its emergence is frequently marked by quickness and significant localization, primarily evident through the fracture of the running surface, as shown in Figure II.21 (b). The thermal cracking process typically occurs between the bearing rollers and race rings, as shown in Figure II.21 (c), where high frictional heating due to the movement sliding of the contact surfaces yields the cracking[63]. Bearing thermal cracks are caused by misalignments, lubricant failure, High loads, bearing overheating, and excess dust.

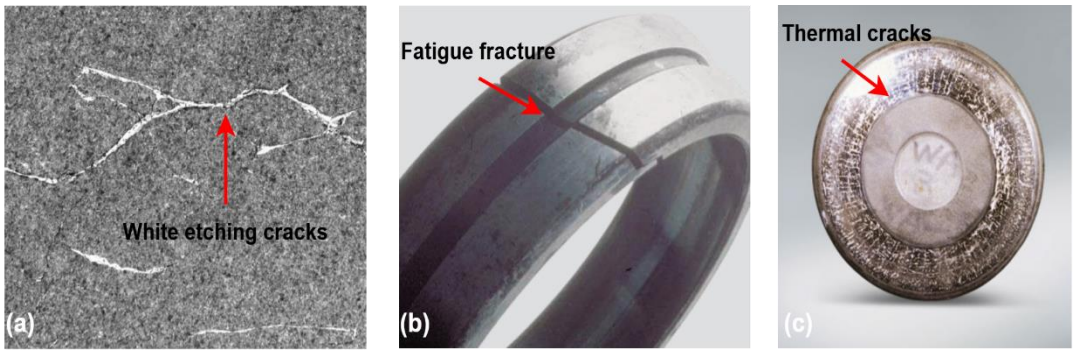

Figure II.21 bearing cracks and fractures modes, (a) Bearing WECs in wind turbine gearbox, (b) fatigue fracture of an outer ring, (c) Thermal cracks occur at roller large face.

d) Contact fatigue

Rolling contact fatigue denotes the initiation of surface or subsurface cracking in the material due to repetitive cyclic contact stresses within the element. Application of outside forces to the bearing rings diminishes the material's strength, resulting in cracking. Over time, cracking advances, rendering the bearing unfit for continued use[119]. The physical characteristics of fatigue spines generally exhibit specific depth and space, with the rolling surface displaying an irregular scale. Persistent loading, inadequate maintenance, and polluted surfaces are all causes of material fatigue. The mechanisms of bearing fatigue damage are often categorized into two classes: surface origin and sub-surface origin. Surface contact fatigue arises when the bearing functions under border lubrication and fails to establish an oil film or adequate grease in the rolling contact zone[120]. Contact fatigue of the subsurface origin type commences with the development of small cracks beneath the bearing raceway surface, and spalling happens when the small cracks reach the bearing area[121]. In this specific case, supplementary noise and vibration may be observed. Furthermore, the temperature during the operation of the bearing escalates. The bearing must be routinely inspected and adequately greased to avert this malfunction. An illustration of bearing material fatigue is presented in the Figure II.22.

Figure II.22 Roller bearing material fatigue [119].

e) Lubricant

The purpose of a lubricant is to prevent direct contact surface between the raceway, rolling element, and cage, ensuring the bearing remains in good and stable working condition[122]. An efficient lubricant can create a lubrication film on the bearing's contact surface, minimize operating noise, dissipate heat, reduce wear, prevent rust and corrosion, and avoid contamination of bearings. The bearings' functioning effectively is contingent upon adequate lubrication between the various parts. Various lubricants may be incompatible, even though each one is entirely sufficient on its own. Lubricant failures can be caused by the following: insufficient lubrication, excessive lubrication, inefficient lubrication, and the use of incorrect types of lubricants. Inadequate lubrication will cause the bearing to enter a suboptimal oil condition, increasing the likelihood of adhesive wear production[111]. Finally, catastrophic failure of gearbox bearings can be caused by lubricant failures, which can cause excessive wear, overheating, and noise. Contamination of lubricants is a significant contributor to wind-bearing failure in turbines. Abrasive particles, moisture, and dust are the most prevalent reasons for lubricant contamination[123]. Contaminated lubricants in the bearing initiate a chain of physical and chemical effects, resulting in diminished lubricating efficacy, producing compounds like oxide gum and oil sludge that damage the machinery structure and lead to bearing failure, as shown in Figure II.23.

Figure II.23 Lubricant darkening (adapted from [119]).

f) Electric erosion

Electric erosion is the spark that occurs when the electric arc travels through the bearing, resulting in a shifting of materials from the contact area surface and localized melting[111]. Electric current may escape from engines, equipment, and other sources, causing excessive heat

that can melt the bearing surface. Electric current may escape from engines, equipment, and other sources, causing excessive heat that can melt the bearing surface[100]; the affected region typically exhibits spots, grooves, dense micro-pits, and metal melting issues. Electro-etching diminishes the mechanical strength of the bearing material, speeds wear and promotes fatigue spalling[124]. Figure II.24 illustrates scaling on the surface of the raceway caused by the passage of electric current through the bearing.

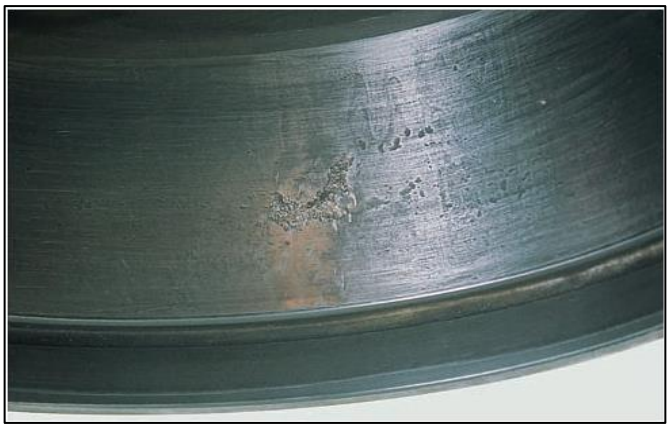

Figure II.24 flaking on the raceway surface causing by electrical damage.

g) Corrosion

Corrosion is a mechanism involving the interaction between a material and its environment, leading to the disintegration of the substance. Furthermore, the surface of rolling bearings is subject to corrosion due to chemical reactions. When moisture infiltrates the bearing from air inside the gearbox, it compromises the lubricant characteristics at particular locations of elevated load on the rings. As the lubricant's characteristics degrade and become contaminated by water or other chemicals, an oxidation process transpires between the water in the lubricating oil and the bearing surface, producing rust and corrosion. Fretting corrosion happens when there is relative motion between a bearing ring and its seating on a shaft. The relative motion may result in the detachment of tiny material particles from unlubricated bearing surfaces, followed by corrosion when exposed to air, as shown in Figure II.25. Due to the varying rates of oxidation of metallic components, the oxidation section appears brownish-red or black, leading to the formation of various compounds. The bearing rings may not be uniformly supported as a consequence of fretting corrosion, which can have a negative impact on the bearing's load

distribution. Adequate lubrication is a critical operational condition that influences the durability of bearings.

Figure II.25 Fretting corrosion on an inner ring cavity.

Numerous reasons and mechanisms for bearing failures have been presented in the preceding subsections. Commonly, Bearing failures arise from several factors associated with diverse failure types. Furthermore, considering the entire wind turbine, the elements contributing to overload, fatigue, wear, corrosion, and other issues are intricate, with external conditions such as wind and other unit elements exerting direct or indirect influence on the gearbox bearing. In recent decades, the advancement of tribological studies has significantly enhanced the knowledge of failure processes and fault classifications. The failure modes of gearbox bearings are categorized into premature fatigue and material failure. Bearing premature fatigue consequences from plastic deformation, unsuitable lubrication, electrical erosion, and engineering failures. In contrast, material failures are induced by components and structures and indicated by phenomena involving cracks and wear. An overview of a comprehensive classification of bearing failure modes is depicted in Figure II.26.

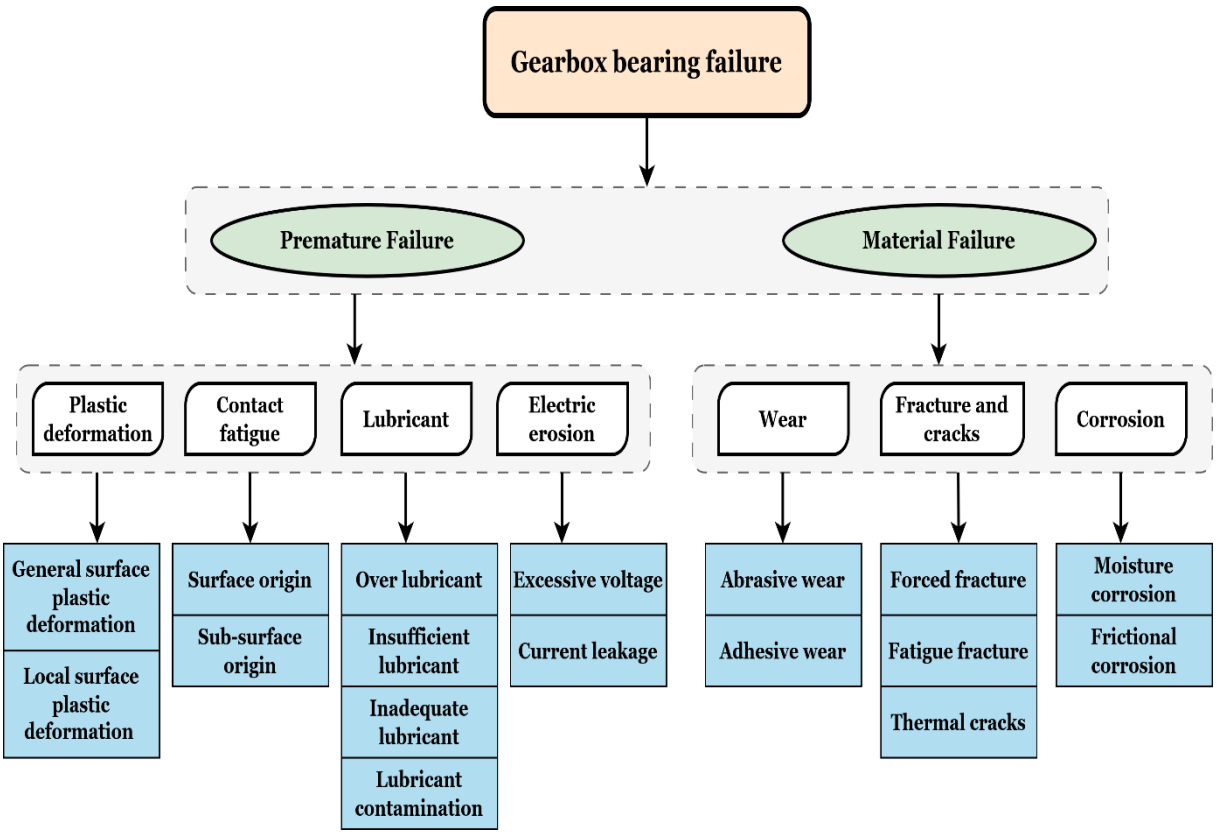

Figure II.26 Failure mode classifications of gearbox bearing (Adapted from [111]).

II.5 Conclusion

A proper maintenance strategy is a vital and strategic part of organizational management, leading to a reduction in failures, cost minimization, and enhanced productivity. This chapter presents a comprehensive overview of various maintenance methods, including reactive, preventive, condition-based, and predictive maintenance, each offering distinct benefits based on operational needs and technological capabilities. The chapter also addressed the critical role of vibration analysis; by integrating condition monitoring and vibration-based fault detection, it is clear that accurate and timely diagnosis plays a vital role in predictive maintenance, allowing for minimizing downtime and extending the life of components. The prevalent failure modes and their root causes in wind turbines have been comprehensively examined, emphasizing how early-stage component anomalies can escalate into severe failures if not addressed promptly. In this chapter, we have focused on reviewing different failure forms commonly occurring in gearbox bearings and the factors that trigger them. This aids researchers

in comprehending the essential tribological challenges and their attributes, hence facilitating the development of more dependable and economical bearing diagnostic techniques.

The following chapter explores diverse signal processing methodologies employed in gearbox-bearing defect diagnosis. This study examines how these algorithms derive significant features from intricate vibration data. The chapter also presents the practical application of one selected technique on a bearing fault dataset, demonstrating its effectiveness in identifying fault patterns and improving diagnostic accuracy.

CHAPTER III

Signal Processing Techniques for Wind Turbine Bearing Fault Diagnosis: Methods and Application

III.1 Introduction

In recent years, diagnosing bearing failures in wind turbine systems has emerged as a crucial research focus, driven by the increasing demand for dependability, efficiency, and diminished maintenance expenses in renewable energy technologies. This chapter presents an overview of signal processing techniques for diagnosing faults in wind turbine bearings, a critical component prone to failure under harsh operating conditions. These methods aim to extract meaningful features from vibration signals to reveal hidden fault signatures.

This chapter is divided into two main parts: the first part presents a comprehensive review of the state-of-the-art signal processing techniques used in the fault diagnosis of wind turbine bearings. It highlights traditional and modern approaches, including time-domain, frequency-domain, and time-frequency domain analysis methods. The review also explores the strengths and limitations of each technique when applied to real-world wind turbine conditions, where non-stationary and noisy signals are prevalent.

In the second part of this chapter, a proposed signal-processing framework is presented, focusing on vibration-based fault diagnosis using Case Western Reserve University (CWRU) bearing dataset. Although the dataset originates from an industrial motor test rig rather than a wind turbine, it serves as a widely accepted benchmark for validating diagnostic methodologies. The proposed method utilizes the discrete wavelet transform (DWT) to decompose the vibration signal into multiple frequency bands, followed by energy analysis and fault identification using the fast Fourier transform (FFT). The outcomes demonstrate the capability of this approach to enhance fault detection performance and establish a foundation for applying similar techniques to real wind turbine systems.

III.2 Research on WT Bearing Fault Diagnosis Techniques

In condition monitoring (CM), mechanical system elements in wind turbines are observed for operational alterations that may indicate the start of a malfunction. Assessments of specific data and functional factors have become the basis of CM strategies, such as vibration analysis, thermography, lubrication analysis, and acoustic emissions. Accurate fault identification has been the focus of extensive practical and theoretical studies for several decades, and no ideal technique can be applied to every fault type. The validity of the selected CM approach is generally directly correlated with the most exhaustive comprehension of the electrical and mechanical features of the component in an error-free condition[125]. Condition monitoring

systems can perform two primary roles: diagnostics and prognostics (Figure III.1). The main objective of diagnosis is to detect, find, and identify existing defects, enabling the implementation of repair techniques before total failures[126]. Presently, failure diagnostic solutions mostly encompass hardware redundancy and software redundancy. Fault detection involves examining the observed system for any malfunctions. Locating the position of an issue component is referred to as failure isolating. Fault identification involves determining the type, shape, and dimensions of the discovered fault.

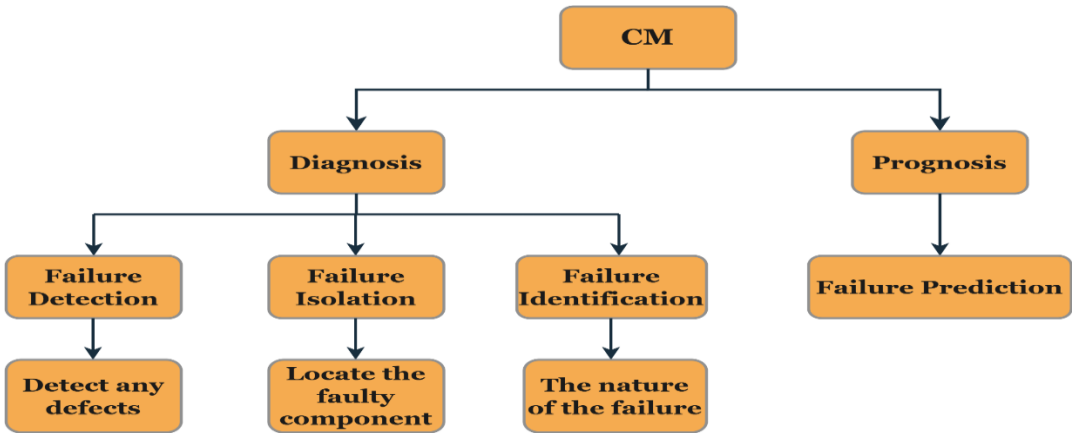

Figure III.1 Status monitoring system

An essential source of knowledge in wind turbine gearbox (WTG) systems is vibration signals. A vibration signal can indicate mechanical failure traits and variations in mechanical health. Although the quality of the vibration signals captured is essential for fault detection, the efficacy of the signal processing and feature extraction methods is equally important. Various methodologies exist for fault diagnostics, encompassing model-based, signal-based, knowledge-based, and hybrid approaches. Figure III.2 presents a schematic illustration depicting the signal-based fault diagnosis methodology.

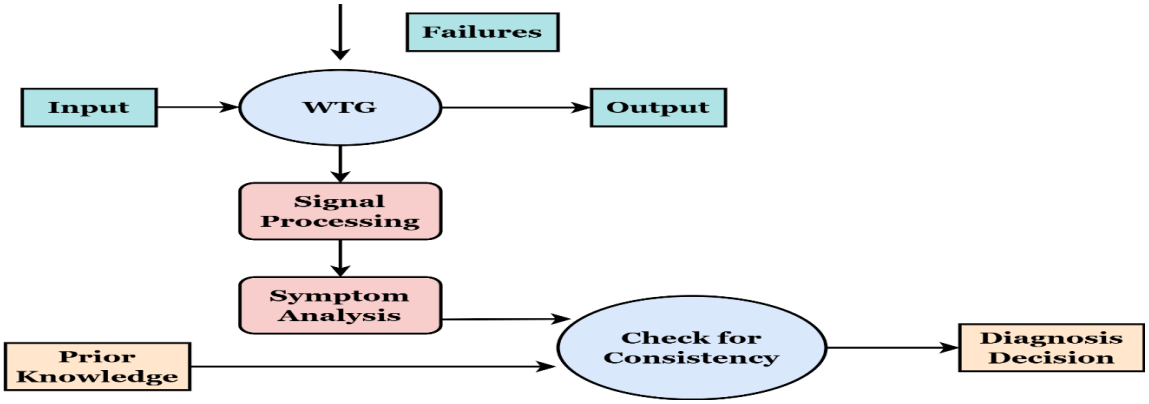

Figure III.2 Schematic representation of signal-based failure diagnosis (Adapted from [126]).

The fundamental concept of the signal-based fault diagnosis approach is obtaining signal characteristics from the fault signal using signal processing methods. Signal analysis techniques encompass the procedures of data collecting, extracting features, detecting faults, identification, and additional processes for obtaining WTG bearing failure signatures[127]. In general, these techniques can be categorized into time-domain approach, frequency-domain technique, and time-frequency method.

III.2.1 Time domain diagnosis techniques

The time-domain analysis (TDA) approach is among the most straightforward and efficient techniques for processing vibration signals for bearing fault detection. TDA is a linear methodology in which the waveforms obtained by accelerometers analyze the structures and features of signals and acquire information regarding changes in attributes over time[128]. Direct extraction of time-domain characteristics from initial vibration signals will not alter properties or result in signal loss. An intriguing summary of TDA is presented in[129], which asserts that a vibration signal can be regarded as an aggregation of time-indexed data points gathered across a temporal record, reflecting acceleration, velocity, or displacement. Despite the utilization of additional advanced time domain methodologies, the visual examination of the time waveform should not be undervalued, as it might yield substantial information. Elevated vibration readings signify the machine is in a failure state, resulting in increased vibration production. Nonetheless, this could not demonstrate the precise location of the fault in the bearing. The existence of noise and the combination of vibrations from many sources complicates the straightforward utilization of raw collected signals for fault diagnostics, particularly at the early stage of failure, when damage-related information is subtle and needs to be enhanced.

As seen in Figure III.3 and Figure III.4, both sourced from [129], it is occasionally feasible to discern amplitude discrepancies between the signal of a new bearing (Figure III.3(a)) and that of a bearing exhibiting an inner race fault (Figure III.3(b)) through a simple visual inspection. These findings indicate that the machine is in an anomalous state. This method of condition surveillance is both simplistic and cost-optimized.

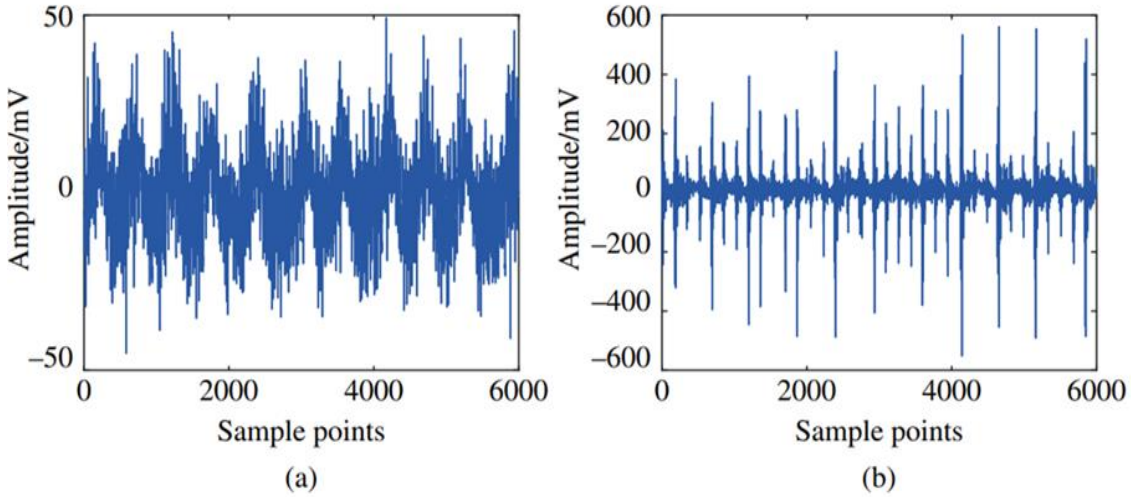

Figure III.3 Roller bearing vibration signal in the time domain: (a) brand-new state; (b) inner race defect state[129].

In most instances, achieving the same result is not straightforward, as evidenced by the absence of any discernible distinctions between Figure III.4 (a) (healthy) and Figure III.4 (b) (faulty). This basic example demonstrates that eye inspection of the raw historical data is insufficient for practical CM evaluation. The explanation of this method was significant, as visual comparison constitutes a nascent kind of signal processing, particularly when combined with other visual examination techniques.

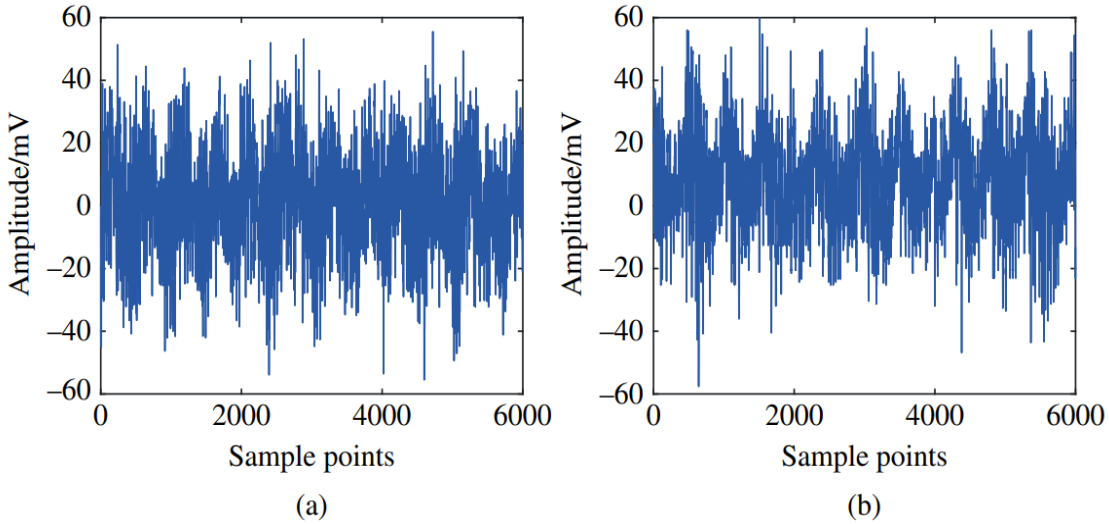

Figure III.4 Roller bearing vibration signal in the time domain: (a) old but undamaged condition; (b) inner race defect state[129].

In time waveform analysis, a more thorough analysis of the time histories involves calculating specific parameters, referred to as features, which characterize certain qualities of the signals. These characteristics can be utilized to distinguish between two vibration signals. Time-domain

statistical features can immediately indicate the operational condition of the apparatus. Dimensional and dimensionless parameters are the primary categories into which time domain statistics are typically classified[130]. Dimensionless metrics are susceptible to impulsive defects, while dimensional factors are responsive to variations in velocity and load. The drawbacks of these statistical values encompass their relatively inadequate selection, implying that a variation in value does not definitively signify a specific defective part of a bearing. The temporal evolution of transient signals, especially vibration signals, can be analyzed by extracting various features from the time domain, such as the root mean square (RMS), crest factor, kurtosis, peak-to-peak, standard deviation, and skewnesses. According to Wang et al. (2019) [131] and Cui et al. (2022) [132], a multitude of features can be derived from a raw vibration signal x consisting of n samples, with the most prevalent ones exhibited in Table III.1

Table III.1 Key Statistical Features with Definitions.

Feature name	Definition	Feature name	Definition
Peak value	$\max(x(n))$	***Kurtosis***	$\frac{\frac{1}{N}\sum_{n=1}^{N}(x(n)-\bar{x})^4}{(\frac{1}{N}\sum_{n=1}^{N}(x(n)-\bar{x})^2)^2}$
Minimum value	$\min(x(n))$	***RMS***	$\sqrt{\frac{1}{N}\sum_{n=1}^{N}(x(n))^2}$
Peak to peak	$\max x(n) - \min x(n)$	***Skewness***	$\frac{\frac{1}{N}\sum_{n=1}^{N}(x(n)-\bar{x})^3}{(\frac{1}{N}\sum_{n=1}^{N}(x(n)-\bar{x})^2)^{2/3}}$
Mean value	$\bar{x} = \frac{1}{N}\sum_{n=1}^{N}x(n)$	***Crest factor***	$\mathrm{CF} = \frac{max(x(n))}{RMS}$
Average absolute value	$\bar{x} = \frac{1}{N}\sum_{n=1}^{N}\lvert x(n)\rvert$	***Impulse factor***	$\frac{\max(x(n)}{\frac{1}{N}\sum_{n=1}^{N}\lvert x(n)\rvert}$
Variance	$\frac{1}{N}\sum_{n=1}^{N}(x(n)-\bar{x})^2$	***Shape factor***	$\frac{\sqrt{\frac{1}{N}\sum_{n=1}^{N}(x(n))^2}}{\frac{1}{N}\sum_{n=1}^{N}\lvert x(n)\rvert}$

Standard deviation	$\sqrt{\frac{1}{N}\sum_{n=1}^{N}(x(n)-\bar{x})^2}$	***Energy operator***	$\frac{\frac{1}{N}\sum_{n=1}^{N}(\Delta x(n)-\Delta\bar{x})^4}{(\frac{1}{N}\sum_{n=1}^{N}(\Delta x(n)-\Delta\bar{x})^2)^2}$

- **Related work**

Each of the previously stated indicators signifies the potential existence of faults. The severity of failures can be assessed by comparing characteristics in an alternative derivation sequence. A vibration signal from a device exhibiting a bearing fault could have a peak value sevenfold greater than that of the vibration signal obtained from the identical machine in a non-failed state. The Crest Factor (CF) is employed to identify modifications in the signal pattern that are caused by impulsive vibration sources, such as tooth damage in transmission or an anomaly in the outer ring of a bearing. The alteration in the vibration pattern of signals resulting from this weakness is evident in a rise of this feature's magnitude[133]. In general, apparatus issues are associated with CF values more than 6. The vibratory energy level in the signal is represented by the root mean square (RMS) value, which can be modeled as a Gaussian random process with amplitude modulation[134]. The RMS value is a crucial parameter for monitoring overall noise levels in measurements and detecting the existence of unbalanced rotating elements[135]. Igba et al. [136] present innovative fault detection methods to monitor the condition of a wind turbine gearbox using RMS and extreme vibration values. This approach, validated on real-world data, enables early detection of failures and better maintenance planning. Liang et al. [137] utilized the energy (RMS) of the vibration signal produced by each tooth as an indicator to identify a broken tooth. The paper in reference [138] gives findings from extensive trials on a defective planetary gearbox system, evaluating the severity of defects. The method utilizes vibration acceleration signals and a comparative analysis of condition monitoring indicators to detect cracks. The findings suggest that the root mean square value analysis may serve as an effective indicator for early detection and characterization of problems when compared to other metrics. Skrimpas et al. [139] evaluate the efficacy of five conventional statistical features derived from the residual signal in two case studies involving a planet carrier bearing problem and planet wheel spalling. The characteristics assessing Gaussianity are effective for localized faults, whereas those evaluating the RMS value are proficient in identifying dispersed faults. In contrast, kurtosis is defined as the fourth moment of the signal, normalized by the square of the variance, and is a metric that quantifies the number of peaks in a signal. Skewness measures the degree of negative or positive asymmetry in a signal. A signal from a healthy bearing has a

skewness value of zero, as it follows a normal distribution[140]. A diagnostic approach based on time-domain signals has been devised in [141] for the monitoring of gear defects, integrating fast dynamic time warping (fast DTW) and correlated kurtosis (CK) methodologies. The rapid DTW method was utilized to extract the periodic impulse excitations resulting from the defective gear tooth, and the extracted signal was subsequently resampled for further diagnostic analysis via the CK approach. By leveraging the periodicity of the geared faults, the CK algorithm can ascertain the location of the local gear problem within the gearbox. Wang et al. [142] integrated kurtosis and meshing modulation phenomena to develop a meshing frequency modulation (MFM) index-based kurtogram capable of identifying the resonant frequency range generated by planet-bearing faults without reliance on a health basis. Jiang [143] examines time-domain vibration signals to identify fault characteristics in wind turbines. The occurrence of faults in the wind turbine was contingent upon the vibration signal's effective value, peak value, and kurtosis. The attributes facilitated the training of a genetic algorithm back-propagation neural network model, resulting in elevated fault diagnostic accuracy. In a pertinent study, Ogaili et al. [144] implemented diverse fault scenarios impacting bearings and gears in the gearbox to derive time-domain properties from vibration signals, such as RMS, kurtosis, skewness, and standard deviation. These characteristics were employed to identify preliminary indications of deterioration. The study utilized different machine learning models to classify gearbox problems, illustrating the efficacy of integrating statistical characteristics with supervised classification techniques for condition monitoring.

For example, Figure III.5 and Figure III.6 illustrate how the features can be employed for defect detection. The RMS, kurtosis, peak value, skewness, and CF are calculated from vibration measurements of bearings obtained from the Case Western Reserve University (CWRU) database under different motor loads (0 to 3 Hp)[145]. The paper[146] comprehensively describes CWRU data.

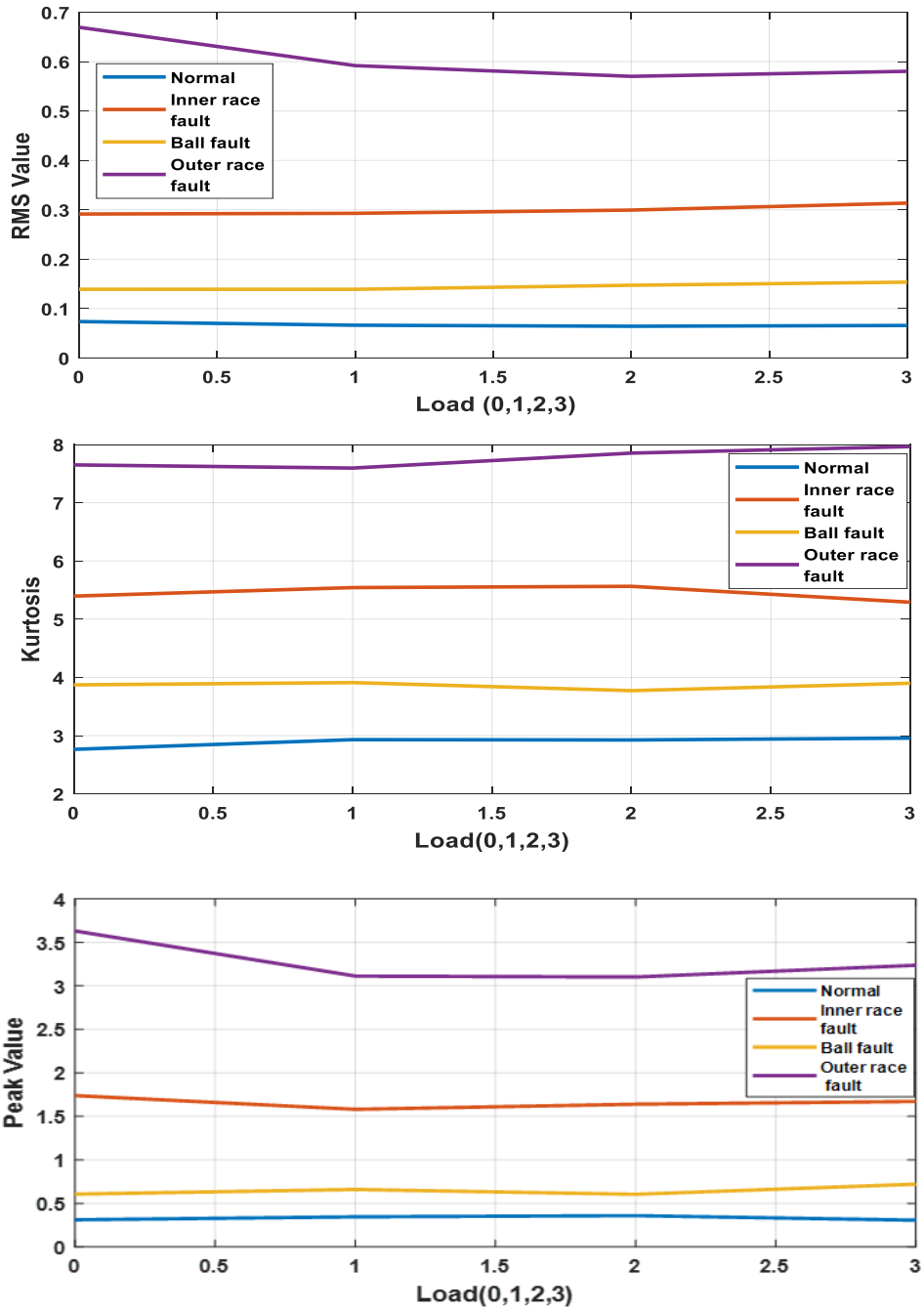

Figure III.5 Variation of RMS, kurtosis, and peak value for four bearing states (normal state, inner race, outer race, and ball faults)[145].

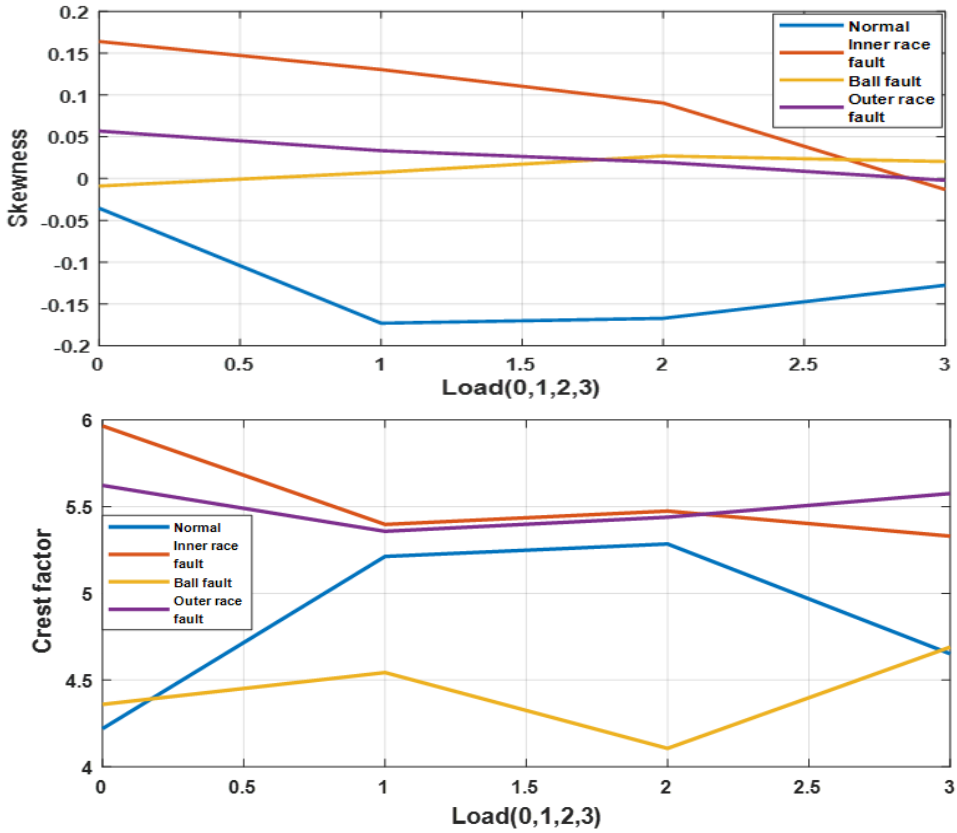

Figure III.6 Variation of skewness and CF for four bearing states (normal state, inner race, outer race, and ball faults).

The time records of both the healthy and faulty datasets comprise 120,000 samples each, with features indicating that the RMS, kurtosis, peak values, and skewness distinctly differentiate the two conditions. Our initial critical observation from the prior curves of time statistics indicators, contingent on varying loads (0, 1, 2, 3), was that in damaged bearings, when the rolling element traverses the faulty region of the bearing, the amplitude of the time features undergoes a rapid shift and increase. This indicates that the above described traits can be utilized to identify statistical disparities between defective and healthy datasets. Figure III.6 clearly illustrates that the crest factor for both healthy bearings and those with ball faults overlaps, rendering it challenging to differentiate between these two conditions based solely on the crest factor. Consequently, employing this parameter to classify bearing failure types proves imprecise. Although this approach is more intricate than a visual examination of raw vibration signals, it is not suitable for comprehensive CM analysis in many cases. The features exhibit an apparent drift only once the problem is fully established, eliminating the opportunity for early diagnosis. Moreover, when the vibration signal is obscured by significant background noise, the calculated characteristics fail to reveal the problem's existence accurately. Consequently, it is uncommon in literature to encounter research that operates feature extraction as the sole

investigative strategy; rather, it is more frequently employed as a foundation for other, more sophisticated approaches, often incorporating machine-learning algorithms[144].

III.2.2 Frequency domain diagnosis techniques

Fault characteristics cannot be sufficiently represented just through TDA; the frequency spectrum concept is essential for the examination of rotating machinery. Frequency domain analysis (FDA), also known as spectral analysis, is a widely employed technique for vibration analysis to assess the condition of devices. The basic idea of FDA is to convert original time domain data into frequency domain signals for subsequent analysis using frequency domain indices[128]. In reality, FDA methods, based on frequency features, have the capacity to reveal information that is not readily apparent in the time domain. This approach enables us to evaluate the signal's rate of alterations. The recorded time domain vibration signals are frequently produced by various parts of a rotating machine, such as bearings, shafts, and fans, where the movement of an individual component generates a sine wave characterized by a specific frequency and magnitude, while additional components provide supplementary frequencies[129]. The amplitudes are exhibited in the frequency domain as a sequence of sine and cosine waveforms that possess both magnitude and phase. Figure III.7 illustrates a graphical representation of the amplitude at the time and frequency domains.

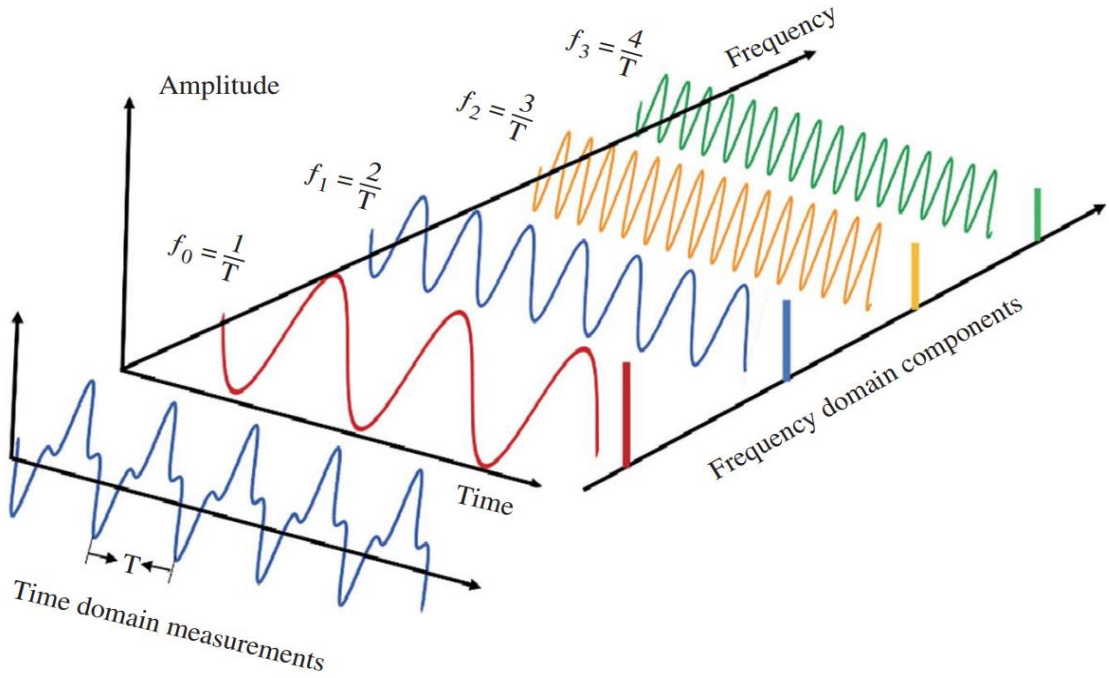

Figure III.7 a diagram of the signal in the time and frequency domain[129].

In FDA, the resonant frequency element is more easily identified when the amplitude is plotted against frequency and compared to the time domain. Under healthy and defective conditions, rotating equipment parts produce diverse vibration signals in the time domain, including random and periodic signals. To make precise conclusions about the vibration source's changing characteristics, it is essential to obtain more particular details about the signal's frequency components. Fourier analysis is frequently employed to generate frequency representations of these signals in the frequency domain. Fourier analysis is typically categorized into Fourier series, continuous Fourier transform (CFT), and discrete Fourier transform (DFT). Common FDA techniques encompass Fast Fourier Transform (FFT), envelope spectrum analysis, cepstrum, bi-spectrum analysis, Hilbert transform (HT), and power spectral density (PSD), among others[147].

III.2.2.1 Fourier analysis

Fourier analysis, also known as harmonic analysis of a periodic signal $x(t)$, involves decomposing the series into a summation of sinusoidal elements, each characterized by a distinct amplitude and phase. A linear combination of all sine and cosine functions with the same period T can represent the Fourier series of a periodic signal $x(t)$. The Fourier series examines periodic signals, specifically those formed by a finite summation of harmonics when the signal's total period is limited. A periodic signal comprises frequencies that are integer multiples of the basic frequency $f_0 = 1/T$. The Fourier series representation of the signal $x(t)$ is provided by[148]:

$$x(t) = \frac{a_0}{2}\sum_{n=1}^{\infty} c_n \cos(2\pi n f_0 t + \varphi_n) \quad \text{(III.1)}$$

Where:

c_n are amplitudes at frequencies f_0, f_1,…

φ_n are phases at frequencies f_0, f_1,…

The complex form is an additional prevalent Fourier series model, and the expression is formulated as follows:

$$x(t) = \sum_{-\infty}^{\infty} h_n e^{j2\pi n\frac{t}{T}} \quad \text{(III.2)}$$

$$h_n = \frac{1}{T}\int_0^T x(t) e^{-j2\pi\frac{nt}{T}}\, dt \quad \text{(III.3)}$$

The Fourier transform does not presuppose that the input signal is periodic. It can be utilized to examine periodic, nearly periodic, or stochastic signals. The Fourier transform (FT) of a signal $x(t)$ can be mathematically expressed using the following equation:

$$x(f) = \int_{-\infty}^{\infty} x(t) e^{-j2\pi ft}\, dt \tag{III.4}$$

Additionally, the opposite relationship can be found by employing eq. (III.5)

$$x(t) = \int_{-\infty}^{\infty} x(f) e^{j2\pi ft}\, dt \tag{III.5}$$

The value of real signals in data acquisition systems is only known at the sampling instances, which is why they are sampled and discrete. Indeed, discrete approaches are frequently necessary for computerized implementation and examination. Collected signals are temporally constrained, as we cannot accumulate and analyze an endless quantity of data. The Discrete Fourier Transform (DFT) is applied to acquire spectra of discrete signals. For a discrete set of points $x(n)$ comprising N samples, the DFT can be mathematically represented by the following equation[148]:

$$x_{DFT}(k) = \sum_{n=0}^{N-1} x(n)\, e^{-i2\pi k\frac{n}{N}},\ \ k = 0,1,\dots,N-1 \tag{III.6}$$

$x(k)$ denotes the signal magnitude located in the $k-th$ band of frequencies of the sequence.

Instead, more effective

$$x_{DFT}(k) = \sum_{n=0}^{N-1} x(n)\, W_N^{nk}\ ,\ k = 0,1,\dots,N-1 \tag{III.7}$$

Where

$$W_N = e^{\frac{-j2\pi}{N}} = \cos(\frac{2\pi}{N}) - j\sin(\frac{2\pi}{N}) \tag{III.8}$$

The opposite result of the DFT that converts $x_{DFT}(k)$ into $x(n)$ can be articulated using the subsequent formula:

$$x(n) = \frac{1}{N}\sum_{n=0}^{N-1} x_{DFT}(k)\, W_N^{-nk}\ , n = 0,1,\dots,N-1 \tag{III.9}$$

III.2.2.2 Fast Fourier transform (FFT)

Although discrete forms are generally more advantageous for real-world data, they are still computationally demanding; a simplistic implementation will require $O(N^2)$ time. As a result, fast Fourier Transform (FFT) algorithms were developed. FFT is an effective technique that calculates the DFT and its inverse for a stationary signal, significantly reducing computational

complexity. This approach is a traditional signal processing strategy renowned for its ability to discern the fundamental frequency properties of signals. The FFT algorithm is highly sensitive to minor frequency variations in the analysis of vibration data; bigger fluctuations result in significant errors in the true signal value. The choice of an adequate sampling rate is crucial for signal digitization to prevent erroneous frequency components resulting from aliasing. The research cited as [149], [150], and [151] leveraged the benefits of the FFT for various applications, including diagnosing rotating equipment, forecasting the remaining usable life (RUL) of bearings, and maintaining electrical machines. Nonetheless, the premises underlying the FFT impose many limitations. A restriction of the Fourier transform is the presumption that the signal is stationary, meaning its statistical properties remain invariant across time and that no changes in its frequency content occur. The assumptions are violated when analyzing real-life signals that exhibit non-stationary behavior, which is typically the case with wind turbines. Moreover, the FFT treats its input information as both periodic and linear. Although this may hold for certain signals, it generally fails to elucidate the intricacies of the majority of real-world signals[152].

III.2.2.3 Envelope analysis

The envelope analysis is a highly effective method utilized mainly for the early identification of rolling element-bearing defects that facilitates enhanced visualization of periodic impulses. This approach is employed when the signal of interest consists of repeating impulses obscured by a significantly stronger signal. Envelope analysis, also known as amplitude demodulation or demodulated resonance analysis, involves a bandpass filtering and demodulation process that extracts the signal envelope, which may contain pertinent diagnostic information within its spectrum[153]. By employing an FT on the envelope signal, a time-variant and refined representation of the signal's amplitude is produced. Envelope analysis requires a refined filter and exact delineation of the frequency band for effective filtering. Concerning bearing failure, the noise components complicate the envelope analysis necessary for defect identification[154]. In practical scenarios, envelope spectrum analysis, including spectral kurtosis analysis, has proven more beneficial than conventional raw vibration examination for the early detection of faults and the identification of anomalies[152].

In addition, Power spectral density (PSD) denotes the quantification of power present within each frequency band of a given signal. The PSD is determined by computing the Fourier Transform of a signal and squaring the amplitude spectrum. It is appropriate for analyzing

signals that are energy-distributed across a range of frequencies, as opposed to being concentrated within a few specific frequencies. The entire power of the signal in a given frequency band is determined by the area under the PSD plot. Vibration analysis using PSD has numerous benefits, including a distinct frequency domain representation of the signal, which facilitates the detection of specific frequency components linked to problems or defects in rotating apparatus. Moreover, it permits quantitative comparisons among various signals or working states, hence enhancing trend analysis and condition monitoring [155].

- **Related work**

The defect diagnostic method for wind turbine bearings, utilizing spectrum analysis as a conventional analytical approach, remains a prominent topic of research. In the frequency domain investigation utilizing the Fourier transform, Bodla et al. [156] employed different techniques such as Fast Fourier transform (FFT), Hilbert Huang Transformation (HHT), Feature extraction, Logistic Regression (LR) to accurately evaluate the health of the wind turbine. A vibration-based condition monitoring strategy was proposed by De Azevedo et al. [157], where accelerometers were installed on critical wind turbine components, and signal processing methods, including Fourier transform and Hilbert-based envelope analysis, were employed. This approach successfully identified bearing faults and enabled a detailed comparison of vibration behavior before and after component replacement, demonstrating its effectiveness for minimizing maintenance efforts, especially in large, remotely located turbines. Strömbergsson et al. [158] evaluates the fast Fourier transform (FFT), discrete wavelet transform (DWT), and wavelet packet transform (WPT) for the identification of faults in wind turbine drivetrain bearings. The findings indicate that WPT surpasses FFT in the early and precise detection of bearing problems, resulting in more stable warning configurations. In [159], a novel algorithm is addressed by integrating fast Fourier transform and uncorrelated multi-linear principal component analysis techniques in order to achieve effective three-dimensional space visualization for fault diagnosis and classification under a variety of actuator and sensor faulty scenarios in 4.8 MW wind turbine benchmark systems. Kramti et al. [160] present a Fast Fourier Transform applied to raw mechanical vibration signals from the wind turbine generators, which are compared with a novel envelope analysis strategy commonly employed to extract mechanical fault harmonics from the envelope signal spectrum. The results demonstrate superior diagnostic efficacy when applied to the same datasets as the Fast Fourier Transform. The paper in [161] proposes a feature extraction method for wind turbine bearing fault diagnosis, utilizing complete ensemble empirical mode decomposition with adaptive

noise, FFT, recursive feature elimination, and classifiers. Experimental data from CWRU and Jiangxi wind farms show the method's effectiveness in real-world wind turbine fault diagnosis. C. Wang et al. [162] propose a wind turbine gearbox fault diagnosis method using BLSCFN model and multi-sensor information fusion. The method uses Fast Fourier Transformation, convolutional neural network, and Bi-directional Long Short-Term Memory network to improve accuracy and reliability compared to single-sensor methods. The proposed technique attains enhanced diagnostic efficacy. Fan and Li [163] used an internal vibration sensor attached to the planetary carrier to detect the faint signal generated by the planetary bearings. Typical rolling bearing fault identification techniques, including Cepstrum whitening, minimum entropy deconvolution (MED), spectral kurtosis (SK), and envelope analysis, were utilized to examine the acquired signals. Nonetheless, it is impractical to install the internal sensor in the actual WT planetary gearbox. Yoon et al. [164] propose a novel methodology for monitoring planetary gearboxes (PGBs) using a single vibration sensor, integrating enveloping, Welch's spectrum averaging, and data mining-based fault classification techniques. This approach effectively captures vibration fault signatures, demonstrating strong diagnostic performance for PGB fault detection. Diagnosing bearing faults in wind turbine gearboxes is particularly challenging due to the masking effects caused by more intense vibration components from gears and shafts. In response to this, numerous signal processing methodologies, such as statistical condition indicators, spectral kurtosis, and envelope analysis have been assessed by Shanbr et al. [165]. The results indicated that spectral kurtosis, in conjunction with envelope analysis, provides enhanced efficacy in early fault detection, especially for recognizing outer race flaws. Koukoura et al. [166] suggested a mechanism for forecasting planetary bearing failures with vibration data obtained from offshore wind turbines. Through the implementation of signal preprocessing, spectral kurtosis, and envelope analysis, they improved defect signature detection and extracted features for classification model input. The results, corroborated using k-fold cross-validation, demonstrated enhanced performance compared to conventional envelope analysis, which employs a fixed demodulation band. Zhang et al. [167] highlight that wind turbine gearboxes exhibit high failure rates and produce vibration signals characterized by intense noise, complexity, and non-stationary behavior, which complicate fault diagnosis. To address this, they propose a hybrid diagnostic approach that combines oil spectral analysis with vibration waveform and frequency spectrum techniques to identify faults and assess their severity. This method improves diagnostic reliability and supports more efficient turbine design, optimization, and maintenance planning. Xu et al. [168] proposed a Modulation Signal

Bispectrum Enhanced Squared Envelope (MSB-ESE) method for diagnosing faults in epicyclic gearboxes using vibration data acquired from an On-Rotor Sensing (ORS) transducer. Their approach enhances squared envelope analysis by mitigating noise and extracting clear fault signatures. Experimental validation demonstrated its effectiveness in identifying compound faults in sun and planet gears. Lakikza et al. [169] offered an integrated approach for diagnosing bearing faults in wind turbines and rotating machinery, leveraging Variational Mode Decomposition (VMD) to extract signal modes, followed by envelope analysis and Fast Fourier Transform (FFT) for feature extraction from frequency bands. These features were used to train a K-Nearest Neighbors (KNN) classifier, validated via cross-validation using metrics like accuracy and F1-score. Applied to both real wind turbine data and the Case Western Reserve dataset, the method demonstrated enhanced energy localization and superior diagnostic performance.

III.2.3 Time-frequency domain diagnosis techniques

In the real life, most waveform signals are nonstationary, meaning their spectra fluctuate with time. During operation, machines produce vibrations, each moment characterized by a unique frequency[155]. FDA possesses many limitations, notably its inefficacy in analyzing non-stationary waveform signals, which are prevalent in machinery failures, particularly in wind turbine gearbox malfunctions. To solve this problem, time-frequency analysis (TFA) has been developed into a valuable tool for analyzing non-stationary signals[170]. The primary benefit of time-frequency analysis over other techniques is its capacity to concurrently represent a vibration signal in both the time and frequency domains, thereby offering essential insights into the frequency structure of the signal and facilitating the investigation of temporal frequency variations. TFA is an approach to defect monitoring for rolling element bearings that fulfills the need to evaluate the vibration time waves as an image[171]. Time-frequency transformations are categorized as linear or nonlinear. Numerous time-frequency analysis methods have been applied, including the short-time Fourier transform (STFT), the Wigner-Vill transform (WVT), the Hilbert-Huang transform (HHT), empirical mode decomposition (EMD), wavelet transform, local mean decomposition (LMD), etc.

III.2.3.1 Short-Time Fourier transform

The STFT, which is an extension of the FFT's ability to analyze non-stationary or chaotic signals in the time-frequency domain, is an approach implemented to address issues with the FFT. The Short-Time Fourier Transform (STFT) is a mathematical concept that involves dividing a

longer-term signal into shorter parts of equal length using a time-localized window function. The FFT is then computed separately for each short segment, expressing the variation in the signal frequency in that segment over time[172], which together creates the time-frequency spectrum of the signal. The selection of window size or function has a significant impact on the STFT outcome. The most frequently utilized windows are Hamming, Gaussian, and Kaiser[173]. The STFT of a time domain signal $x(t)$ is defined as:

$$STFT_{x(t)}(t,g) = \int_{-\infty}^{+\infty} x(t)\ g(t-\tau)e^{-jgt}\ d\tau \quad \text{(III.10)}$$

Where $g(\tau)$ denotes a window function, and τ represents a time variable.

The concept of applying STFT to the signal is illustrated in Figure III. 8, which depicts a sliding window within which the signal is regarded as stationary.

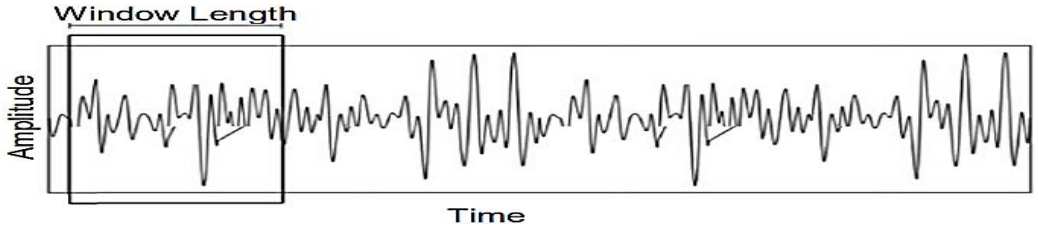

Figure III.8 The STFT concept [174].

The amplitude squared of the STFT, also known as the spectrogram or sonogram, is used to determine the frequency content of the signal. A spectrogram is a graphical depiction of a signal that assesses the power distribution of the signal across the time-frequency domain[175]. The spectrogram can be expressed mathematically by the following formula[175]:

$$SPEC_{x(n)} = \left|STFT_{x(n)}(n,g)^2\right| \quad \text{(III.11)}$$

Enhancing the temporal resolution of signal representations can be performed by reducing the window size; however, this may result in prolonged calculation times. Furthermore, to enhance frequency resolution, an extended time interval is necessary; however, this may compromise the stationary assumption. In reality, the STFT employs apertures that are predetermined in size and must be selected beforehand. In the context of rotating machine condition monitoring, identifying defects from non-stationary data that are occasionally weak and obscured by noise may necessitate more adaptable and efficient strategies. The main drawback of the STFT is that it does not employ window functions of various sizes for all frequency components.

III.2.3.2 Wavelet transform

A mathematical tool that surpasses the constraints of the Short-Time Fourier Transform (STFT) is the Wavelet, which facilitates localized analysis and can uncover signal characteristics overlooked by other approaches, such as trends and discontinuities. Wavelet analysis efficiently localizes a signal's information in the time-frequency domain via variable spectrograms, rendering it a superior option to the STFT technique for analyzing nonstationary signals. Wavelet families possess fixed shapes, such as Haar, Daubechies, symlets, Morlets, and coiflets (some examples of wavelet functions are shown in Figure III.9); nevertheless, the wavelet function is scalable, allowing the wavelet transformation to be adjustable across many frequency and time resolutions. The following equation can be utilized to represent the mother wavelet $\psi(t)$ mathematically:

$$\psi_{a,b}(t) = \frac{1}{\sqrt{a}}\psi\left(\frac{t-b}{a}\right) a > 0, b \in R \qquad \text{(III.12)}$$

Where a is the scaling factor, and b is the translation factor.

The wavelet basis functions are derived from the mother wavelet $\psi(t)$ via dilation and translation processes. Mathematically, the wavelet analysis is obtained by calculating the convolution between a signal and a wavelet function. There are two varieties of wavelet transform: continuous wavelet transform (CWT), and discrete wavelet transform (DWT).

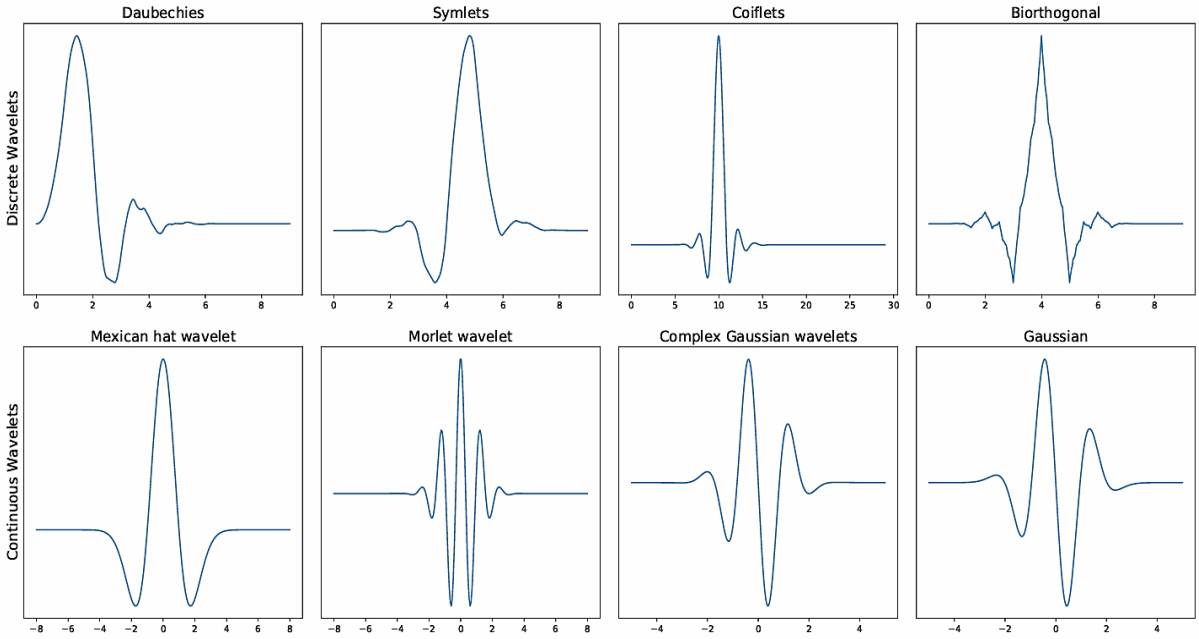

Figure III.9 Examples of several types of mother functions applicable to the wavelet transform.

- **Continuous wavelet transform (CWT)**

Morlet and Grossman were inspired by the Gabor transform to create the continuous wavelet transform in the early 1980s[176]. CWT is a technique that allows for multi-resolution analysis, providing a functional decomposition of the input signal through convolution with shifted and scaled versions of the mother wavelet function. This procedure generates wavelet coefficients that vary with scale and position. The continuous wavelet transform can, therefore, be considered as a bandpass filter. Given its benefits, CWT has considerable success in machinery fault diagnosis. Continuous wavelets use a quasi-continuous discretization to offer a high-resolution and linear representation of the time-frequency field.

Likewise, when signal $x(t)$ has a finite amount of energy ($x(t) \in L^2(R)$), the CWT of a signal $f(t)$ can be described as the following inner product:

$$CWT(a,b) = \frac{1}{\sqrt{|a|}} \int_{-\infty}^{+\infty} x(t)\, \psi^*\left(\frac{t-b}{a}\right) dt \quad \text{(III.13)}$$

Where '*' implies a complex conjugate.

Wavelet representations typically refer to time-scale representations rather than time-frequency representations, with frequency being the inverse of scale[177]. Thus, the frequency response matching the scale of the signal is possible to calculate using equation III.14

$$F_a = \frac{F_c \cdot f_s}{a} \quad \text{(III.14)}$$

Where F_c is the center frequency of the wavelet, f_s is the frequency at which the signal is sampled, and F_a is the real frequency that relates to a.

The admissibility conditions of energy limitation and zero overage must be satisfied by the wavelet $\psi(t)$ basis function, as shown in the following equations (III.15) and (III.16):

$$C_\psi = \int_{-\infty}^{+\infty} \frac{|\psi(\omega)|^2}{|\omega|} d\omega < \infty \quad \text{(III.15)}$$

$$\psi(0) = \int_{-\infty}^{+\infty} \psi(t)\, dt = 0 \quad \text{(III.16)}$$

Where ω indicates the angular frequency, and $\psi(\omega)$ is the Fourier transform of $\psi(t)$.

Results of the CWT analysis (wavelet coefficients) are typically represented in a scalogram, a 2D color plot that is a function of both scale and wavelength. The choice of the wavelet used

depends on the type of signal (time series data or an image) and the purpose of the application[178]. To obtain an accurate diagnosis, the selection of the mother wavelet is a crucial part car there is a significant correlation between the wavelet that is utilized and the result of the wavelet analysis of a waveform. Morlet, Mexican-Hat, Gaussian, and complex Gaussian wavelets are the most popular wavelets of the CW family.

- **Discrete wavelet transform (DWT)**

A disadvantage of the CWT is the generation of superfluous information during this process, which significantly increases the required computer power. To mitigate this redundancy, the scale parameter may be discretized dyadically in a linear ratio to the step size of the translation parameter as follows[158]:

$$\begin{cases} a = 2^j \\ b = 2^j k \end{cases} \tag{III.17}$$

The DWT signifies the discrete version of the CWT. The DWT of the time domain vibration signal $x(t)$ can be represented by the following equation:

$$DWT(j,k) = \frac{1}{2^j}\int_{-\infty}^{+\infty} x(t)\,\psi^*\left(\frac{t-k2^i}{2^j}\right) dt \tag{III.18}$$

The Discrete Wavelet Transform is often executed using a low-pass scaling filter $h(k)$ and a high-pass wavelet filter $g(k) = (-1)^k h(1-k)$. Mallat provided the scaling function $\phi(t)$ for use with the wavelet function $\psi(t)$ in the dual scale equation as follows:

$$\phi(t) = \sqrt{2}\sum_k h(k)\phi(2t-k) \tag{III.19}$$

$$\psi(t) = \sqrt{2}\sum_k g(k)\psi(2t-k) \tag{III.20}$$

The original signal is decomposed into a set of low- and high-frequency components, which is further detailed using the Mallat algorithm as follows:

$$a_{j,k} = \sum_k h(n)a_{j-1,k} \tag{III.21}$$

$$d_{j,k} = \sum_k g(n)a_{j-1,k} \tag{III.22}$$

To execute the Discrete Wavelet Transform (DWT), also known as multiresolution analysis (MRA), on a discrete signal x (t), the signal is subjected to filtering via specialized low-pass (L) and high-pass (H) filters, resulting in two vectors representing low and high sub-bands at the initial level. The initial vector represents the approximation coefficient (A1), whereas the subsequent vector denotes the detailed coefficient (D1). In the subsequent stage of decomposition, the approximation coefficient, or low-pass sub-band, undergoes additional filtering with L and H filters, yielding a further approximation coefficient (A2) and detailed coefficient (D2) at the second level. The length of coefficients at each level is half that of the preceding level. Figure III.10 illustrates the DWT, comprising five stages of decomposition.

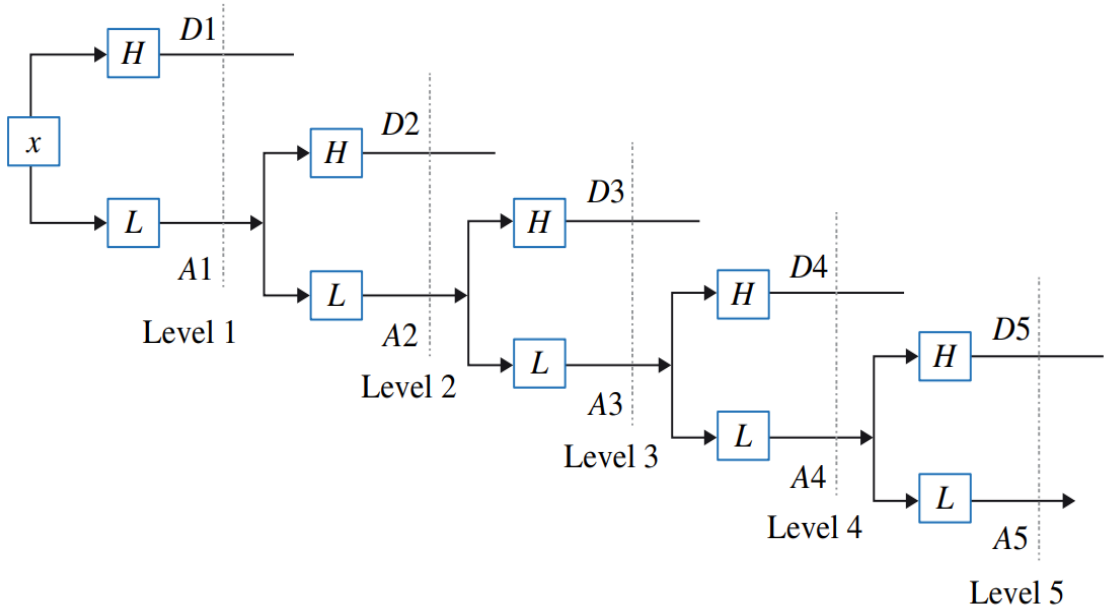

Figure III.10 The discrete wavelet transform Depiction with five stages of breakdown.

The benefits of employing the wavelet transform for vibration analysis in rotating machinery include the ability to identify localized changes in vibration signals and enhanced temporal resolution. Nonetheless, there are constraints associated with its application because it is not very adaptive, such as the meticulous selection of the wavelet function and the potential occurrence of cross terms in the wavelet scalogram[154].

III.2.3.3 Empirical mode decomposition (EMD)

Empirical Mode Decomposition (EMD) is a signal decomposition approach in the time-frequency domain that has garnered considerable attention in the field of output-only modal identification of systems. The EMD approach was created on the premise that any signal consists of various fundamental intrinsic oscillatory modes. A fundamental oscillation is

represented by each intrinsic mode, whether linear or nonlinear, and can be numerically described by an intrinsic mode function (IMF)[175]. The EMD is a nonlinear and adaptive data analysis method that decomposes the time-domain signal $x(t)$ into a finite number of intrinsic mode functions (IMFs). The IMF encompasses time-frequency domain details and represents the signal's intrinsic physical features[179]. Numerous researchers have employed EMD to assess vibration signals for machine defect diagnostics. Nonetheless, the conventional EMD exhibits certain limitations, including the mode-mixing issue in the resultant IMFs and challenges in addressing multichannel vibration measurements. To address mode mixing in the IMFs, particularly when analyzing signals with near-spaced frequencies and measuring noise, EMD was enhanced through its variants: ensemble EMD (EEMD) and time-varying filter-based EMD (TVF-EMD). EMD has recently been expanded to include a multivariate version, Multivariate EMD (MEMD), which is qualified for processing multichannel vibration data[179].

III.2.3.4 Hilbert-Huang Transform (HHT)

The Hilbert–Huang Transform is a technique for analyzing both stationary and non-stationary data, as well as transient data. It integrates EMD with the Hilbert transform to generate a Hilbert spectrum applicable for fault identification in the apparatus[154]. Calculating the instantaneous frequency of a signal $x(t)$ is possible through the use of the Hilbert transform. The Hilbert transform (HT) of a signal $x(t)$ can be depicted by its complex conjugate $y(t)$, which is defined as

$$H(t) = \frac{P}{\pi} \int_{-\infty}^{+\infty} \frac{x(\tau)}{t-\tau}\, dt \tag{III.23}$$

Where, P denotes the principal value of the singular integral.

The HHT has two primary stages. The EMD approach initially breaks down the signal into a sequence of IMFs, which represent vibration components characterized by distinct instantaneous frequencies. Each IMF denotes a distinct frequency part of the signal, facilitating a more nuanced examination of the time-varying characteristics. Upon acquiring the IMFs, the Hilbert transform is employed on each IMF to determine the instantaneous frequency as a function of time. In this manner, a frequency that fluctuates over time of the signal is represented, enabling the analysis of frequency changes and the detection of transient events[180]. In conclusion, HHT is an effective method for vibration analysis in rotating equipment, offering a comprehensive time-frequency representation of non-stationary signals

and facilitating defect detection and diagnostics. Its utilization alongside other analytical approaches can enhance the comprehension of vibrational behavior and aid in the formulation of appropriate CM and maintenance procedures[181].

- **Related work**

Bajric et al. [182] introduced a novel approach for diagnosing gearbox faults. The Time Synchronous Averaging (TSA) signals can be rapidly split into multiple sub-band signals using the DWT. Li et al. [183] employed the Wavelet Packet Transform (WPT) to evaluate acoustic and vibration inputs for the detection of gearbox issues. The gearbox malfunction is determined using deep learning with the Random Forest (RF) methodology. RF may effectively incorporate features derived from several sensors. The experimental results demonstrate a significant superiority over others through a range of comparison analyses. Vamsi et al. [184] generated feature vectors from raw vibration and audio inputs utilizing DWT. The choice of wavelet basis functions is examined. Guo et al. [185] employed a three-level WPT breakdown to examine data exhibiting fault features. The produced feature space was entered into the neural network. It enhanced the precision of defect diagnosis and classification outcomes. Hu et al. [186] introduced an advanced technique known as the Multi-taper Empirical Wavelet Transform (MTEWT) for analyzing non-stationary data in wavelet transform. The theoretical and experimental results demonstrate that defect features can be effectively retrieved from masking components. Li et al. [187] propose a fault detection methodology for wind turbine drive trains that combines the Wigner-Ville distribution for time-frequency data extraction with convolutional neural networks for classification. The model consistently identifies spectral peaks and structures in vibration signals to provide precise defect detection. Experimental findings from a wind turbine test rig demonstrate the efficacy of the method in identifying flaws between the gearbox and rolling bearing. Patel et al. [188] propose a diagnostic approach for planetary gearboxes using Auto-Regressive (AR) modeling and Continuous Wavelet Transform to extract features from non-stationary vibration signals in planetary gearbox across various frequency ranges. Their method effectively identifies fault types and severities without requiring visual inspection despite the mechanical complexity of planetary gear systems. Experimental validation using signals with different fault conditions confirms the reliability of the technique in characterizing unique fault behaviors and detecting defective parts. Li et al. [189] address the limitations of wind turbine generator-bearing fault diagnosis caused by complex operating conditions and limited fault samples by proposing a data augmentation approach based on an improved Multi-scale Conditional Generative Adversarial Network

(MCGAN). Using STFT-extracted time-frequency features, the enhanced MCGAN generates diverse synthetic vibration signals that preserve fault characteristics. Experimental results show that the augmented data significantly improves diagnostic accuracy, surpassing 80%, and enhances the generalization of fault classifiers, offering a promising solution to sample scarcity in real-world applications. Feng et al. [190] employed the EEMD to extract IMFs from the vibrational signal of a WT gearbox and proposed a method for selecting the optimal IMF. To address the issue of modal mixing inherent in EMD, Variational Mode Decomposition (VMD) was added, demonstrating superior separation results. A hybrid model integrating EMD and autoregression (AR) was presented in [191] for the fusing of diverse domain features and dimensionality reduction. Nonetheless, EMD is susceptible to modal mixing. The Ensemble Empirical Mode Decomposition (EEMD) is proposed to address this issue. In EEMD, a sequence of white noise is superimposed upon raw signals. Yan et al. [192] conducted VMD to monitor the operational conditions of rolling bearings, and the experimental findings demonstrate its remarkable self-adaptability. Inturi et al. [193] employed the EMD method to analyze acoustic and vibrational signals for the diagnosis of defects in wind turbine gears. A decision tree is used to identify the most significant traits. Maheswari et al. [194]applied Multivariate Empirical Mode Decomposition (MEMD) to dissect raw signals into monocomponents, including IMFs. Characteristics are efficiently retrieved from several channels using MEMD and the Dynamic Bayesian Belief Network. Li et al. [195] address the high failure rate of rolling bearings in wind turbines by conducting a comprehensive failure analysis and implementing a diagnostic approach using EMD. Vibration signals are decomposed into IMFs, which are then filtered using the kurtosis criterion to extract meaningful fault features. By comparing actual and theoretical fault frequencies, the study performs accurate fault analysis. It enhances diagnostic precision by applying and evaluating multiple classifiers on both time-domain and time-frequency features derived from EMD. Zhang et al. [196] propose an advanced fault diagnosis framework for wind turbine planetary gearboxes by integrating improved multivariate variational mode decomposition (IMVMD) with ensemble refined composite multivariate multiscale dispersion entropy (ERCmvMDE). The IMVMD optimizes decomposition parameters for more effective signal processing, while ERCmvMDE extracts rich multi-channel features from vibration data. These features are then used to train a least squares support vector machine (LSSVM), achieving high diagnostic accuracy, as demonstrated through simulations and experimental validation.

III.3 Bearing fault diagnosis based on signal processing techniques using CWRU dataset: Application

Numerous methodologies outlined in the preceding section have been employed to provide an approach for bearing condition monitoring, based on CWRU data. This research, published in the paper [197], incorporated both normal and defective bearing data to validate the methodology. In this study, the DWT was employed using Daubechies wavelets to analyze and diagnose bearing faults from vibration signal data effectively. Daubechies wavelets (db) are well suited for signal decomposition due to their compact support and ability to capture both time and frequency information, which is essential when dealing with the non-stationary nature of vibration signals in rotating machinery. The bearing signals were decomposed into multiple frequency bands using the discrete wavelet transform (DWT), allowing the isolation of different signal components that correspond to various fault-induced frequencies. This step-by-step decomposition enables the separation of noise from fault-relevant features, thereby enhancing the clarity and interpretability of the signal.

The analysis is conducted in the time domain, wherein the energy content of each decomposed frequency band is calculated. The energy distribution is a crucial indicator of fault presence and severity; anomalous energy concentrations in specific bands typically indicate the occurrence of a defect. Analyzing the energy patterns across frequency bands for defective bearings enables the identification of abnormalities linked to bearing degradation. To further investigate the fault and determine its exact location, the fast Fourier transform was applied to the frequency bands that exhibited high energy levels during the DWT analysis. This combination of wavelet and Fourier analysis provides a two-fold benefit: DWT enhances the time-frequency localization of fault features, while the FT offers insight into the frequency content of those features. This integrated approach ensures both precise detection and accurate fault localization for both inner race and outer race-bearing elements.

III.3.1 CWRU dataset description

The vibration data obtained from the Case Western Reserve University Bearing Data [198] was used in the research findings presented in this work. It serves as a common database for health monitoring applications, which allows access to ball-bearing test data for both healthy and damaged bearings. As illustrated in Figure III.11, the experimental test apparatus to create the bearing data includes a 2 hp induction motor, a dynamometer, and a torque transducer/ encoder placed in the center. Moreover, the test rig is equipped with bearings at the motor's drive-end

(DE) and fan-end (FE). The bearing at the DE and FE are 6205-2RS JEM and 6203-2RS JEM, respectively. Single point defects with failure sizes from 0.18 mm to 0.71 mm (0.007 inches to 0.028 inches) were induced to the test ball bearings using electro-discharge machining (EDM). The accelerometers were used to record vibration data in each of the following four test-bearing cases: normal condition, ball failure, inner-race failure (IRF), and outer-race failure (ORF). A 16-channel DAT recorder was utilized to acquire the data at two sampling rates, one of 12 kHz, and the other of 48 kHz. At motor speeds ranging from 1730 to 1797 rpm, bearing condition vibration signals were obtained for motor loads ranging from 0 to 3 hp.

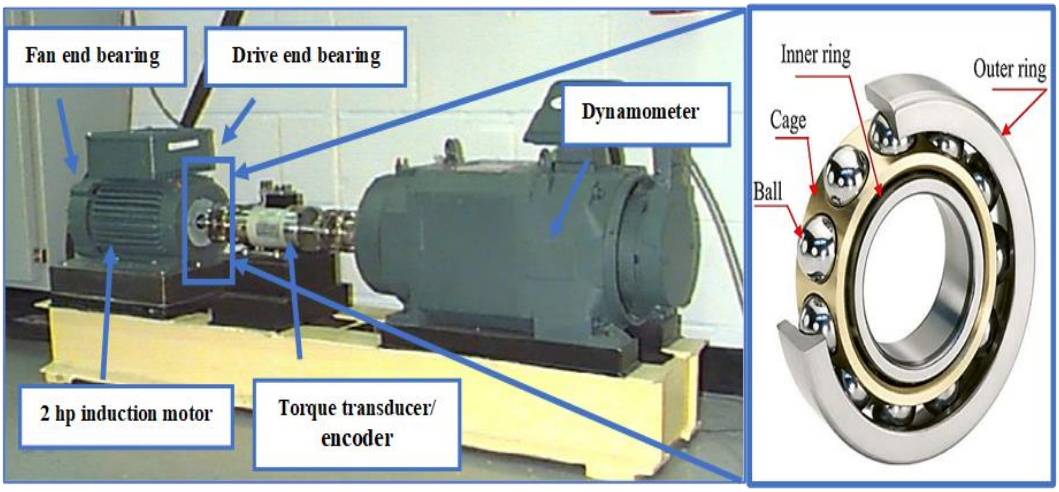

Figure III.11 Test setup arrangement for ball bearing of CWRU.

In this work, our analysis was based on the vibration data of the Drive-end bearing that were recorded at a sampling rate of 12 kHz when the load condition of 0 hp was applied to the motor shaft at a rotation velocity of 1779 rpm. For the data preprocessing in this experiment, the vibration signal, comprising 4096 data points, was used for each of three cases: normal condition, inner race defect, and outer race defect, with a diameter of 0.53 mm. Figures III.12 (a), III.12 (b), and III.12 (c) show the vibration signals corresponding to the normal condition, IRF, and ORF, respectively.

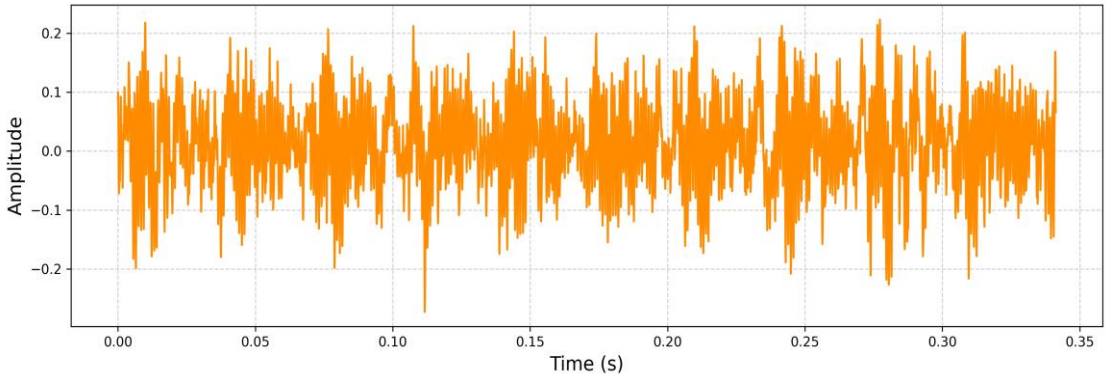

(a)

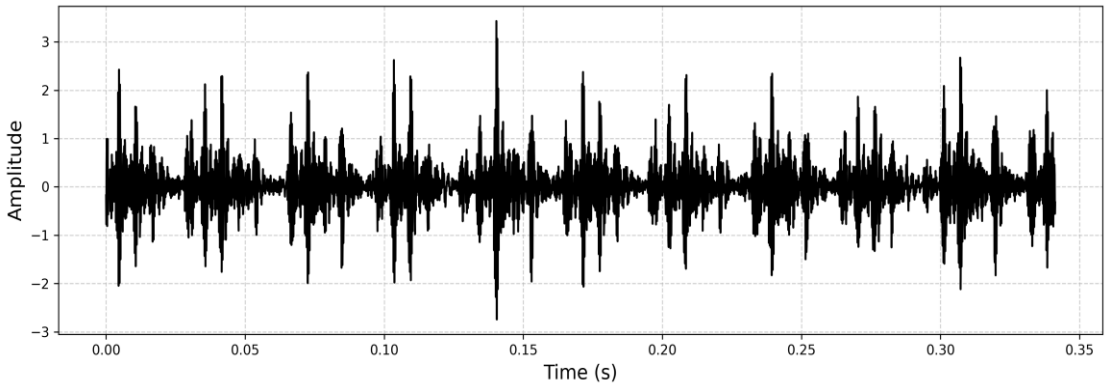

(b)

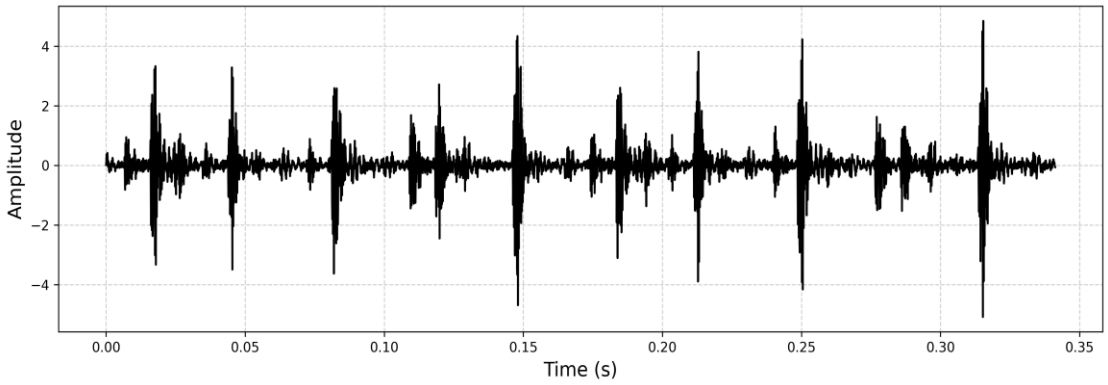

(c)

Figure III.12 Bearing vibration signals: (a) normal condition, (b) inner race failure, and (c) outer race failure.

Each bearing element typically acquires a characteristic frequency. The frequencies of SKF faults related to the defective inner and outer races can be calculated as follows:

$$BPFI = \left(\frac{n}{2}\right) f_r \left(1 + \left(\frac{d}{D}\right) cos\alpha\right) \quad \text{(III.24)}$$

$$BPFO = \left(\frac{n}{2}\right) f_r (1 - \left(\frac{d}{D}\right) cos\alpha) \quad \text{(III.25)}$$

Where $BPFI$ denotes the inner-race ball pass frequency, $BPFO$ signifies the outer-race ball pass frequency, n indicates the number of rolling elements, f_r represents the shaft speed, d refers to the rolling element diameter, D symbolizes the bearing pitch diameter, and α denotes the contact angle.

According to the standard bearing fault frequency calculation formula, specifically equations (III.24) and (III.25), the characteristic fault frequencies for the bearing were determined based on its geometry and rotational speed. Using the specific bearing dimensions and operating speed, the $BPFI$ was calculated to be approximately **162 Hz**, and the $BPFO$ was estimated to be around **107 Hz**, which are indicative of characteristic frequencies associated with faults in the inner and outer races, respectively. These frequencies are crucial in condition monitoring and vibration analysis for fault detection and diagnosis.

Table III.2 presents the structural details of the 6205-2RS JEM SKF bearing utilized in the study.

Table III.2 Bearing parameters.

Inside Diameter	Outside Diameter	Thickness	Ball Diameter	Pitch Diameter
25	52	15	7.94	39.04

III.3.2 Signal energy distribution across wavelet coefficients

According to Parseval's theorem, which states that the total energy of a signal is preserved across different domains (such as time, frequency, or wavelet domains), the energy of a signal $f\ (t)$ remains constant regardless of the transformation applied, provided the transform is orthonormal. In the context of DWT, this means that the total energy of the original signal is exactly equal to the sum of the energies of its wavelet coefficients after decomposition. When a signal undergoes an m-level DWT decomposition, it is split into one set of approximation coefficients at level m (denoted as A_m) and multiple sets of detail coefficients at each level from 1 to m (denoted as $D_1, D_2,..., D_m$). Based on Parseval's theorem, the overall energy E of the signal in the wavelet domain can be articulated as [199]:

$$E = \sum_1^N |f(t)|^2 = EA_m + \sum_j^m ED_j \quad \text{(III.26)}$$

$$EA_m = \sum_1^N |A_m|^2 \quad \text{(III.27)}$$

$$ED_j = \sum_1^N |D_j|^2 \quad \text{(III.28)}$$

Where EA_m presents the energy of the approximation coefficient, ED_j indicates the energy of the detail coefficient, N represents the number of samples, and m signifies the maximum wavelet decomposition level.

Wavelet energy distribution is employed to identify local characteristic differences at various levels. The energy content of the band is the aggregate of the energies from the scale and detail components[199]. Consequently, the energy distribution is calculated to extract the most pertinent information from the different resolution levels. It derives from:

$$P_a = \sum_1^{N/2^m} |A_m|^2 / N_m \quad \text{(III.29)}$$

$$P_d = \sum_1^{N/2^j} \frac{|D_j|^2}{N_j} \qquad j = 1,2,3, \dots m \quad \text{(III.30)}$$

Commonly applied wavelets include Haar, Daubechies, and Symlets due to their ability to capture transient and localized features[178], which aids in analyzing non-stationary time-series signals in vibration-based fault diagnosis. In this study, the Daubechies wavelet of order 3 (db3) is chosen for its balanced time-frequency resolution and effectiveness in identifying fault-related frequencies in bearing components.

III.3.3 Results and discussions

In this study, multi-scale wavelet analysis is applied to vibration signals collected from both healthy (normal) and faulty (abnormal) SKF bearings operating at a rotational speed of 1797 rpm, which corresponds to a fundamental frequency of 30 Hz. To capture the signal's transient and frequency-varying characteristics, a 5-level DWT is performed using the db3 wavelet. Through this decomposition, the signal is broken down into a hierarchy of components: five sets of detail coefficients denoted as cD1 to cD5, corresponding to the high-frequency content at each level and one set of approximation coefficients (cA5), which captures the low-frequency trend of the signal at the final level.

The results of the db3 decomposition for both normal and defective bearing signals are displayed in Figures III.13, III.14, and III.15, accordingly.

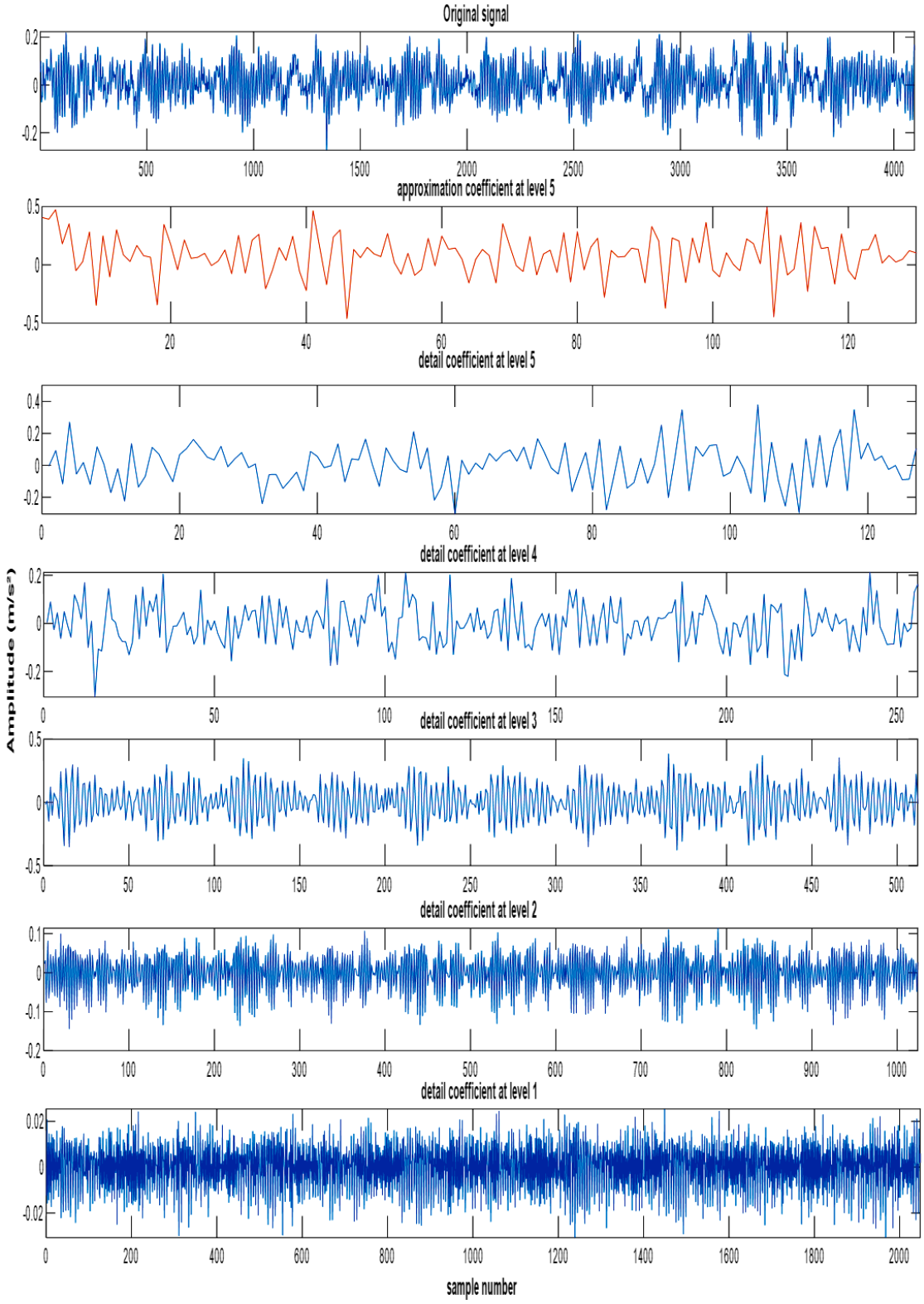

Figure III.13 db3 wavelet decomposition of normal bearing signal.

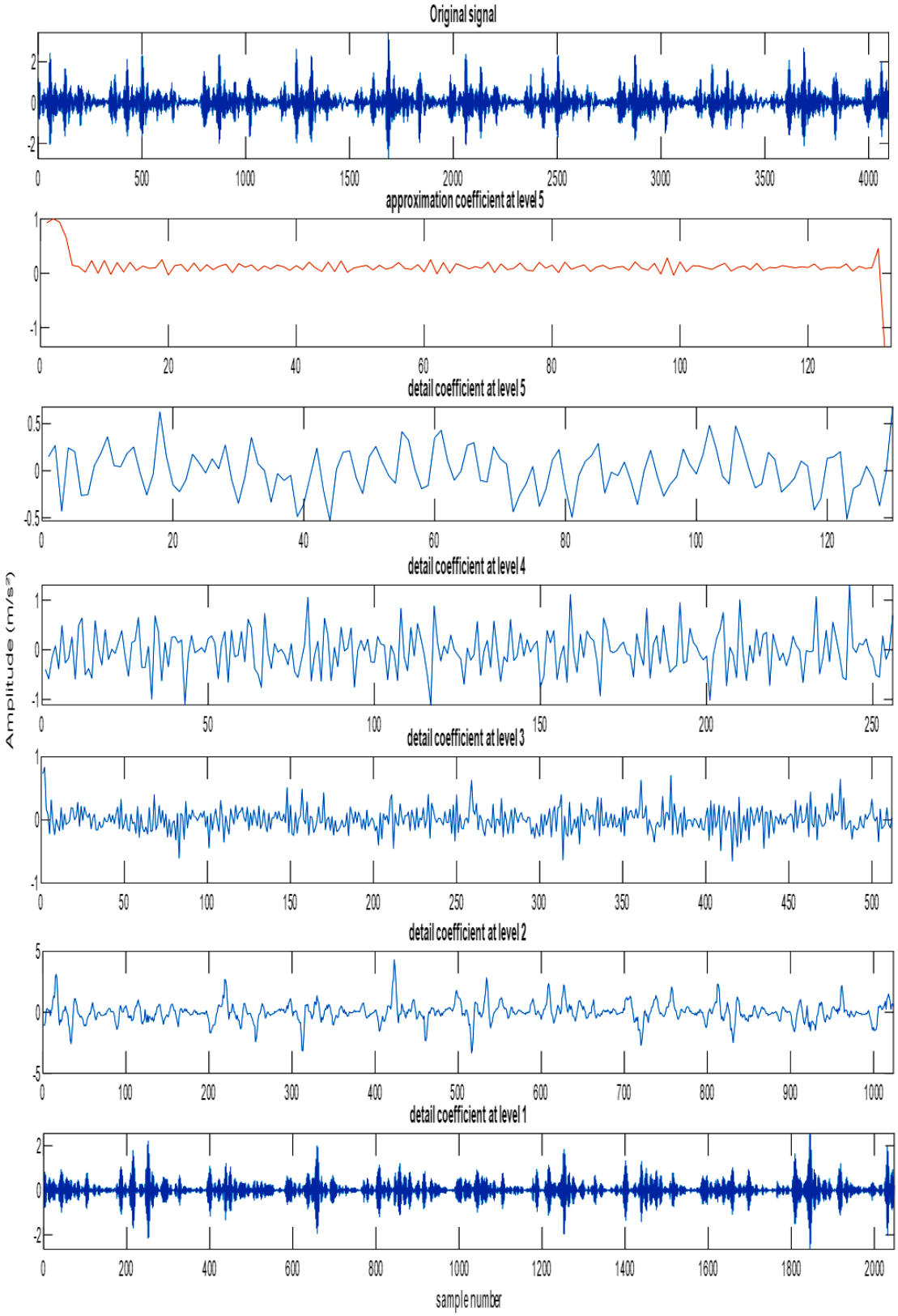

Figure III.14 db3 wavelet decomposition of IRF bearing signal.

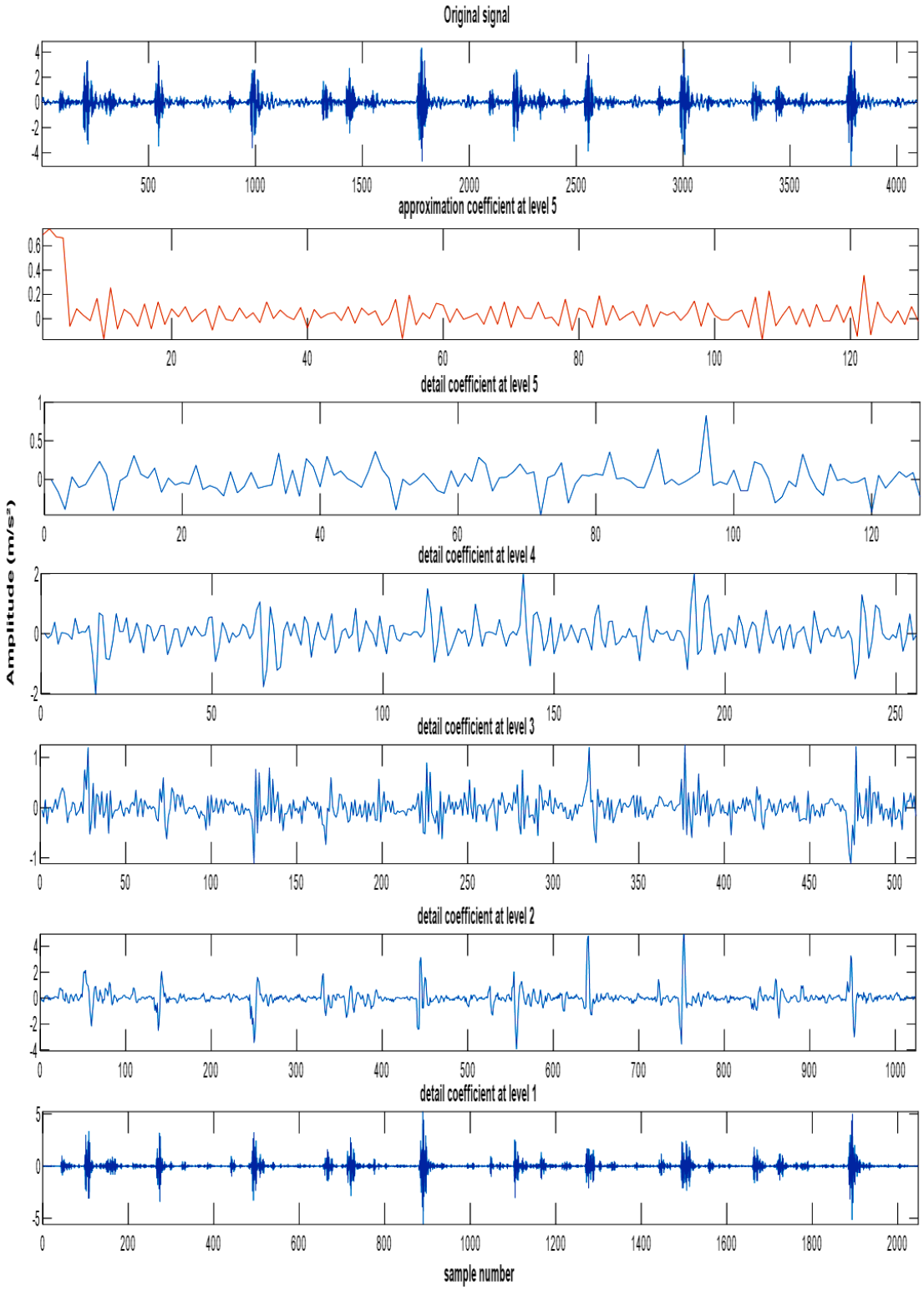

Figure III.15 db3 wavelet decomposition of ORF bearing signal.

The process of diagnosing the condition of a rolling bearing begins with detecting the presence of any abnormalities in the vibration signal, followed by determining the specific location of the fault whether it lies in the inner race, outer race, or rolling elements. A reliable method for distinguishing between healthy and defective bearings is through energy distribution analysis in the frequency domain. In general, healthy bearings tend to concentrate their signal energy in lower frequency bands, resulting in relatively low energy content at higher frequencies. In contrast, defective bearings generate impulsive signals due to mechanical impacts or surface roughness, resulting in a higher concentration of energy in the high-frequency components.

This behavior can be effectively analyzed using DWT, which allows the signal to be decomposed into multiple frequency bands (or sub-bands) while preserving temporal resolution. From Figure III.13, which represents the wavelet decomposition of a normal (healthy) bearing signal, we observe that the magnitudes across all sub-bands remain relatively stable and low in amplitude, indicating the absence of fault-induced impulses.

However, in Figures III.14 and III.15, which correspond to defective bearing conditions, notable amplitude fluctuations are observed across all levels of DWT decomposition. These significant changes suggest that the signal is no longer stationary and contains components arising from fault impacts. Among these sub-bands, sub-band D2, which corresponds to a relatively higher frequency range, exhibits the most prominent magnitude variations in the presence of defects. This consistent pattern of increased activity in D2 suggests that it is susceptible to the early signs of localized faults. Therefore, the D2 sub-band should be given special attention in the diagnostic process, as it may contain critical features for accurate fault detection.

To attain deeper insight into the bearing condition, the energy distribution of the decomposed signal was calculated for each sub-band resulting from the 5-level Discrete Wavelet Transform (DWT). This analysis enables the identification of which frequency bands contain the most significant signal activity, particularly related to fault conditions.

Figure III.16 (a) and Figure III.16 (b) display the energy distribution at each level of inner race and outer race faults, respectively.

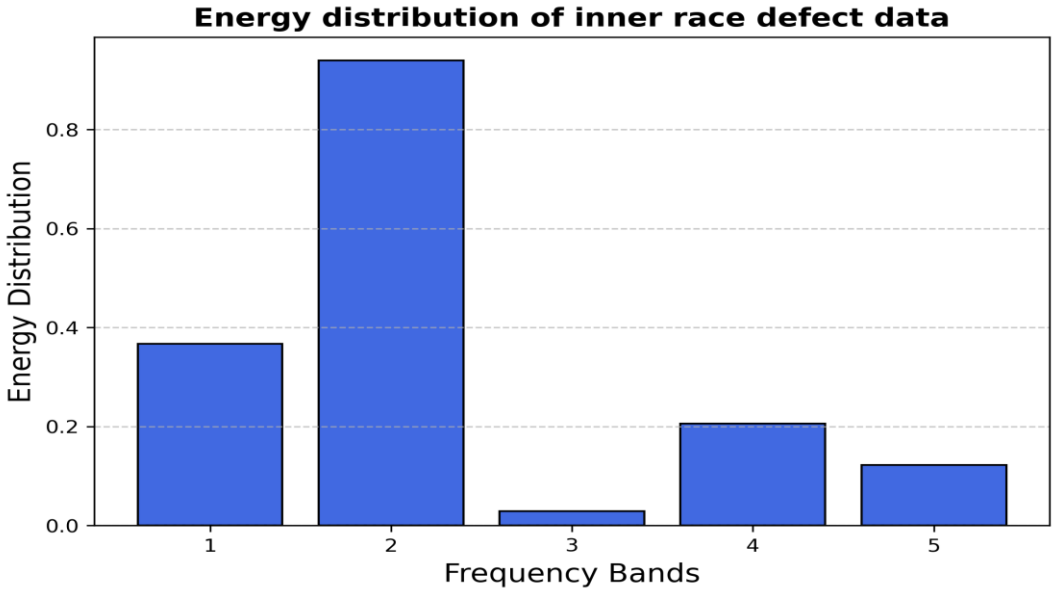

(a)

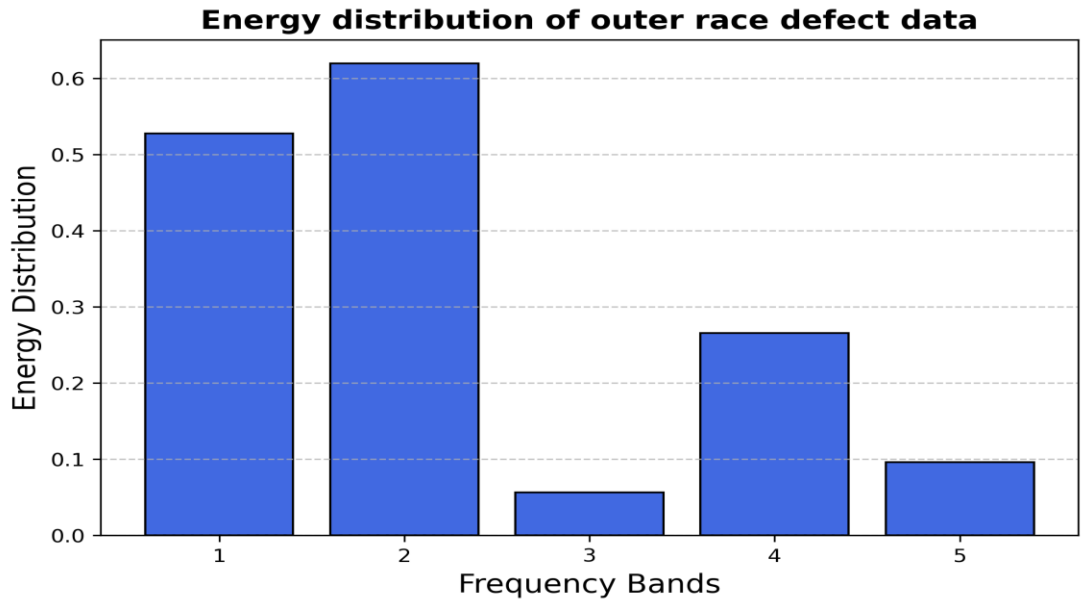

(b)

Figure III.16 Energy distribution of wavelet sub-bands: (a) inner race fault and (b) outer race.

As shown in Figure III.16, there are noticeable abnormalities in the energy content at level 2 (D2 sub-band) for both inner-race and outer-race fault signals. The elevated energy concentration in the D2 sub-band reflects the presence of high-frequency components often generated by localized defects, such as pitting or spalling, on the bearing races. These fault-induced impulses excite natural frequencies that fall within the range captured by D2, making it particularly sensitive to such anomalies. Therefore, this sub-band effectively captures the dynamic behavior introduced by fault progression and becomes a key focus in fault detection

and classification tasks. Figure III.16 visually confirms that the D2 sub-band consistently contains a higher proportion of energy in faulty conditions, thus validating its importance in diagnostic feature extraction for condition monitoring of rolling bearings.

To accurately determine the location of bearing faults, the Fast Fourier Transform (FFT) is explicitly applied to the D2 sub-band of the wavelet-decomposed signals for both IRF and ORF conditions. The D2 level is chosen based on prior analysis. By focusing the FFT on this sub-band, noise from irrelevant frequencies is reduced, allowing for more precise identification of characteristic fault frequencies. Figures III.17 and III.18 display the FFT spectra of the D2 sub-band for the IRF and ORF signals, respectively.

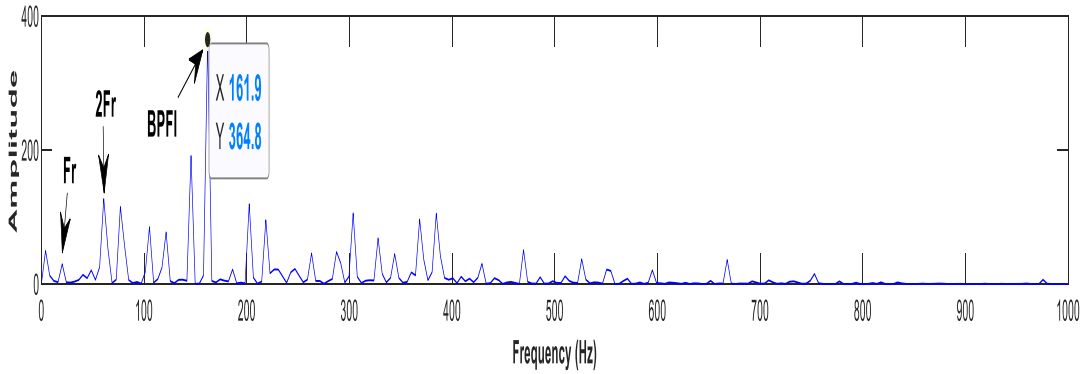

Figure III.17 FFT spectrum of signal D2 sub-bands of IRF.

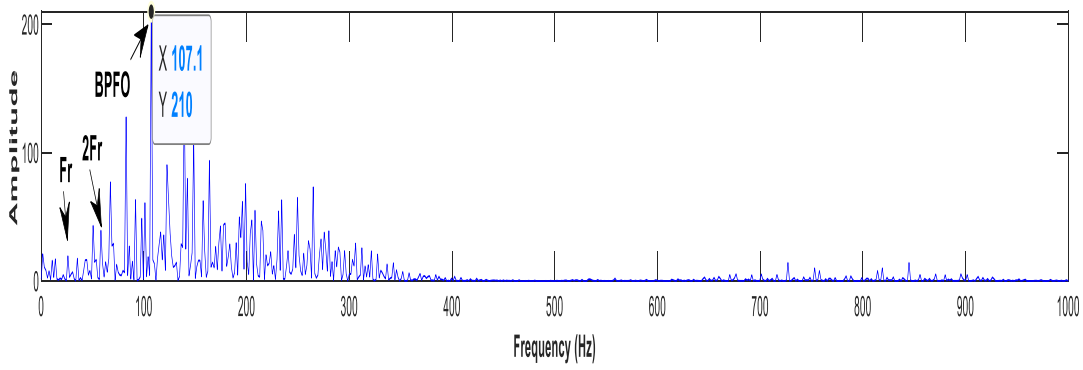

Figure III.18 FFT spectrum of signal D2 sub-bands of ORF.

The spectral analysis reveals prominent peaks at 162 Hz for the inner race fault and 107 Hz for the outer race fault. These frequencies align precisely with theoretical fault frequencies calculated based on bearing geometry and rotation speed, confirming the diagnostic value of the D2 sub-band. Additionally, the presence of harmonic components further reinforces the

identification of fault-related impacts, as these harmonics are typically generated by periodic impulses resulting from repeated contact with damaged surfaces. This targeted approach, which combines wavelet decomposition with FFT, provides an effective strategy for localizing faults within bearings and enhances the reliability of the diagnosis.

III.4 Conclusion

This chapter presented a comprehensive overview of the state-of-the-art signal processing techniques employed for fault detection and diagnosis in wind turbine bearings. Advanced signal processing methodologies, such as the Fast Fourier Transform (FFT), Short-Time Fourier Transform (STFT), Empirical Mode Decomposition (EMD), Hilbert-Huang Transform (HHT), and Wavelet Transform, have been extensively utilized to identify and localize defects in wind turbine bearings. Wavelet-based approaches, particularly the Discrete Wavelet Transform (DWT), demonstrate exceptional proficiency in analyzing non-stationary vibration signals through their ability to provide both temporal and spectral localization. These methods have shown great promise in extracting fault signatures from noisy environments typical in wind turbine systems.

Building upon these insights, this chapter introduces a proposed fault diagnosis methodology based on the DWT and FFT, utilizing the well-established Case Western Reserve University (CWRU) bearing dataset. The enhanced technique relies on multiresolution analysis, utilizing the DWT and energy distribution to efficiently extract fault features. Vibration signals from healthy and faulty bearings are subjected to a 5-level DWT using the Daubechies 3 (db3) wavelet, enabling the isolation of high-frequency fault-related components. Subsequent analysis focuses on energy distribution across the wavelet sub-bands and FFT analysis of specific levels, particularly D2, which consistently exhibits significant energy concentrations and fault-characteristic frequencies. This approach effectively identifies and localizes faults, such as inner race and outer race defects, with detected frequencies matching theoretical fault signatures. This hybrid time-frequency analysis not only enhances fault sensitivity but also improves interpretability, making it a promising tool for future applications in wind turbine-bearing health monitoring systems.

CHAPTER IV

Bearing Fault Diagnosis and Classification using Machine Learning Algorithms: Application to Real-World Wind Turbine Data

IV.1 Introduction

In the Industrial 4.0 era, Artificial Intelligence (AI)-driven Prognostics and Health Management is essential for maintaining the reliability and resilience of Industrial Cyber-Physical Systems (ICPS), including wind turbines, aircraft, and manufacturing machinery [200]. Real-time defect detection and diagnosis of rotating mechanical elements, including gears, bearings, and rotors, are essential for ensuring safe operation, minimizing downtime, and reducing maintenance expenses. Most current deep learning-based diagnostic algorithms are designed to address closed-set recognition issues, wherein the target fault categories and operational conditions (e.g., rotational speed and load level) are predetermined and constant. Compared with conventional machine learning, the deep learning approach demonstrates an undeniable superiority in the field of fault diagnosis affecting rotating machines, particularly with regard to bearing faults.

This chapter presents a comprehensive exploration of machine learning-based approaches for fault diagnosis in wind turbine systems. The first part offers a concise review of state-of-the-art machine learning algorithms, highlighting their applications, strengths, and limitations in diagnosing wind turbine faults. It covers a range of techniques, from traditional classifiers to more advanced ensemble methods, with a focus on their relevance to real-world SCADA data and industrial condition monitoring.

In the second part, a novel hybrid diagnostic method is presented, which integrates a deep learning model, specifically a Convolutional Neural Network (CNN), with a stacking ensemble strategy based on different base models to enhance classification accuracy and robustness. This hybrid approach is evaluated on two distinct datasets: the CWRU dataset, which involves bearing fault detection, and the Aventa AV-7 wind turbine SCADA dataset, which includes various types of operational faults. The combined use of deep feature extraction and ensemble learning enables the proposed method to achieve high diagnostic performance across both benchmark and real-world scenarios.

IV.2 Brief review of machine learning approaches for health monitoring of WT

To guarantee the economical and secure operation of critical rotating machinery, PHM have been an essential concept [201]. Due to the rapid advancements in artificial intelligence (AI), numerous algorithms based on machine learning (ML) are seen as up-and-coming technologies for industrial applications within PHM [202]. This is attributed to their robust ability to process high-dimensional data and their ease of use across various disciplines by researchers. For instance, the success of simultaneous fault detection and maintenance planning using ML has been illustrated by de Lima Munguba et al. [203]. The features chosen as input, as many machine-learning approaches are sensitive to these details, can significantly influence the efficiency of the diagnostic algorithm. Characteristic attributes can be classified as one-dimensional, two-dimensional, or multi-dimensional [204]. The two-dimensional transformed images are more practical for data analysis and intelligent classification tasks and are also an essential step towards improving feature quality. As a rule, two-dimensional features are acquired using time-frequency analysis. Figure IV.1 illustrates that defect diagnostic approaches for wind turbines based on machine learning are categorized into three main types: unsupervised learning, semi-supervised learning, and supervised learning[205].

The failure detection of wind turbine bearings with artificial intelligence is categorized into two primary types: symbolic reasoning (knowledge-based) and numerical computation (neural-network-based) defect identification [206]. The knowledge-based approach is predicated on the extraction of a knowledge base by utilizing symbolic and computational intelligence techniques, as well as a substantial amount of historical data, to represent the dependencies of system variables clearly. A diagnostic decision is made by verifying the consistency between the knowledge base and the real-time operational behavior with the assistance of a classifier[126]. Regarding wind turbine defect diagnosis, traditional ML strategies, such as Support Vector Machine (SVM) [207], Naïve Bayes, K-Nearest Neighbor (KNN) [208], Random Forest [209], Decision Tree (DT), Logistic Regression (LR) [210], Stacking Classifier [211], and Extreme Learning Machine [212], typically require human intervention to extract fault-related features from the raw data. Once extracted, the most relevant features must be selected to build a diagnostic model that can autonomously determine the machine's health condition. Recently, the application of DL techniques for gearbox condition monitoring (CM)

has attracted renewed interest from researchers due to their ability to automatically extract deep features from vibration signals through end-to-end learning [213]. Popular DL models used in this context include convolutional neural networks (CNNs), auto-encoders (AEs), recurrent neural networks (RNNs), deep Q-networks (DQNs), deep belief networks (DBNs), long short-term memory (LSTM), and generative adversarial networks (GANs).

In particular, CNNs, a deep learning algorithm widely used, are employed with high accuracy in identifying both one-dimensional and two-dimensional signals in the field of diagnosing faults in rotating machinery [214]. Kaya et al. [215] present a technique for detecting fault size using vibration data from different types of bearing failures, employing CWT and two-dimensional convolutional neural networks (2DCNN). The achieved success rates ranged from 96.67% to 100%. Kong et al. [216] proposed a method for diagnosing compound faults in untrained planetary gearboxes, utilizing adaptive learning variational mode decomposition (ALVMD) and dual-scale squeeze-and-excitation convolutional neural network (DSSECNN). Liang et al. [217] integrated the Deep Capsule Neural Network (CapsNet) with the Stockwell Transform (ST) and Data Augmented Generative Adversarial Networks (DAGANs) to diagnose composite faults in WTG. Chen et al. [218] introduced CNNs that utilize discrete wavelet transform (DWT) for fault diagnosis in a planetary gearbox based on vibration signals. The combination of DWT and CNNs resulted in a fault classification accuracy of 99.3%. Chen et al. [219] introduced a method based on LSTM and AEs neural networks to assess sequential CM data from WTs. The effectiveness of the proposed approach has been validated through a case study employing real-world data from a wind turbine CM dataset. In their study, Zhang et al. [220] conducted feature extraction of one-dimensional vibration signals from WTG bearings using a one-dimensional CNN (1D-CNN). They employed SVM optimization via particle swarm optimization (PSO) for fault classification. Experimental results suggest that the proposed method is effective for single-bearing conditions and is more accurate than alternative approaches.

Moreover, to ensure the consistent operation of WTs, many studies have explored the application of advanced technologies, such as DL and ensemble techniques for gearbox-bearing fault diagnosis. Attallah et al. [221] introduced an ensemble DL method that integrates three CNN models (Inception, Xception, and MobileNet) with discrete wavelet transformation and

PCA to analyze infrared images of an induction generator-based wind turbine, achieving nearly 100% accuracy. Yang et al. [222] introduced a wind turbine fault-diagnosis strategy with strong noise immunity. It combines the 2DCNN with random forest (RF), aiming to harness the automatic feature-extraction capability of CNN and the robust discrimination performance of RF classifiers. Khan and Byun [223] developed a stacking classifier named AKL-SE. This classifier amalgamates AdaBoost, KNN, and LR to categorize five fault types in a 3 MW direct-drive wind turbine employing Supervisory Control and Data Acquisition (SCADA) data. Zhang et al. [224] proposed a method for detecting and diagnosing anomalies in WTs, utilizing LSTM-based stacked denoising autoencoders (LSTM-SDAE) and extreme gradient boosting (XGBoost). Likewise, Beretta et al. [225] presented an unsupervised ensemble technique incorporating neural networks and isolation forests. This method accurately predicted primary bearing faults months in advance using only SCADA data, achieving 100% accuracy in a case study. De Lima Munguba et al. [226] introduced an ensemble technique channel aimed at bolstering robustness by integrating multiple models for anomaly detection. These models utilize vibration data from selected wind turbine bearings obtained through the CM system. Dong et al. [227] proposed an ensemble learning model using a stacking framework to enhance the precision and consistency of wind power forecasting. These experimental outcomes indicate that the suggested model exhibits greater prediction accuracy and stability when compared to other individual forecasting models.

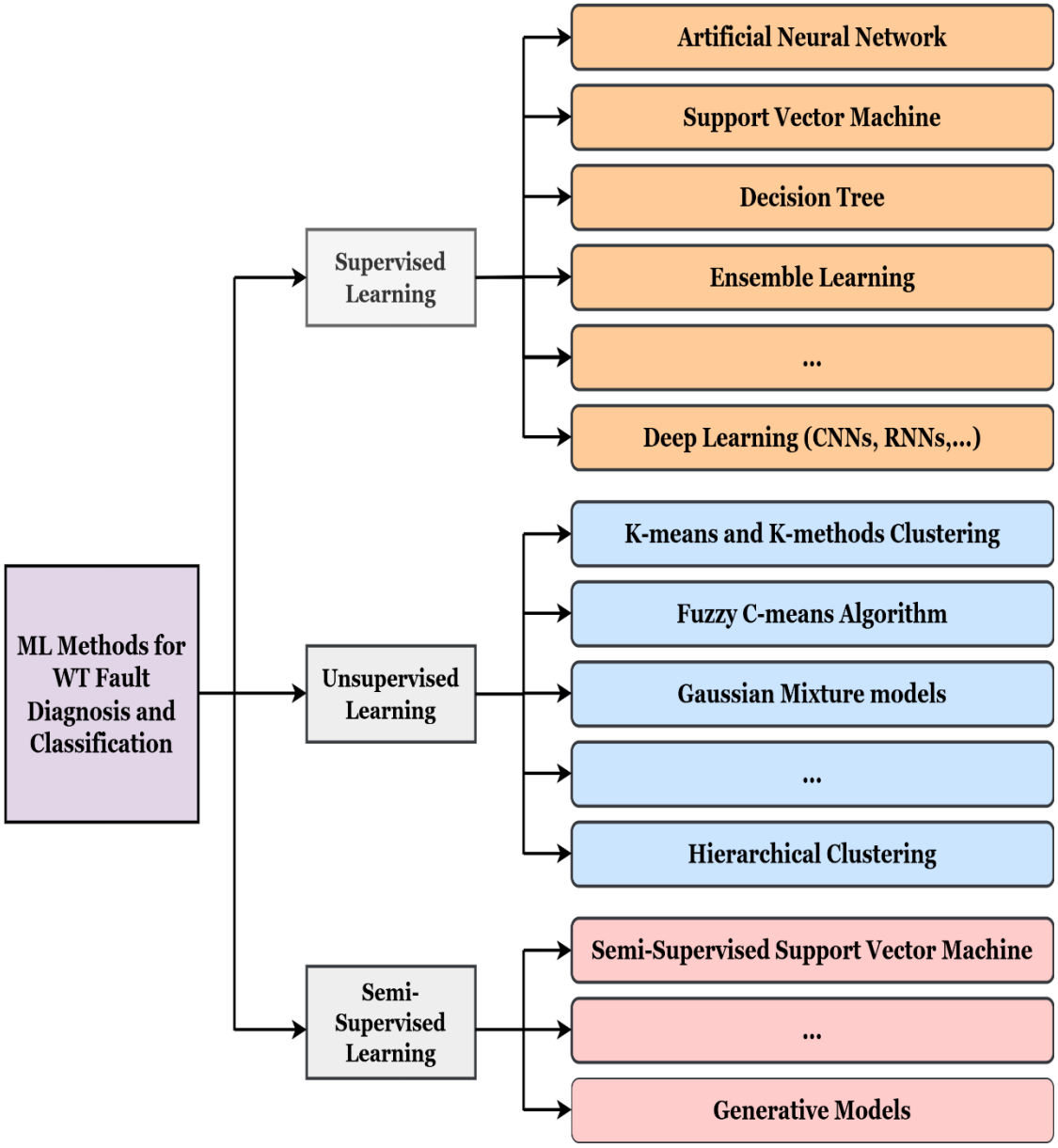

Figure IV.1 ML techniques for WT failure diagnosis (Adapted from [205]).

IV.2.1 Convolutional Neural Networks (CNNs)

One of the most popular supervised learning algorithms is CNNs, developed by Lecun to process images [228]. A convolutional neural network is a feed-forward neural network with multiple hidden layers that has proven its worth in various computer vision applications, including image segmentation, object identification, CM, and image classification. The basic framework of CNNs consists of an input layer and two main blocks with distinct functions: the

feature extraction block, which comprises convolutional layers and pooling layers, and the second block, the classification block, which essentially contains several fully connected layers and an output layer [229]. CNNs are designed to apt any complex data distribution and locate small-scale details in images. In addition, CNNs have the property of sharing parameters, which enables the considerable reduction of trainable parameters without compromising the ability to represent features [230]. As a result of their unique capability to automatically extract meaningful information from visual data, CNNs are entrusted with the role of prediction. On the other hand, using a back-propagation process based on a gradient descent algorithm, it is straightforward to train CNNs, and these architectures are compatible with all hardware. The standard design of a convolutional network is shown in Figure IV.2.

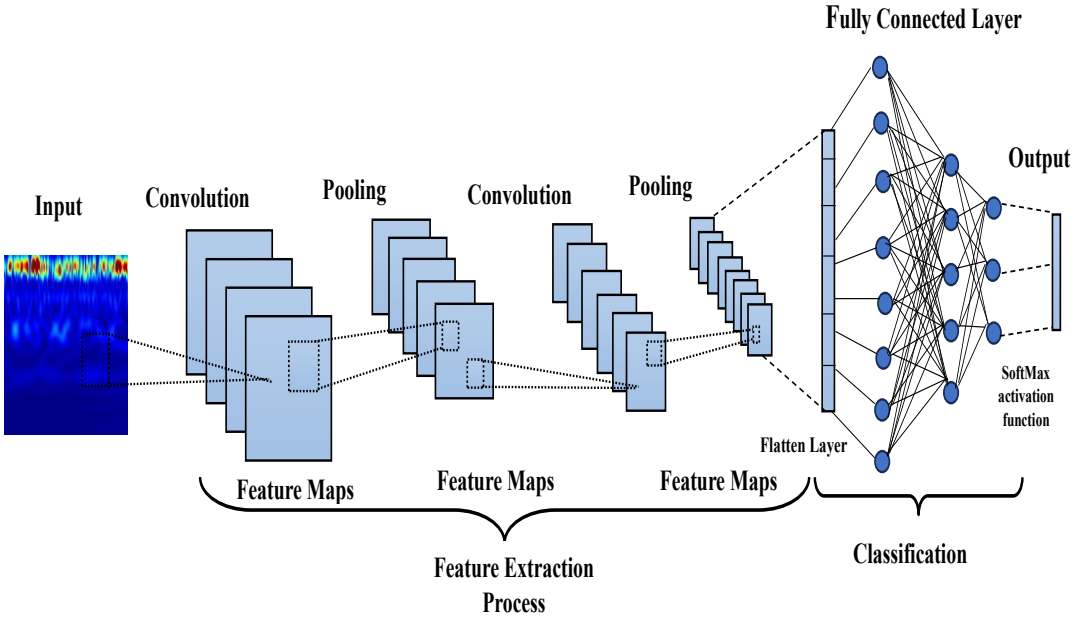

Figure IV.2 Classical CNNs architecture.

The convolutional layer is a fundamental component of CNNs utilized to learn and extract different local features from an input image by the convolution operation using a set of filters or kernels. A convolution layer includes several convolution kernels with learnable parameters [231]. Each filter is a small matrix containing learnable weights. Throughout the training stage, these weights are determined and adjusted within the convolutional layer to enhance network functionality [232]. The intermediate outputs of the convolutional layers are called "feature

maps", which become the inputs for the succeeding layers of the CNNs structure. The output feature map can be expressed as (IV.1)[177]:

$$x_j^l = f(\sum_{i \in M_j} x_i^{l-1} * w_{ij}^l + b_j^l) \quad \text{(IV.1)}$$

In the convolutional layer l, x_j^l indicates the jth output feature map, w_{ij} and $b_j$represent the shared value of the ith kernel weight and bias, respectively. f is the activation function in the network.

In recent years, a number of effective technologies, notably activation function, Dropout, batch normalization, and DistrubLabel, have been developed to accelerate CNN convergence and avoid overfitting. An activation function is a mathematical function embedded in the convolution layer that works on the neurons of a neural network, mapping the inputs of the neurons to their outputs [233]. Many typical activation functions are used after each convolution operation such as sigmoid, tanh, and rectified linear unit (ReLU) (Figure IV.3). ReLU is a widely used activation function in DL models, as it is simple and capable of solving the vanishing gradient problem. The ReLU introduces non-linearity into the NN by returning the original input value if the input value is positive, and giving a null response if the input value is negative. The ReLU activation function can be stated numerically as follows [234]:

$$ReLU(x) = \begin{cases} x, & x > 0 \\ 0, & x \leq 0 \end{cases} \quad \text{(IV.2)}$$

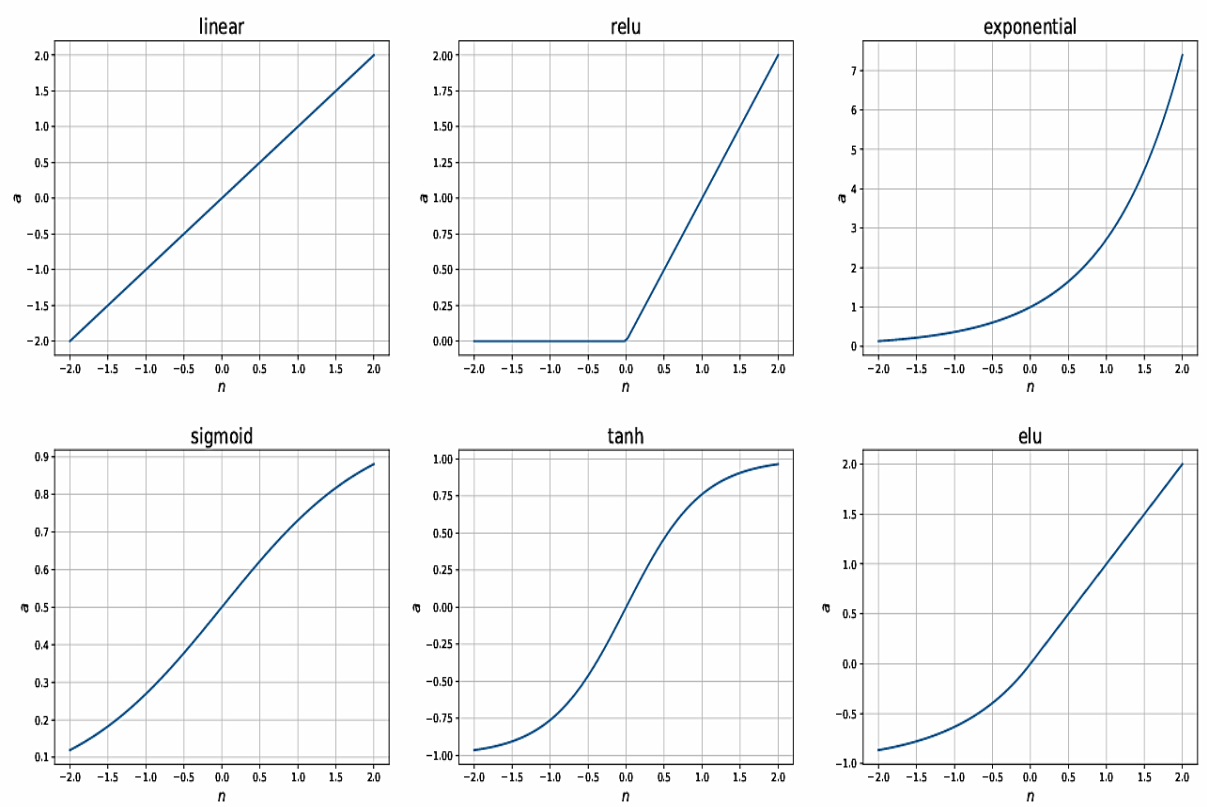

Figure IV.3 Representation of the most prevalent activation function utilized in a neural network

Next is the pooling layer, also known as the downsampling layer, which reinforces the robustness of the extracted features. It shrinks the visual dimensions of the feature pictures resulting from the convolution layer while preserving important information and increasing the speed of the computation process [235]. For subsampling data, various pooling procedures are used, including maximum pooling, average pooling, and random pooling. The most common use of all these procedures is maximum pooling [236].

The fully connected layer, the top layer of the network, is configured after the convolution and pooling layers [237]. The output of the pooling layer is flattened and then transmitted to a fully connected layer, which is responsible for performing the final classification or regression task in the system. The full connection links each neuron with every neuron in the previous layer and then uses the softmax activation function for classification. The output of a fully connected layer can be represented as shown in equation (IV.3) below:

$$y_{features} = \frac{e^{Wx+b}}{\sum e^{Wx+b}} \quad \text{(IV.3)}$$

Where $y_{features}$ is fully connected layer's output, w denotes the matrix of the weight's neuron, b refers to the bias vector, x is the input vector, and f represents the activation function.

IV.2.2 Stacking Ensemble Model

Ensemble methods are an approach of ML algorithms that achieves better predictive performance of any fault diagnosis model. The predictions of multiple learners are merged using a combination of algorithms to produce a more accurate forecast than relying on a single model. In ensemble learning, the process aims to improve the overall system efficiency and to solve many classification problems by combining the predictions of multiple base models constructed using a particular classifier algorithm. There are many varieties of ensemble learning techniques, namely voting ensembles, bagging, boosting, and ensemble stacking [238]. Stacking classifier is one of the most prevalent ensemble techniques for enhancing classification accuracy by combining several distinct classifiers (base classifiers). This model consists of two levels mainly, the base and the meta-classifier [239], for example as shown in Figure IV.4. In the first stage, various base learners are trained using training sets, and each base classifier is utilized to make predictions. The meta-classifier employs the outputs of the sub-models as input and subsequently learns how best to integrate the predictions made by the other base algorithms to get a final classification that is more comprehensive and precise [240]. Notably, a stacking classifier's success mainly relies on selecting a proper diversity of base models and a suitable meta-classifier [241].

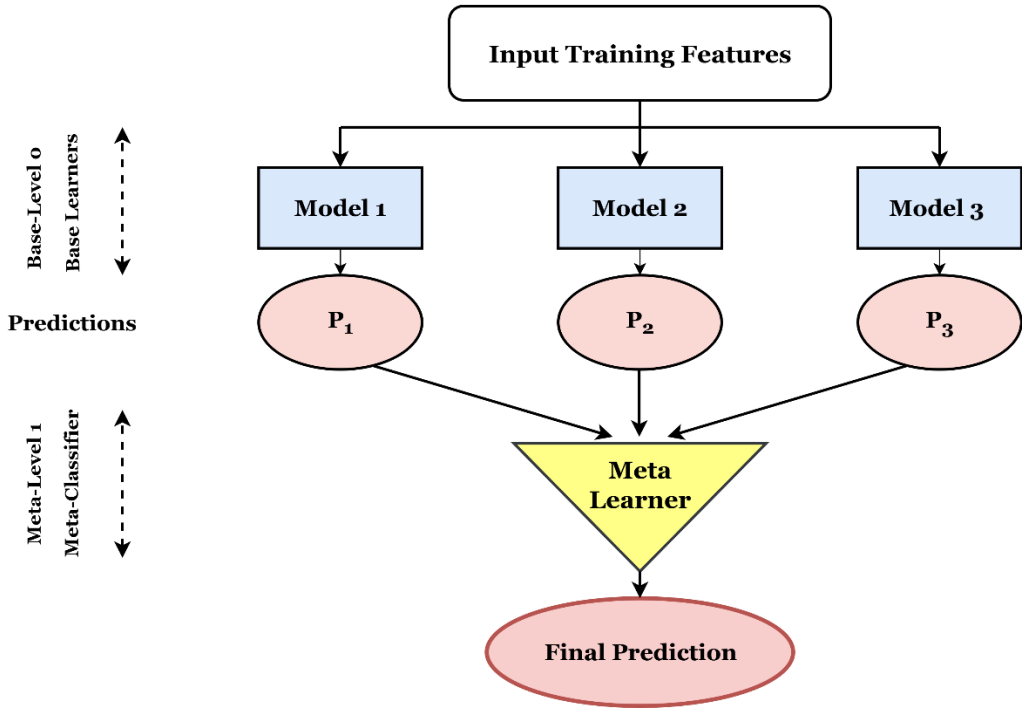

Figure IV.4 Stacking algorithm process.

IV.2.3 Extreme Gradient Boosting (XGBoost)

Extreme Gradient Boosting is a highly effective machine-learning model of gradient-boosting techniques that uses a supervised learning process for classification and regression issues by integrating the outcomes of multiple weak algorithms (decision trees). The XGBoost implementation provides a computational speed that is tenfold greater than that of the random forest approach [242]. This algorithm comprises a collection of decision trees. The XGBoost model was built using a sequential procedure, wherein a new tree is added and adjusted at each step to update the residuals of the preceding trees. The XGBoost employs a second-order Taylor expansion strategy on the objective function to identify the ideal solution for balancing the reduction of the loss function with a regularization term that decreases the risk of overfitting, compared with the classic gradient boosting decision tree (GBDT) only uses first-order derivative details in optimization [243]. The primary process of XGBoost is illustrated below (Figure IV.5).

The output $\hat{y}_i$ of an XGBoost model with K decision trees is described as follows:

$$\hat{y}_i = \sum_{k=1}^{K} f_k(x_i) \quad , \quad f_k \in F \tag{IV.4}$$

The loss function in the XGBoost can be represented as

$$Obj = \sum_{i=1}^{n} L(y_i, \hat{y}_i) + \sum_{k=1}^{K} \Omega(f_k) \quad \text{(IV.5)}$$

$\Omega(f_k)$ defines the regulation term, and it is written in the form of:

$$\Omega(f_k) = \gamma T + \frac{1}{2}\lambda \|\omega\|^2 \quad \text{(IV.6)}$$

Where γ denotes the complexity factor, T is the number of leaves, λ represents a penalty parameter, and ω indicates the output of leaf nodes.

The following equation depicts the objective function's Second-Taylor expansion [244]:

$$Obj^{(t)} = \sum_{i=1}^{n} [L(y_i, \hat{y}_i^{(t-1)}) + g_i f_t(x_i) + \frac{1}{2} h_i f_t^2(x_i)] + \Omega(f_t) \quad \text{(IV.7)}$$

Where g_i and h_i reflect the first and the second loss function derivatives, respectively.

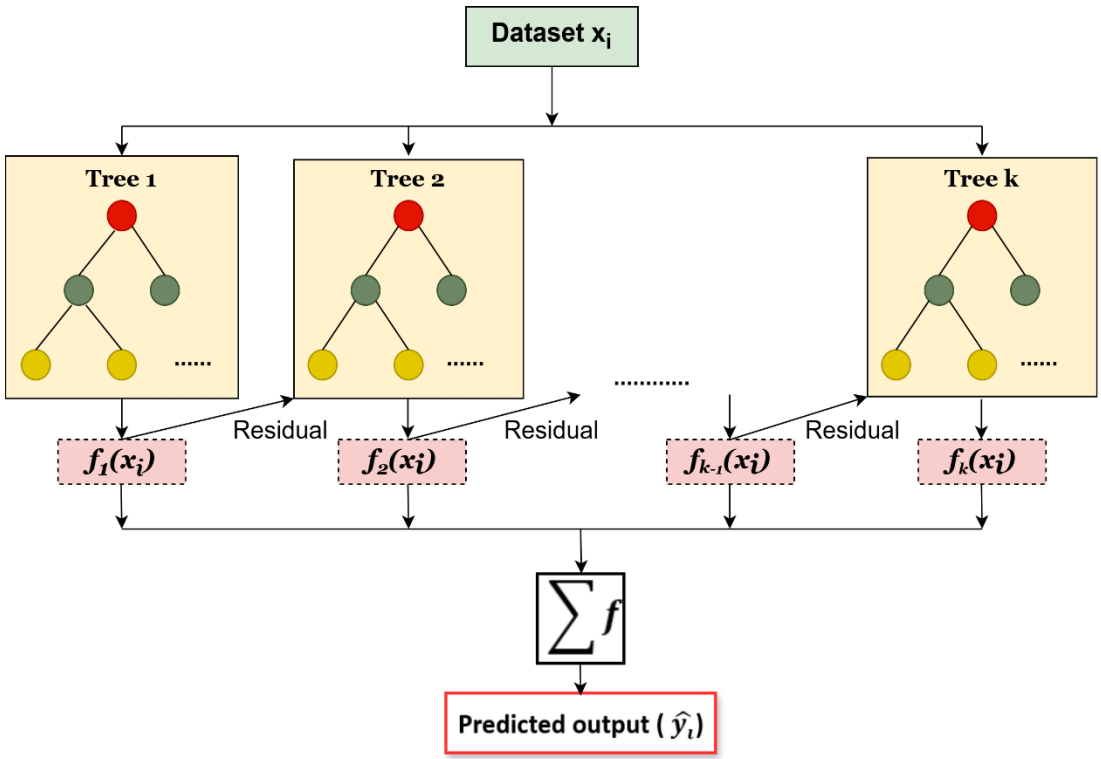

Figure IV.5 Schematic diagram of the XGBoost process.

IV.2.4 Light Gradient Boosting Machine

The Light Gradient Boosting Machine (LightGBM) is an implementation system for gradient improvement based on decision tree approaches, employing a leaf-wise algorithm, as explained in Figure IV.6. It was developed by Microsoft researchers in 2017. One of the critical benefits of LightGBM is its ability to train with incredible speed, more elevated accuracy, and lower memory usage compared to numerous other algorithms. The cause of this effect can be attributed to the exploitation of two innovative techniques in the LightGBM model, namely Gradient-based One-Sided Sampling (GOSS) and Exclusive Feature Bundling (EFB) [245]. The fundamental concept behind LightGBM is employing a leaf-wise split strategy instead of a level-wise split process to construct decision trees in a manner that optimally minimizes the loss function. As a result, the procedure exhibits a preference for selecting the node that yields the most substantial enhancement in the model's performance. In terms of drawbacks, the LightGBM tends to overfit small training datasets, as it is more effective with large datasets. Additionally, overfitting may occur as a consequence of the tree's leaf-wise division, as it generates more intricate trees. The reference [246] provides a mathematically exhaustive outline of the LightGBM algorithm.

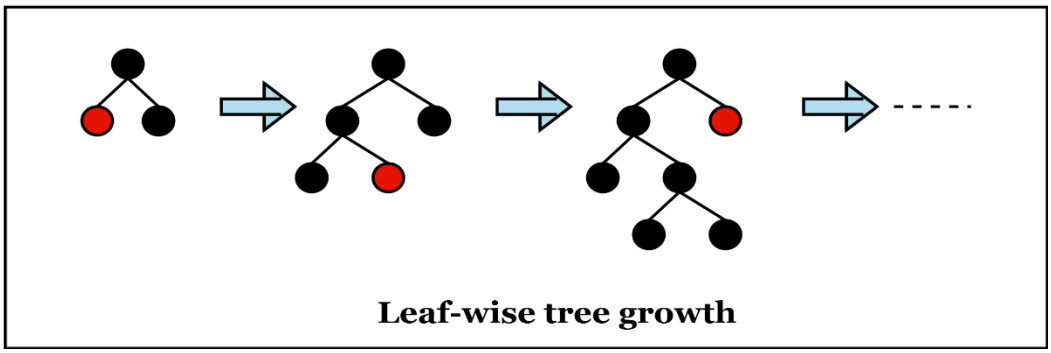

Figure IV.6 Illustration of the leaf-wise split strategy in LightGBM.

IV.2.5 Support Vector Classifier (SVC)

The SVC is a statistical method for supervised learning to evaluate data and identify patterns. It is commonly employed in the fields of classification and regression applications. The basic support vector machine (SVM) classifier is a robust algorithm for a binary classification using a linear separating hyperplane, nevertheless, multiple hyperplanes are required to classify datasets with numerous classes [83]. The hyperplane is generated via an algorithm to minimize the error. Two variants of SVM learners, including C-SVC and V-SVC. The quadratic modeling

framework is widely recognized as the typical approach for implementing SCMs in classification tasks: C-SVC (also called SVC). The essential concept underlying C-SVC is identifying an ideal hyperplane that maximizes a margin between two categories using a regulation parameter 'C'. In our study, there are more than two classes of bearing faults, and the SVC can be improved to manage multiple classes using different methods like 'One-vs-One', and 'One-vs-Rest' [84]. SVC employ a method known as the kernel trick. The kernel trick converts the data into a higher-dimensional space, facilitating the fitting of a linear decision boundary (hyperplane). Various kernel types are employed to execute this transition. The standard SVM kernels, including the polynomial kernel**,** sigmoid kernel, and radial basis function (RBF) kernel. Figure IV.7 demonstrates the principle of SVM classification, showing the optimal decision boundary that maximizes the margin between two classes, as well as the support vectors that lie closest to the boundary.

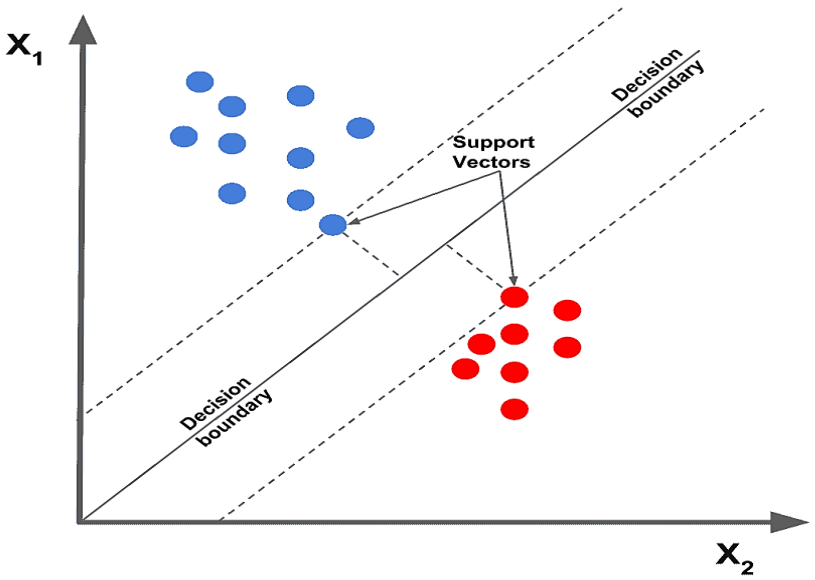

Figure IV.7 SVM binary classification with decision boundaries.

IV.3 An intelligent framework for wind turbine bearing diagnosis and classification based on 2D-Convolutional Neural Networks and Stacking Ensemble Method

IV.3.1 Proposed Method

This work presents a novel DL approach (2DCNN-SC) for wind turbine bearing-fault diagnosis and classification. It combines elements of CNN with a new ensemble model developed using extreme gradient boosting (XGBoost), light gradient boosting machine (LightGBM), and a support vector classifier (SVC)-based stacking ensemble classifier, and is evaluated on two vibration datasets: the CWRU dataset for singular bearing faults and the Aventa WT SCADA dataset for mixed defects. The research approach implemented in the present study is shown in Figure IV.8. The hybrid 2DCNN-SC Framework includes three modules, the module where the scalogram images are generated, a feature extraction module, and a bearing fault classification module. The bearing component is evaluated under two conditions: in a healthy state and in a defective state. The hybrid model takes advantage of the automatic feature ability of CNN and the high distinction performance of the stacking ensemble model. Initially, the primary bearing vibration 1D signals are transformed into RGB images using the CWT. This is not only to improve diagnostic performance but also to drive interpretable characteristics of each baring health state within the ML framework. Subsequently, a 2DCNN-SC model is constructed to process these 2D scalogram maps. Furthermore, upon training the CNN, the resulting feature vectors are fed into the stacking classifier to enhance fault prediction accuracy and generalization capability. To create the stacking ensemble model, we used three classifiers as base learners: XGBoost, LightGBM, and SVC. The prediction results of these three models serve as meta-inputs. SVC, used as the second layer predicting model within the stacking classifier, aggregates the meta-input to derive the final turbine gearbox forecasting outcomes. Notably, the model incorporates k-fold cross-validation to achieve high performance in bearing fault diagnosis. The evaluation results of our proposed model are then compared with those of existing individual algorithms and other methods proposed in previous studies.

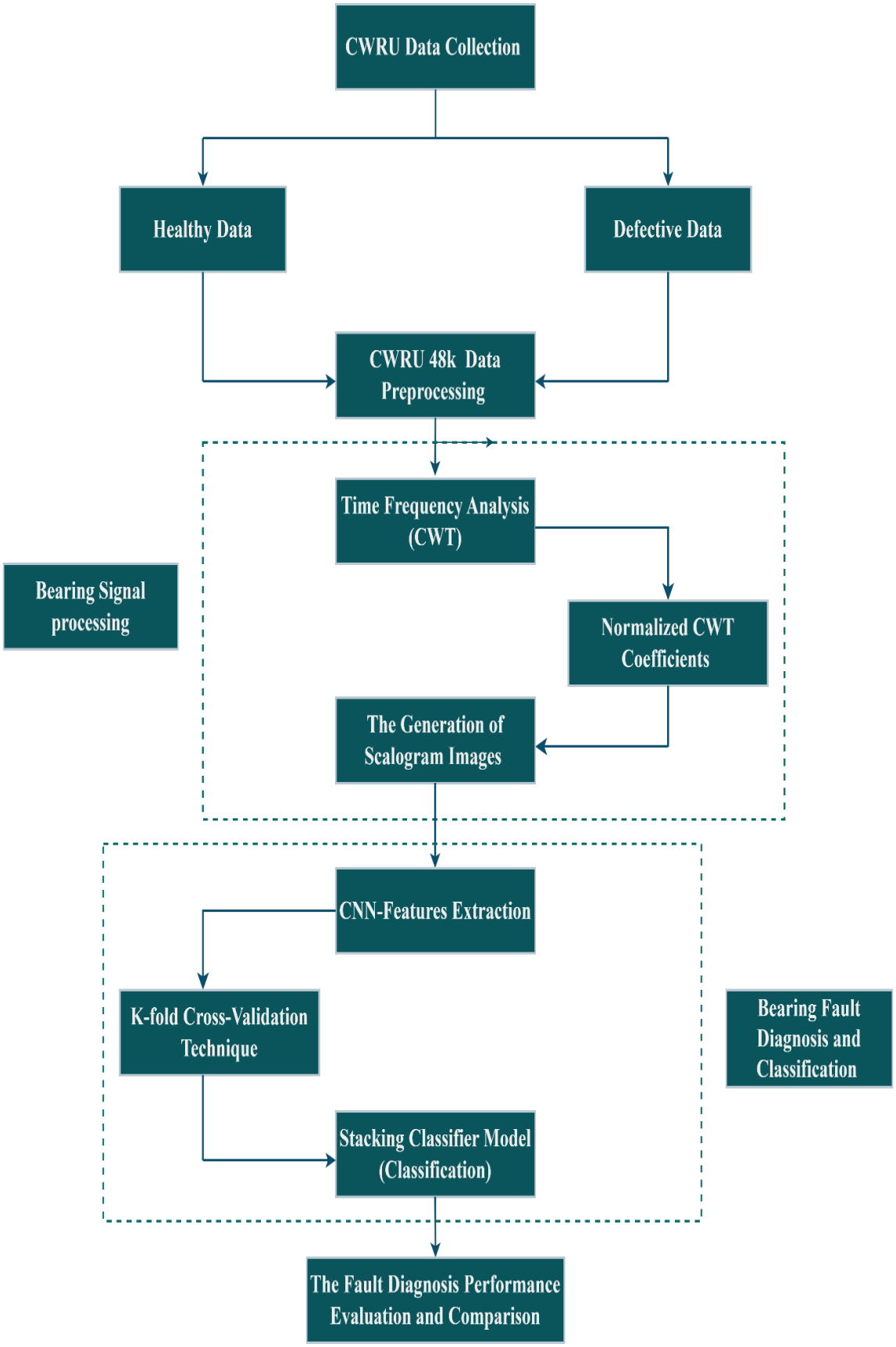

Figure IV.8 Flowchart of the proposed method.

IV.3.2 Experimental validation

A. Case one: CWRU dataset pre-processing

Initially, to validate the suggested fault diagnosis and classification technique, the available dataset from CWRU was used in this study. In this work, our analysis was based on the vibration data of the Drive-end bearing that were recorded at a sampling rate of 48 kHz when the load condition of 1 hp was applied to the motor shaft at a rotation velocity of 1772 rpm. The database includes four different operational states of the bearing: normal state, BF, INF, and OUF (fault in the 6 o'clock position). Every vibration data fault kind has three stages of damage severity with diameters of 0.007, 0.014, and 0.021 inches. For the data pre-processing in this experiment, the vibration data are grouped into 10 categories, including 9 failure conditions and 1 normal condition, depending on defect size and type. We process the dataset in order to identify various bearing faults and classify them. Therefore, the process of down-sampling the raw data is implemented to optimize computational efficiency, reduce the intricacy of the obtained data, and increase the overall performance of the model.

Down-sampling the 48 kHz vibration signals in the preprocessing step reduces data dimensionality while keeping the most appropriate features for analysis. This allows for faster training and inference without extremely compromising model accuracy. Moreover, down-sampling reduces the possibility of overfitting by inhibiting the model from storing overly intricate patterns (noise or redundant information from high-frequency components) that may not apply effectively to new data. Down-sampling maintained a similar classification accuracy level while significantly reducing the training time, as our experiments discovered. These findings suggest that the model effectively depicts the essential characteristics of vibration signals, even after data reduction, making it feasible and successful for real-time fault detection systems. Under every working health state, the raw vibration data is separated into 460 samples and there are a total of 4600 samples with 1024 data points in each sample. To train the model, we employed 80% of them, and the rest of the 20% was utilized as a test set to assess the efficacy of the model. The training dataset is randomly selected. The database's comprehensive information and class labels under several conditions are shown in Table IV.1.

Table IV.1 Comprehensive information and class labels of the CWRU dataset.

Bearing health status	Labels	Size of the fault(mm)	Train set samples	Test set samples	Total samples	Class labels
Ball defect	0	0.18	368	92	460	Bal_007
	1	0.36	368	92	460	Bal_014
	2	0.53	368	92	460	Bal_021
Inner-race defect	3	0.18	368	92	460	INR_007
	4	0.36	368	92	460	INR _014
	5	0.53	368	92	460	INR _021
Normal	6	-	368	92	460	Normal
Outer-race defect	7	0.18	368	92	460	OUR_007
	8	0.36	368	92	460	OUR_014
	9	0.53	368	92	460	OUR_021

IV.3.2.1 Generation of wavelet scalogram images

Basically, the CWT applied to a signal generates a scalogram, which is a mapping of the time-scale and intensity spectrum. A scalogram is the absolute value of wavelet coefficients estimated by the implementation of CWT on a waveform. The measurement of the energy distribution E_{cwt} of a signal as a function of the time shift b and the scale factor a in the form of a two-dimensional image is called a scalogram. The energy is expressed as follows [247]:

$$E_{cwt} = \sum_b \sum_a (X_{cwt}(a,b))^2 \quad \text{(IV.8)}$$

In the early stages of a defect, scalograms are more beneficial than spectrograms when studying real-world signals with characteristics that exist at different scales for diagnosing the problem. The next step, after pre-processing, is to create a time-frequency image for each

sample, this was achieved using the analytical Morlet wavelet in Python. For each segment of bearing vibration data, the wavelet scalogram was generated by utilizing the normalized correlation values of CWT from 0 to 1. We applied CWT with scales ranging from 1 to 64 on bearing signals. In this way, the produced scalograms have 65536 pixels (1024 samples per 64 scales). Then, the images are resized to a 32×32×3 matrix to minimize the amount of computation, which is fed into the proposed model to extract and classify various features. Moreover, every graph is presented by an RGB color map, which consists of three channels with red and blue colors indicating the lowest and highest energy values, respectively.

IV.3.2.2 Experimental process

In this article, all the fault-diagnosis tests were executed on a DELL PC with Intel core i5 CPU, 8 GB memory, and the operating system is Windows 10-64 bits. The software used for developing our proposed model includes Matlab R2018b and Python 3.9, and the algorithm was implemented by applying the prominent deep-learning platform called TensorFlow.

The efficacy of an approach can be substantially impacted by feature engineering, which is an integral part of any machine-learning procedure. In our study, Time-frequency domain features are among the characteristics extracted from raw signal data. The analytic Morlet wavelet, often known as the Gabor wavelet, is the chosen wavelet basis because a problem in a rotating component of a wind turbine such as a bearing, a planetary gearbox, or shafts, can lead to periodic pulses which are always a sign of a fault. With CWT Gabor wavelet, vibration signals are converted into equivalent RGB images, as shown in Figures IV.9, IV.10, IV.11, and IV.12. The intensity and time-frequency information of the signal are represented in these images. The resulting 2-D maps are resized to dimensions of 32×32 pixels and prepared for training our model. We have collected a total of 4600 images for ten different fault classes. According to the train-test ratio of 0.8:0.2, the training phase utilized 80% of the generated scalogram images, corresponding to 3680 pictures. The remaining 20% of the data set, equivalent to 920 images, was allocated for testing.

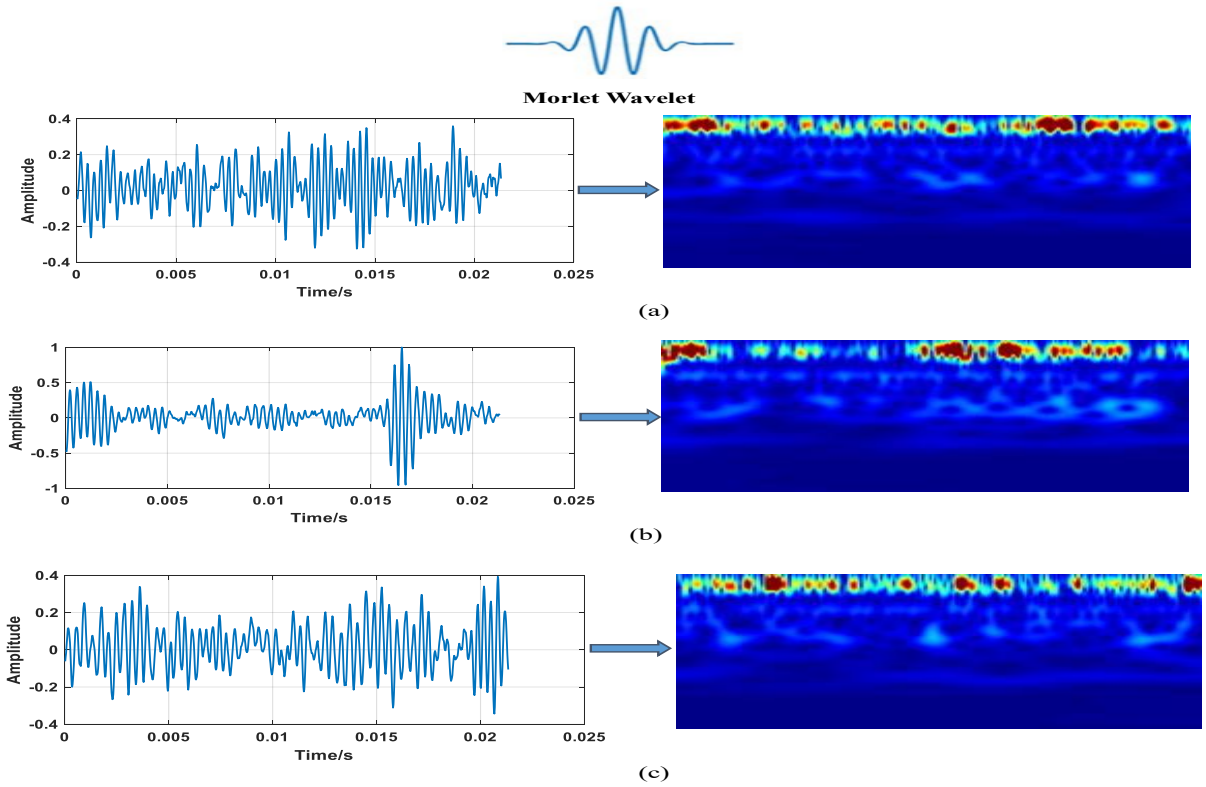

Figure IV.9 Scalogram presentation of ball fault signals with different diameters: (a) 0.007 inches, (b) 0.014 inches, (c) 0.021 inches.

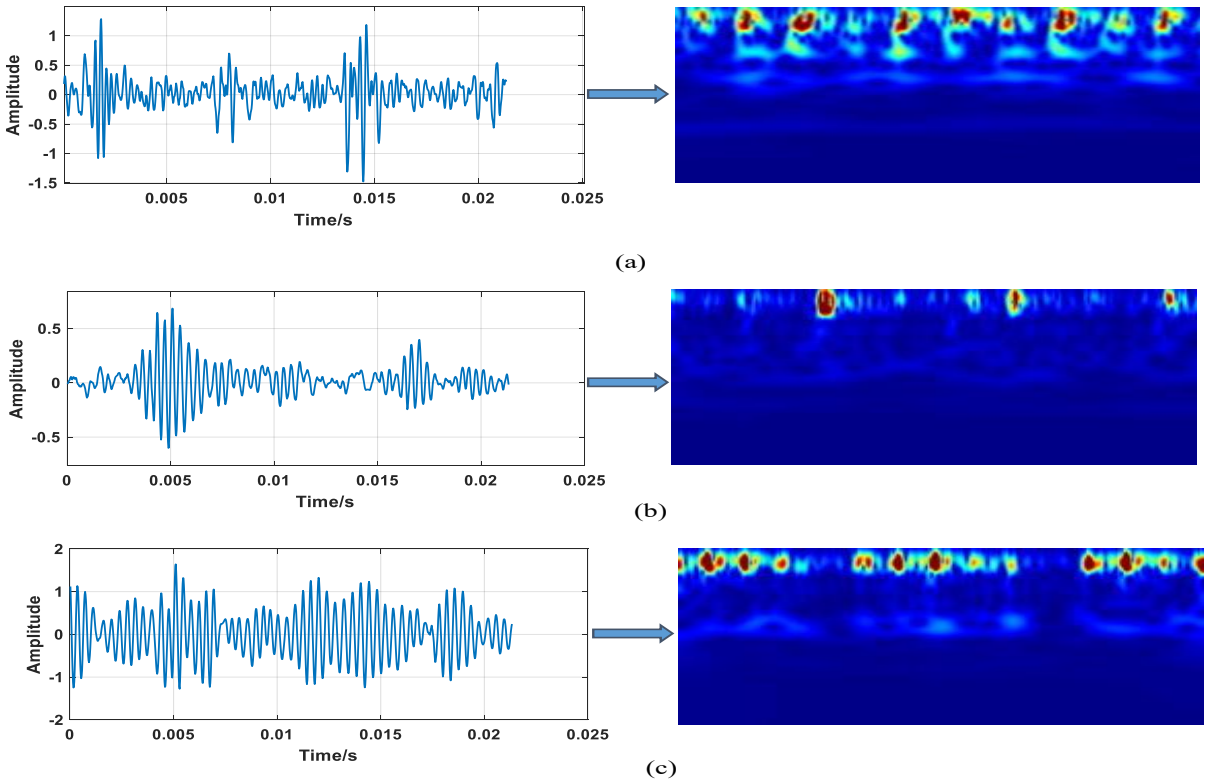

Figure IV.10 Scalogram presentation of inner race fault signals with different diameters: (a) 0.007 inches, (b) 0.014 inches, (c) 0.021 inches.

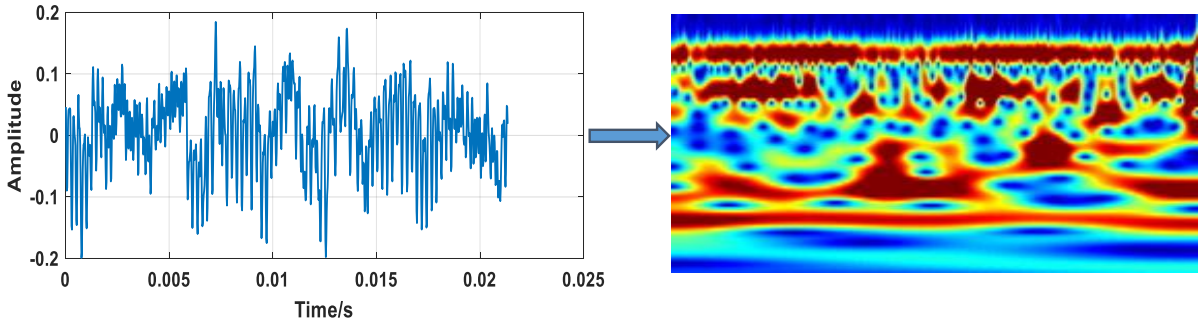

Figure IV.11 Scalogram presentation of the normal signal.

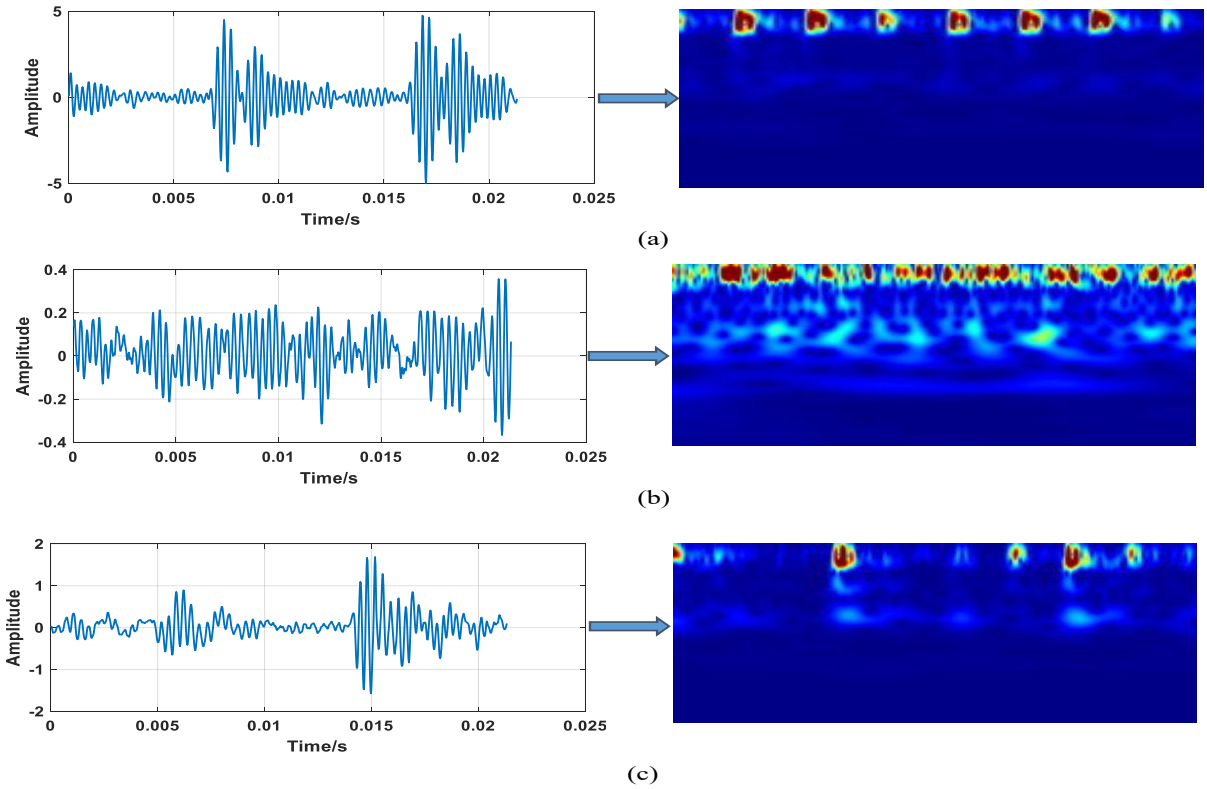

Figure IV.12. Scalogram presentation of outer race fault signals with different diameters: (a) 0.007 inches, (b) 0.014 inches, (c) 0.021 inches.

As shown in Figure IV.13, the developed CNN-stacking classifier model is structured sequentially through its layers, where the CNN model is used for extracting deep features, and the stacking ensemble model is used to improve the final classification. The first sub-network CNN includes an input layer, three 2D convolution layers, three layers of max-pooling, one layer for flattening, and three full connection layers. The CNN blocks use convolution kernel filters with different numbers and sizes to extract the bearing vibration features under various

conditions. Adding max-pooling layers with a window size of two simplifies calculations and reduces map dimensions by performing the down-sampling operation. By flattening, the outcomes of the final pooling layer are merged into only one vector. In this research, the proposed technique uses a 0.2 dropout between each pooling and convolutional layer to reduce overfitting by randomly eliminating neurons.

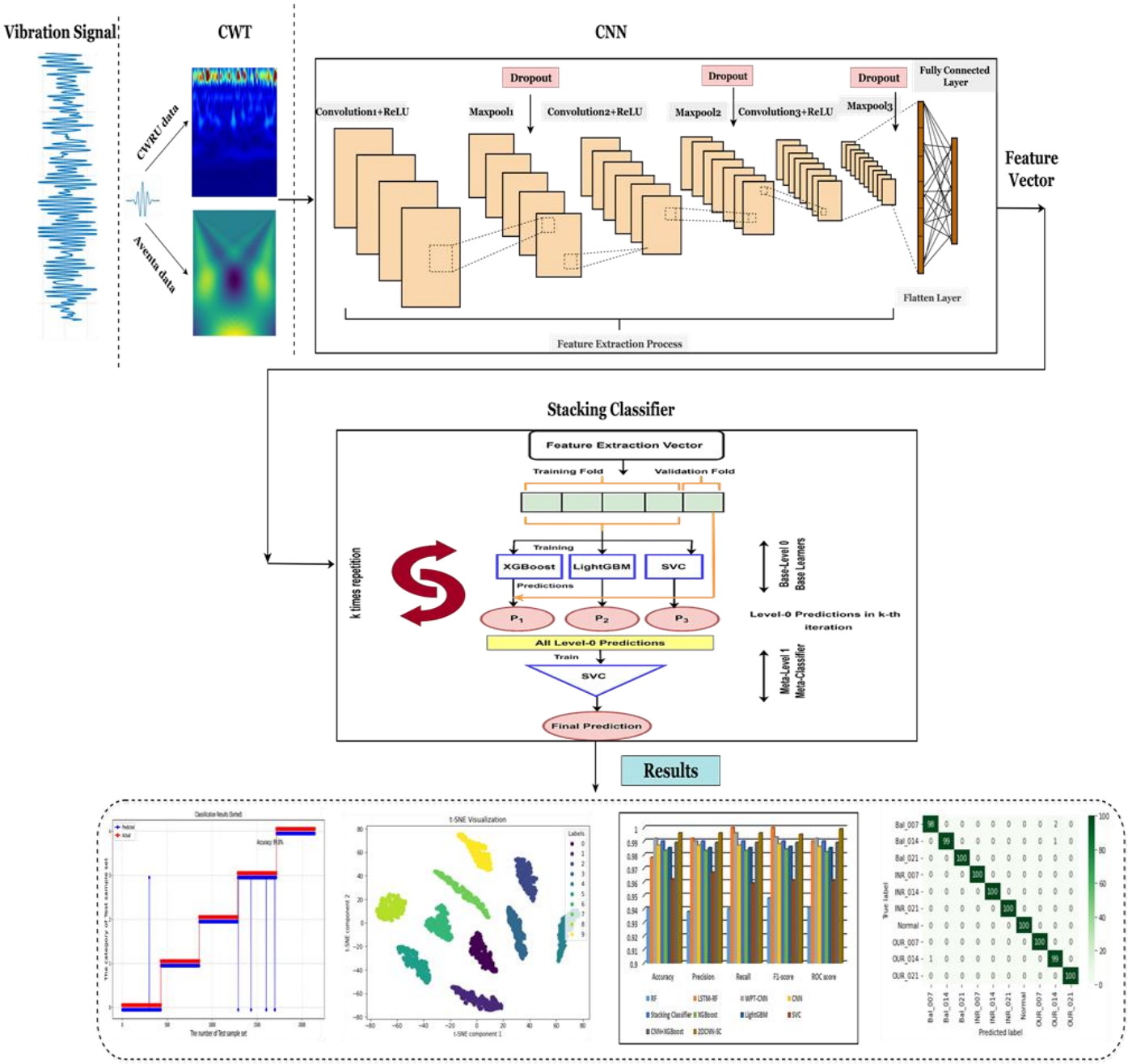

Figure IV.13 The complete structure of the suggested approach.

After learning features for the image data, the output feature vector is extracted from the final fully connected layer and then inputted into the stacking classifier model to derive the ultimate classification results. The Softmax is replaced with a stacking classifier layer trained and tested on the extracted characteristics. XGBoost, LightGBM, and SVC are the level 0 base classifiers using the training input features in this ensemble model. Next, the resulting predictions from the base models are combined and provided as new input data for the meta-model classifier at level 1. By adopting a meta-categorization approach in the final decision stage, it becomes possible to determine class tags accurately.

To optimize the learning process from the delivered data and avoid the overfitting issue, the first-level prediction of the stacking ensemble model operates the k-fold cross-validation strategy during training, as illustrated in Figure IV.14. The input feature vector is randomly split into k-folds of equal length (s_1, s_2, s_3, …, s_k). This procedure comprises k iterations, where k-1 sections are used as a training set to acquire k predicting outcomes and the remaining subset as a test set. We selected XGBoost, LightGBM, and SVC as base machine-learning classifiers and implemented 5-fold cross-validation in our methodology. For the meta-level, the SVC classifier is used as the meta-learner due to its efficacy in managing high-dimensional feature spaces and its robust performance with constrained, well-separated classes. Moreover, SVC's regularization features mitigate overfitting, which is particularly advantageous when integrating outputs from many models. The model's efficiency is evaluated by comparing it with other classifiers that depend on manually designed characteristics. For this purpose, various classifiers have been tested to perform an extensive comparison, including CNN, XGBoost, LightGBM, SVC, CNN-XGBoost and stacking ensemble classifier, in addition to the suggested 2DCNN-stacking classifier model. To wrap up the evolution of our suggested approach, we proposed finding the most successful kernel type for training the meta-classifier SVC by estimating the final forecasting accuracy of three kernel types: Linear kernel, Polynomial kernel, and Radial Basis Function (RBF) kernel.

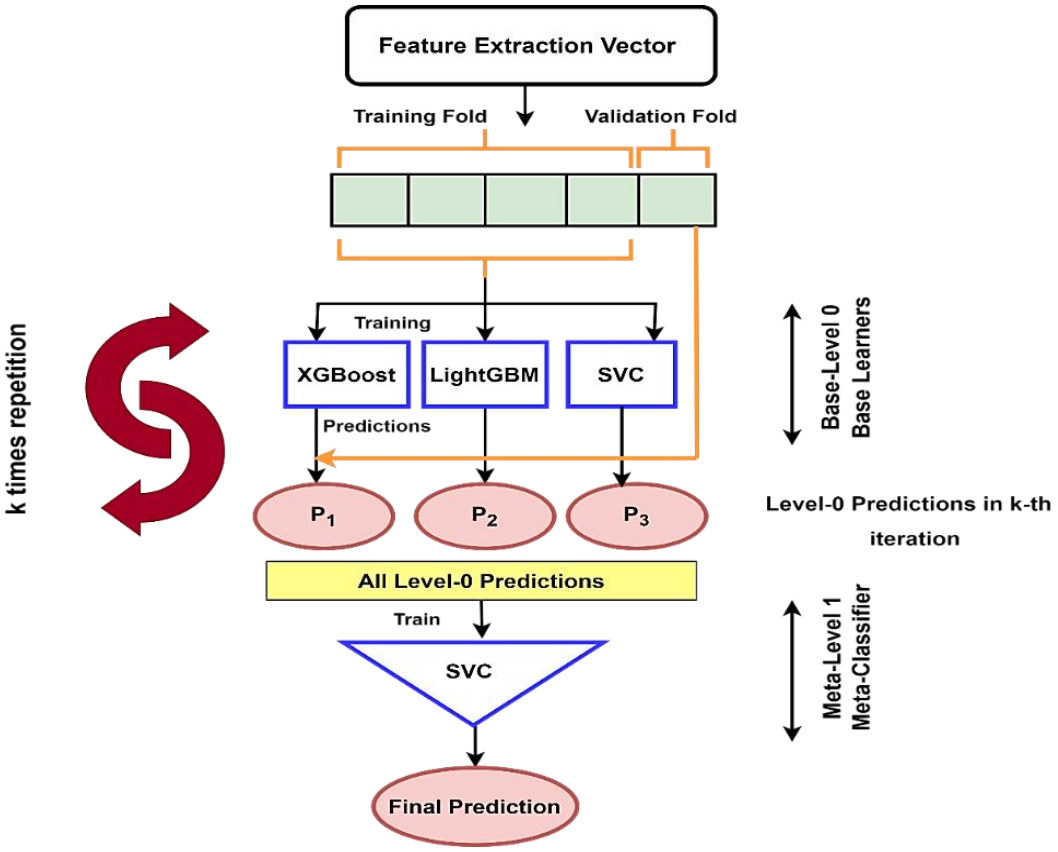

Figure IV.14. Structure of the stacked ensemble classification model.

IV.3.3 2DCNN-SC Model Parameter Selection

Identifying hyperparameters is an essential element in the training process of ML models. The selection of appropriate model parameters greatly influences the precision and generalizability of the model. By enhancing the model's overall forecasting accuracy, suitable parameters can accelerate the development of model variables to their optimum values. In this paper, the optimization of the hyperparameters was conducted using random search, which allowed us to efficiently explore a wide range of hyperparameter values. After multiple experiments, we fine-tuned key hyperparameters for both the CNN and the stacking ensemble, assuring that the selected parameters yielded optimal performance for the model, as detailed in Tables IV.2 and IV.3. On the other hand, the training phase was carried out with several training epochs, reaching a maximum of 45 for the deep CNN model.

Table IV.2 The Proposed CNN Structure Parameters.

Number of Layer	Layer Type	Filter Size	Filter Number	Stride	Padding	Output Size
1	Input Layer	/	/	/	No	32×32
2	2DConv Layer 1	3×3	32	1×1	Yes	32×32×32
3	Maxpool Layer 1	1×2	/	1×2	No	16×16×32
4	Dropout	0.2	/	/	No	16×16×32
5	2DConv Layer 2	5×5	64	1×1	Yes	16×16×64
6	Maxpool Layer 2	1×2	/	1×2	No	8×8×64
7	Dropout	0.2	/	/	No	8×8×64
8	2DConv Layer 3	3×3	128	1×1	Yes	8×8×128
9	Maxpool Layer 3	1×2	/	1×2	No	4×4×128
10	Dropout	0.2	/	/	No	4×4×128
11	Flatten	/	/	/	No	128×1
12	Full-Connected Layer1	/	/	/	No	512×1
13	Full-Connected Layer2	/	/	/	No	256×1
14	Softmax Layer	/	/	/	No	10×1

Table IV.3 Selected Parameters for Different classifiers.

Parameters	Values
XGBoost Parameters	
max_depth	20
learning rate	0.3
n_estimator	500
LightGBM Parameters	
n_estimator	100

max_bin	180
num_iterations	300
num_leaves	45
SVC Parameters	
Kernel	RBF
penalty for error	C=3
Gamma	auto
Probability	true

IV.3.4 Model evaluation process

In machine learning and data science, the distinction of classification model efficiency is contingent upon using performance indicators. Assessing an algorithmic model based solely on its accuracy may require a more comprehensive evaluation. To validate the proposed methodology, we utilized commonly employed performance indices, encompassing accuracy, precision, f1-score, and recall. The confusion matrix provides a direct means of obtaining these metrics, which are defined by the mathematical formulas (IV.9), (IV10), (IV.11) and (IV.12) as follows [248]:

$$Accuracy_{nc} = \frac{(TP_{nc}+TN_{nc})}{TP_{nc}+TN_{nc}+FP_{nc}+FN_{nc}} \quad \text{(IV.9)}$$

$$Precision_{nc} = \frac{TP_{nc}}{(TP_{nc}+FP_{nc})} \quad \text{(IV.10)}$$

$$Recall_{nc} = \frac{TP_{nc}}{(TP_{nc}+FN_{nc})} \quad \text{(IV.11)}$$

$$F1 - Score_{nc} = 2\times(\frac{Precision_{nc}\times Recall_{nc}}{Precision_{nc}+Recall_{nc}}) \quad \text{(IV.12)}$$

Where nc implies the number of categories, TP signifies true positives, FP denotes false positives, TN corresponds to true negatives, and FN represents false negatives. Accuracy serves as the metric to assess proper classifications. Precision is operated to gauge the accuracy of correctly identified predicted samples. Recall evaluates the accurate prediction of positive

labels about the original samples. The F1-score is utilized to comprehensively evaluate overall performance in classification scenarios.

We also evaluated the predictive performance of the classification approach using the Area under the Receiver Operating Characteristic curve plot (AUC-ROC). In this paper, we have applied the micro-averaging and One-vs-Rest techniques for multiclass classification tasks. The AUC score falls between 0 and 1, with higher values indicating superior model performance.

- **t-SNE Data Visualization**

t-SNE (t-Distributed Stochastic Neighbor Embedding) is a popular strategy for visualizing high-dimensional data by reducing its dimensionality and projecting it into a lower-dimensional space [90]. It is possible to iteratively execute t-SNE representation as a component of the model evaluation procedure. By assigning colors to the feature map points of the test data based on their true labels, we can clearly identify structured data as clusters, which correspond to healthy signals and signals exhibiting various types of bearing faults. We compared the t-SNE visualization for different models, and it gives an insight into how well the predictions are made in our suggested model.

IV.3.5 Results and Discussion

Relying solely on the time domain representation of the defect signal poses challenges in determining the precise location and nature of bearing faults, as illustrated in Figure IV.9. The objective of the proposed approach is to determine the operational state of wind turbine bearings using unprocessed machine-controlling datasets. This section presents the results of the suggested diagnosis model applied to the CWRU-bearing database, followed by a comparative analysis. A series of experiments was conducted to further assess performance and validate the efficacy of our method. For the experimental model aimed at verifying the feasibility of our approach, we have selected widely used forecast accuracy evaluation criteria to compare with CNN, XGBoost, LightGBM, SVC, CNN-XGBoost, stacking ensemble classifier, and 2DCNN-stacking classifier model. These criteria include accuracy, precision, recall, F1 score, the confusion matrix, area under the ROC curve, and Cohen's Kappa coefficient. After the signal-to-image transformation based on CWT and the construction of the 2DCNN-stacking classifier model, the training and testing procedures for fault diagnosis were carried out using the processed input wavelet time-frequency map.

In this study, "early diagnosis" refers to the detection of bearing faults at the incipient stage, well before they escalate into severe failures that could lead to significant damage or operational disruptions. Early detection is defined as identifying faults when they are still developing, typically before they reach a critical severity level that could negatively impact system performance. In the context of wind turbine bearings, early diagnosis could be seen as the ability to detect faults after a minimal number of operational hours or when the fault has just started to manifest as a subtle anomaly in the vibration data.

1. Selecting the Best Batch Size for Training a CNN Model

In this part, before delving into the details, we first discuss the outcomes of our study comparing CNN models trained with varying batch sizes. Our goal was to evaluate the impact of batch size on model performance and efficiency in image classification tasks. A comparative analysis was performed on three sets of batch sizes to underscore the significance of these metrics and their influence on model training and algorithmic accuracy. We used sample sizes of 32, 64, and 128 to train the CNN models. It is evident that the accuracy of CNN with a large size of 128 is competitive with that attained by the CNN algorithm using batch sizes of 64 and 32, as depicted in Figure IV.15. The average accuracy of the proposed CNN model with different batch sizes is 97.79%, 98.17%, and 98.7%, respectively, revealing that the CNN model exhibits greater sensitivity to variations in sample sizes. After examining the three sample sizes collectively, distinct diagnostic performance patterns become apparent: CNN model with a batch size of 128 shows superior performance by all metrics, achieving an accuracy of 98.78%, precision (98.7%), recall (98.7%), and F1-score (98.8%). A diagnosis accuracy of 98.17%, precision of 98.3%, recall of 98.2%, and F1-score of 98.1% were obtained with a batch size equal to 64. When the batch size is similar to 32, the CNN demonstrates the lowest efficient results, with an accuracy of 97.79%, precision of 97.9%, recall of 97.8%, and F1-measure of 97.8%. The classification ability of CNN gradually declines as the batch size decreases.

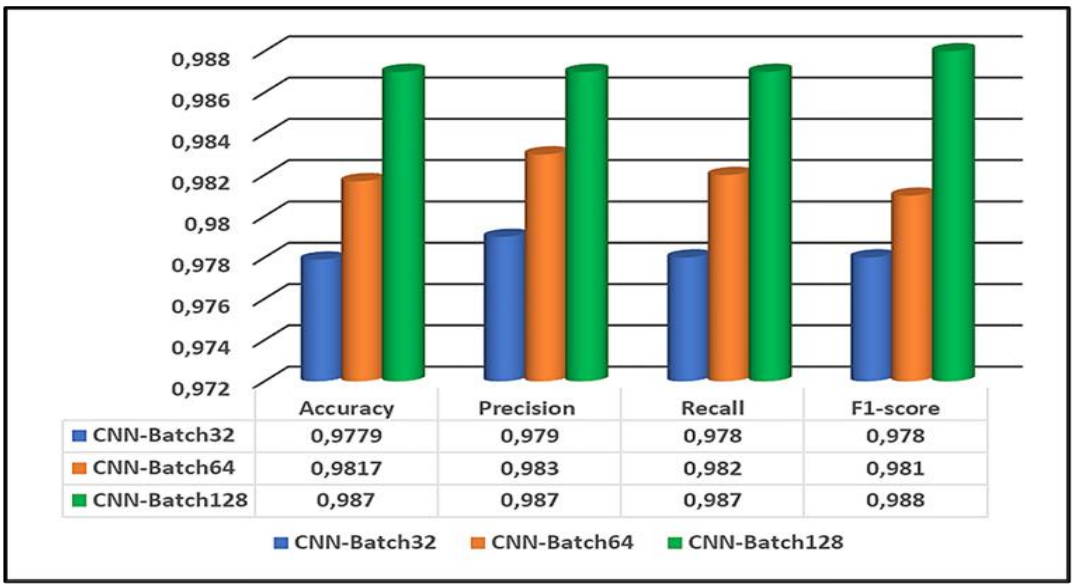

Figure IV.15 Performance evaluation results of the CNN model with different batch sizes ranging from 32 to 128.

Figure IV.16 shows the experimental results graphs of fault diagnostic accuracy and loss values during the training process and test process of the CNN model for different batch sizes. Obviously, it can be seen from the figure that after 45 training epochs, the training and test loss values reduce to 0, and the accuracy rate increases from about 66.29% to 98.7%, which indicates that the designed CNN model with batch size equal to 128 was reasonable. The stability in both the training and assessment phases demonstrates that the proposed CNN algorithm with a sample size of 128 has good learning capability. Furthermore, the highest accuracy is consistently achieved when the training batch size is 128, which improves at a faster rate compared to batch sizes of 64 and 32. In addition, the dropout is used to improve the structure of the CNN, resulting in a substantial reduction in overfitting, as shown by the curves in Figure IV.16. Through analysis, as a result of the reality that the model receives gradients computed from a comprehensive sample of the training data with a large batch size. Each iteration of the training process involves more data samples, which leads to the assessment of the gradient of the loss function in relation to the model parameters becoming more dependable. On the contrary, smaller group sizes, such as 32 or 64, are estimates as a result of their limited sampling size. Employing a sample size of 128 enhances the stability of training dynamics, leading to more consistent progress in convergence and ultimately improved classification accuracy.

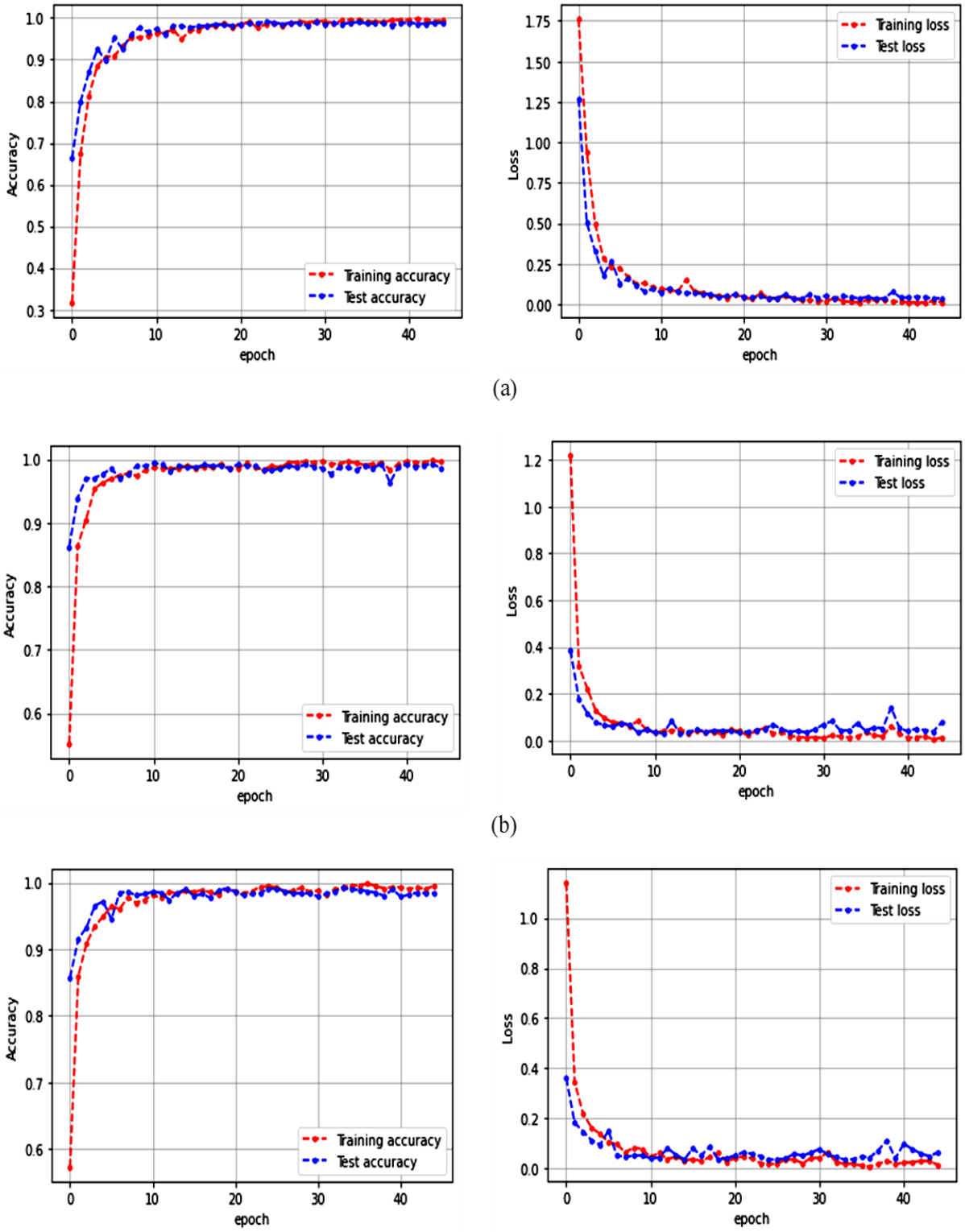

Figure IV.16 Accuracy and loss curves during training and testing of the CNN model with batch sizes of (a) 128, (b) 64, and (c) 32.

2. Comparative Analysis of several Machine-Learning Models

The strength and learning efficacy of the suggested approach should be evaluated under various working conditions. After training the CNN model based on the scalogram images training dataset, the CNN feature extraction outputs with a length of 256 values were fed into the stacking classifier model. In the current case, the model's performance was assessed regarding the accuracy and effectiveness of fault-bearing diagnosis. To gain a deeper understanding of the usefulness of the proposed algorithm and consolidate its superiority and advantages. This analysis involves an experimental comparison of several machine learning models on the above-mentioned database. The fault diagnosis performance of five measures from CNN, stacking classifier, XGBoost, LightGBM, SVC, CNN-XGBoost, and the proposed 2DCNN-SC model has been compared against research models such as Random Forest (RF) [249], LSTM-RF [250], and WPT-CNN [251] in Table IV.4 and Figure IV.17. All mentioned methods are trained on the same training set and tested on the same testing set from the dataset.

As observed in Table IV.4, RF and SVC performed the lowest, likely due to limitations in capturing complex patterns. Hybrid models like CNN+XGBoost, LSTM-RF, and WPT-CNN achieved notably better results; these hybrid approaches were able to leverage the strengths of both techniques. The proposed model 2DCNN-SC achieves the best performance for all evaluation indicators: the accuracy (99.6%), precision (99.6%), recall (99.6%), F1-score (99.5%), and Roc score (99.9%). This suggests that the proposed method demonstrates superior forecasting performance and facilitates the straightforward extraction of sample characteristics, effectively identifying their differences from the other comparison models, as clearly shown in Figure IV.17. As mentioned earlier, the cross-validation technique was employed to impartially consider the sensitivity of the approach.

Table IV.4 Comparing Evaluation Metrics among Various Classifiers.

Model	Accuracy	Precision	Recall	F1-score	ROC score
RF	0.941	0.938	0.94	0.948	0.941
LSTM-RF	0.978	0.992	0.1	0.1	0.99
WPT-CNN	0.992	0.99	0.996	0.993	0.992

CNN	0.987	0.987	0.987	0.988	0.986
Stacking Classifier	0.99	0.99	0.99	0.99	0.99
XGBoost	0.983	0.983	0.983	0.984	0.982
LightGBM	0.985	0.985	0.985	0.986	0.985
SVC	0.962	0.967	0.959	0.961	0.961
CNN+XGBoost	0.989	0.989	0.989	0.989	0.989
2DCNN-SC	**0.996**	**0.996**	**0.996**	**0.995**	**0.999**

The enhanced stacking ensemble classifier was the individual model with the highest diagnosis test accuracy, reaching 99% compared to the other sub-models, and it showed performance improvements of 99% in terms of precision, recall, F1-measure, and ROC score. In contrast, SVC exhibits 96.2% of average accuracy, recall, precision, F1-score, and Roc values were obtained as 95.9%, 96.7%, 96.1%, and 96.1%, respectively, performing the worst in classification and generalization. Three accuracies are above 98%, which come from CNN, LightGBM, and XGBoost individual models. The hybrid model CNN-XGBoost achieves an average accuracy rate of 98.9%, with corresponding precision, recall, F1-measure, and ROC score values also reaching up to 98.9%. According to Figure IV.17 and Table IV.4, the overall test results show that the suggested technique has excellent bearing fault diagnostic ability, and the classification accuracy associated with different working conditions is considerably improved.

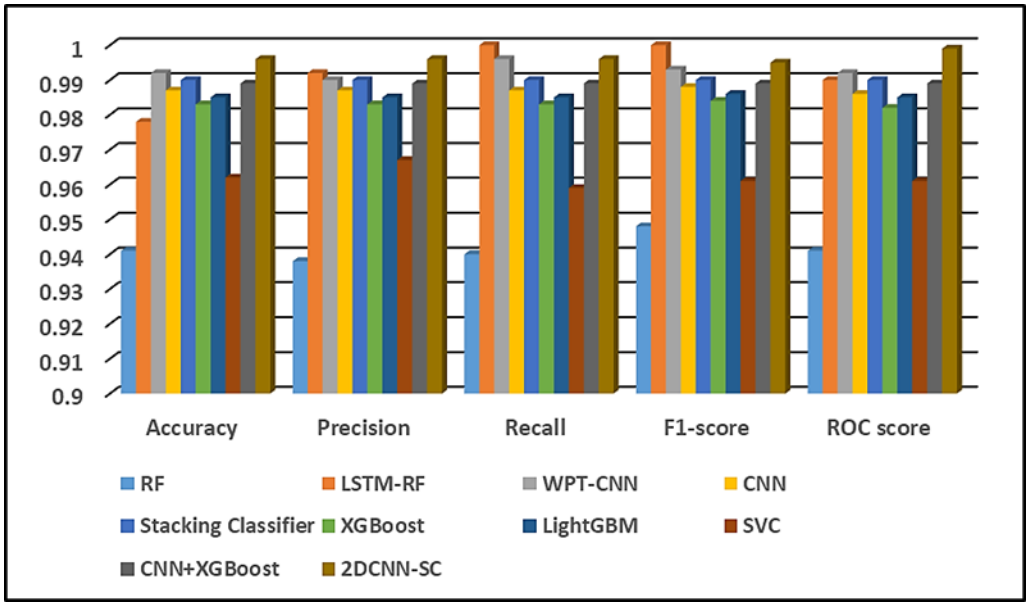

Figure IV.17 Comparison of diagnostic results of the proposed approach with various classifiers.

The confusion matrix is utilized to assess how effectively the model categorizes data into different classes, offering a graphical representation of the ML algorithm's performance in classification and diagnosis. It systematically organizes predicted class labels according to real class labels, where each row represents the type of the bearing defect forecast by the classification model, and each column represents the true type of the bearing defect. Figures IV.18 and IV.19 represent the comparison of the confusion matrix obtained by the CNN, Stacking classifier, XGBoost, LightGBM, SVC, CNN+XGBoost, and 2DCNN-SC models, respectively. Here we can see that all models in the network correctly specify the healthy machine's operating state with 100% accuracy for the normal class in the test set. In Figure IV.19, we found that for CWRU data, the hybrid model of CNN and stacking classifier produces the best detection accuracy for most bearing samples, achieving a correct classification rate of up to 100%. Additionally, it should be noted that the proposed model occasionally erroneously distinguishes between an outer ring defect and ball defects. Minor mistakes are present with "OUR_014", where one case is erroneously classed as "OUR_021", and with "Bal_007", where two instances are incorrectly identified as "OUR_021", present more challenges. The model effectively addresses most misclassification issues found in the rest of the models, demonstrating enhanced feature extraction capabilities. Among the models, the individual CNN model, as shown in Figure IV18, achieves 100% accuracy for fault types like INR_007,

INR_014, INR_021, Normal, OUR_007, and OUR_021, indicating that the model can distinctly recognize these classes. Nonetheless, specific weaknesses exist, where 3 images of 0.021-inch ball fault are misclassified to 0.014-inch outer race fault, and 5 images of 0.014-inch outer race fault are misclassified to 0.007-inch ball fault. The model of the stacking classifier has enhanced performance compared to the CNN Model, with near-optimal classification accuracy for most fault kinds. Certain issues remain, especially with Bal_007, which is intermittently mistaken for OUR_021 (3 instances). The OUR_014 fault type exhibits a slight ambiguity with Bal_007, occurring on three images. The enhanced precision for outer race defect classes indicates that this technique more effectively delineates complex differences across comparable fault types. The XGBoost model reveals a minor decline in performance for the OUR_014 class, with 7 cases incorrectly categorized as OUR_021. The Bal_007 failure type exhibits four misclassifications, indicating that differentiating across identical fault types continues to be challenging. However, the model maintains excellent accuracy across different groups, signifying overall effective generalization. From the confusion matrices, the LightGBM algorithm shows an improvement relative to the XGBoost Model, with four incorrect categorizations in the OUR_014 class, indicating a decrease from 7 in the XGBoost Model. Additionally, The Bal_007 class exhibits three misclassifications, indicating a marginal improvement. These minor errors illustrate the difficulty of distinguishing between specific defect types that may demonstrate overlapping features or related signal parts. On the other hand, in Figure IV.19, the SVC sub-model encountered the most significant difficulties with time-frequency images containing an outer race defect with a depth of 0.014 inches, 29 of which were incorrectly classified as OUR_021 fault type, and 5 instances from Bal_021 where mispredicted as outer race failure classes with a diameter of 0.021 inches. Compared to the SVC Model, the hybrid model of XGBoost-CNN indicates a critical advance, as the number of OUR_014 inaccurate classifications has been reduced to only two instances being predicted as OUR_021. There is a minor issue with the Bal_007 type, as four instances are incorrectly classified as OUR_021, and two instances are incorrectly anticipated as Bal_007 in the Bal_014 fault type. Based on these results, we can confidently state that the proposed model 2DCNN-SC achieves outstanding performance in gearbox-bearing fault detection and classification.

In addition, Figure IV.20 presents a comparative analysis of gearbox bearing fault classification using various machine learning models, evaluated with Cohen's Kappa coefficient, a robust

metric for assessing classifier agreement beyond event. The 2DCNN-SC model achieves the highest Kappa value (0.9956), indicating superior accuracy and consistency with a narrow confidence interval, making it the most reliable model. Ensemble methods, including the Stacking Classifier (0.9889) and CNN+XGBoost (0.9878), are closely followed. The pure CNN model (0.9856) also demonstrates strong performance, slightly lower than the ensemble approaches. Traditional gradient-boosting methods, LightGBM (0.9833) and XGBoost (0.9811), cluster together, reflecting their limitations in addressing complex gearbox-bearing fault patterns compared to hybrid models. SVC exhibits the lowest Kappa value (0.9567) with a wider confidence interval. Color coding distinguishes top performers, ensembles, pure CNN, and baseline models, emphasizing how the proposed hybrid method (2DCNN-SC) enhances classification performance compared to traditional techniques. Even minor differences in Kappa values can have significant real-world implications for precision-driven bearing fault detection systems.

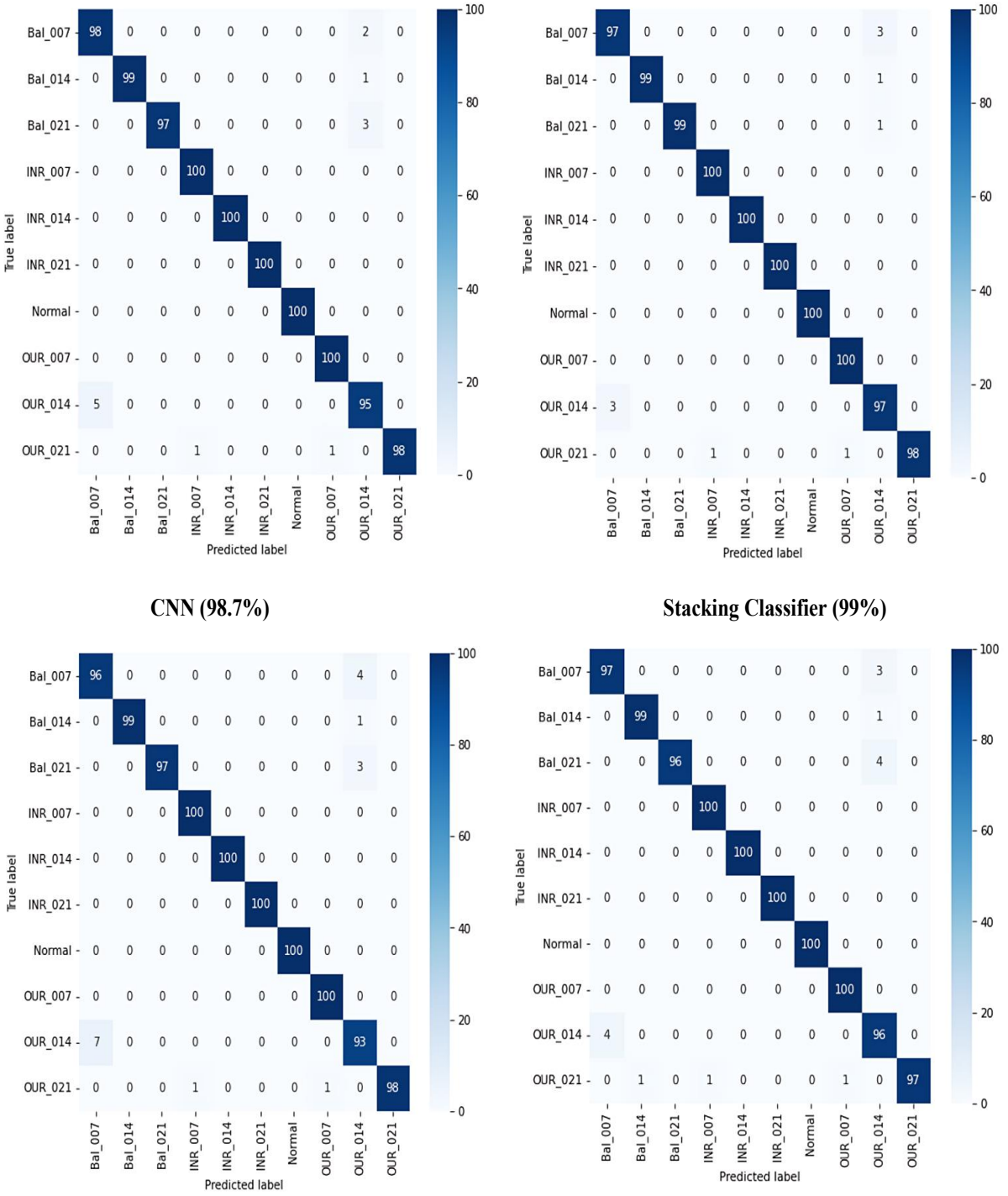

Figure IV.18 Confusion matrices for prediction test outcomes of CNN, Stacking classifier, XGBoost, and LightGBM.

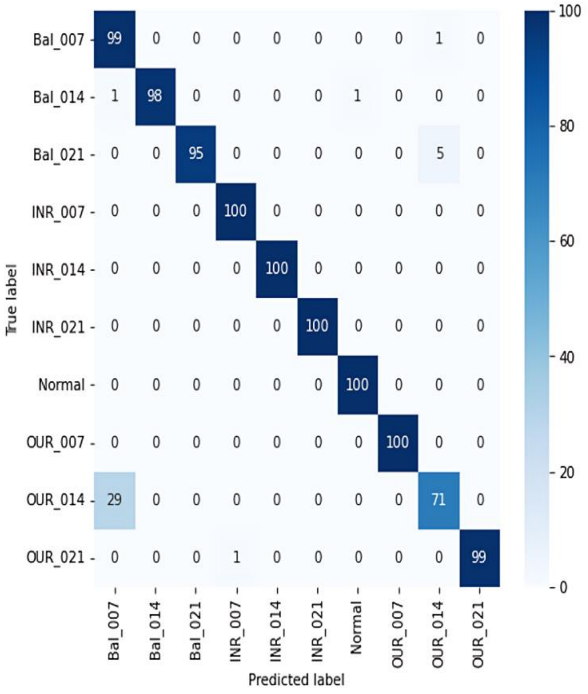

SVC (96.2%)

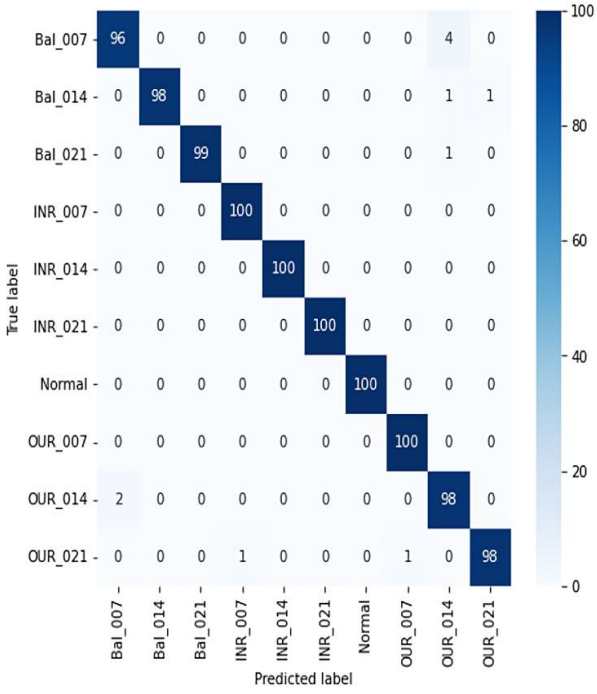

CNN+XGBoost (98.9%)

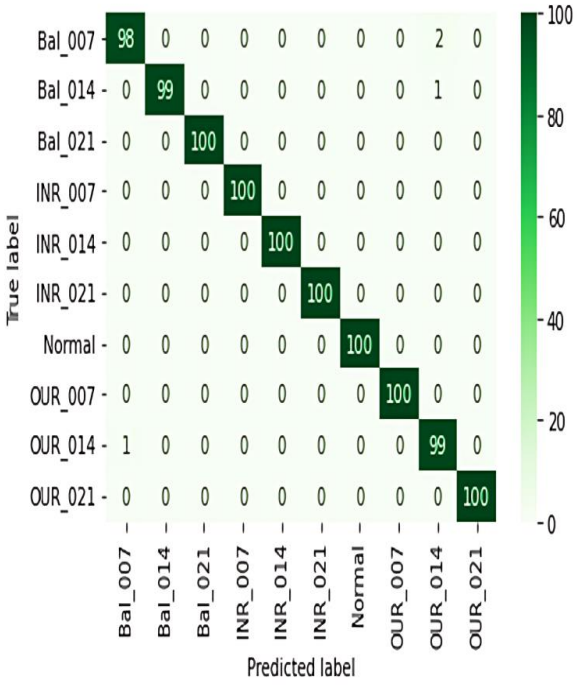

2DCNN-SC (99.6%)

Figure IV.19 Confusion matrices for prediction test outcomes of SVC, CNN+XGBoost, and the proposed 2DCNN-SC model.

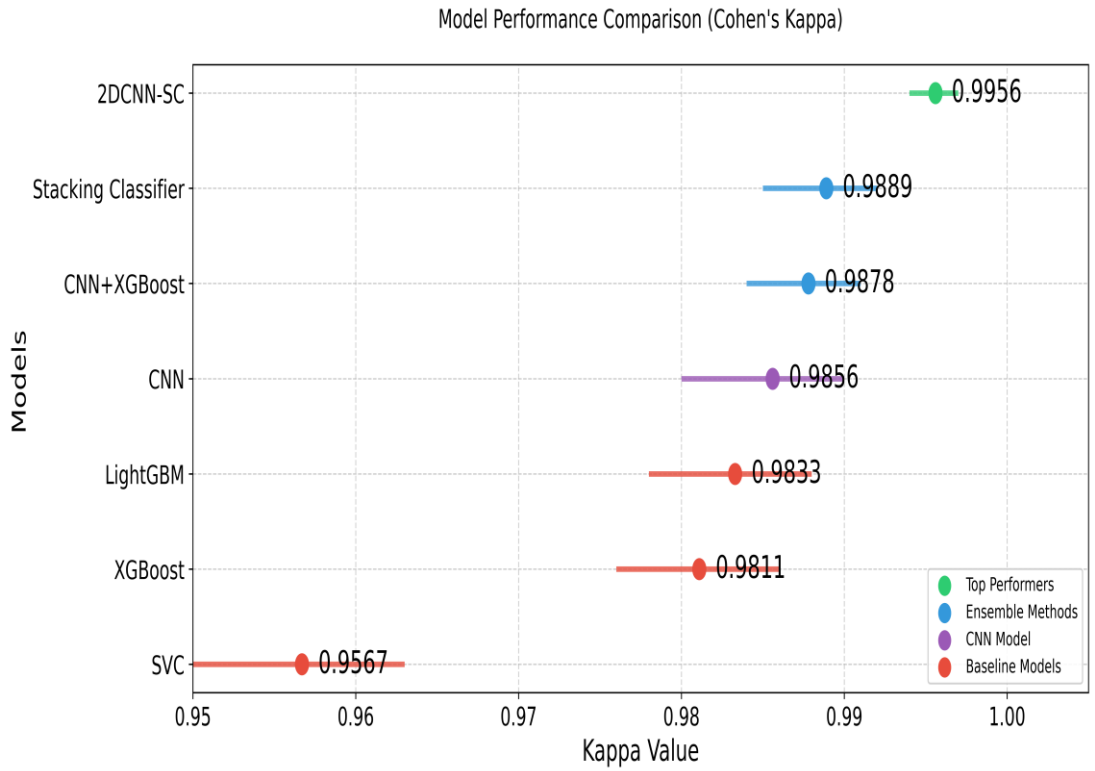

Figure IV.20 Comparison of bearing fault classification models using Cohen's Kappa.

We also analyzed the receiver operating characteristic (ROC) curve and the accuracy graph during the training and test phases to estimate our model, as shown in Figure IV.21. In diagnostic situations, distinguishing between positive and negative classes in the data is crucial. The ROC curve indicates whether the proposed CNN and stacking ensemble model is stable, where a higher level of success is marked by a larger area under the curve. In graph IV.21 (a), the current model attained an average AUC of 1.00 for all categories, which is typically considered a perfect score. To optimize diagnostic accuracy, the test was performed several times. From Figure IV.21 (b), it can be seen that the model reaches an accuracy of 100% at the start of the training session and remains stable throughout subsequent training sessions. In the test phase, the test accuracy of the hybrid model remains constant at 99.6% over several iterations. In general, the suggested method performs well with high accuracy on the test data.

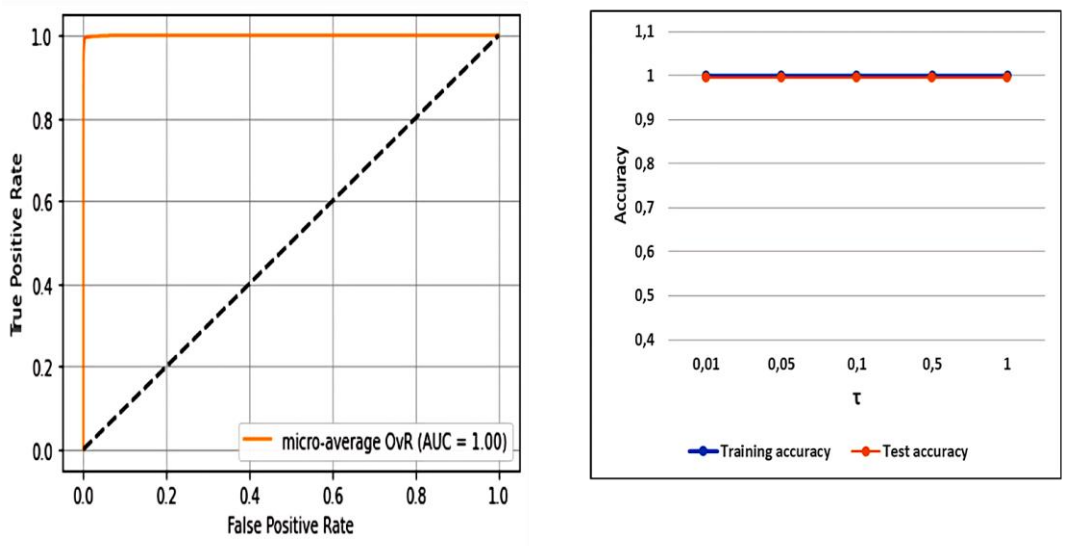

(a) (b)

Figure IV.21 Evaluation results of the proposed method: (a) ROC Curve, (b) training and test accuracy.

3. *Comparative Analysis of different kernel function types for training the meta-classifier SVC*

Having a meta-learner that exhibits robust forecasting performance enhances the overall predictive effectiveness. In this study, to get the best possible performance, it's important to experiment with various kernel functions of the meta-classifier (SVC) and fine-tune the matching parameters. The kernel function, an essential element of SVC, identifies a hyperplane that correctly separates distinct classes by transforming the input data into a higher-dimensional space [252]. This experiment presented to illustrate the influence of the different kernel functions on the performance of the suggested method. Hence, certain kernel functions have been verified for their usefulness in SVC implementation. These include the linear kernel function (Linear), the RBF, the polynomial kernel function (Polynomial), and the sigmoid kernel filter. We have obtained three distinct SVC classifier configurations based on the selection of specific kernel filters, which are SVC-R (i-e SVC with RBF), SVC-P (i-e SVC with polynomial kernel filter), and SVC-L (i-e SVC with linear kernel function). To clarify further, the 2DCNN-SC results achieved earlier employed SVC-R as the meta-learner for generating the final predictions.

Table IV.5 Comparative Results under Different Fault States Using Various Meta-Kernel Functions.

	2DCNN-SC with SVC-R				**2DCNN-SC with SVC-P**				**2DCNN-SC with SVC-L**			
Labels	Accuracy	Precision	Recall	F1-score	Accuracy	Precision	Recall	F1-score	Accuracy	Precision	Recall	F1-score
0	0.98	0.99	0.98	0.98	0.98	0.97	0.98	0.98	0.97	0.96	0.97	0.97
1	0.99	1.00	0.99	0.99	0.99	1.00	0.99	0.99	0.99	1.00	0.99	0.99
2	1.00	1.00	1.00	1.00	1.00	1.00	1.00	1.00	1.00	1.00	1.00	1.00
3	1.00	1.00	1.00	1.00	1.00	1.00	1.00	1.00	1.00	1.00	1.00	1.00
4	1.00	1.00	1.00	1.00	1.00	1.00	1.00	1.00	1.00	1.00	1.00	1.00
5	1.00	1.00	1.00	1.00	1.00	1.00	1.00	1.00	1.00	1.00	1.00	1.00
6	1.00	1.00	1.00	1.00	1.00	1.00	1.00	1.00	1.00	1.00	1.00	1.00
7	1.00	1.00	1.00	1.00	1.00	1.00	1.00	1.00	1.00	0.99	1.00	1.00
8	0.99	0.97	0.99	0.98	0.99	0.97	0.97	0.97	0.96	0.96	0.96	0.96
9	1.00	1.00	1.00	1.00	1.00	1.00	1.00	1.00	0.99	1.00	0.99	0.99
Average	**0.996**	**0.996**	**0.996**	**0.995**	**0.994**	**0.994**	**0.994**	**0.994**	**0.991**	**0.991**	**0.991**	**0.991**

The test results of four evaluation indicators for each condition of bearing fault diagnosis using the proposed model with the three SVC kernel types are displayed in Table IV.5. According to Table IV.5, the highest predictive accuracy rate for bearing fault time-frequency data is acquired with the SVC-R meta-learner, reaching 99.6%, outperforming the rates of other meta-classifier models. The proposed approach with SVC-P has a good diagnostic accuracy value of 99.4%, and the precision score, recall, and F1 score were also 99.4%. Conversely, SVC-L demonstrated the lowest performance within its class, with average accuracy, precision, recall, and F1 measurement values of up to 99.1%. The results indicate clearly that the SVC-R achieved the highest fault diagnosis accuracy because of its flexibility and capability to capture intricate

decision boundaries. On the other hand, the linear kernel makes a minimal contribution to the SVC classifier due to its simplicity and lack of parameters.

In Addition, the classification findings are provided in the form of a confusion matrix, giving a clear representation of diagnostic accuracy, as shown in Figure IV.22. It distinctly displays the outcomes of identifying and the misclassification of all bearing fault states. Obviously, OUR_014 and Bal_007 are misclassified to each other from 2DCNN-SC with SVC-P and 2DCNN-SC with SVC-L models, while 2DCNN-SC with SVC-R model greatly improved the forecasting performance in each type of defect.

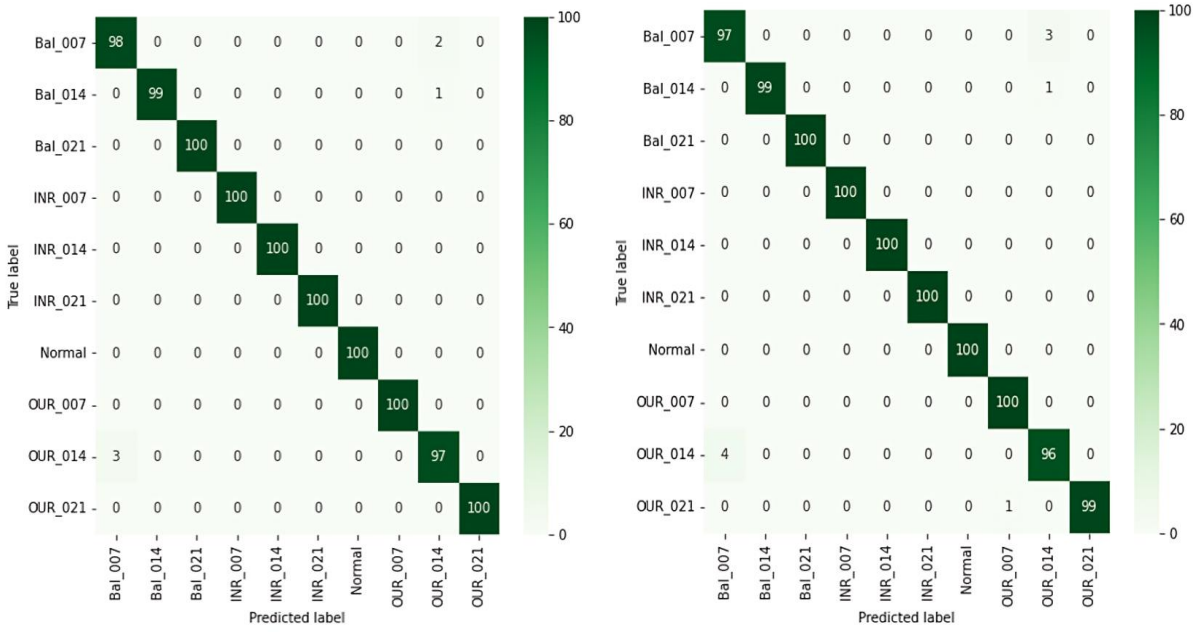

(a) (b)

Figure IV.22 Confusion matrix for 2DCNN-SC model with a) SVC-P and b) SVC-L.

- **Statistical Effectiveness Test**

In machine learning, various statistical tests that go beyond simple accuracy comparisons are essential to comprehensively assess the effect of kernel choice. To compare the performance of the different kernel types of meta-classifier used in this study, we employed the permutation test, which is a statistical significance test. This assessment determines if a notable disparity in precision exists between kernel functions (SVC-R vs SVC-P vs SVC-L) using Accuracy, Precision, Recall, and F1-score metrics obtained from each model on the test set. For each pair

of kernels, we computed the observed disparity in their average scores. Subsequently, we randomized the precision ratings and recalculated the differences across many permutations (the test involved 10,000 permutations). In the end, the ratio of permuted differences (p-value) is calculated, with a p-value of less than 0.05 indicating a statistically significant difference in performance between the kernels. The outcomes of the permutation test are presented in the Table IV.6 below:

Table IV.6 The results of the permutation test.

Metric	SVC-R vs SVC-P	SVC-R vs SVC-L	SVC-P vs SVC-L
Accuracy	1.00	0.2495	0.2493
Precision	1.00	0.2552	0.2447
Recall	1.00	0.241	0.2464
F1-score	1.00	0.2582	0.2463

The permutation test results indicate no statistically significant differences between the three SVC models (SVC-R, SVC-P, and SVC-L) across all evaluation metrics (Accuracy, Precision, Recall, and F1-Score). In the comparisons between SVC-R and SVC-P, all metrics demonstrate total statistical equivalence (p=1.00), signifying that the radial and polynomial kernels yield similar performance outcomes across all assessment variables. The consistently non-significant p-values (0.241-0.258) in the comparisons of SVC-R vs SVC-L and SVC-P over SVC-L indicate considerable yet inconclusive evidence of performance disparities favoring radial and polynomial kernels over the linear variety. While performance indicators exhibit minor discrepancies, these are likely attributable to arbitrary instabilities rather than real disparities in model efficacy.

4. Visualization of Classification Performance Based on Feature Distribution

To evaluate the effectiveness of feature extraction capabilities and gain a more comprehensive understanding of how models achieve bearing fault diagnosis abilities, the t-SNE algorithm is implemented to present the characteristic clustering of various health conditions of the bearings derived from different network models, as shown in Figure IV.23. The plot Figure IV.23 (a) displays the t-SNE representation of the raw data without any model processing. From the

visualization testing results, it can be observed through unclear limits between areas, the original database demonstrates a substantial overlap of features within several categories. The feature distribution of the SVC model reveals clustering characteristics that are clearly separate from those of the initial input data, as shown in Figure IV.23 (b), with the observations of some data classes, such as 0, 2, and 8, which can be differentiated but some fault categories are still overlapped or weakly grouped. This implies that the SVC model has identified specific distinguishing properties; nonetheless, the class separation is still insufficient. Figure IV.23 (c) shows that the captured features become increasingly distinguishable after the last CNN convolution layer, illustrating that the CNN algorithm proficiently identifies distinctive characteristics for fault classification. However, slight overlaps persist among certain fault categories. The t-SNE graph of a stacking classifier (Figure IV.23 (d)) displays clearly defined and compact clusters, enhancing the distinction between classes. Combining various base classifiers via stacking has improved representation learning, yielding distinct boundaries among fault types. Anyway, minor overlaps suggest that specific fault types continue to provide difficulties in classification. Figure IV.23 (e) demonstrates that using a polynomial kernel with the 2DCNN-SC model yields more refined and separate categories with minimal overlap. This confirms the kernel's capacity to map characteristics into a higher-dimensional space, thereby making differentiation more practicable. However, the outcomes depicted in Figure IV.23 (f) indicate that the suggested approach improves the differentiation of inter-class samples among all visualizations and the aggregation of intra-class samples with greater effectiveness, leading to a distinct and identifiable classification boundary characteristic with no overlap. Therefore, the proposed CWT+2DCNN-SC model has a powerful representational learning ability and can achieve high accuracy in bearing fault detection.

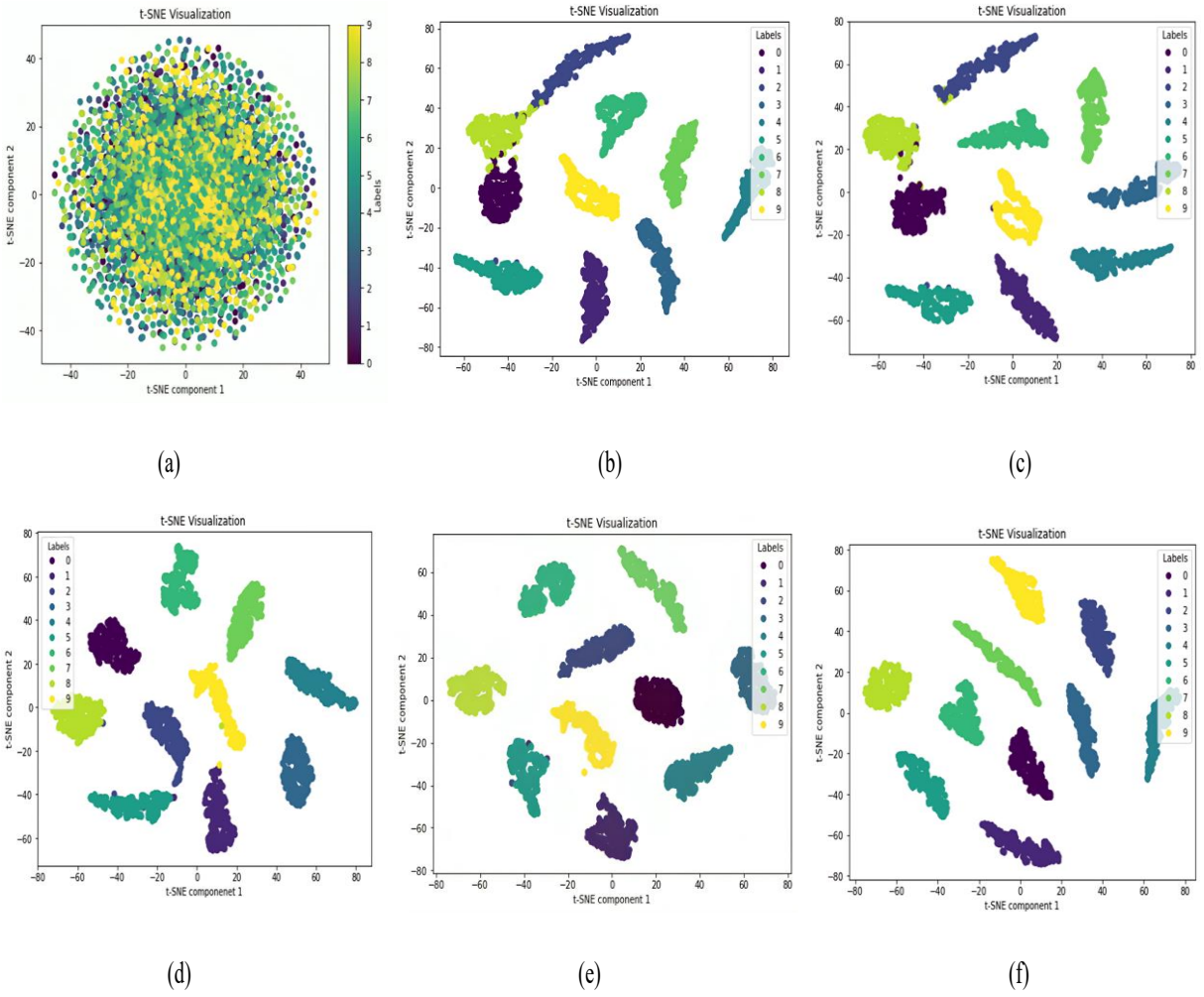

Figure IV.23 t-SNE feature visualization for various models on the CWRU dataset: (a) original data, (b) SVC model, (c) the last CNN convolution layer, (d) stacking classifier, (e) 2DCNN-SC with polynomial kernel, (f) the proposed 2DCNN-SC model.

B. Case two: The Aventa AV-7 Wind Turbine SCADA and SHM Dataset

SCADA (Supervisory Control and Data Acquisition) systems were initially designed for the remote operation of wind turbines, but they have evolved into a robust tool for condition monitoring. The latest wind turbine models gather numerous measurements, standardized to a uniform averaging period, often 10 minutes. Despite the extended average period, SCADA is a potent instrument for monitoring machine status over a broad and continuous timeframe, effectively managing the most critical attributes. The SCADA measurements used in this work were collected in February 2022.

i. Data description and pre-processing

Open datasets obtained from an ETH Zurich measurement campaign on the Aventa AV-7 research wind turbine were supplied by RTDT Laboratories AG [253]. The Aventa AV-7 wind turbine, owned by ETH Zurich and manufactured by Aventa AG in Switzerland, was commissioned in December 2002. This small-scale turbine is equipped with a belt-driven generator connected to a frequency converter, allowing for variable-speed operation. Table IV.7 provides a description of this wind turbine [254].

Table IV.7 Properties of the Aventa wind turbine[254].

Manufacturer	Aventa AG
Commissioned	2002
Location	Taggenberg, Switzerland
Coorindates	47°31'12.2"N 8°40'55.7"E
Rated power	7 kW
Drivetrain	Belt-driven generator, frequency converter, and variable speed drive
Cut-in speed	2 m/s
Cut-out speed	14 m/s
Rotor diameter	12.8 m/s
Number of blades	3
Hub height	18 m
Max. rotational speed	63 rpm
Control system	Variable speed and variable pitch
Tower	Tubular reinforced concrete
Blades	Fibreglass with a tubular and main spar

To monitor its structural and operational performance, the turbine has been extensively instrumented. Eleven accelerometers are mounted along the tower, on the nacelle main frame, the main bearing, and the generator to capture dynamic responses. Two full-bridge strain gauges

are installed on the concrete tower to measure fore-aft and side-to-side strains, which can be converted to bending moments. Both acceleration and strain signals are recorded at a sampling rate of 200 Hz. Environmental conditions such as temperature and humidity are also monitored at the tower base at 1 Hz. Additionally, operational data is collected through the SCADA system at 10 Hz, including wind speed, nacelle yaw orientation, rotor speed (RPM), power output, and turbine status.

The preprocessing of the Aventa AV-7 wind turbine dataset focused on preparing both healthy and faulty condition data for analysis. Healthy-state data were obtained exclusively from the main shaft bearing accelerations recorded on February 6, 2022, during verified regular operation. In contrast, the faulty-state data were collected on February 16, 2022. They included signals from multiple components and axes, namely power output, tower-top accelerations, main shaft bearing accelerations, and nacelle main frame accelerations. Figures IV.24-28 illustrate the signals from wind turbine components under healthy and faulty conditions, respectively. The first preprocessing step involved cleaning the raw data by removing any entries containing NaN (Not a Number) values to ensure the reliability of subsequent analysis. After data cleaning, each continuous signal under both healthy and faulty conditions was segmented into smaller time windows, with each segment representing one minute of data. This segmentation approach allows for consistent analysis and facilitates feature extraction over fixed-length intervals. For the data pre-processing in this experiment, the signals data are grouped into 5 categories, including 4 defect conditions and 1 normal condition. From each condition, 1,429 samples were extracted, resulting in a total of 7,145 samples. For model development, 70% of the samples were randomly selected and used for training, while the remaining 30% were reserved as a test set to evaluate model performance. This approach ensures a balanced and randomized distribution of training and testing data across all classes. Table IV.8 presents the database's extensive detail and class labels across various conditions.

Table IV.8 Class labels of the Aventa AV-7 dataset.

Signals	Channel label	WT health status	Train set samples	Test set samples	Total	Labels
Main bearing acceleration	MSB-ACC-XX-01	Normal	5001	2143	7145	0
Main bearing acceleration	MSB-ACC-ZZ-02	Faulty	5001	2143	7145	1
Power output	WM2	Faulty	5001	2143	7145	2
Tower top acceleration	L5-ACC-YY-01	Faulty	5001	2143	7145	3
Nacelle main frame acceleration	NMF-ACC-YY-01	Faulty	5001	2143	7145	4

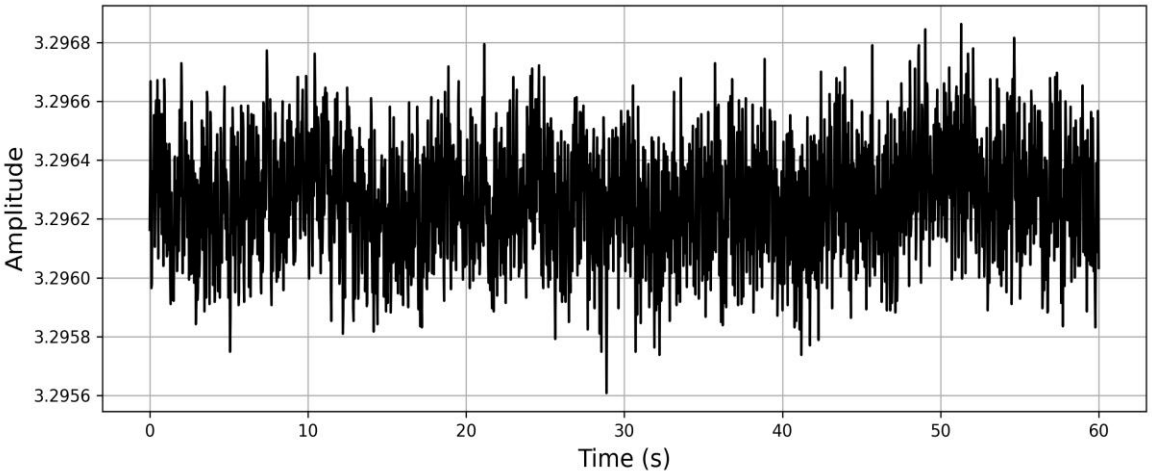

Figure IV.24 Main shaft bearing signal in healthy state.

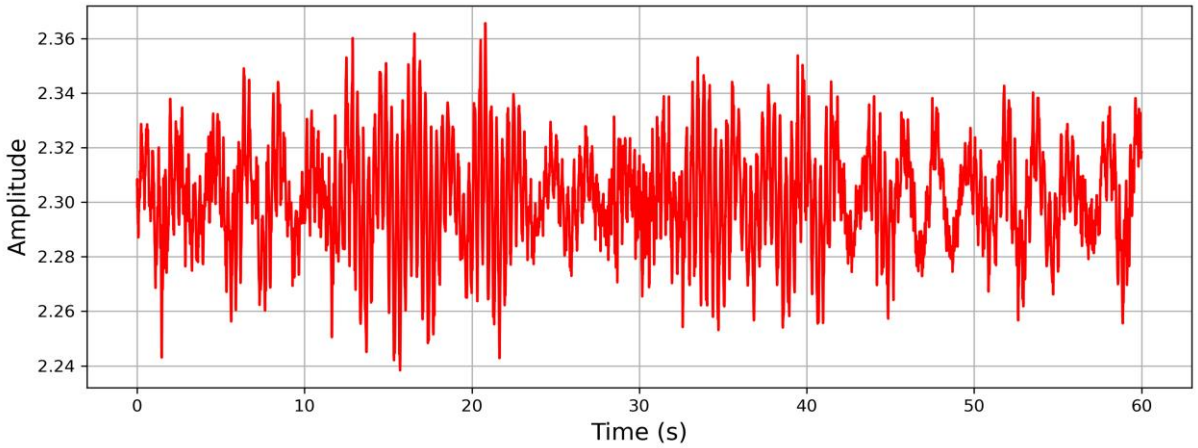

Figure IV.25 Main shaft bearing signal in faulty state.

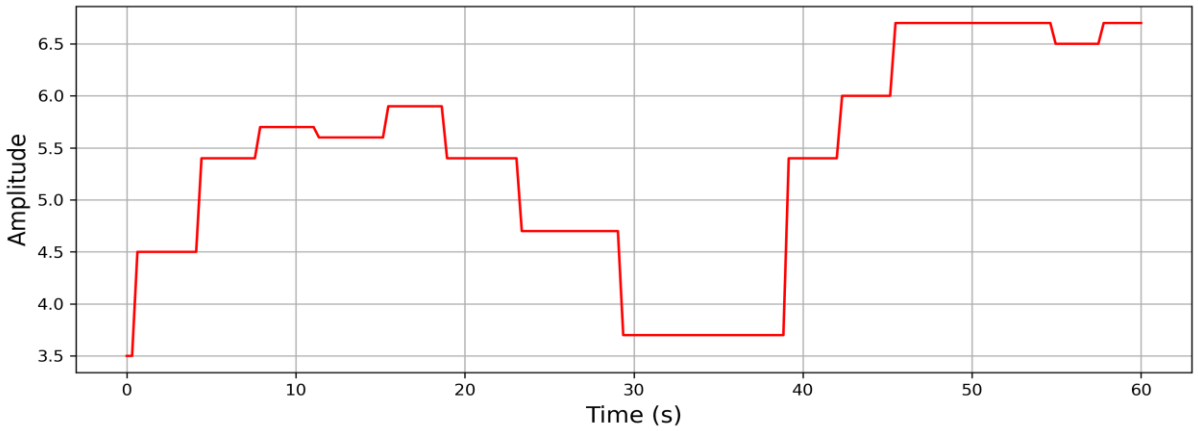

Figure IV.26 Power output for WT in faulty state.

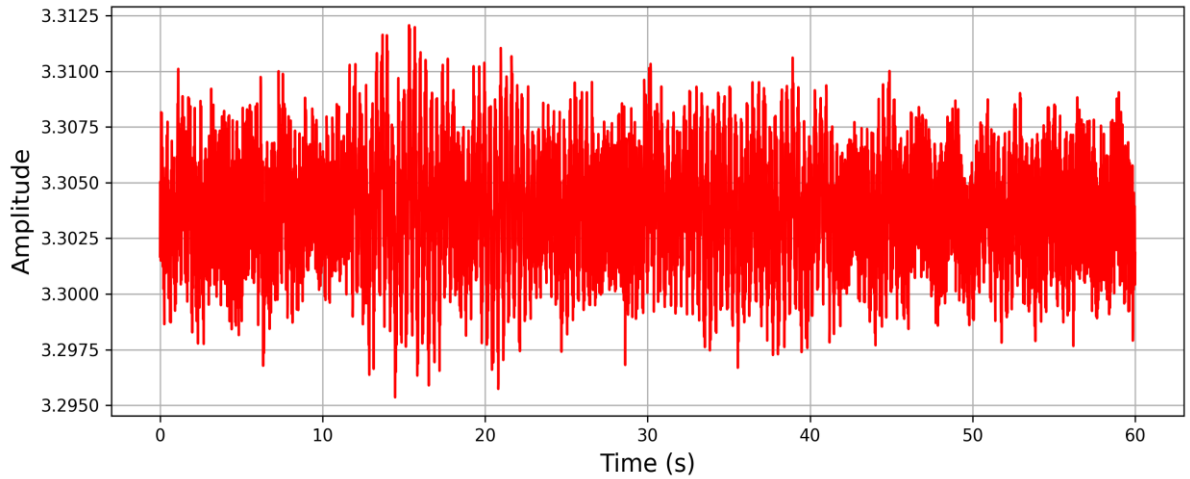

Figure IV.27 Tower top signal in faulty state.

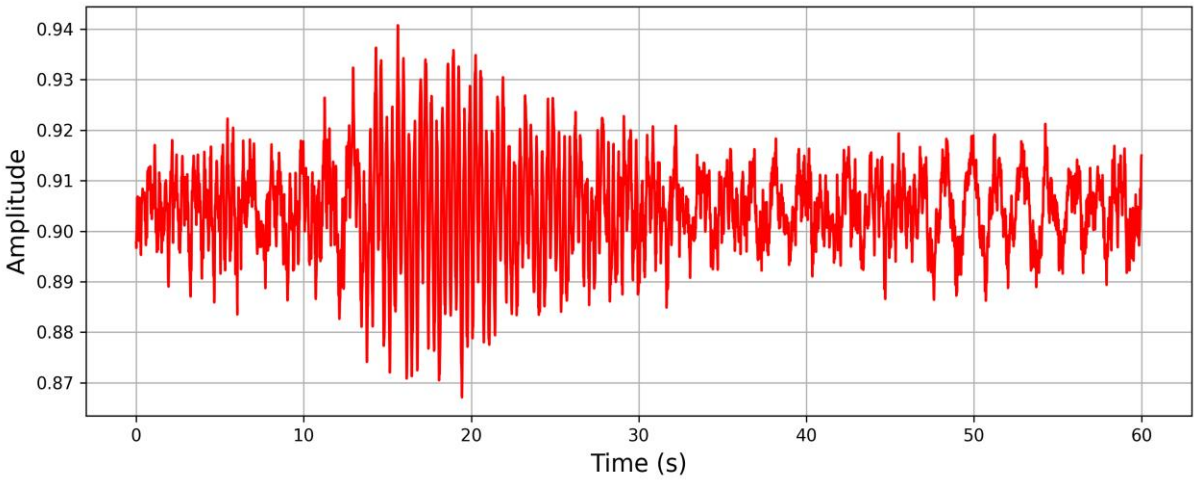

Figure IV.28 Nacelle main frame signal in faulty state.

ii. Results and Discussion

This section presents the results obtained from applying the proposed diagnostic model to the Aventa Wind Turbine SCADA dataset, along with a comparative analysis against other established methods. A series of experiments was conducted to evaluate the model's performance and validate the effectiveness of the proposed approach. To assess its feasibility, standard evaluation metrics were employed, and the results were compared with those of conventional models, including a standalone CNN, a stacking ensemble classifier, and a 2D CNN–stacking hybrid classifier. The evaluation criteria include accuracy, precision, recall, F1 score, confusion matrix, and Cohen's Kappa coefficient. In the proposed stacking model, 10-fold cross-validation was operated to ensure robust performance evaluation and minimize overfitting.

For each signal segment obtained from various wind turbine components, including the main shaft bearing, power output, nacelle main frame, and tower top. CWT was applied to extract rich time-frequency information. Each signal consists of 4096 samples, and the CWT was computed using scale values ranging from 1 to 64. This transformation yields a two-dimensional wavelet scalogram, which represents the distribution of signal energy across time and frequency. The CWT coefficients were normalized to a range of 0 to 1 to generate scalograms, where color intensity corresponds to signal energy. Each resulting scalogram consists of 262144 pixels (4096 × 64 samples per scale), capturing fine-grained information across multiple frequency bands. To reduce computational complexity and ensure compatibility

with the model input, the scalograms were resized to a 64×64×3 RGB format. With CWT Gabor wavelet, the resulting 2-D maps for each condition are shown in Figure IV.29.

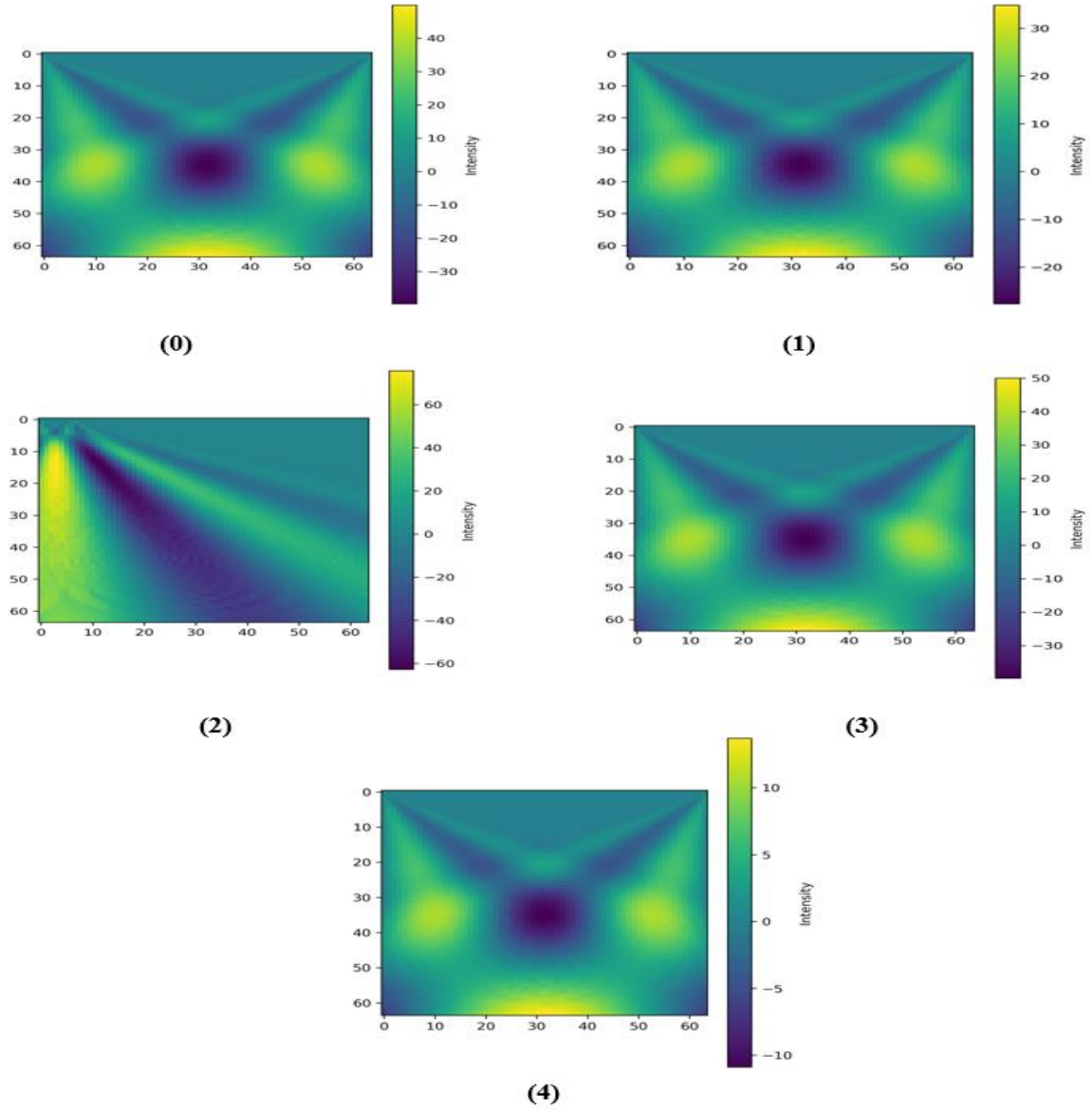

Figure IV.29 Scalogram representations of different condition classes.

To evaluate the usefulness of the proposed CNN architecture in the context of wind turbine fault diagnosis, the model was trained and tested using scalogram images generated from Aventa AV-7 wind turbine vibration signals. Figures IV.30 and IV.31 illustrate the evolution of training and test loss, respectively, and accuracy across 70 epochs. As shown in Figure IV.30, the training loss decreased rapidly and stabilized at a low value, indicating efficient learning. Although the

test loss followed a similar trend, some fluctuations were observed after epoch 10 and notably around epoch 50, suggesting mild sensitivity to specific data samples. Correspondingly, Figure IV.31 demonstrates that both training and test accuracy improved significantly during the early epochs, reaching a consistent level of around 80%. These results indicate that the model generalizes well, with only minor signs of overfitting.

When compared to the CNN model applied to the well-known CWRU bearing dataset, which achieved a classification accuracy of 98.7%, the performance on the wind turbine data is relatively lower. This discrepancy may be attributed to the increased complexity and variability of operational and environmental conditions in real wind turbine systems, as well as the heterogeneous nature of the sensor signals involved (e.g., nacelle, tower-top, and shaft vibrations). Nonetheless, the results validate CNN's potential as a reliable diagnostic tool in wind turbine monitoring, even under more challenging real-world conditions.

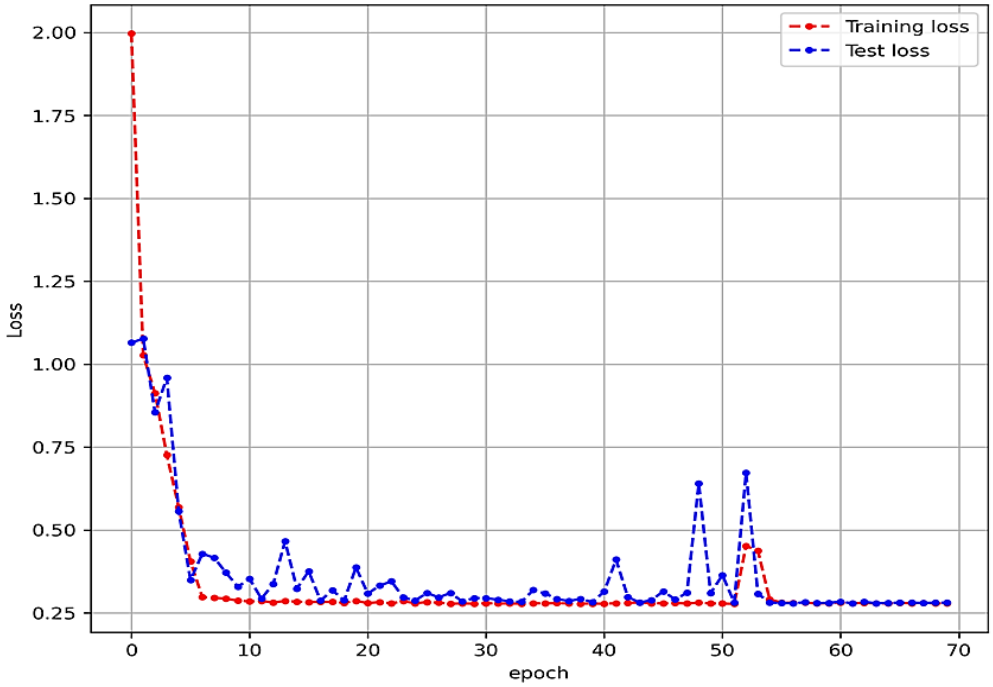

Figure IV.30 training and test loss curves of CNN model over epochs.

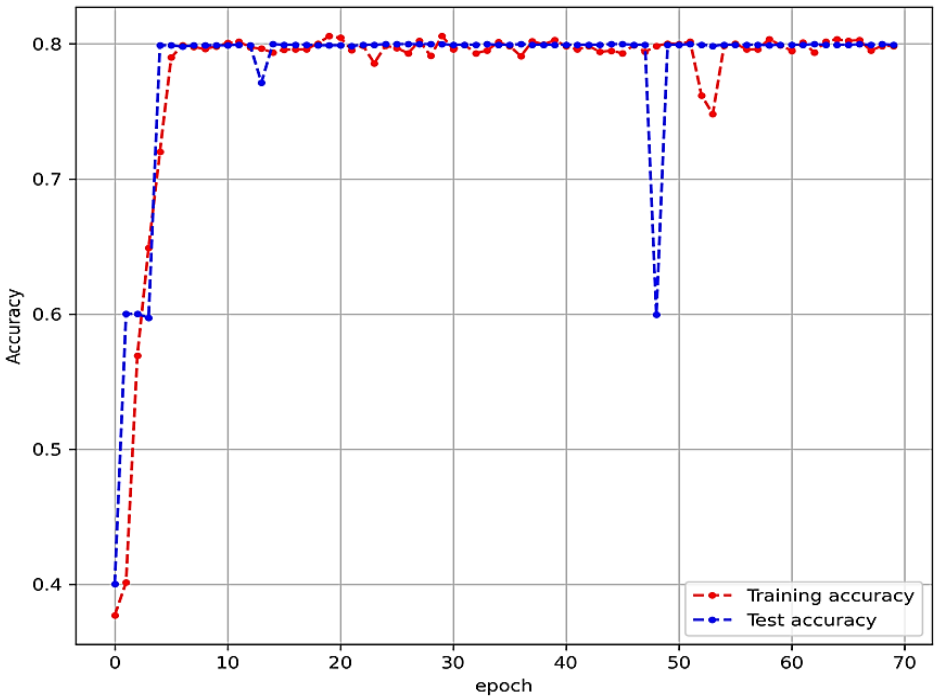

Figure IV.31 training and test accuracy curves of CNN model over epochs.

The classification results presented in Table IV.9 demonstrate a clear performance hierarchy among the three evaluated models: the CNN, the Stacking Classifier, and the proposed 2D CNN–Stacking Classifier (2DCNN-SC). The CNN model shows a significant limitation in classifying fault type Label 3, where it fails completely (precision, recall, and F1-score all equal to 0). This failure drastically impacts the model's average performance, resulting in an overall accuracy of 79.9% and a relatively low average F1-score of 73.2%, despite perfect scores in other classes. This inconsistency reveals CNN's sensitivity to class imbalance or complex fault patterns. In contrast, the Stacking Classifier, which integrates multiple base learners, shows a substantial improvement. It correctly identifies all fault classes, including Label 3, with an accuracy of 94.6% and achieves an overall average accuracy of 98.5% and an F1-score of 98.8%. The precision and recall values are consistently high across all labels, indicating a well-generalized model. However, the proposed 2DCNN-SC model outperforms both baselines. It achieves nearly perfect classification results, with an average accuracy of 99.76% and average precision, recall, and F1-scores all exceeding 99.6%. The model's strength lies in its hybrid architecture, which effectively combines the spatial feature extraction capabilities of 2D CNNs with the decision robustness of an ensemble stacking classifier. This hybrid approach allows the model to capture fine-grained differences across fault types and avoid the misclassifications

observed in the CNN model. Notably, the proposed method correctly classifies Label 3, which was problematic for CNN, demonstrating its superiority in handling subtle or complex fault patterns.

Table IV.9 Comparing evaluation metrics among various models.

	CNN				**Stacking Classifier**				**2DCNN-SC**			
Labels	Accuracy	Precision	Recall	F1-score	Accuracy	Precision	Recall	F1-score	Accuracy	Precision	Recall	F1-score
0	1.00	0.50	1.00	0.67	0.995	1.00	1.00	1.00	0.997	0.99	1.00	0.99
1	1.00	1.00	1.00	0.99	0.99	1.00	1.00	1.00	1.00	1.00	1.00	1.00
2	1.00	1.00	1.00	1.00	1.00	0.95	1.00	0.97	1.00	1.00	1.00	1.00
3	0.00	0.00	0.00	0.00	0.946	1.00	0.95	0.97	0.99	1.00	0.99	0.99
4	1.00	1.00	1.00	1.00	0.997	1.00	1.00	1.00	1.00	1.00	1.00	1.00
Average	**0.7995**	**0.875**	**0.8**	**0.732**	**0.985**	**0.99**	**0.99**	**0.988**	**0.9976**	**0.998**	**0.998**	**0.996**

The images presented in Figures IV.32–34 illustrate normalized confusion matrices, which are valuable tools for assessing the classification performance of the proposed model. In each matrix, the rows correspond to the actual classes, while the columns represent the predicted classes. The values inside the cells indicate the percentage of samples from a true class that were assigned to each predicted class.

The confusion matrix of the CNN model, as shown in Figure IV.32, reveals a mixed performance across the five fault condition classes. Notably, classes 0, 1, 2, and 4 were classified with perfect accuracy, as evidenced by the 100% values on the diagonal for these classes and 0% misclassification rates across all other classes. This indicates that the model successfully learned and generalized the patterns associated with these classes. However, the performance in class 3 shows a significant shortcoming. All instances (100%) of class 3 were misclassified as class 0, and none of the samples were correctly identified as class 3. This suggests that the CNN model struggles to distinguish features unique to class 3 due to

similarities in signal patterns with class 0 or the model's inability to extract sufficient discriminative features. This type of misclassification can be critical in practical applications, as it implies that faults corresponding to class 3 may go undetected or be mistaken for normal or less severe conditions. Overall, while the CNN model performs excellently on most classes, the complete misclassification of one fault type (class 3) significantly affects its reliability and robustness.

The confusion matrix of the stacking classifier model indicates a generally high classification performance (Figure IV.33), with noticeable improvement over the standalone CNN, particularly for class 3, which previously exhibited significant misclassification. Classes 1, 2, and 4 were classified with perfect accuracy, showing 100%, 100%, and 99.77% correct predictions, respectively. Class 0 was accurately identified in 99.53% of the cases, with a minimal misclassification rate of 0.23% into class 1, an insignificant deviation that does not significantly affect the model's reliability. The most significant improvement is evident in Class 3, where 94.64% of the samples were correctly predicted, representing a substantial improvement over the CNN model, which failed in this category. Nevertheless, some challenges persist, as 5.36% of class 3 instances were misclassified as class 2, and 100% of class 3 instances were also incorrectly predicted as class 0 in a separate occurrence, likely indicating overlapping features or signal ambiguity. Despite these minor errors, the stacking classifier exhibits improved resilience and generalization, especially in its capacity to differentiate class 3 from the others. This enhancement highlights the effectiveness of ensemble learning in combining the strengths of various base learners (XGBoost, LightGBM, and SVC) to more accurately identify the complex patterns inherent in wind turbine fault data. The stacking model demonstrates superior performance across all categories, providing a more balanced and reliable diagnostic instrument than the baseline CNN model.

According to Figure IV.34, the results reveal excellent classification performance, as evidenced by the dominant percentages concentrated along the diagonal of the matrix (from the top-left to the bottom-right corner), indicating correct predictions. Specifically, 99.77% of the samples from class '0' were correctly predicted, while classes '1', '2', and '4' were ideally classified with 100% accuracy. The model also demonstrated substantial precision for class '3', correctly identifying 99.07% of its instances. Misclassifications were minimal: only 0.23% of class '0'

samples were incorrectly predicted as class '3', and 0.93% of class '3' instances were misclassified as class '0'. No misclassifications occurred between the other class pairs, as indicated by the zero values in the remaining off-diagonal cells. Overall, this confusion matrix confirms that the proposed 2DCNN–SC model delivers highly accurate and reliable predictions, with a strong ability to distinguish between different conditions classes in the wind turbine dataset.

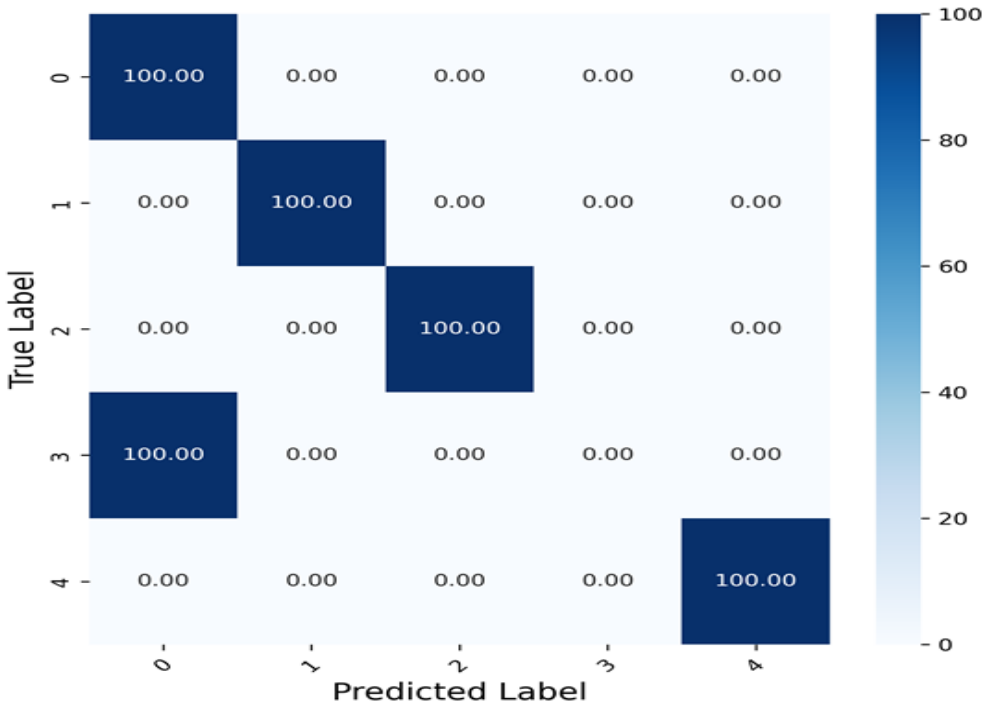

Figure IV.32 Confusion matrix for prediction test outcome of CNN model.

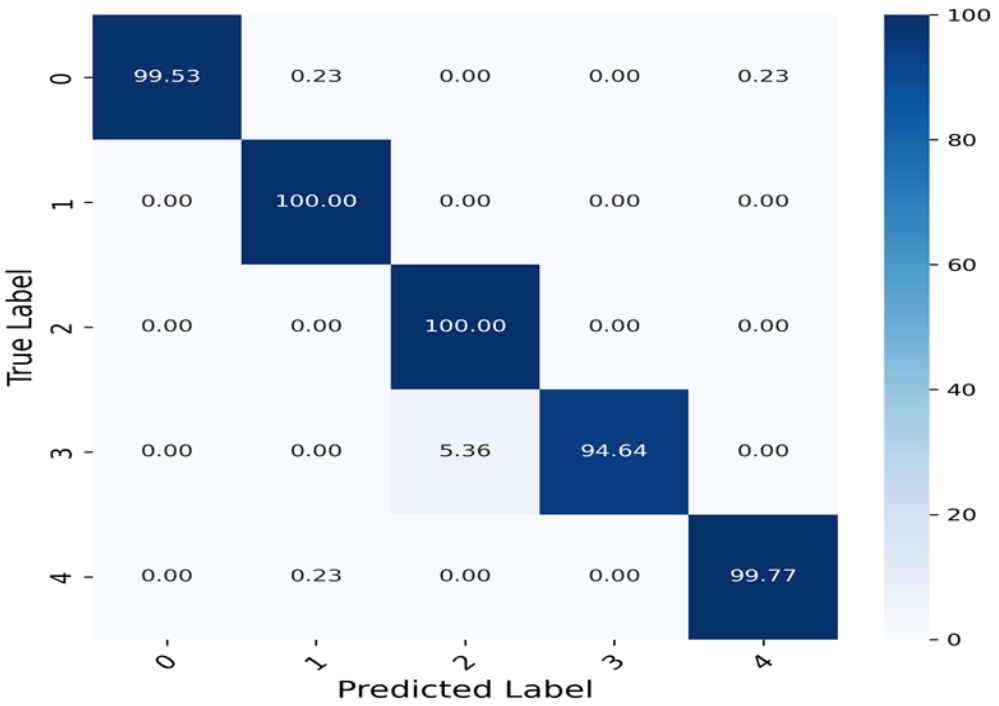

Figure IV.33 Confusion matrix for prediction test outcome of stacking classifier model.

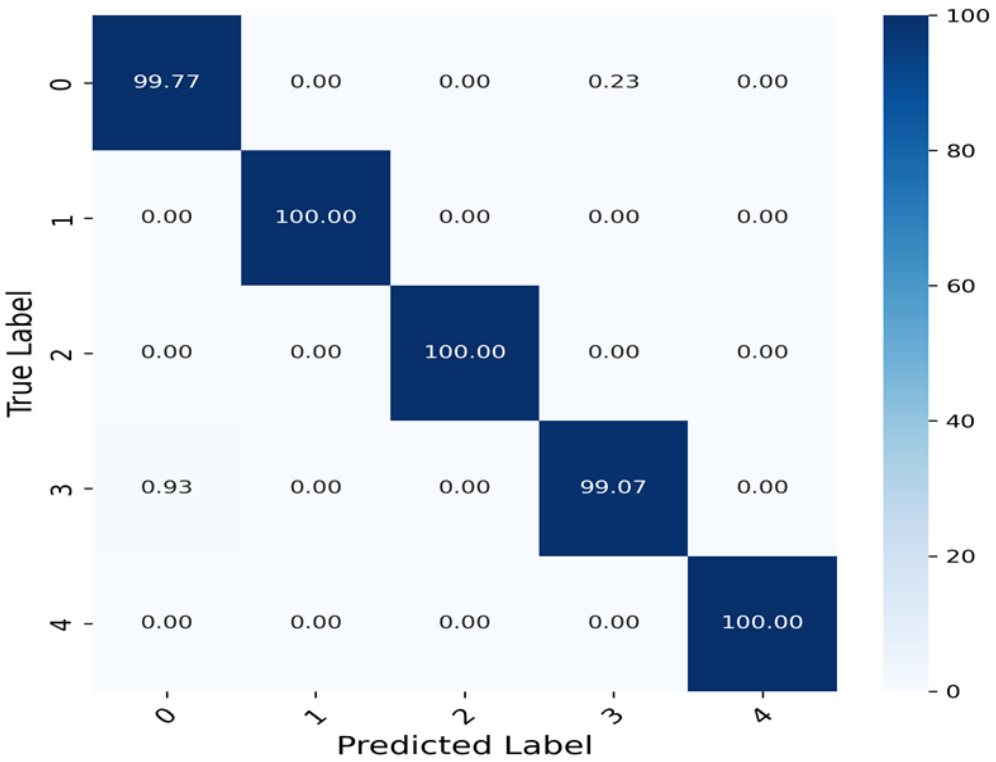

Figure IV.34 Confusion matrix for prediction test outcome of 2DCNN-SC model.

A comparative analysis of the three models reveals a clear progression in performance, as listed in Figures IV.35-37. The proposed method stands out as the top performer, achieving an impressive 99.8% accuracy and exhibiting nearly perfect classification, with only negligible errors across all five classes, despite a notable class imbalance (where class sizes range from approximately 500 to 1,500 samples). From Figure IV.36, it can be seen that the stacking classifier also achieves very high performance, with an accuracy of 98.8%. Still, it shows a slightly higher rate of misclassifications (e.g., class 1 and 3), suggesting reduced robustness in distinguishing similar fault patterns. In contrast, the CNN model, with an accuracy of 80.0%, falls significantly short of the target. It displays a critical misclassification pattern, frequently labeling higher-severity fault classes (such as 3) as class 0, which likely corresponds to the 'normal' operating condition. Such errors are especially concerning in the context of wind turbine fault diagnosis, as they could lead to undetected failures and increased operational risk. Overall, while both the proposed method and the Stacking classifier demonstrate strong diagnostic capabilities, the proposed method offers superior reliability and consistency. The CNN model, however, proves inadequate for this application due to its tendency to misclassify faults as usual.

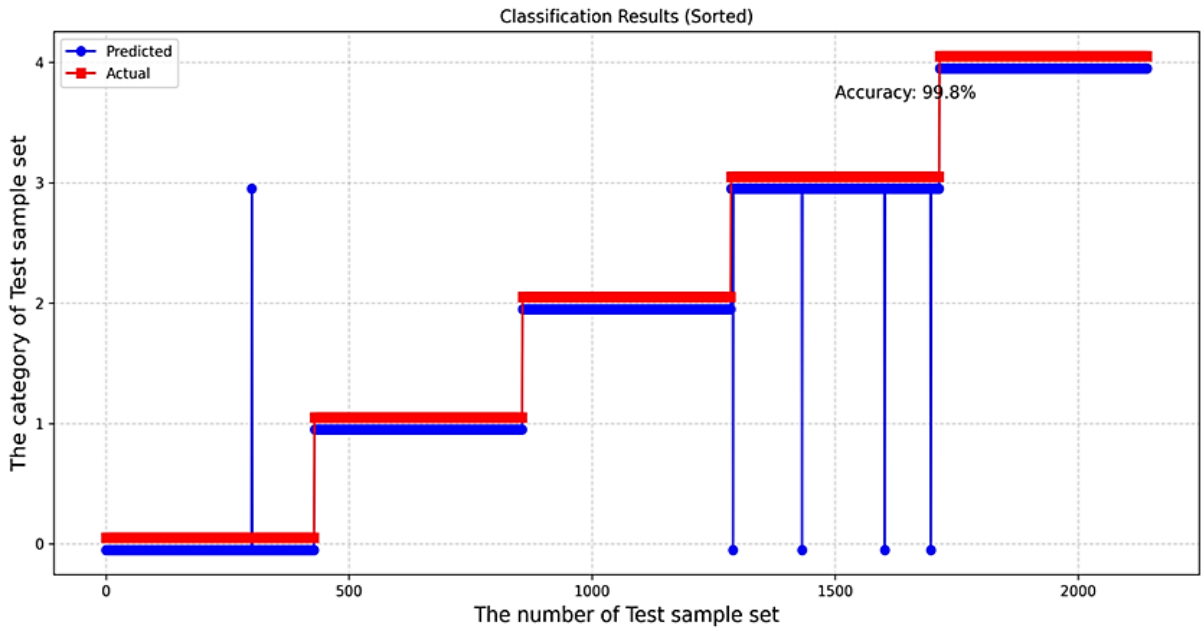

Figure IV.35 Fault type identification error in the fault feature vectors using 2DCNN-SC.

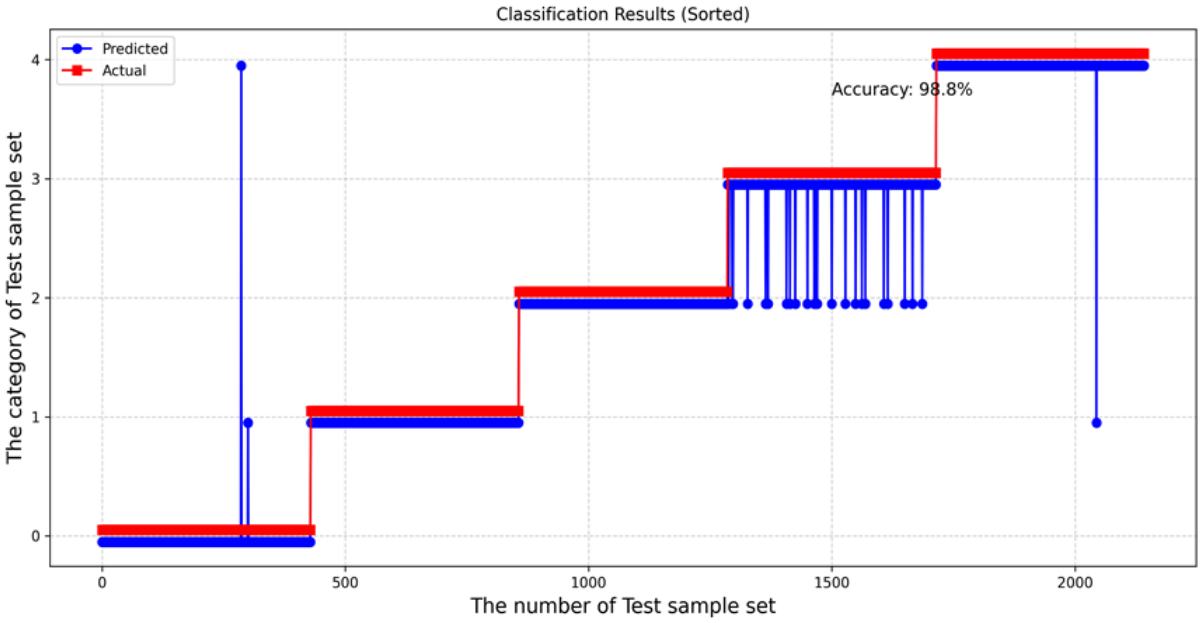

Figure IV.36 Fault type identification error in the fault feature vectors using stacking classifier.

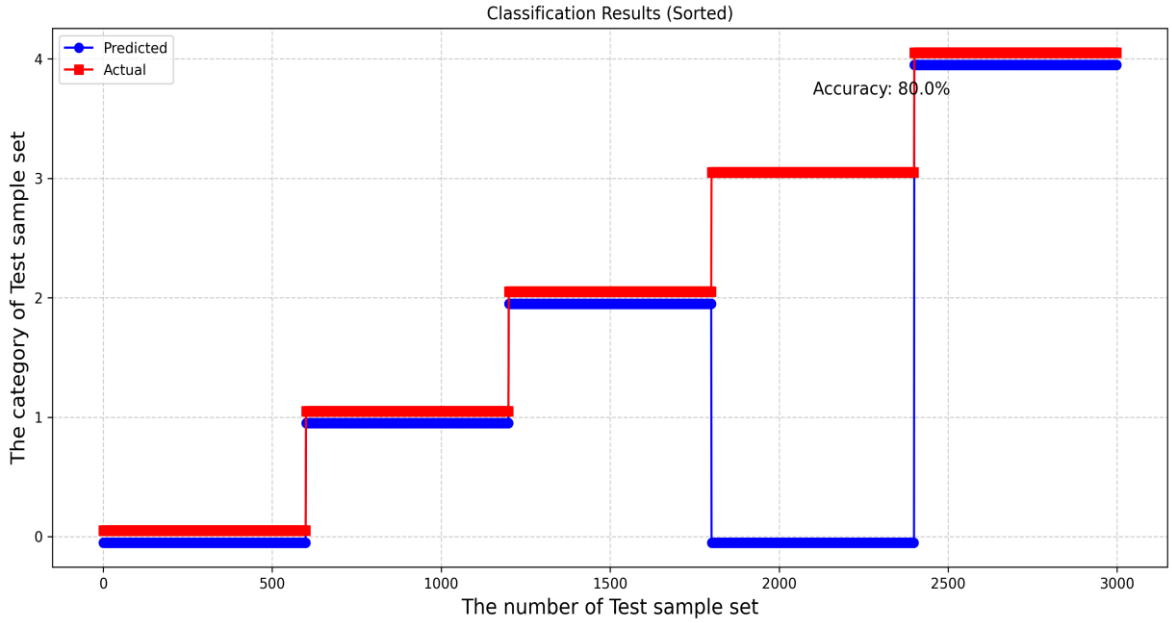

Figure IV.37 Fault type identification error in the fault feature vectors using CNN model.

To provide a more robust and insightful evaluation of classification performance beyond simple accuracy, Cohen's Kappa coefficient was employed. Unlike raw accuracy, Cohen's Kappa accounts for the possibility of agreement occurring by chance, offering a more reliable measure of model consistency, particularly in imbalanced datasets. In the context of the current study, Cohen's Kappa was calculated for the CNN, Stacking Classifier, and the proposed 2DCNN-SC

models to assess their reliability in fault classification for wind turbine condition monitoring, as shown in Figure IV.38.

The proposed 2DCNN-SC model achieves the highest kappa value of 0.997, with a tight confidence interval ranging from 0.996 to 0.99, indicating an almost perfect level of agreement between predicted and actual labels. This not only reflects exceptional classification performance but also demonstrates the model's high stability and consistency across fault categories, even under possible variations in the dataset.

The Stacking Classifier also performs strongly, with a kappa value of 0.985 and a confidence interval between 0.980 and 0.99. Although slightly lower than the proposed model, it still reflects excellent agreement, confirming its effectiveness. However, the somewhat wider confidence range suggests it may be more sensitive to class boundary overlaps or data variation compared to the 2DCNN-SC.

In contrast, the standard CNN model yields a substantially lower kappa value of 0.75, with a broader confidence interval spanning from 0.72 to 0.78. This places it within the range of moderate agreement, revealing significant challenges in distinguishing between fault classes. The wider confidence interval further suggests inconsistent performance, likely due to weaker feature extraction capabilities or difficulties in generalizing across complex or imbalanced fault categories. From Figure IV.38, these results underscore the superiority of the proposed 2DCNN-SC model in terms of both classification accuracy and reliability while also highlighting the limitations of conventional CNN architectures in handling nuanced fault detection scenarios in wind turbines.

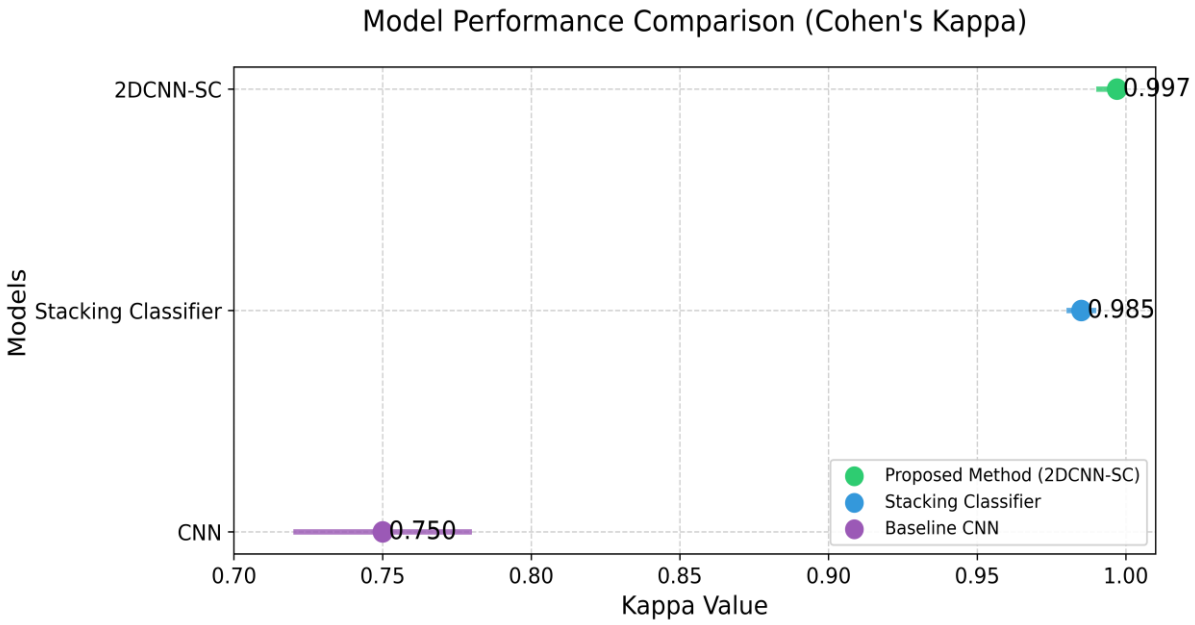

Figure IV.38 Comparison of WT fault classification models using Cohen's Kappa.

IV.4 Conclusion

Condition monitoring and weakness diagnosis are critical for continuous grid operation and wind farm functionality, serving as fundamental tasks and pivotal technologies within operation and maintenance. In this chapter, an intelligent bearing fault diagnosis approach based on CWT, CNN, and stacking ensemble model is proposed. It is implemented to enable early detection of WT faults and classification under variable working conditions. The proposed approach was tested and validated on two benchmark datasets, namely CWRU used for bearing single faults and Aventa wind turbine SCADA data considering multi-fault state.

The suggested model comprises elements for feature extraction and classification. Firstly, the original vibration signals of bearing under different health states are transformed into time-frequency maps by CWT (Morlet wavelet), which exhibits enhanced visibility of the non-stationary fault characteristic of the signal and is advantageous in improving the monitoring accuracy of the model. ML-based approaches frequently integrate feature extraction algorithms to optimize precision and processing rate. Second, a convolutional neural network (CNN) is employed to automatically extract the features of the scalogram images, hence preventing the loss of fault information without operator intervention. Then, the extracted features were used to train the classifiers (XGBoost, LightGBM, and SVC) at the base level of the proposed new

stacking classifier. The prediction of each base model is utilized as the input for the meta-learner (SVC) to perform the optimal WT fault classification.

To offer an in-depth evaluation, we compared several well-established machine-learning methodologies, including CNN, stacking classifier, XGBoost, LightGBM, SVC, and the CNN-XGBoost approach. The outcomes of the experiments demonstrate that the suggested method was applied to two datasets: the CWRU bearing dataset and the Aventa wind turbine SCADA dataset, achieving superior diagnostic accuracies of 99.6% and 99.76%, respectively. These results highlight the model's robustness and generalization capability across different industrial monitoring scenarios. By visualizing classification performance based on feature distribution, t-SNE also confirmed the superiority and effectiveness of the proposed 2DCNN-SC model for diagnosing and classifying wind turbine-bearing faults.

General Conclusion

The primary objective of this research project is to develop an intelligent defect diagnosis method for generating early warnings of emerging issues in wind turbine system under variable operating conditions with high accuracy. This thesis develops and validates two complementary diagnostic methods designed to enhance the accuracy and robustness of fault detection in wind turbine systems, particularly in bearings. This proposed diagnosis system is part of a conditional preventive maintenance strategy.

The first proposed method centers on a signal processing-based approach using bearing vibration data. Specifically, the fault diagnosis methodology combines the Discrete Wavelet Transform (DWT) and the Fast Fourier Transform (FFT) for analyzing bearing faults, utilizing the widely recognized Case Western Reserve University (CWRU) bearing dataset. The approach leverages multiresolution signal analysis, as provided by the DWT, to decompose vibration signals into different frequency bands, effectively capturing both transient and stationary fault-related information. Specifically, a 5-level discrete wavelet transform (DWT) is applied using the Daubechies 3 (db3) wavelet, which enables the isolation of high-frequency components typically associated with localized defects. The diagnostic process emphasizes the analysis of energy distribution across the decomposed wavelet sub-bands. Among these, the second detail level (D2) consistently reveals elevated energy signatures correlated with common fault types, such as inner race and outer race defects. To further enhance fault detection, FFT is performed on the selected wavelet levels, enabling frequency-domain analysis that reveals characteristic fault frequencies associated with both inner-race and outer-race defects. These frequencies align closely with theoretical expectations, confirming the method's ability to detect and localize faults accurately.

By integrating DWT's time-frequency localization with FFT's spectral analysis, the method achieves high sensitivity to incipient faults while maintaining interpretability. This hybrid signal processing framework has demonstrated effectiveness on benchmark data and shows strong potential for future application to real-world wind turbine-bearing health monitoring systems.

The existence of anomalies in wind turbine parts, particularly in bearings, poses substantial risks of prolonged periods of inactivity and maintenance, underscoring the crucial need for timely identification to ensure reliable operation. To this end, developing prognostic and health

management solutions for fault detection and diagnosis based on machine learning (ML) algorithms that align with the equipment is essential, as their efficiencies are highly correlated with the extracted features, the nature of the signal, and the quality of the data. According to the non-stationary characteristics of bearing vibration signals, converting these signals into time-frequency images has been recognized as a potentially effective method for identifying faults.

The second proposed method in our research involves a hybrid artificial intelligence framework that combines deep learning and ensemble learning techniques. This work proposes a wavelet transform-related method and a novel multistage approach that combines a 2D convolutional neural network and a stacking ensemble model created using multiple classifiers, including extreme gradient boosting (XGBoost), light gradient boosting machine (LightGBM), and support vector classifier (SVC), to facilitate the diagnosis of enhancement-bearing faults. The rolling bearing fault signal is initially transformed into a wavelet time-frequency map via continuous wavelet transform. This map is subsequently partitioned into samples representing the training and test sets. Due to the complexity and low signal-to-noise ratio of wind turbine vibration signals, deep learning models (primarily convolutional neural networks) are employed to automatically extract fault-discriminative characteristics from raw vibration data acquired by accelerometers. Secondly, the training samples are utilized as input for the constructed 2DCNN-SC model. The stacked ensemble model incorporates the k-fold cross-validation technique throughout the training process to improve the classification accuracy and mitigate overfitting. Ultimately, the accuracy and performance of the proposed method were evaluated through testing. Several machine learning models were employed to compare and assess its effectiveness in fault classification. The study further includes a sensitivity analysis focused on the impact of kernel function types.

Performance is evaluated using two datasets: the Case Western Reserve University (CWRU) bearing fault dataset, which includes 10 bearing conditions, and the Aventa wind turbine (WT) SCADA dataset, containing five distinct fault conditions. The proposed 2DCNN-SC model with a Radial Basis Function (RBF) kernel achieves a diagnostic accuracy of 99.6% on the CWRU dataset and 99.76% on the Aventa SCADA data, demonstrating its effectiveness across experimental benchmarks and practical wind turbine operating conditions. The results prove the effectiveness, generality, and convenience of this approach in anomaly diagnosis and classification for wind turbine, and highlight the advantages of machine learning-based bearing fault detection.

Future work will include several potential directions:

- The proposed diagnostic frameworks could be extended to support online and real-time monitoring by integrating them with edge computing platforms and SCADA systems in actual operational environments.
- An optimization algorithm will be explored to automatically identify optimal hyperparameters for training the proposed model. This aims to maintain high diagnostic accuracy while reducing computational time and minimizing the need for extensive manual experimentation.
- Another valuable direction involves the application of transfer learning or domain adaptation techniques to enhance the generalization capability of trained models across different wind turbine types and varying operating conditions without requiring full retraining.
- Incorporating additional sensor data, such as temperature, pressure, and acoustic emissions, could further enhance multimodal fault detection performance and system robustness.

Bibliography

[1] T. Sebbagh, M. E. Şahin, and C. Beldjaatit, "Green hydrogen revolution for a sustainable energy future," *Clean Techn Environ Policy*, vol. 26, no. 12, pp. 4017–4040, Dec. 2024, doi: 10.1007/s10098-024-02995-9.

[2] L. Rajaoarisoa, M. Kuk, S. Bobek, and M. Sayed-Mouchaweh, "Hybrid and co-learning approach for anomalies prediction and explanation of wind turbine systems," *Engineering Applications of Artificial Intelligence*, vol. 133, p. 108046, Jul. 2024, doi: 10.1016/j.engappai.2024.108046.

[3] L. Zhang, B. Wang, P. Liang, X. Yuan, and N. Li, "Semi-supervised fault diagnosis of gearbox based on feature pre-extraction mechanism and improved generative adversarial networks under limited labeled samples and noise environment," *Advanced Engineering Informatics*, vol. 58, p. 102211, Oct. 2023, doi: 10.1016/j.aei.2023.102211.

[4] X. Wang, T. Wang, A. Ming, W. Zhang, A. Li, and F. Chu, "Cross-Operating Condition Degradation Knowledge Learning for Remaining Useful Life Estimation of Bearings," *IEEE Trans. Instrum. Meas.*, vol. 70, pp. 1–11, 2021, doi: 10.1109/TIM.2021.3091461.

[5] X. Tang *et al.*, "Intelligent fault diagnosis of helical gearboxes with compressive sensing based non-contact measurements," *ISA Transactions*, vol. 133, pp. 559–574, Feb. 2023, doi: 10.1016/j.isatra.2022.07.020.

[6] Y. Liu and H. Liang, "Review on the Application of the Nonlinear Output Frequency Response Functions to Mechanical Fault Diagnosis," *IEEE Trans. Instrum. Meas.*, vol. 72, pp. 1–12, 2023, doi: 10.1109/TIM.2023.3234087.

[7] Z. Chen, A. Mauricio, W. Li, and K. Gryllias, "A deep learning method for bearing fault diagnosis based on Cyclic Spectral Coherence and Convolutional Neural Networks," *Mechanical Systems and Signal Processing*, vol. 140, p. 106683, Jun. 2020, doi: 10.1016/j.ymssp.2020.106683.

[8] Z. Chen and W. Li, "Multisensor Feature Fusion for Bearing Fault Diagnosis Using Sparse Autoencoder and Deep Belief Network," *IEEE Trans. Instrum. Meas.*, vol. 66, no. 7, pp. 1693–1702, Jul. 2017, doi: 10.1109/TIM.2017.2669947.

[9] L. Wen, X. Li, L. Gao, and Y. Zhang, "A New Convolutional Neural Network-Based Data-Driven Fault Diagnosis Method," *IEEE Trans. Ind. Electron.*, vol. 65, no. 7, pp. 5990–5998, Jul. 2018, doi: 10.1109/TIE.2017.2774777.

[10] D. Huang, W.-A. Zhang, F. Guo, W. Liu, and X. Shi, "Wavelet Packet Decomposition-Based Multiscale CNN for Fault Diagnosis of Wind Turbine Gearbox," *IEEE Trans. Cybern.*, vol. 53, no. 1, pp. 443–453, Jan. 2023, doi: 10.1109/TCYB.2021.3123667.

[11] J. Yan, A. Nuertayi, Y. Yan, S. Liu, and Y. Liu, "Hybrid physical and data driven modeling for dynamic operation characteristic simulation of wind turbine," *Renewable Energy*, vol. 215, p. 118958, Oct. 2023, doi: 10.1016/j.renene.2023.118958.

[12] D. Gemayel, M. Abdelwahab, T. Ghazal, and H. Aboshosha, "Modelling of vertical axis wind turbine using large eddy simulations," *Results in Engineering*, vol. 18, p. 101226, Jun. 2023, doi: 10.1016/j.rineng.2023.101226.

[13] "global-wind-report-2024." Accessed: Jul. 04, 2024. [Online]. Available: https://gwec.net/global-wind-report-2024/

[14] M. Abdelateef Mostafa, E. A. El-Hay, and M. M. ELkholy, "Recent Trends in Wind Energy Conversion System with Grid Integration Based on Soft Computing Methods: Comprehensive Review, Comparisons and Insights," *Arch Computat Methods Eng*, vol. 30, no. 3, pp. 1439–1478, Apr. 2023, doi: 10.1007/s11831-022-09842-4.

[15] D. J. Arent *et al.*, "Challenges and opportunities in decarbonizing the U.S. energy system," *Renewable and Sustainable Energy Reviews*, vol. 169, p. 112939, Nov. 2022, doi: 10.1016/j.rser.2022.112939.

[16] A. Chaudhuri, R. Datta, M. P. Kumar, J. P. Davim, and S. Pramanik, "Energy Conversion Strategies for Wind Energy System: Electrical, Mechanical and Material Aspects," *Materials*, vol. 15, no. 3, p. 1232, Feb. 2022, doi: 10.3390/ma15031232.

[17] H. Y. Peng, X. R. Yang, H. J. Liu, and S. Y. Sun, "Aerodynamic analysis of vertical axis wind turbines at various turbulent levels: Insights from 3D LES simulations," *Journal of Building Engineering*, vol. 94, p. 109899, Oct. 2024, doi: 10.1016/j.jobe.2024.109899.

[18] P. Ghiasi, G. Najafi, B. Ghobadian, A. Jafari, R. Mamat, and M. Fairusham Ghazali, "CFD-Study of the H-Rotor Darrius wind turbine performance in Drag-Lift and lift Regime: Impact of Type, thickness and chord length of blades," *Alexandria Engineering Journal*, vol. 67, pp. 51–64, Mar. 2023, doi: 10.1016/j.aej.2022.10.013.

[19] B. Hand, G. Kelly, and A. Cashman, "Aerodynamic design and performance parameters of a lift-type vertical axis wind turbine: A comprehensive review," *Renewable and Sustainable Energy Reviews*, vol. 139, p. 110699, Apr. 2021, doi: 10.1016/j.rser.2020.110699.

[20] W. Ostachowicz, M. McGugan, J.-U. Schröder-Hinrichs, and M. Luczak, Eds., *MARE-WINT*. Cham: Springer International Publishing, 2016. doi: 10.1007/978-3-319-39095-6.

[21] A. G. Olabi *et al.*, "A Review on Failure Modes of Wind Turbine Components," *Energies*, vol. 14, no. 17, p. 5241, Aug. 2021, doi: 10.3390/en14175241.

[22] G. Ertek and L. Kailas, "Analyzing a Decade of Wind Turbine Accident News with Topic Modeling," *Sustainability*, vol. 13, no. 22, p. 12757, Nov. 2021, doi: 10.3390/su132212757.

[23] K. Mushtaq *et al.*, "A comprehensive approach to wind turbine power curve modeling: Addressing outliers and enhancing accuracy," *Energy*, vol. 304, p. 131981, Sep. 2024, doi: 10.1016/j.energy.2024.131981.

[24] F. Bilendo, A. Meyer, H. Badihi, N. Lu, P. Cambron, and B. Jiang, "Applications and Modeling Techniques of Wind Turbine Power Curve for Wind Farms—A Review," *Energies*, vol. 16, no. 1, p. 180, Dec. 2022, doi: 10.3390/en16010180.

[25] E. Kulunk, "Aerodynamics of Wind Turbines," *Fundamental and Advanced Topics in Wind Power*.

[26] A. Pellegri, "The Complementary Betz's Theory".

[27] C. Dirscherl, C. M. Hackl, and K. Schechner, "Modeling and control of modern wind turbine systems: An introduction," 2015, pp. 1540–1614. doi: 10.1007/978-3-642-30096-7_24.

[28] P. Coelho, "The Betz limit and the corresponding thermodynamic limit," *Wind Engineering*, vol. 47, no. 2, pp. 491–496, Apr. 2023, doi: 10.1177/0309524X221130109.

[29] T. Sebbagh, R. Kelaiaia, A. Zaatri, T. Bechara, and L. Abdelouahed, "Investigation of the use of a central unique renewable energy system versus distributed units for crop irrigation," *Clean Techn Environ Policy*, vol. 20, no. 10, pp. 2365–2373, Dec. 2018, doi: 10.1007/s10098-018-1599-y.

[30] L. T. Contreras Montoya, M. Y. Hayyani, M. Issa, A. Ilinca, H. Ibrahim, and M. Rezkallah, "Wind power plant planning and modeling," in *Hybrid Renewable Energy Systems and Microgrids*, Elsevier, 2021, pp. 259–312. doi: 10.1016/B978-0-12-821724-5.00012-X.

[31] A. Lukin, G. Demidova, A. Rassõlkin, D. Lukichev, T. Vaimann, and A. Anuchin, "Small Magnus Wind Turbine: Modeling Approaches," *Applied Sciences*, vol. 12, no. 4, p. 1884, Feb. 2022, doi: 10.3390/app12041884.

[32] *Wind Energy Engineering*. Elsevier, 2023. doi: 10.1016/C2021-0-00258-3.

[33] J. G. González-Hernández and R. Salas-Cabrera, "Representation and estimation of the power coefficient in wind energy conversion systems," *Rev. Fac. Ing.*, vol. 28, no. 50, pp. 77–90, Jan. 2019, doi: 10.19053/01211129.v28.n50.2019.8816.

[34] O. C. Castillo, V. R. Andrade, J. J. R. Rivas, and R. O. González, "Comparison of Power Coefficients in Wind Turbines Considering the Tip Speed Ratio and Blade Pitch Angle," *Energies*, vol. 16, no. 6, p. 2774, Mar. 2023, doi: 10.3390/en16062774.

[35] F. Kendouli, K. Nabti, K. Labed, and H. Benalla, "Modélisation, simulation et contrôle d'une turbine éolienne à vitesse variable basée sur la génératrice asynchrone à double alimentation," *J. Ren. Energies*, vol. 14, no. 1, Oct. 2023, doi: 10.54966/jreen.v14i1.245.

[36] H. Hichem, M. Abdellah, T. A. Abderrazak, B. Abdelkader, and S. Ramzi, "A wind turbine sensorless automatic control systems, analysis, modelling and development of IDA-PBC method," *IJPEDS*, vol. 11, no. 1, p. 45, Mar. 2020, doi: 10.11591/ijpeds.v11.i1.pp45-55.

[37] B. Benyachou, S. Men-la-yakhaf, B. Bahrar, and M. Tamani, "Modelling with Matlab/Simulink of a wind turbine connected to a generator asynchronous dual power (GADP)," 2017.

[38] L. Abderrazak, R. Adlene, and K. Mohamed, "Modeling and Simulation of a Wind Turbine Driven Induction Generator Using Bond Graph," *Ren. Ener. & Sust. Dev.*, vol. 1, no. 2, p. 236, Dec. 2015, doi: 10.21622/resd.2015.01.2.236.

[39] C. Beldjaatit and T. Sebbagh, "Studying, modeling, and simulation of wind turbine using MATLAB/Simulink," 2024.

[40] A. Persson, "How Do We Understand the Coriolis Force?," *Bull. Amer. Meteor. Soc.*, vol. 79, no. 7, pp. 1373–1385, Jul. 1998, doi: 10.1175/1520-0477(1998)079<1373:HDWUTC>2.0.CO;2.

[41] R. S. Velmurugan and T. Dhingra, "Maintenance strategy selection and its impact in maintenance function: A conceptual framework," *International Journal of Operations & Production Management*, vol. 35, no. 12, pp. 1622–1661, Dec. 2015, doi: 10.1108/IJOPM-01-2014-0028.

[42] H. Tang, H. Wang, and C. Li, "Time-varying cost modeling and maintenance strategy optimization of plateau wind turbines considering degradation states," *Applied Energy*, vol. 377, p. 124464, Jan. 2025, doi: 10.1016/j.apenergy.2024.124464.

[43] M. Bevilacqua and M. Braglia, "The analytic hierarchy process applied to maintenance strategy selection," *Reliability Engineering & System Safety*, vol. 70, no. 1, pp. 71–83, Oct. 2000, doi: 10.1016/S0951-8320(00)00047-8.

[44] P. Mallioris, E. Aivazidou, and D. Bechtsis, "Predictive maintenance in Industry 4.0: A systematic multi-sector mapping," *CIRP Journal of Manufacturing Science and Technology*, vol. 50, pp. 80–103, Jun. 2024, doi: 10.1016/j.cirpj.2024.02.003.

[45] J. A. Erkoyuncu, S. Khan, A. L. Eiroa, N. Butler, K. Rushton, and S. Brocklebank, "Perspectives on trading cost and availability for corrective maintenance at the equipment type level," *Reliability Engineering & System Safety*, vol. 168, pp. 53–69, Dec. 2017, doi: 10.1016/j.ress.2017.05.041.

[46] O. M. E. S. Khayal, "Introduction to Maintenance Management," 2024, doi: 10.13140/RG.2.2.36438.46408.

[47] J. Sharma, M. L. Mittal, and G. Soni, "Condition-based maintenance using machine learning and role of interpretability: a review," *Int J Syst Assur Eng Manag*, vol. 15, no. 4, pp. 1345–1360, Apr. 2024, doi: 10.1007/s13198-022-01843-7.

[48] R. M. Ayo-Imoru and A. C. Cilliers, "A survey of the state of condition-based maintenance (CBM) in the nuclear power industry," *Annals of Nuclear Energy*, vol. 112, pp. 177–188, Feb. 2018, doi: 10.1016/j.anucene.2017.10.010.

[49] A. Ali and A. Abdelhadi, "Condition-Based Monitoring and Maintenance: State of the Art Review," *Applied Sciences*, vol. 12, no. 2, p. 688, Jan. 2022, doi: 10.3390/app12020688.

[50] M. M. Hamasha *et al.*, "Strategical selection of maintenance type under different conditions," *Sci Rep*, vol. 13, no. 1, p. 15560, Sep. 2023, doi: 10.1038/s41598-023-42751-5.

[51] F. Tao, Q. Qi, A. Liu, and A. Kusiak, "Data-driven smart manufacturing," *Journal of Manufacturing Systems*, vol. 48, pp. 157–169, Jul. 2018, doi: 10.1016/j.jmsy.2018.01.006.

[52] P. Gackowiec, "General overview of maintenance strategies – concepts and approaches," *Multidisciplinary Aspects of Production Engineering*, vol. 2, no. 1, pp. 126–139, Sep. 2019, doi: 10.2478/mape-2019-0013.

[53] D. V. Carvalho, E. M. Pereira, and J. S. Cardoso, "Machine Learning Interpretability: A Survey on Methods and Metrics," *Electronics*, vol. 8, no. 8, p. 832, Jul. 2019, doi: 10.3390/electronics8080832.

[54] A. J. Guillén, A. Crespo, M. Macchi, and J. Gómez, "On the role of Prognostics and Health Management in advanced maintenance systems," *Production Planning & Control*, vol. 27, no. 12, pp. 991–1004, Sep. 2016, doi: 10.1080/09537287.2016.1171920.

[55] A. Bousdekis, K. Lepenioti, D. Apostolou, and G. Mentzas, "A Review of Data-Driven Decision-Making Methods for Industry 4.0 Maintenance Applications," *Electronics*, vol. 10, no. 7, p. 828, Mar. 2021, doi: 10.3390/electronics10070828.

[56] D. Wu, C. Jennings, J. Terpenny, and S. Kumara, "Cloud-based machine learning for predictive analytics: Tool wear prediction in milling," in *2016 IEEE International*

Conference on Big Data (Big Data), Washington DC,USA: IEEE, Dec. 2016, pp. 2062–2069. doi: 10.1109/BigData.2016.7840831.

[57] A. Rastegari and M. Bengtsson, "Implementation of Condition Based Maintenance in manufacturing industry - A pilot case study," in *2014 International Conference on Prognostics and Health Management*, Cheney, WA, USA: IEEE, Jun. 2014, pp. 1–8. doi: 10.1109/ICPHM.2014.7036377.

[58] A. K. S. Jardine, D. Lin, and D. Banjevic, "A review on machinery diagnostics and prognostics implementing condition-based maintenance," *Mechanical Systems and Signal Processing*, vol. 20, no. 7, pp. 1483–1510, Oct. 2006, doi: 10.1016/j.ymssp.2005.09.012.

[59] O. AlShorman *et al.*, "Advancements in condition monitoring and fault diagnosis of rotating machinery: A comprehensive review of image-based intelligent techniques for induction motors," *Engineering Applications of Artificial Intelligence*, vol. 130, p. 107724, Apr. 2024, doi: 10.1016/j.engappai.2023.107724.

[60] R. Ahmad and S. Kamaruddin, "An overview of time-based and condition-based maintenance in industrial application," *Computers & Industrial Engineering*, vol. 63, no. 1, pp. 135–149, Aug. 2012, doi: 10.1016/j.cie.2012.02.002.

[61] B. A. Tama, M. Vania, S. Lee, and S. Lim, "Recent advances in the application of deep learning for fault diagnosis of rotating machinery using vibration signals," *Artif Intell Rev*, vol. 56, no. 5, pp. 4667–4709, May 2023, doi: 10.1007/s10462-022-10293-3.

[62] D. Goyal and B. S. Pabla, "Condition based maintenance of machine tools—A review," *CIRP Journal of Manufacturing Science and Technology*, vol. 10, pp. 24–35, Aug. 2015, doi: 10.1016/j.cirpj.2015.05.004.

[63] Z. Liu and L. Zhang, "A review of failure modes, condition monitoring and fault diagnosis methods for large-scale wind turbine bearings," *Measurement*, vol. 149, p. 107002, Jan. 2020, doi: 10.1016/j.measurement.2019.107002.

[64] X. Zhu, C. Zhong, and J. Zhe, "Lubricating oil conditioning sensors for online machine health monitoring – A review," *Tribology International*, vol. 109, pp. 473–484, May 2017, doi: 10.1016/j.triboint.2017.01.015.

[65] J. M. Wakiru, L. Pintelon, P. N. Muchiri, and P. K. Chemweno, "A review on lubricant condition monitoring information analysis for maintenance decision support," *Mechanical Systems and Signal Processing*, vol. 118, pp. 108–132, Mar. 2019, doi: 10.1016/j.ymssp.2018.08.039.

[66] Y. He *et al.*, “An overview of acoustic emission inspection and monitoring technology in the key components of renewable energy systems,” *Mechanical Systems and Signal Processing*, vol. 148, p. 107146, Feb. 2021, doi: 10.1016/j.ymssp.2020.107146.

[67] S. A. Niknam, V. Songmene, and Y. H. J. Au, “PROPOSING A NEW ACOUSTIC EMISSION PARAMETER FOR BEARING CONDITION MONITORING IN ROTATING MACHINES,” *Transactions of the Canadian Society for Mechanical Engineering*, vol. 37, no. 4, pp. 1105–1114, Dec. 2013, doi: 10.1139/tcsme-2013-0094.

[68] A. Mehta, D. Goyal, A. Choudhary, B. S. Pabla, and S. Belghith, “Machine Learning-Based Fault Diagnosis of Self-Aligning Bearings for Rotating Machinery Using Infrared Thermography,” *Mathematical Problems in Engineering*, vol. 2021, pp. 1–15, Apr. 2021, doi: 10.1155/2021/9947300.

[69] R. Wang, X. Zhan, H. Bai, E. Dong, Z. Cheng, and X. Jia, “A Review of Fault Diagnosis Methods for Rotating Machinery Using Infrared Thermography,” *Micromachines*, vol. 13, no. 10, p. 1644, Sep. 2022, doi: 10.3390/mi13101644.

[70] G. K. Balakrishnan *et al.*, “A Review of Infrared Thermography for Condition-Based Monitoring in Electrical Energy: Applications and Recommendations,” *Energies*, vol. 15, no. 16, p. 6000, Aug. 2022, doi: 10.3390/en15166000.

[71] M. Nurshafiq Ramli, A. M. A. Rani, N. Sallih, A. A. A. Aliyu, and T. V. V. L. N. Rao, “Vibration Analysis Methods for Misalignment and Tolerance Problems in Machine Systems: A Review,” in *Advances in Material Sciences and Engineering*, 2020, pp. 57–66. doi: 10.1007/978-981-13-8297-0_8.

[72] T. Chu, T. Nguyen, H. Yoo, and J. Wang, “A review of vibration analysis and its applications,” *Heliyon*, vol. 10, no. 5, p. e26282, Mar. 2024, doi: 10.1016/j.heliyon.2024.e26282.

[73] M. H. Mohd Ghazali and W. Rahiman, “Vibration Analysis for Machine Monitoring and Diagnosis: A Systematic Review,” *Shock and Vibration*, vol. 2021, no. 1, p. 9469318, Jan. 2021, doi: 10.1155/2021/9469318.

[74] B. Deb Majumder, J. K. Roy, and S. Padhee, “Recent Advances in Multifunctional Sensing Technology on a Perspective of Multi-Sensor System: A Review,” *IEEE Sensors J.*, vol. 19, no. 4, pp. 1204–1214, Feb. 2019, doi: 10.1109/JSEN.2018.2882239.

[75] *Mechanical Vibrations and Condition Monitoring*. Elsevier, 2020. doi: 10.1016/C2019-0-00474-8.

[76] D. Goyal and B. S. Pabla, "The Vibration Monitoring Methods and Signal Processing Techniques for Structural Health Monitoring: A Review," *Arch Computat Methods Eng*, vol. 23, no. 4, pp. 585–594, Dec. 2016, doi: 10.1007/s11831-015-9145-0.

[77] M. Romanssini, P. C. C. De Aguirre, L. Compassi-Severo, and A. G. Girardi, "A Review on Vibration Monitoring Techniques for Predictive Maintenance of Rotating Machinery," *Eng*, vol. 4, no. 3, pp. 1797–1817, Jun. 2023, doi: 10.3390/eng4030102.

[78] I. U. Hassan, K. Panduru, and J. Walsh, "An In-Depth Study of Vibration Sensors for Condition Monitoring," *Sensors*, vol. 24, no. 3, p. 740, Jan. 2024, doi: 10.3390/s24030740.

[79] K. Guru Manikandan, K. Pannirselvam, J. J. Kenned, and C. Suresh Kumar, "Investigations on suitability of MEMS based accelerometer for vibration measurements," *Materials Today: Proceedings*, vol. 45, pp. 6183–6192, 2021, doi: 10.1016/j.matpr.2020.10.506.

[80] S. Bikash Chaudhury, M. Sengupta, and K. Mukherjee, "Vibration Monitoring of Rotating Machines Using MEMS Accelerometer," *IJSER*, vol. 2, no. 9, pp. 5–11, Sep. 2014, doi: 10.70729/J2013358.

[81] A. Rossi, G. Bocchetta, F. Botta, and A. Scorza, "Accuracy Characterization of a MEMS Accelerometer for Vibration Monitoring in a Rotating Framework," *Applied Sciences*, vol. 13, no. 8, p. 5070, Apr. 2023, doi: 10.3390/app13085070.

[82] A. Hu, L. Xiang, and L. Zhu, "An engineering condition indicator for condition monitoring of wind turbine bearings," *Wind Energy*, vol. 23, no. 2, pp. 207–219, Feb. 2020, doi: 10.1002/we.2423.

[83] M. Rezamand, M. Kordestani, R. Carriveau, D. S.-K. Ting, M. E. Orchard, and M. Saif, "Critical Wind Turbine Components Prognostics: A Comprehensive Review," *IEEE Trans. Instrum. Meas.*, vol. 69, no. 12, pp. 9306–9328, Dec. 2020, doi: 10.1109/TIM.2020.3030165.

[84] H. Peng, S. Li, L. Shangguan, Y. Fan, and H. Zhang, "Analysis of Wind Turbine Equipment Failure and Intelligent Operation and Maintenance Research," *Sustainability*, vol. 15, no. 10, p. 8333, May 2023, doi: 10.3390/su15108333.

[85] J. Park, C. Kim, M.-C. Dinh, and M. Park, "Design of a Condition Monitoring System for Wind Turbines," *Energies*, vol. 15, no. 2, p. 464, Jan. 2022, doi: 10.3390/en15020464.

[86] W. Wang, Y. Xue, C. He, and Y. Zhao, "Review of the Typical Damage and Damage-Detection Methods of Large Wind Turbine Blades," *Energies*, vol. 15, no. 15, p. 5672, Aug. 2022, doi: 10.3390/en15155672.

[87] X. Song *et al.*, "Review on the Damage and Fault Diagnosis of Wind Turbine Blades in the Germination Stage," *Energies*, vol. 15, no. 20, p. 7492, Oct. 2022, doi: 10.3390/en15207492.

[88] B. Steffen, M. Beuse, P. Tautorat, and T. S. Schmidt, "Experience Curves for Operations and Maintenance Costs of Renewable Energy Technologies," *Joule*, vol. 4, no. 2, pp. 359–375, Feb. 2020, doi: 10.1016/j.joule.2019.11.012.

[89] R. Koitz, F. Wotawa, J. Lüftenegger, C. S. Gray, and F. Langmayr, "Wind Turbine Fault Localization: A Practical Application of Model-Based Diagnosis," in *Diagnosability, Security and Safety of Hybrid Dynamic and Cyber-Physical Systems*, M. Sayed-Mouchaweh, Ed., Cham: Springer International Publishing, 2018, pp. 17–43. doi: 10.1007/978-3-319-74962-4_2.

[90] W. Wang, Y. Xue, C. He, and Y. Zhao, "Review of the Typical Damage and Damage-Detection Methods of Large Wind Turbine Blades," *Energies*, vol. 15, no. 15, p. 5672, Aug. 2022, doi: 10.3390/en15155672.

[91] D. Al. Katsaprakakis, N. Papadakis, and I. Ntintakis, "A Comprehensive Analysis of Wind Turbine Blade Damage," *Energies*, vol. 14, no. 18, p. 5974, Sep. 2021, doi: 10.3390/en14185974.

[92] M. Civera and C. Surace, "Non-Destructive Techniques for the Condition and Structural Health Monitoring of Wind Turbines: A Literature Review of the Last 20 Years," *Sensors*, vol. 22, no. 4, p. 1627, Feb. 2022, doi: 10.3390/s22041627.

[93] H. Liu, Y. Wang, T. Zeng, H. Wang, S. Chan, and L. Ran, "Wind turbine generator failure analysis and fault diagnosis: A review," *IET Renewable Power Gen*, vol. 18, no. 15, pp. 3127–3148, Nov. 2024, doi: 10.1049/rpg2.13104.

[94] M. Luengo and A. Kolios, "Failure Mode Identification and End of Life Scenarios of Offshore Wind Turbines: A Review," *Energies*, vol. 8, no. 8, pp. 8339–8354, Aug. 2015, doi: 10.3390/en8088339.

[95] A. G. Olabi *et al.*, "A Review on Failure Modes of Wind Turbine Components," *Energies*, vol. 14, no. 17, p. 5241, Aug. 2021, doi: 10.3390/en14175241.

[96] S. Yusuf, D. J. Brown, A. Mackinnon, and R. Papanicolaou, "Fault classification improvement in industrial condition monitoring via Hidden Markov Models and Naïve Bayesian modeling," in *2013 IEEE Symposium on Industrial Electronics & Applications*, Kuching, Malaysia: IEEE, Sep. 2013, pp. 75–80. doi: 10.1109/ISIEA.2013.6738971.

[97] J. Faiz and M. Ojaghi, "Different indexes for eccentricity faults diagnosis in three-phase squirrel-cage induction motors: A review," *Mechatronics*, vol. 19, no. 1, pp. 2–13, Feb. 2009, doi: 10.1016/j.mechatronics.2008.07.004.

[98] C. M. C. G. Fernandes, L. Blazquez, J. Sanesteban, R. C. Martins, and J. H. O. Seabra, "Energy efficiency tests in a full scale wind turbine gearbox," *Tribology International*, vol. 101, pp. 375–382, Sep. 2016, doi: 10.1016/j.triboint.2016.05.001.

[99] R. Bharani and A. Sivaprakasam, "A Review Analysis on Performance and Classification of Wind Turbine Gearbox Technologies," *IETE Journal of Research*, vol. 68, no. 5, pp. 3341–3355, Sep. 2022, doi: 10.1080/03772063.2020.1756936.

[100] A. Dhanola and H. C. Garg, "Tribological challenges and advancements in wind turbine bearings: A review," *Engineering Failure Analysis*, vol. 118, p. 104885, Dec. 2020, doi: 10.1016/j.engfailanal.2020.104885.

[101] G. Shen, D. Xiang, K. Zhu, L. Jiang, Y. Shen, and Y. Li, "Fatigue failure mechanism of planetary gear train for wind turbine gearbox," *Engineering Failure Analysis*, vol. 87, pp. 96–110, May 2018, doi: 10.1016/j.engfailanal.2018.01.007.

[102] A. Bejger, E. Frank, and P. Bartoszko, "Failure Analysis of Wind Turbine Planetary Gear," *Energies*, vol. 14, no. 20, p. 6768, Oct. 2021, doi: 10.3390/en14206768.

[103] V. L. Jantara and M. Papaelias, "Wind turbine gearboxes: Failures, surface treatments and condition monitoring," in *Non-Destructive Testing and Condition Monitoring Techniques for Renewable Energy Industrial Assets*, Elsevier, 2020, pp. 69–90. doi: 10.1016/B978-0-08-101094-5.00005-8.

[104] J. Li, X. Zhang, X. Zhou, and L. Lu, "Reliability assessment of wind turbine bearing based on the degradation-Hidden-Markov model," *Renewable Energy*, vol. 132, pp. 1076–1087, Mar. 2019, doi: 10.1016/j.renene.2018.08.048.

[105] Z. Liu and L. Zhang, "A review of failure modes, condition monitoring and fault diagnosis methods for large-scale wind turbine bearings," *Measurement*, vol. 149, p. 107002, Jan. 2020, doi: 10.1016/j.measurement.2019.107002.

[106] Z. Xie, J. Jiao, K. Yang, T. He, R. Chen, and W. Zhu, "Experimental and numerical exploration on the nonlinear dynamic behaviors of a novel bearing lubricated by low viscosity lubricant," *Mechanical Systems and Signal Processing*, vol. 182, p. 109349, Jan. 2023, doi: 10.1016/j.ymssp.2022.109349.

[107] R. Ruiz De La Hermosa González-Carrato, F. P. García Márquez, K. Alexander, and M. Papaelias, "Methods and Tools for the Operational Reliability Optimisation of Large-Scale Industrial Wind Turbines," in *Proceedings of the Ninth International Conference on*

Management Science and Engineering Management, vol. 362, 2015, pp. 1175–1188. doi: 10.1007/978-3-662-47241-5_99.

[108] S. M. Gbashi, O. O. Olatunji, P. A. Adedeji, and N. Madushele, "From academic to industrial research: A comparative review of advances in rolling element bearings for wind turbine main shaft," *Engineering Failure Analysis*, vol. 163, p. 108510, Sep. 2024, doi: 10.1016/j.engfailanal.2024.108510.

[109] R. M. Arias Velásquez, "Bearings faults and limits in wind turbine generators," *Results in Engineering*, vol. 21, p. 101891, Mar. 2024, doi: 10.1016/j.rineng.2024.101891.

[110] J. Xue, K. Li, and Y. Shi, "Study on Permeability Characteristics of Gas Bearing Coal under Cyclic Load," *Sustainability*, vol. 14, no. 18, p. 11483, Sep. 2022, doi: 10.3390/su141811483.

[111] H. Peng, H. Zhang, Y. Fan, L. Shangguan, and Y. Yang, "A Review of Research on Wind Turbine Bearings' Failure Analysis and Fault Diagnosis," *Lubricants*, vol. 11, no. 1, p. 14, Dec. 2022, doi: 10.3390/lubricants11010014.

[112] J. Pei, X. Han, Y. Tao, and S. Feng, "Mixed elastohydrodynamic lubrication analysis of line contact with Non-Gaussian surface roughness," *Tribology International*, vol. 151, p. 106449, Nov. 2020, doi: 10.1016/j.triboint.2020.106449.

[113] N. Gao, C. T. Wang, R. J. K. Wood, and T. G. Langdon, "Tribological properties of ultrafine-grained materials processed by severe plastic deformation," *J Mater Sci*, vol. 47, no. 12, pp. 4779–4797, Jun. 2012, doi: 10.1007/s10853-011-6231-z.

[114] Ranko Antunović, Goran Siniković, Nikola Vučetić, and Amir Halep, "DIAGNOSTICS AND FAILURE OF PLAIN BEARINGS," *IETI Transactions on Engineering Research and Practice*, vol. 2, no. 2, Dec. 2018, doi: 10.6723/TERP.201812_2(2).0002.

[115] H. Li, Z. Yin, and Y. Wang, "A study on the wear behavior of tin-based journal bearing under different working conditions," *ILT*, vol. 72, no. 3, pp. 359–368, Sep. 2019, doi: 10.1108/ILT-04-2019-0123.

[116] X. Liang, C. Yang, Y. Guo, X. Sun, C. Ma, and L. Gu, "The Comprehensive Review of Wind Turbine Main Bearing Failures, Reinforcement Measures and Condition Monitoring," 2024. doi: 10.2139/ssrn.4683457.

[117] F. Manieri, K. Stadler, G. E. Morales-Espejel, and A. Kadiric, "The origins of white etching cracks and their significance to rolling bearing failures," *International Journal of Fatigue*, vol. 120, pp. 107–133, Mar. 2019, doi: 10.1016/j.ijfatigue.2018.10.023.

[118] M.-H. Evans, "An updated review: White etching cracks (WECs) and axial cracks in wind turbine gearbox bearings," *Materials Science and Technology*, vol. 32, no. 11, pp. 1133–1169, Jul. 2016, doi: 10.1080/02670836.2015.1133022.

[119] K. Kudelina, T. Baraškova, V. Shirokova, T. Vaimann, and A. Rassõlkin, "Fault Detecting Accuracy of Mechanical Damages in Rolling Bearings," *Machines*, vol. 10, no. 2, p. 86, Jan. 2022, doi: 10.3390/machines10020086.

[120] G. E. Morales-Espejel and A. Gabelli, "The Progression of Surface Rolling Contact Fatigue Damage of Rolling Bearings with Artificial Dents," *Tribology Transactions*, vol. 58, no. 3, pp. 418–431, May 2015, doi: 10.1080/10402004.2014.983251.

[121] F. Sadeghi, B. Jalalahmadi, T. S. Slack, N. Raje, and N. K. Arakere, "A Review of Rolling Contact Fatigue," *Journal of Tribology*, vol. 131, no. 4, p. 041403, Oct. 2009, doi: 10.1115/1.3209132.

[122] M. Stammler, A. Reuter, and G. Poll, "Cycle counting of roller bearing oscillations – case study of wind turbine individual pitching system," *Renewable Energy Focus*, vol. 25, pp. 40–47, Jun. 2018, doi: 10.1016/j.ref.2018.02.004.

[123] S. Zhao, L. Tie, Z. Guo, and J. Li, "Water deteriorates lubricating oils: removal of water in lubricating oils using a robust superhydrophobic membrane," *Nanoscale*, vol. 12, no. 21, pp. 11703–11710, 2020, doi: 10.1039/D0NR03305G.

[124] J. Kang, L. Sun, H. Sun, and C. Wu, "Risk assessment of floating offshore wind turbine based on correlation-FMEA," *Ocean Engineering*, vol. 129, pp. 382–388, Jan. 2017, doi: 10.1016/j.oceaneng.2016.11.048.

[125] R. Jaros *et al.*, "Advanced Signal Processing Methods for Condition Monitoring," *Arch Computat Methods Eng*, vol. 30, no. 3, pp. 1553–1577, Apr. 2023, doi: 10.1007/s11831-022-09834-4.

[126] Z. Gao and X. Liu, "An Overview on Fault Diagnosis, Prognosis and Resilient Control for Wind Turbine Systems," *Processes*, vol. 9, no. 2, p. 300, Feb. 2021, doi: 10.3390/pr9020300.

[127] W. Hu *et al.*, "Vibration-based bearing fault diagnosis of high-speed trains: A literature review," *High-speed Railway*, vol. 1, no. 4, pp. 219–223, Dec. 2023, doi: 10.1016/j.hspr.2023.11.001.

[128] S. Zhang, J. Zhou, E. Wang, H. Zhang, M. Gu, and S. Pirttikangas, "State of the art on vibration signal processing towards data-driven gear fault diagnosis," *IET Collab Intel Manufact*, vol. 4, no. 4, pp. 249–266, Dec. 2022, doi: 10.1049/cim2.12064.

[129] A. Nandi and H. Ahmed, *Condition Monitoring with Vibration Signals: Compressive Sampling and Learning Algorithms for Rotating Machine*, 1st ed. Wiley, 2019. doi: 10.1002/9781119544678.

[130] X. Long, P. Yang, H. Guo, Z. Zhao, and X. Wu, "A CBA-KELM-Based Recognition Method for Fault Diagnosis of Wind Turbines with Time-Domain Analysis and Multisensor Data Fusion," *Shock and Vibration*, vol. 2019, no. 1, p. 7490750, Jan. 2019, doi: 10.1155/2019/7490750.

[131] T. Wang, Q. Han, F. Chu, and Z. Feng, "Vibration based condition monitoring and fault diagnosis of wind turbine planetary gearbox: A review," *Mechanical Systems and Signal Processing*, vol. 126, pp. 662–685, Jul. 2019, doi: 10.1016/j.ymssp.2019.02.051.

[132] B. Cui, Y. Weng, and N. Zhang, "A feature extraction and machine learning framework for bearing fault diagnosis," *Renewable Energy*, vol. 191, pp. 987–997, May 2022, doi: 10.1016/j.renene.2022.04.061.

[133] K. F. Tom, "A Primer on Vibrational Ball Bearing Feature Generation for Prognostics and Diagnostics Algorithms:," Defense Technical Information Center, Fort Belvoir, VA, Mar. 2015. doi: 10.21236/ADA614145.

[134] B. R. Nayana and P. Geethanjali, "Analysis of Statistical Time-Domain Features Effectiveness in Identification of Bearing Faults From Vibration Signal," *IEEE Sensors J.*, vol. 17, no. 17, pp. 5618–5625, Sep. 2017, doi: 10.1109/JSEN.2017.2727638.

[135] A. S. Sait and Y. I. Sharaf-Eldeen, "A Review of Gearbox Condition Monitoring Based on vibration Analysis Techniques Diagnostics and Prognostics," in *Rotating Machinery, Structural Health Monitoring, Shock and Vibration, Volume 5*, T. Proulx, Ed., in Conference Proceedings of the Society for Experimental Mechanics Series. , New York, NY: Springer New York, 2011, pp. 307–324. doi: 10.1007/978-1-4419-9428-8_25.

[136] J. Igba, K. Alemzadeh, C. Durugbo, and E. T. Eiriksson, "Analysing RMS and peak values of vibration signals for condition monitoring of wind turbine gearboxes," *Renewable Energy*, vol. 91, pp. 90–106, Jun. 2016, doi: 10.1016/j.renene.2016.01.006.

[137] X. Liang, M. J. Zuo, and L. Liu, "A windowing and mapping strategy for gear tooth fault detection of a planetary gearbox," *Mechanical Systems and Signal Processing*, vol. 80, pp. 445–459, Dec. 2016, doi: 10.1016/j.ymssp.2016.04.034.

[138] S. A. Abouel-seoud, "Fault detection enhancement in wind turbine planetary gearbox via stationary vibration waveform data," *Journal of Low Frequency Noise, Vibration and Active Control*, vol. 37, no. 3, pp. 477–494, Sep. 2018, doi: 10.1177/1461348417725950.

[139] G. A. Skrimpas, T. Ursin, C. Sweeney, K. Marhadi, N. Mijatovic, and J. Holboell, "Residual signal feature extraction for gearbox planetary stage fault detection," *Wind Energy*, vol. 20, no. 8, pp. 1389–1404, Aug. 2017, doi: 10.1002/we.2099.

[140] W. Caesarendra and T. Tjahjowidodo, "A Review of Feature Extraction Methods in Vibration-Based Condition Monitoring and Its Application for Degradation Trend Estimation of Low-Speed Slew Bearing," *Machines*, vol. 5, no. 4, p. 21, Sep. 2017, doi: 10.3390/machines5040021.

[141] L. Hong and J. S. Dhupia, "A time domain approach to diagnose gearbox fault based on measured vibration signals," *Journal of Sound and Vibration*, vol. 333, no. 7, pp. 2164–2180, Mar. 2014, doi: 10.1016/j.jsv.2013.11.033.

[142] T. Wang, F. Chu, and Z. Feng, "Meshing frequency modulation (MFM) index-based kurtogram for planet bearing fault detection," *Journal of Sound and Vibration*, vol. 432, pp. 437–453, Oct. 2018, doi: 10.1016/j.jsv.2018.06.051.

[143] X. Jiang, "Research on Wind Turbine Fault Diagnosis Method Realized by Vibration Monitoring," *Ann. Data. Sci.*, vol. 11, no. 2, pp. 749–758, Apr. 2024, doi: 10.1007/s40745-023-00497-x.

[144] A. Ogaili, K. Mohammed, A. Jaber, and E. Al-Ameen, "Automated wind turbines gearbox condition monitoring: A comparative study of machine learning techniques based on vibration analysis," *FME Transactions*, vol. 52, no. 3, pp. 471–485, 2024, doi: 10.5937/fme2403471O.

[145] C. Beldjaatit, T. Sebbagh, and H. Guentri, "TIME DOMAIN APPROACH FOR ROLLING ELEMENT BEARING FAULT DETECTION AND DIAGNOSIS IN VIBRATION MONITORING," 2022.

[146] D. Neupane and J. Seok, "Bearing Fault Detection and Diagnosis Using Case Western Reserve University Dataset With Deep Learning Approaches: A Review," *IEEE Access*, vol. 8, pp. 93155–93178, 2020, doi: 10.1109/ACCESS.2020.2990528.

[147] X. Xu, X. Huang, H. Bian, J. Wu, C. Liang, and F. Cong, "Total process of fault diagnosis for wind turbine gearbox, from the perspective of combination with feature extraction and machine learning: A review," *Energy and AI*, vol. 15, p. 100318, Jan. 2024, doi: 10.1016/j.egyai.2023.100318.

[148] T. Barszcz, *Vibration-Based Condition Monitoring of Wind Turbines*, vol. 14. in Applied Condition Monitoring, vol. 14. Cham: Springer International Publishing, 2019. doi: 10.1007/978-3-030-05971-2.

[149] A. Kafeel *et al.*, "An Expert System for Rotating Machine Fault Detection Using Vibration Signal Analysis," *Sensors*, vol. 21, no. 22, p. 7587, Nov. 2021, doi: 10.3390/s21227587.

[150] X. Chen, B. Zhang, and D. Gao, "Bearing fault diagnosis base on multi-scale CNN and LSTM model," *J Intell Manuf*, vol. 32, no. 4, pp. 971–987, Apr. 2021, doi: 10.1007/s10845-020-01600-2.

[151] J. Zhang, G. Squicciarini, D. J. Thompson, W. Sun, and X. Zhang, "A hybrid time and frequency domain beamforming method for application to source localisation on high-speed trains," *Mechanical Systems and Signal Processing*, vol. 200, p. 110494, Oct. 2023, doi: 10.1016/j.ymssp.2023.110494.

[152] I. Bagri, K. Tahiry, A. Hraiba, A. Touil, and A. Mousrij, "Vibration Signal Analysis for Intelligent Rotating Machinery Diagnosis and Prognosis: A Comprehensive Systematic Literature Review," *Vibration*, vol. 7, no. 4, pp. 1013–1062, Oct. 2024, doi: 10.3390/vibration7040054.

[153] D. Abboud, J. Antoni, S. Sieg-Zieba, and M. Eltabach, "Envelope analysis of rotating machine vibrations in variable speed conditions: A comprehensive treatment," *Mechanical Systems and Signal Processing*, vol. 84, pp. 200–226, Feb. 2017, doi: 10.1016/j.ymssp.2016.06.033.

[154] M. H. Mohd Ghazali and W. Rahiman, "Vibration Analysis for Machine Monitoring and Diagnosis: A Systematic Review," *Shock and Vibration*, vol. 2021, no. 1, p. 9469318, Jan. 2021, doi: 10.1155/2021/9469318.

[155] D. Goyal and B. S. Pabla, "The Vibration Monitoring Methods and Signal Processing Techniques for Structural Health Monitoring: A Review," *Arch Computat Methods Eng*, vol. 23, no. 4, pp. 585–594, Dec. 2016, doi: 10.1007/s11831-015-9145-0.

[156] M. K. Bodla, S. M. Malik, M. T. Rasheed, M. Numan, M. Z. Ali, and J. B. Brima, "Logistic regression and feature extraction based fault diagnosis of main bearing of wind turbines," in *2016 IEEE 11th Conference on Industrial Electronics and Applications (ICIEA)*, Hefei, China: IEEE, Jun. 2016, pp. 1628–1633. doi: 10.1109/ICIEA.2016.7603846.

[157] H. D. M. De Azevedo, P. H. C. De Arruda Filho, A. M. Araújo, N. Bouchonneau, J. S. Rohatgi, and R. M. C. De Souza, "Vibration monitoring, fault detection, and bearings replacement of a real wind turbine," *J Braz. Soc. Mech. Sci. Eng.*, vol. 39, no. 10, pp. 3837–3848, Oct. 2017, doi: 10.1007/s40430-017-0853-2.

[158] D. Strömbergsson, P. Marklund, K. Berglund, and P. Larsson, "Bearing monitoring in the wind turbine drivetrain: A comparative study of the FFT and wavelet transforms," *Wind Energy*, vol. 23, no. 6, pp. 1381–1393, Jun. 2020, doi: 10.1002/we.2491.

[159] Y. Fu, Z. Gao, Y. Liu, A. Zhang, and X. Yin, "Actuator and Sensor Fault Classification for Wind Turbine Systems Based on Fast Fourier Transform and Uncorrelated Multi-Linear Principal Component Analysis Techniques," *Processes*, vol. 8, no. 9, p. 1066, Sep. 2020, doi: 10.3390/pr8091066.

[160] S. E. Kramti, J. B. Ali, E. Bechhoefer, K. Takrouni, A. Darghouthi, and M. Sayadi, "Toward an online strategy for mechanical failures diagnostics inside the wind turbine generators based on spectral analysis," *Wind Engineering*, vol. 45, no. 4, pp. 782–792, Aug. 2021, doi: 10.1177/0309524X211028759.

[161] Z. Tang, M. Wang, T. Ouyang, and F. Che, "A wind turbine bearing fault diagnosis method based on fused depth features in time–frequency domain," *Energy Reports*, vol. 8, pp. 12727–12739, Nov. 2022, doi: 10.1016/j.egyr.2022.09.113.

[162] C. Wang, S. Wan, X. Zhang, and X. Wang, "Research on a multi-sensor information fusion method for wind turbine gearbox fault diagnosis based on the BLSCFN model," *Meas. Sci. Technol.*, vol. 36, no. 1, p. 015126, Jan. 2025, doi: 10.1088/1361-6501/ad9512.

[163] Z. Fan and H. Li, "A hybrid approach for fault diagnosis of planetary bearings using an internal vibration sensor," *Measurement*, vol. 64, pp. 71–80, Mar. 2015, doi: 10.1016/j.measurement.2014.12.030.

[164] J. Yoon, D. He, B. Van Hecke, T. J. Nostrand, J. Zhu, and E. Bechhoefer, "Vibration-based wind turbine planetary gearbox fault diagnosis using spectral averaging," *Wind Energy*, vol. 19, no. 9, pp. 1733–1747, Sep. 2016, doi: 10.1002/we.1940.

[165] S. Shanbr, F. Elasha, M. Elforjani, and J. Teixeira, "Detection of natural crack in wind turbine gearbox," *Renewable Energy*, vol. 118, pp. 172–179, Apr. 2018, doi: 10.1016/j.renene.2017.10.104.

[166] S. Koukoura, J. Carroll, A. McDonald, and S. Weiss, "Wind turbine gearbox planet bearing failure prediction using vibration data," *J. Phys.: Conf. Ser.*, vol. 1104, p. 012016, Oct. 2018, doi: 10.1088/1742-6596/1104/1/012016.

[167] S. Wang, B. Zhao, and Y. Luo, "Wind turbine gearbox fault diagnosis based on the vibration spectrum analysis," *JCM*, vol. 19, no. 1, pp. 137–151, Jan. 2019, doi: 10.3233/JCM-180856.

[168] Y. Xu, G. Feng, X. Tang, S. Yang, F. Gu, and A. D. Ball, "A Modulation Signal Bispectrum Enhanced Squared Envelope for the detection and diagnosis of compound

epicyclic gear faults," *Structural Health Monitoring*, vol. 22, no. 1, pp. 562–580, Jan. 2023, doi: 10.1177/14759217221098577.

[169] A. Lakikza, H. Cheghib, and N. Kahoul, "Diagnosis of bearing faults in wind turbine systems using vibrational signal processing and machine learning," *Diagnostyka*, vol. 25, no. 3, pp. 1–8, Aug. 2024, doi: 10.29354/diag/191393.

[170] Y. Yang, Z. Peng, W. Zhang, and G. Meng, "Parameterised time-frequency analysis methods and their engineering applications: A review of recent advances," *Mechanical Systems and Signal Processing*, vol. 119, pp. 182–221, Mar. 2019, doi: 10.1016/j.ymssp.2018.07.039.

[171] J. Wang, Z. Mo, H. Zhang, and Q. Miao, "A Deep Learning Method for Bearing Fault Diagnosis Based on Time-Frequency Image," *IEEE Access*, vol. 7, pp. 42373–42383, 2019, doi: 10.1109/ACCESS.2019.2907131.

[172] D. Goyal and B. S. Pabla, "Condition based maintenance of machine tools—A review," *CIRP Journal of Manufacturing Science and Technology*, vol. 10, pp. 24–35, Aug. 2015, doi: 10.1016/j.cirpj.2015.05.004.

[173] R. A. Ayon-Sicaeros, E. Cabal-Yepez, L. M. Ledesma-Carrillo, and G. Hernandez-Gomez, "Broken-Rotor-Bar Detection Through STFT and Windowing Functions," in *2019 IEEE Sensors Applications Symposium (SAS)*, Sophia Antipolis, France: IEEE, Mar. 2019, pp. 1–5. doi: 10.1109/SAS.2019.8706086.

[174] A. H. Boudinar, A. F. Aimer, M. E. A. Khodja, and N. Benouzza, "Induction Motor's Bearing Fault Diagnosis Using an Improved Short Time Fourier Transform," in *Advanced Control Engineering Methods in Electrical Engineering Systems*, vol. 522, pp. 411–426. doi: 10.1007/978-3-319-97816-1_31.

[175] A. Nandi and H. Ahmed, *Condition Monitoring with Vibration Signals: Compressive Sampling and Learning Algorithms for Rotating Machine*, 1st ed. Wiley, 2019. doi: 10.1002/9781119544678.

[176] W. C. Lang and K. Forinash, "Time-frequency analysis with the continuous wavelet transform," *American Journal of Physics*, vol. 66, no. 9, pp. 794–797, Sep. 1998, doi: 10.1119/1.18959.

[177] C. Li, X. Yin, J. Chen, H. Yang, and L. Hong, "Bearing Fault Diagnosis Based on Wavelet Transform and Convolutional Neural Network," *OALib*, vol. 09, no. 06, pp. 1–14, 2022, doi: 10.4236/oalib.1108845.

[178] R. Nishat Toma and J.-M. Kim, "Bearing Fault Classification of Induction Motors Using Discrete Wavelet Transform and Ensemble Machine Learning Algorithms," *Applied Sciences*, vol. 10, no. 15, p. 5251, Jul. 2020, doi: 10.3390/app10155251.

[179] J. Shen *et al.*, "Exploring the Intrinsic Features of EEG Signals via Empirical Mode Decomposition for Depression Recognition," *IEEE Trans. Neural Syst. Rehabil. Eng.*, vol. 31, pp. 356–365, 2023, doi: 10.1109/TNSRE.2022.3221962.

[180] A. Susanto, C.-H. Liu, K. Yamada, Y.-R. Hwang, R. Tanaka, and K. Sekiya, "Application of Hilbert–Huang transform for vibration signal analysis in end-milling," *Precision Engineering*, vol. 53, pp. 263–277, Jul. 2018, doi: 10.1016/j.precisioneng.2018.04.008.

[181] D. Zhang and Z. Feng, "Enhancement of time-frequency post-processing readability for nonstationary signal analysis of rotating machinery: Principle and validation," *Mechanical Systems and Signal Processing*, vol. 163, p. 108145, Jan. 2022, doi: 10.1016/j.ymssp.2021.108145.

[182] R. Bajric, N. Zuber, G. A. Skrimpas, and N. Mijatovic, "Feature Extraction Using Discrete Wavelet Transform for Gear Fault Diagnosis of Wind Turbine Gearbox," *Shock and Vibration*, vol. 2016, pp. 1–10, 2016, doi: 10.1155/2016/6748469.

[183] C. Li, R.-V. Sanchez, G. Zurita, M. Cerrada, D. Cabrera, and R. E. Vásquez, "Gearbox fault diagnosis based on deep random forest fusion of acoustic and vibratory signals," *Mechanical Systems and Signal Processing*, vol. 76–77, pp. 283–293, Aug. 2016, doi: 10.1016/j.ymssp.2016.02.007.

[184] I. Vamsi, G. R. Sabareesh, and P. K. Penumakala, "Comparison of condition monitoring techniques in assessing fault severity for a wind turbine gearbox under non-stationary loading," *Mechanical Systems and Signal Processing*, vol. 124, pp. 1–20, Jun. 2019, doi: 10.1016/j.ymssp.2019.01.038.

[185] Z. Guo, Z. Pu, W. Du, H. Wang, and C. Li, "Improved adversarial learning for fault feature generation of wind turbine gearbox," *Renewable Energy*, vol. 185, pp. 255–266, Feb. 2022, doi: 10.1016/j.renene.2021.12.054.

[186] Y. Hu, X. Tu, F. Li, and G. Meng, "Joint High-Order Synchrosqueezing Transform and Multi-Taper Empirical Wavelet Transform for Fault Diagnosis of Wind Turbine Planetary Gearbox under Nonstationary Conditions," *Sensors*, vol. 18, no. 1, p. 150, Jan. 2018, doi: 10.3390/s18010150.

[187] J. Li, A. Deng, Y. Yang, and Q. Cheng, "Fault Diagnosis of Wind Turbine Drive Train using Time-Frequency Estimation and CNN," in *2019 Prognostics and System Health*

Management Conference (PHM-Qingdao), Qingdao, China: IEEE, Oct. 2019, pp. 1–5. doi: 10.1109/PHM-Qingdao46334.2019.8942851.

[188] I. Manarikkal, F. Elasha, and D. Mba, "Diagnostics and prognostics of planetary gearbox using CWT, auto regression (AR) and K-means algorithm," *Applied Acoustics*, vol. 184, p. 108314, Dec. 2021, doi: 10.1016/j.apacoust.2021.108314.

[189] Z. Jia and B. Yu, "A fault diagnosis method for rolling bearings of wind turbine generators based on MCGAN data enhancement," *SN Appl. Sci.*, vol. 5, no. 10, p. 259, Oct. 2023, doi: 10.1007/s42452-023-05485-7.

[190] Z. Feng, M. Liang, Y. Zhang, and S. Hou, "Fault diagnosis for wind turbine planetary gearboxes via demodulation analysis based on ensemble empirical mode decomposition and energy separation," *Renewable Energy*, vol. 47, pp. 112–126, Nov. 2012, doi: 10.1016/j.renene.2012.04.019.

[191] B. Tang, T. Song, F. Li, and L. Deng, "Fault diagnosis for a wind turbine transmission system based on manifold learning and Shannon wavelet support vector machine," *Renewable Energy*, vol. 62, pp. 1–9, Feb. 2014, doi: 10.1016/j.renene.2013.06.025.

[192] X. Yan and M. Jia, "A novel optimized SVM classification algorithm with multi-domain feature and its application to fault diagnosis of rolling bearing," *Neurocomputing*, vol. 313, pp. 47–64, Nov. 2018, doi: 10.1016/j.neucom.2018.05.002.

[193] V. Inturi, S. G R, and V. Sharma, "Integrated Vibro-Acoustic Analysis and Empirical Mode Decomposition for Fault Diagnosis of Gears in a Wind Turbine," *Procedia Structural Integrity*, vol. 14, pp. 937–944, 2019, doi: 10.1016/j.prostr.2019.07.074.

[194] R. Uma Maheswari and R. Umamaheswari, "Wind Turbine Drivetrain Expert Fault Detection System: Multivariate Empirical Mode Decomposition based Multi-sensor Fusion with Bayesian Learning Classification," *Intelligent Automation & Soft Computing*, vol. 26, no. 3, pp. 479–488, 2020, doi: 10.32604/iasc.2020.013924.

[195] D. Meng, H. Wang, S. Yang, Z. Lv, Z. Hu, and Z. Wang, "Fault Analysis of Wind Power Rolling Bearing Based on EMD Feature Extraction," *Computer Modeling in Engineering & Sciences*, vol. 130, no. 1, pp. 543–558, 2022, doi: 10.32604/cmes.2022.018123.

[196] X. Xia, X. Wang, and W. Chen, "Fault Diagnosis of Wind Turbine Gearbox Based on Improved Multivariate Variational Mode Decomposition and Ensemble Refined Composite Multivariate Multiscale Dispersion Entropy," *Entropy*, vol. 27, no. 2, p. 192, Feb. 2025, doi: 10.3390/e27020192.

[197] C. Beldjaatit, "Discrete Wavelet Transform and Energy Distribution for Effective Bearing Fault Detection and Analysis," *ELECTROTECHNICAL REVIEW*, vol. 1, no. 7, pp. 26–30, Jul. 2023, doi: 10.15199/48.2023.07.05.

[198] Bearing Data Center | Case School of Engineering. (n.d.). https://engineering.case.edu/bearingdatacenter

[199] J. Khelil, K. Khelil, M. Ramdani, and N. Boutasseta, "Bearing Faults Diagnosis Using Discrete Wavelets and Artificial Intelligence Approaches," in *2019 1st International Conference on Sustainable Renewable Energy Systems and Applications (ICSRESA)*, Tebessa, Algeria: IEEE, Dec. 2019, pp. 1–7. doi: 10.1109/ICSRESA49121.2019.9182516.

[200] J. Chae, S. Lee, J. Jang, S. Hong, and K.-J. Park, "A Survey and Perspective on Industrial Cyber-Physical Systems (ICPS): From ICPS to AI-Augmented ICPS," *Trans. Ind. Cyb-Phy. Sys.*, vol. 1, pp. 257–272, 2023, doi: 10.1109/TICPS.2023.3323600.

[201] Y. Zhang, Y. Xin, Z. Liu, M. Chi, and G. Ma, "Health status assessment and remaining useful life prediction of aero-engine based on BiGRU and MMoE," *Reliability Engineering & System Safety*, vol. 220, p. 108263, Apr. 2022, doi: 10.1016/j.ress.2021.108263.

[202] S. Jia, Y. Li, X. Wang, D. Sun, and Z. Deng, "Deep causal factorization network: A novel domain generalization method for cross-machine bearing fault diagnosis," *Mechanical Systems and Signal Processing*, vol. 192, p. 110228, Jun. 2023, doi: 10.1016/j.ymssp.2023.110228.

[203] C. F. De Lima Munguba, G. De Novaes Pires Leite, A. A. V. Ochoa, and E. Lopez Droguett, "Condition-based maintenance with reinforcement learning for refrigeration systems with selected monitored features," *Engineering Applications of Artificial Intelligence*, vol. 122, p. 106067, Jun. 2023, doi: 10.1016/j.engappai.2023.106067.

[204] X. Xu, X. Huang, H. Bian, J. Wu, C. Liang, and F. Cong, "Total process of fault diagnosis for wind turbine gearbox, from the perspective of combination with feature extraction and machine learning: A review," *Energy and AI*, vol. 15, p. 100318, Jan. 2024, doi: 10.1016/j.egyai.2023.100318.

[205] M. Tang, Q. Zhao, H. Wu, Z. Wang, C. Meng, and Y. Wang, "Review and Perspectives of Machine Learning Methods for Wind Turbine Fault Diagnosis," *Front. Energy Res.*, vol. 9, p. 751066, Nov. 2021, doi: 10.3389/fenrg.2021.751066.

[206] H. Malik and S. Mishra, "Artificial neural network and empirical mode decomposition based imbalance fault diagnosis of wind turbine using TurbSim, FAST and Simulink," *IET Renewable Power Gen*, vol. 11, no. 6, pp. 889–902, May 2017, doi: 10.1049/iet-rpg.2015.0382.

[207] J. Vrba, M. Cejnek, J. Steinbach, and Z. Krbcova, "A Machine Learning Approach for Gearbox System Fault Diagnosis," *Entropy*, vol. 23, no. 9, p. 1130, Aug. 2021, doi: 10.3390/e23091130.

[208] S. Awasthi, G. Singh, and N. Ahamad, "Classifying Electrical Faults in a Distribution System Using K-Nearest Neighbor (KNN) Model in Presence of Multiple Distributed Generators," *J. Inst. Eng. India Ser. B*, vol. 105, no. 3, pp. 621–634, Jun. 2024, doi: 10.1007/s40031-024-00994-4.

[209] S. Kumar, V. Kumar, S. Sarangi, and O. P. Singh, "Gearbox fault diagnosis: A higher order moments approach," *Measurement*, vol. 210, p. 112489, Mar. 2023, doi: 10.1016/j.measurement.2023.112489.

[210] W.-S. Zhao, C.-Y. Qu, and H.-B. Zhang, "Direct-Drive Wind Turbine Fault Diagnosis Based on Logistic Regression," in *2018 15th International Computer Conference on Wavelet Active Media Technology and Information Processing (ICCWAMTIP)*, Chengdu, China: IEEE, Dec. 2018, pp. 69–72. doi: 10.1109/ICCWAMTIP.2018.8632605.

[211] P. Waqas Khan and Y.-C. Byun, "Multi-Fault Detection and Classification of Wind Turbines Using Stacking Classifier," *Sensors*, vol. 22, no. 18, p. 6955, Sep. 2022, doi: 10.3390/s22186955.

[212] H. Wang, X. Zhao, and W. Wang, "Fault diagnosis and prediction of wind turbine gearbox based on a new hybrid model," *Environ Sci Pollut Res*, vol. 30, no. 9, pp. 24506–24520, Nov. 2022, doi: 10.1007/s11356-022-23893-x.

[213] X. Zheng, Y. Huang, Y. Xin, Z. Zhang, W. Liu, and D. Liu, "Sparse measure of bearing fault features based on Legendre wavelet multi-scale multi-mode Entropy," *Computers and Electrical Engineering*, vol. 116, p. 109204, May 2024, doi: 10.1016/j.compeleceng.2024.109204.

[214] J. Jiao, M. Zhao, J. Lin, and K. Liang, "A comprehensive review on convolutional neural network in machine fault diagnosis," *Neurocomputing*, vol. 417, pp. 36–63, Dec. 2020, doi: 10.1016/j.neucom.2020.07.088.

[215] Y. Kaya, F. Kuncan, and H. M. Ertunç, "A new automatic bearing fault size diagnosis using time-frequency images of CWT and deep transfer learning methods," *Turkish Journal of Electrical Engineering and Computer Sciences*, vol. 30, no. 5, pp. 1851–1867, Jul. 2022, doi: 10.55730/1300-0632.3909.

[216] X. Kong, L. Meng, Y. Su, T. Xu, X. Lan, and Y. Li, "Untrained Compound Fault Diagnosis for Planetary Gearbox Based on Adaptive Learning VMD and DSSECNN,"

IEEE Sensors J., vol. 23, no. 11, pp. 11838–11854, Jun. 2023, doi: 10.1109/JSEN.2023.3265724.

[217] P. Liang, C. Deng, X. Yuan, and L. Zhang, "A deep capsule neural network with data augmentation generative adversarial networks for single and simultaneous fault diagnosis of wind turbine gearbox," *ISA Transactions*, vol. 135, pp. 462–475, Apr. 2023, doi: 10.1016/j.isatra.2022.10.008.

[218] R. Chen, X. Huang, L. Yang, X. Xu, X. Zhang, and Y. Zhang, "Intelligent fault diagnosis method of planetary gearboxes based on convolution neural network and discrete wavelet transform," *Computers in Industry*, vol. 106, pp. 48–59, Apr. 2019, doi: 10.1016/j.compind.2018.11.003.

[219] H. Chen, H. Liu, X. Chu, Q. Liu, and D. Xue, "Anomaly detection and critical SCADA parameters identification for wind turbines based on LSTM-AE neural network," *Renewable Energy*, vol. 172, pp. 829–840, Jul. 2021, doi: 10.1016/j.renene.2021.03.078.

[220] X. Zhang, P. Han, L. Xu, F. Zhang, Y. Wang, and L. Gao, "Research on Bearing Fault Diagnosis of Wind Turbine Gearbox Based on 1DCNN-PSO-SVM," *IEEE Access*, vol. 8, pp. 192248–192258, 2020, doi: 10.1109/ACCESS.2020.3032719.

[221] O. Attallah, R. A. Ibrahim, and N. E. Zakzouk, "Fault diagnosis for induction generator-based wind turbine using ensemble deep learning techniques," *Energy Reports*, vol. 8, pp. 12787–12798, Nov. 2022, doi: 10.1016/j.egyr.2022.09.139.

[222] S. Yang *et al.*, "A 2DCNN-RF Model for Offshore Wind Turbine High-Speed Bearing-Fault Diagnosis under Noisy Environment," *Energies*, vol. 15, no. 9, p. 3340, May 2022, doi: 10.3390/en15093340.

[223] P. Waqas Khan and Y.-C. Byun, "Multi-Fault Detection and Classification of Wind Turbines Using Stacking Classifier," *Sensors*, vol. 22, no. 18, p. 6955, Sep. 2022, doi: 10.3390/s22186955.

[224] C. Zhang, D. Hu, and T. Yang, "Anomaly detection and diagnosis for wind turbines using long short-term memory-based stacked denoising autoencoders and XGBoost," *Reliability Engineering & System Safety*, vol. 222, p. 108445, Jun. 2022, doi: 10.1016/j.ress.2022.108445.

[225] M. Beretta, A. Julian, J. Sepulveda, J. Cusidó, and O. Porro, "An Ensemble Learning Solution for Predictive Maintenance of Wind Turbines Main Bearing," *Sensors*, vol. 21, no. 4, p. 1512, Feb. 2021, doi: 10.3390/s21041512.

[226] C. F. De Lima Munguba *et al.*, "Ensemble learning framework for fleet-based anomaly detection using wind turbine drivetrain components vibration data.," *Engineering*

Applications of Artificial Intelligence, vol. 133, p. 108363, Jul. 2024, doi: 10.1016/j.engappai.2024.108363.

[227] Y. Dong, H. Zhang, C. Wang, and X. Zhou, "Wind power forecasting based on stacking ensemble model, decomposition and intelligent optimization algorithm," *Neurocomputing*, vol. 462, pp. 169–184, Oct. 2021, doi: 10.1016/j.neucom.2021.07.084.

[228] Y. Lecun, L. Bottou, Y. Bengio, and P. Haffner, "Gradient-based learning applied to document recognition," *Proc. IEEE*, vol. 86, no. 11, pp. 2278–2324, Nov. 1998, doi: 10.1109/5.726791.

[229] M. Jalayer, C. Orsenigo, and C. Vercellis, "Fault detection and diagnosis for rotating machinery: A model based on convolutional LSTM, Fast Fourier and continuous wavelet transforms," *Computers in Industry*, vol. 125, p. 103378, Feb. 2021, doi: 10.1016/j.compind.2020.103378.

[230] Z. Chen, A. Mauricio, W. Li, and K. Gryllias, "A deep learning method for bearing fault diagnosis based on Cyclic Spectral Coherence and Convolutional Neural Networks," *Mechanical Systems and Signal Processing*, vol. 140, p. 106683, Jun. 2020, doi: 10.1016/j.ymssp.2020.106683.

[231] L. Chen, S. Li, Q. Bai, J. Yang, S. Jiang, and Y. Miao, "Review of Image Classification Algorithms Based on Convolutional Neural Networks," *Remote Sensing*, vol. 13, no. 22, p. 4712, Nov. 2021, doi: 10.3390/rs13224712.

[232] S. Djaballah, K. Meftah, K. Khelil, and M. Sayadi, "Deep Transfer Learning for Bearing Fault Diagnosis using CWT Time–Frequency Images and Convolutional Neural Networks," *J Fail. Anal. and Preven.*, vol. 23, no. 3, pp. 1046–1058, Jun. 2023, doi: 10.1007/s11668-023-01645-4.

[233] Fei Shen, Chao Chen, R. Yan, and R. X. Gao, "Bearing fault diagnosis based on SVD feature extraction and transfer learning classification," in *2015 Prognostics and System Health Management Conference (PHM)*, Beijing, China: IEEE, Oct. 2015, pp. 1–6. doi: 10.1109/PHM.2015.7380088.

[234] D. Neupane, Y. Kim, and J. Seok, "Bearing Fault Detection Using Scalogram and Switchable Normalization-Based CNN (SN-CNN)," *IEEE Access*, vol. 9, pp. 88151–88166, 2021, doi: 10.1109/ACCESS.2021.3089698.

[235] C. Cui, "Intelligent Analysis of Exercise Health Big Data Based on Deep Convolutional Neural Network," *Computational Intelligence and Neuroscience*, vol. 2022, pp. 1–11, Jun. 2022, doi: 10.1155/2022/5020150.

[236] M. S. Rathore and S. P. Harsha, "Roller Bearing Failure Analysis using Gaussian Mixture Models and Convolutional Neural Networks," *J Fail. Anal. and Preven.*, vol. 22, no. 5, pp. 1853–1871, Oct. 2022, doi: 10.1007/s11668-022-01469-8.

[237] R. M. Souza, E. G. S. Nascimento, U. A. Miranda, W. J. D. Silva, and H. A. Lepikson, "Deep learning for diagnosis and classification of faults in industrial rotating machinery," *Computers & Industrial Engineering*, vol. 153, p. 107060, Mar. 2021, doi: 10.1016/j.cie.2020.107060.

[238] M. Mohammed, H. Mwambi, B. Omolo, and M. K. Elbashir, "Using stacking ensemble for microarray-based cancer classification," in *2018 International Conference on Computer, Control, Electrical, and Electronics Engineering (ICCCEEE)*, Khartoum: IEEE, Aug. 2018, pp. 1–8. doi: 10.1109/ICCCEEE.2018.8515872.

[239] W. Jiang, Z. Chen, Y. Xiang, D. Shao, L. Ma, and J. Zhang, "SSEM: A Novel Self-Adaptive Stacking Ensemble Model for Classification," *IEEE Access*, vol. 7, pp. 120337–120349, 2019, doi: 10.1109/ACCESS.2019.2933262.

[240] S. Agarwal and C. R. Chowdary, "A-Stacking and A-Bagging: Adaptive versions of ensemble learning algorithms for spoof fingerprint detection," *Expert Systems with Applications*, vol. 146, p. 113160, May 2020, doi: 10.1016/j.eswa.2019.113160.

[241] T. M. Hospedales, A. Antoniou, P. Micaelli, and A. J. Storkey, "Meta-Learning in Neural Networks: A Survey," *IEEE Trans. Pattern Anal. Mach. Intell.*, pp. 1–1, 2021, doi: 10.1109/TPAMI.2021.3079209.

[242] Md. S. Khan, N. Salsabil, Md. G. R. Alam, M. A. A. Dewan, and Md. Z. Uddin, "CNN-XGBoost fusion-based affective state recognition using EEG spectrogram image analysis," *Sci Rep*, vol. 12, no. 1, p. 14122, Aug. 2022, doi: 10.1038/s41598-022-18257-x.

[243] J. Xie, Z. Li, Z. Zhou, and S. Liu, "A Novel Bearing Fault Classification Method Based on XGBoost: The Fusion of Deep Learning-Based Features and Empirical Features," *IEEE Trans. Instrum. Meas.*, vol. 70, pp. 1–9, 2021, doi: 10.1109/TIM.2020.3042315.

[244] J. Guo *et al.*, "An XGBoost-based physical fitness evaluation model using advanced feature selection and Bayesian hyper-parameter optimization for wearable running monitoring," *Computer Networks*, vol. 151, pp. 166–180, Mar. 2019, doi: 10.1016/j.comnet.2019.01.026.

[245] I. D. Mienye and Y. Sun, "A Survey of Ensemble Learning: Concepts, Algorithms, Applications, and Prospects," *IEEE Access*, vol. 10, pp. 99129–99149, 2022, doi: 10.1109/ACCESS.2022.3207287.

[246] Y. Wang and T. Wang, "Application of Improved LightGBM Model in Blood Glucose Prediction," *Applied Sciences*, vol. 10, no. 9, p. 3227, May 2020, doi: 10.3390/app10093227.

[247] A. Narin, "Detection of Focal and Non-focal Epileptic Seizure Using Continuous Wavelet Transform-Based Scalogram Images and Pre-trained Deep Neural Networks," *IRBM*, vol. 43, no. 1, pp. 22–31, Feb. 2022, doi: 10.1016/j.irbm.2020.11.002.

[248] M.-L. Huang and Y.-C. Liao, "Stacking Ensemble and ECA-EfficientNetV2 Convolutional Neural Networks on Classification of Multiple Chest Diseases Including COVID-19," *Academic Radiology*, vol. 30, no. 9, pp. 1915–1935, Sep. 2023, doi: 10.1016/j.acra.2022.11.027.

[249] M. Imane, C. Rahmoune, and D. Benazzouz, "Rolling bearing fault feature selection based on standard deviation and random forest classifier using vibration signals," *Advances in Mechanical Engineering*, vol. 15, no. 4, p. 168781322311685, Apr. 2023, doi: 10.1177/16878132231168503.

[250] S. Djaballah, L. Saidi, K. Meftah, A. Hechifa, M. Bajaj, and I. Zaitsev, "A hybrid LSTM random forest model with grey wolf optimization for enhanced detection of multiple bearing faults," *Sci Rep*, vol. 14, no. 1, p. 23997, Oct. 2024, doi: 10.1038/s41598-024-75174-x.

[251] S. Xiong *et al.*, "A Novel End-To-End Fault Diagnosis Approach for Rolling Bearings by Integrating Wavelet Packet Transform into Convolutional Neural Network Structures," *Sensors*, vol. 20, no. 17, p. 4965, Sep. 2020, doi: 10.3390/s20174965.

[252] A. Tharwat, "Parameter investigation of support vector machine classifier with kernel functions," *Knowl Inf Syst*, vol. 61, no. 3, pp. 1269–1302, Dec. 2019, doi: 10.1007/s10115-019-01335-4.

[253] E. Chatzi, I. Abdallah, M. Hofsäß, O. Bischoff, S. Barber, and Y. Marykovskiy, "Aventa AV-7 ETH Zurich Research Wind Turbine SCADA and high frequency Structural Health Monitoring (SHM) data." Zenodo, Aug. 08, 2023. doi: 10.5281/ZENODO.4964458.

[254] S. Barber, Y. Marykovskiy, and I. Abdallah, "Improving data sharing in wind energy - structural health monitoring case study," *J. Phys.: Conf. Ser.*, vol. 2767, no. 3, p. 032007, Jun. 2024, doi: 10.1088/1742-6596/2767/3/032007.